University of Oxford
Department of Physics

Frequency metrology at the 10^{-18} level with an ytterbium ion optical clock

Charles Baynham

The Queen's College

A thesis submitted for the degree of

Doctor of Philosophy

Supervisors:

Prof. Patrick Baird
&
Dr. Rachel Godun

December 2018

Acknowledgements

I am and will remain endlessly grateful to all those at the NPL, who welcomed me with open arms and wide grins into the wonderful and intricate world that all physicists inhabit. In the entire time I've spent here, I don't think I met a single person who wasn't willing at the drop of a hat to take half an hour out of their busy day and explain what they're doing for a clueless DPhil student. You made me feel welcomed and you taught me a lot.

I can't possibly list everyone to whom I owe thanks or this thesis will exceed its word limit, but let me name a few anyway. On the ytterbium project, thank you to Jonny for his taste in music and his wry humour; to Pete, the only person I've met who loves space more than I do; to Steve, who flew from project to project, filling us all with his own enthusiasm; to Anne for her endless supply of stories (and Oreos) and to Billy for his daily exuberance. Thank you also to Sean for his unfailingly logical approach to every aspect of life, and to Will for his easy smile and open heart. To Patrick and Patrick, for wisdom and perspective. To Helen, for her optimism. To Richard, to Ian, to Sean D, Hugh, Geoff, Guilong, Ross, Marco, Michael, Leonardo, Marco M, Miguel... the list could go on but I had better stop. And finally, to Rachel; for her ability to cut straight to the heart of a problem, for putting up with me for 4 years (and counting) and for being the most supportive supervisor I could have dreamed of.

But this section would be clearly incomplete without mentioning my family: they are the ones who made me who I am, so you have them to blame or thank. Georgie and Harry, who have been my closest friends, confidants and sometimes rivals since my memories began. Gaby, who brings me new adventures every day whether we're in the suburbs of Kingston or the jungles of Nepal: you've given my life a new and wonderful flavour. Dad, who taught me to take pride in what I do: I hope you'd still be proud today. And my Mum, who gave me everything that she had and would do it all again without a second of hesitation if she had to. Words cannot express my gratitude.

Thank you all.

Charles Baynham
September 2018

Abstract

Atomic clocks, the most accurate instruments in existence, are reaching new levels of precision. These devices now find novel uses—from the exploration of relativity [1] to the detection of dark matter [2, 3]—all from same principle: measurement of the frequency of the light that excites a reference atomic transition. The $^2S_{1/2}$ (F=0) $\rightarrow$ $^2F_{7/2}$ (F=3) electric octupole (E3) transition in $^{171}Yb^+$, with its $\Delta\nu \approx 1$ nHz [4] linewidth and low sensitivity to external electromagnetic fields, lends itself to this usage [5].

We probe this transition in a single $^{171}Yb^+$ ion held in a newly-designed end-cap RF trap [6]. This design achieves a low temperature rise of 0.14(14) K. Excess micromotion in the trap is automatically compensated, resulting in a fractional frequency uncertainty of the combined RF-Stark and 2nd order Doppler shifts of 3.6×10^{-19}. Anomalous phonon heating rates in the radial plane were measured as $(-4.9 \pm 5.2)\,s^{-1}$ and $(-1.3 \pm 3.6)\,s^{-1}$ for secular frequencies of 446 kHz and 470 kHz.

The ion's differential polarisability at $\lambda = 7\,\mu$m has been measured, suggesting a reduction in the BBR-related systematic error of the electric quadrupole (E2) transition by a factor of 5 and confirming the results of a previous measurement for the E3, performed using a different method [7]. However, a limitation prevented full confidence in our uncertainty levels.

To pre-stabilize the frequency of our laser a 28 cm long, ultra-stable Fabry-Pérot cavity was constructed and used to drive the E3 atomic resonance with a linewidth of 1.64(2) Hz. Its finesse was measured as 458 000 and, in an atomic lock, a clock stability of 1.9×10^{-15} $(\tau/1\,s)^{-1/2}$ was observed. The laser's frequency was measured and its stability transferred to other wavelengths via a femtosecond optical frequency comb.

An international clock comparison campaign was carried out via satellite-mediated microwave links: the first of its scale, involving 4 National Measurement Institutes (NMIs) and 5 optical atomic clocks. A new technique was developed to analyse the resulting data and to characterize its uncertainty. The lowest fractional uncertainty in the comparison between any pair of clocks was 2.8×10^{-16}.

Finally, an absolute measurement of the E3 transition has been carried out through a link to International Atomic Time (TAI), without a local primary standard. The transition frequency was measured to be 642 121 496 772 645.17(22) Hz: the best measurement of this transition to date [8, 9].

Contents

List of Figures

A note on notation

For the typesetting of mathematics and physical constants, this thesis uses the following conventions:

Item	Representation	Components
Scalar / complex number	a	
Vector	$\mathbf{A}$	$\mathrm{A_i}$
Unit vector	$\hat{\mathbf{n}}$	
Cartesian unit vectors	$\hat{\mathbf{e}}_\mathbf{x}, \hat{\mathbf{e}}_\mathbf{y}, \hat{\mathbf{e}}_\mathbf{z}$	
Matrix	$\boldsymbol{A}$	A_{ij}
Operator	$\tilde{H}$	$\tilde{H}_{ij}$
Vector operator	$\tilde{\mathbf{x}}$	$\tilde{\mathrm{x}}_\mathrm{i}$
Differentiation w.r.t. time	$\dot{a}$, $\dot{\mathbf{A}}$, $\dot{\tilde{\mathbf{x}}}$	
Displacement from origin	$\mathbf{x}$	
Expectation over time	$\langle \ldots \rangle$	
Expectation over values of x	$\langle \ldots \rangle_x$	
$\sqrt{-1}$	i	
Definition of x	$x \stackrel{\text{def}}{=} \ldots$	
atomic Hamiltonian	$\tilde{H}_0$	
Bohr magneton	μ_B	
Boltzmann constant	k_B	
differential polarizability	$\Delta\alpha$	
electric permittivity	ϵ_0	
Elementary charge	e	
Euler's number	e	
fine-structure constant	α	
mass of electron	m_e	
$\mathrm{n^{th}}$ Bessel function	J_n	
Planck's constant	h	
proton-to-electron mass ratio	μ	
reduced Planck's constant	$\hbar$	
speed of light	c	
Stefan-Boltzmann constant	σ_{SB}	

The field of atomic physics is prey to a bewildering array of acronyms. In an attempt to combat this, every acronym in this thesis has been recorded in a list of acronyms and typeset as, e.g. ECDL.

Introduction 1

> Time is an illusion. Lunchtime doubly so.
>
> — *Douglas Adams*

Time began in Aberdeen, Scotland, where the first recorded example of a calendar was built over 10 000 years ago [10]. In Egypt, humanity became fully aware of its passage, making sundials to split the days into hours. The concept was refined in Persia with the water clocks that first allowed humans to agree on units of time as small as the second [10, 11]. In the 16th century, time started to work for us: on the ships of Europe and beyond, as sailors carried accurate time with them across the oceans and used it to navigate them home again [12, 13].

But the field reached maturity in 1955 when Louis Essen invented the first atomic clock. Soon after, in 1967, time outgrew its age-old link with the Earth and was linked instead to fundamental properties of the universe, via the energy gap between hyperfine states in the only stable isotope of caesium. Since then, successive generations have shaved off first the nanoseconds, then the pico- and the femtoseconds from their timekeeping. Now, optical atomic clocks routinely operate at the attosecond level and

it is very conceivable that in the next few years we will push lower still, to exponents so small that most people are not familiar with their name.*

With this breathtaking level of accuracy† comes capabilities that clock-makers of the past may not have expected. Modern clocks still navigate us around the world, but now they can measure our position to less than 10 m anywhere on the globe [14, 15]. Their cousins, the oscillators, act as metronomes for the latest generation of communication networks [16].

Perhaps more surprisingly, the role of clocks in science is changing. Until now, clocks have served as references against which other things are measured. Now, clocks probe general relativity's mixing of time and space [1, 17]. They can search for changes in the constants that govern our universe [18, 19], for topological dark matter [2, 20, 21] and measure the Higgs' coupling to the electron [22].

As a new generation of instruments with an unprecedented level of sensitivity, optical atomic clocks are shining light into areas of physics at the very edges of our understanding. If the clock came of age in 1955, then today we may be witnessing the beginning of its golden age.

1.1 The How?

But first, how do they work? Humans have built clocks for generations and the basic principles remain the same. In this section those principles and how they have been refined will be explored.

*Next comes the zeptosecond...
†See §1.1.2 for a discussion of the term "accuracy".

1.1.1 Clocks, of the atomic variety

Most clocks have three parts: the reference, the oscillator and the counter. The reference serves to provide some unchanging, constant frequency upon whose value distant experimenters can agree. The oscillator is a local device whose oscillation rate can be steered to match the reference that we take as a standard. And the counter allows us to measure accurately these oscillations so that we may use them to tell the time. All three of these components are essential to a clock's operation, and so improving your clock involves parallel development in three directions.

Broadly, clocks may be split into two categories: active and passive. Active clocks merge the reference and the oscillator: the counter directly counts the reference, dispensing with a *local oscillator*. Examples include sundials, whose reference is the diurnal rotation of the planet and which directly read the shadow cast by this effect. Some modern clocks do use this architecture, notably the hydrogen maser [23] that commonly drives national timescales [24], but the most accurate systems are now passive.

In a passive system, the oscillator and the reference are now distinct and the oscillator's frequency is controlled by the experimenter to match that of the reference. The classic example is a traditional pendulum clock, whose oscillator is the constant swing of a pendulum, but whose reference was the rotation of the earth. By adjusting the period of the pendulum's oscillation, the horologist ensures that the clock reads noon when the sun is at its highest in the sky: a manual feedback loop of very low bandwidth.[‡] This passive architecture allows for the use of much weaker reference signals: useful in atomic systems since stronger signals often come with stronger perturbations.

The first atomic clocks were based on the energy gap between the hyperfine levels in an atom of caesium, the microwave transition which is still used today to define the

[‡]This process is called "locking" or "servoing" and these terms will be used interchangeably in this thesis.

SI second. The benefit of using an atomic clock over the previous system of solar or ephemeris time[§] is clear: all atoms are quantum mechanically identical, and so their properties can act as universal references valid even at the far ends of the universe. These caesium clocks have improved by 6 orders of magnitude since their advent—no mean feat (see Figure 1.4)—but now there is a newcomer to the scene.

1.1.2 Optical clocks

The optical atomic clock works on the same principle as the microwave atomic clock, but instead measures a transition with optical energies.[¶] This brings key advantages which motivate the pursuit, but also challenges. To understand these advantages, we introduce some formalism.

The fluctuations in an oscillator can be described by use of the Allan variance (AVAR). This quantity is defined for a time-series of measurements $y_0 \dots y_n$ taken at discrete times $t_0 \dots t_n$ spaced by δt as [25, 26]

$$\sigma_y^2(\tau) \stackrel{\text{def}}{=} \frac{1}{2} \left\langle (\bar{y}(t_i) - \bar{y}(t_i + \tau))^2 \right\rangle_i \tag{1.1}$$

$$\text{where} \quad \bar{y}(t_i) \stackrel{\text{def}}{=} \frac{1}{\tau} \sum_{j=i}^{i+\frac{\tau}{\delta t}-1} y_j \quad . \tag{1.2}$$

$\sigma_y^2(\tau)$ is a measure of the expected RMS instability at a timescale of τ, where τ is an integer multiple of δt.

This quantity has the useful effect of revealing different "colours" of noise—defined according to their Power Spectral Densities (PSDs)—by its slope. The exception to

[§]Gone are the days where there was such a thing as "the time". Now, there is a multitude of different time scales for different purposes, some of them historical. Ephemeris time refers to a time scale defined by the movements of astronomical bodies in their orbits.

[¶]One could argue that there is currently no such thing as an optical atomic clock, and that we are in the business of making frequency standards. Of course it's easy to convert a frequency standard to a clock; you just run it continuously and integrate. This simple task has kept experimentalists busy for quite some time, but we are getting there: as the systems underpinning optical clocks become more robust, their uptimes are now reaching the point at which we may start to truthfully call them clocks.

this occurs for white phase versus flicker phase noise, between which the Allan variance cannot discriminate. For this reason the Modified Allan variance (MVAR) was introduced [26], which can. For more information on these measures, see [26–29].

This useful figure of merit defined, we now consider the statistical fluctuations of a clock limited by atomic statistics, the scenario expected when all sources of technical noise have been minimised: [30]

$$\sigma_y(\tau) \approx \frac{1}{\sqrt{N}} \frac{\Delta\nu}{\nu_0} \sqrt{\frac{t_m}{\tau}} \tag{1.3}$$

with N the number of atoms; $\Delta\nu, \nu_0$ the width and frequency of the atomic resonance; and t_m the time required to take one measurement. This equation represents the fastest possible averaging, limited by the randomness introduced when the wavefunction of an atomic excitation is collapsed, a noise source known as Quantum Projection Noise (QPN) [31].[‖]

The advantage of an optical clock is now immediately apparent: the *quality factor* $\mathcal{Q} = \nu_0/\Delta\nu$ is boosted in optical clocks by the much larger transition frequencies ν_0. Comparing the frequencies of $^{171}Yb^+$'s E3 transition to the caesium hyperfine transition, $\mathcal{Q}$ could theoretically be increased by a factor of 70 000, all else being equal.[**]

This boost in achievable *stability* is not the only benefit. Systematic effects that perturb transition frequencies affect the *accuracy* of the clock, and usually operate by moving the atom's energy levels. With a larger gap between these levels, the fractional impact of these effects is often reduced as well.

These two terms, accuracy and stability, are the most important measures of a clock's performance. The clock's stability (often quoted as its fractional stability

[‖]It may be possible to get around this limit by avoiding making a projective measurement. §8.2.1.6 will mention this idea.

[**]The $\mathcal{Q}$-factor is actually dependent on τ, the time spent probing the transition, since the observable linewidth is subject to the Fourier limit: see §1.1.4.

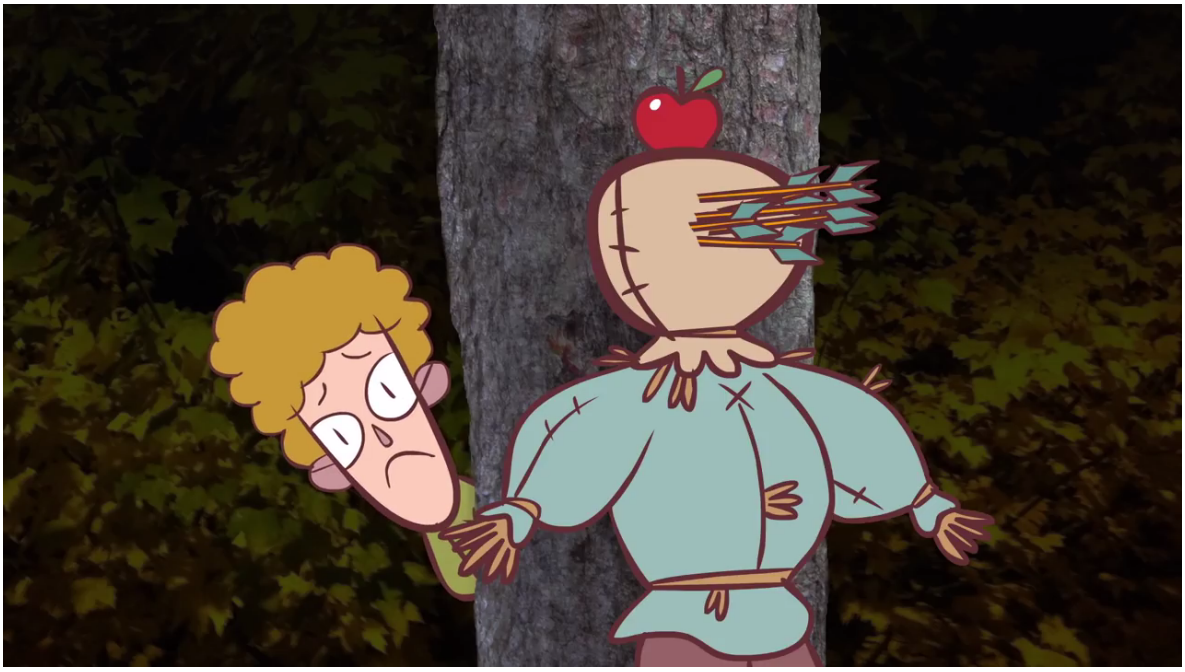

Figure 1.1: An example of a system with high stability but low accuracy. Image from [34]

at $\tau_0 = 1\,\mathrm{s}$ with the assumption that its noise processes are white, implying that $\sigma(\tau) = \sigma(\tau_0)/\sqrt{\tau/\tau_0}$) measures how quickly a clock's uncertainty reduces with averaging. Its accuracy, commonly given as a fractional frequency uncertainty $\Delta\nu/\nu_0$, is the level at which further averaging no longer helps, since statistical uncertainty is now outweighed by uncertainty in the offset between the observed transition frequency and its unperturbed value (see Chapter 5). In the limit of infinite averaging time, a clock's accuracy defines the uncertainty with which it realises the SI second, currently defined by caesium [32]. By definition therefore, it is not possible to perform an absolute frequency measurement with more accuracy than the best caesium clock: a motivating factor in the impending redefinition of the second [33].

1.1.2.1 The reference

As mentioned before, our reference in an optical atomic clock is the frequency of a transition between energy levels. For us, this is either the electric quadrupole (E2) $^2S_{1/2}$ (F=0) $\rightarrow$ $^2D_{3/2}$ (F=2) transition or the electric octupole (E3) $^2S_{1/2}$ (F=0) $\rightarrow$ $^2F_{7/2}$ (F=3) transition in an ion of $^{171}Yb^+$ ($I = 1/2$) confined in a quadrupole Paul trap.

Pretty much any optical transition could provide the large value of ν_0 that we want, but not every transition is suitable for operation as a clock. First and most obviously, the other term in the $\mathcal{Q}$-factor, $\delta\nu$, must be considered.

For a high $\mathcal{Q}$-factor, a narrow line is needed. The Uncertainty Principle is often used to link uncertainty in the energy of a transition to uncertainty in its duration through $\Delta E\,\tau \geq \hbar/2$. [35, 36] Another way of seeing the same thing is to treat the atom-electron system as a classical damped oscillator:

$$\mathbf{F} = m\frac{\mathrm{d}^2}{\mathrm{d}t^2}\mathbf{r} = -m\omega_0^2\,\mathbf{r} - m\gamma\frac{\mathrm{d}\mathbf{r}}{\mathrm{d}t} \tag{1.4}$$

for an electron of mass m and position $\mathbf{r}$. ω_0 is the transition frequency which this simple model cannot predict and $\gamma = 1/\tau$ is the damping coefficient which represents spontaneous decay and is equal to the Einstein A coefficient [35–39]. This equation of motion results in damped oscillations: an oscillating dipole which radiates the electromagnetic wave shown in Figure 1.2. The Fourier transform of these decaying oscillations has a Lorentzian profile and a width of $\gamma = 1/\tau$: the transition's natural linewidth. A fully rigorous, quantum mechanical treatment of this subject is given by Weisskopf-Wigner theory and can be found in [40–42].

For a narrow line therefore, a transition with a long lifetime is needed, precluding electric dipole-allowed transitions. Some clock systems, $^{171}Yb^+$ included, use quadrupole- or octupole-permitted transitions (ours uses both) [5, 43–47]. Others use $J = 0 \rightarrow 0$

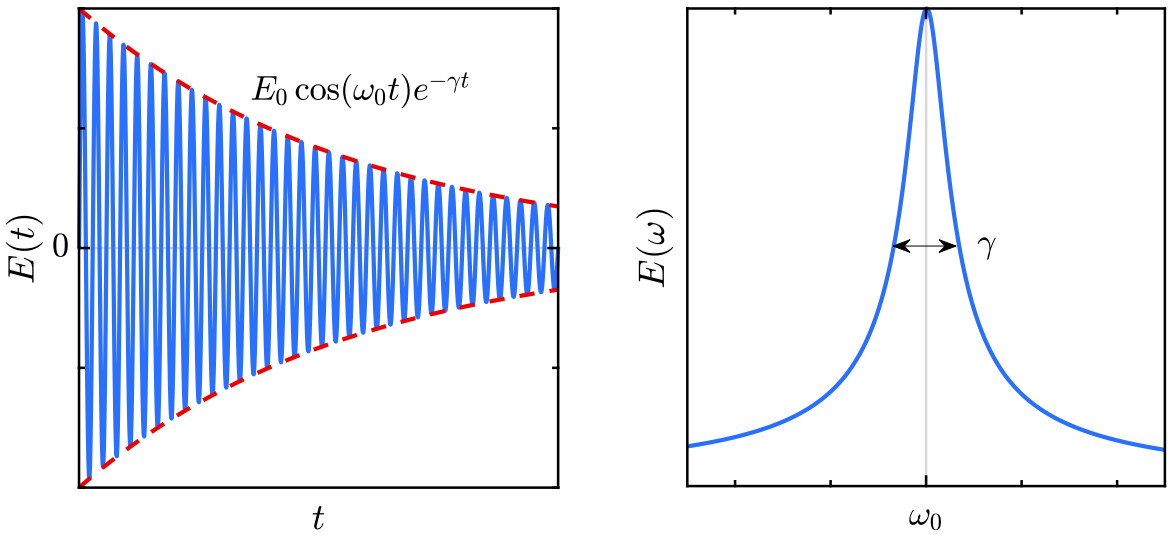

Figure 1.2: Electric field radiated by an oscillating electron in the classical damped-oscillator model.
(a) The electric field radiated by the electron decays with a time constant τ.
(b) Fourier transformed, this appears as a Lorentzian function with linewidth $1/\tau$.

transitions [47–52] (using either large magnetic bias fields or nuclear spin to permit the transition) or spin-forbidden intercombination transitions [53]. Whatever the choice, the $\mathcal{Q}$-factor is not the only consideration. Systematic effects such as sensitivity to IR radiation from environmental Black-Body Radiation (BBR), magnetic fields or electric quadrupole fields must also be considered; the ideal candidate would respond as little as possible to changes in its environment.

Your reference chosen, the atom must now be trapped. The best microwave clocks use a fountain of atoms, performing Ramsey interrogation over the atom's time of flight. For optical clocks however, atoms are typically confined in either an ion trap or an optical lattice. The appeal of a lattice of atoms is the large signal they provide: the factor $\sqrt{N}$ in Equation 1.3 is not 1. The downside is that shifts to the atoms' transitions tend to be larger, making them harder to eliminate. The pros and cons of an ion clock are roughly the inverse of these.

1.1.2.2 The oscillator

For an optical clock, there is no other choice for a local oscillator than a laser. The lasers used for precision spectroscopy are commonly referred to as "ultra stable", since their frequency stability over short timescales can be breathtaking: better that 1 Hz at 1 s. The stability of your local oscillator is important for three reasons:

Spectral density Operators of clocks based on ultra-narrow transitions who wish to see their clock transitions driven must achieve Rabi frequencies on the order of 1 Hz. Considering the $^{171}Yb^{+}$ E3 transition whose natural linewidth is on the order of 1 nHz [4], the spectral overlap of a typical stable laser with a linewidth of several kilohertz would be negligible. The huge powers needed to drive your transition would themselves become problematic, causing shifts to the transition's frequency (see Section 5.2).

Dick effect Equation 1.3 contains a term for the time taken to make a measurement $t_m = t_p + t_D$ where t_D is the *dead time* in a clock's cycle. During this time the local oscillator is free-running and so its stability affects the clock's. This t_D is typically a limiting factor in lattice-based clocks since their dead-time fraction is larger and their QPN is lower than for ion-based systems [54, 55].

Coherence time §1.1.4 will explain how long probe times result in narrower spectral lines. However the laser's stability places a limit on how long a probe time is possible before the local oscillator's phase can no longer be predicted [56]. This is typically a larger problem for ion clocks, since these usually operate at the QPN limit and so an increase in $\delta\nu$ is equivalent to a worse stability (see Equation 1.3).

1.1.2.3 The counter

The counter was one of the main challenges when optical clocks were first suggested. Counting the frequency of a microwave transition is possible with electronics and frequency counters that go up to 46 GHz can be bought off-the-shelf [57]. The same is not possible for the ∼500 THz frequencies associated with optical transitions.

A field-changing innovation was found in the optical frequency comb by John Hall and Theodor Hänsch, an invention that earned them the Nobel prize for Physics [58–60]. A frequency comb appears as an evenly spaced set of "teeth" in frequency space and is (usually[††]) generated from a pulse-chain of ultra-short laser pulses. Interference between these teeth and the frequency of interest produces a beat which can be measured with conventional electronics. Section 2.6 will treat this incredible machine, which lies at the heart of all optical clock experiments worldwide, more thoroughly.

1.1.3 Driving the forbidden

§1.1.2.1 mentioned a variety of forbidden transitions that experimenters around the world have turned into optical clocks. But how is it possible to drive these transitions if they are so "forbidden?" The answer lies in the *electric dipole approximation* usually made when considering the interaction of light with matter in the semi-classical picture.

The Hamiltonian for an ensemble of electrons in the presence of an electromagnetic plane wave can be shown to be [§10.3.2 62, eq.4.31 63]

$$\begin{aligned}\tilde{H} &= \tilde{H}_0 + \tilde{V} \\ &= \tilde{H}_0 + \frac{e}{2m_e}\sum_j \mathbf{A_0}\cdot\tilde{\mathbf{p}}_\mathbf{j}\left(\mathrm{e}^{i(\mathbf{k}\cdot\tilde{\mathbf{x}}_\mathbf{j}-\omega t)} + \mathrm{e}^{-i(\mathbf{k}\cdot\tilde{\mathbf{x}}_\mathbf{j}-\omega t)}\right)\end{aligned} \tag{1.5}$$

[††]Work is under way to create optical frequency combs using the interaction between the Kerr nonlinearity of monolithic high-$\mathcal{Q}$ micro-resonators and a continuous-wave (CW) pump laser [61]. Such a comb would be more compact and less complex than current mode-locked laser devices, while also permitting much higher repetition rates.

where $\mathbf{A_0}$ is the amplitude of the electromagnetic vector potential for a plane wave propagating with wave-vector $\mathbf{k}$ and angular frequency ω and the sum is over all electrons. $\tilde{H}_0$ is the usual atomic Hamiltonian, $\tilde{\mathbf{p}}_\mathbf{j}$ is the momentum operator for the jth electron and the perturbation $V(t)$ caused by the wave is small.

It is usual at this point to consider the Taylor expansion of the exponentials,

$$\mathrm{e}^{i(\mathbf{k}\cdot\tilde{\mathbf{x}}_\mathbf{j}-\omega t)} = \left[1 + i\,\mathbf{k}\cdot\tilde{\mathbf{x}}_\mathbf{j} - \frac{1}{2}(\mathbf{k}\cdot\tilde{\mathbf{x}}_\mathbf{j})^2 + \ldots\right]\mathrm{e}^{-i\omega t} \quad , \tag{1.6}$$

and make the approximation that, since the radiation's wavelength is much larger than the extent of the atom, $\mathbf{k}\cdot\tilde{\mathbf{x}}_\mathbf{j} \ll 1$ and the whole exponential can be replaced by 1. This is the *electric dipole approximation* referred to above and results in the matrix elements $\tilde{\mathrm{V}}_{\mathrm{ij}} \propto \langle i|\hat{\mathbf{A}}_\mathbf{0}\cdot\tilde{\mathbf{x}}|j\rangle$. The usual atomic selection rules disallow transitions where this operator's symmetry causes this matrix element to vanish between states.

For electric quadrupole (E2) and electric octupole (E3) transitions $\langle g|\tilde{\mathbf{x}}|e\rangle = \mathbf{0}$, but it is the extra terms in the multipole expansion of Equation 1.6 that result in a non-zero total matrix element and therefore a finite transition rate when Fermi's golden rule is applied [64].

1.1.4 The Fourier limit

As alluded to above, the $\mathcal{Q}$-factor of a clock transition depends on the time spent probing it: this comes about via the Fourier broadening of laser pulses.

Neglecting the finite frequency width of our probe laser, its electric field at the ion's position can be written as a perfect sinusoid: $\mathbf{E_L} = E_0\hat{\mathbf{n}}\cos(\omega t)$. To form a pulse, we turn our laser on for a time t_p and then extinguish it. The field experienced by the ion

is therefore the laser's electric field multiplied by the Heaviside step function:

$$\mathbf{E}(t) = E_0 \hat{\mathbf{n}} \cos(\omega_0 t) \times \Pi\left(\frac{t}{t_p}\right) \tag{1.7}$$

$$\text{where } \Pi(\alpha) = \begin{cases} 1 & \text{if } |\alpha| < \frac{1}{2}, \\ \frac{1}{2} & \text{if } |\alpha| = \frac{1}{2} \text{ and} \\ 0 & \text{otherwise.} \end{cases}$$

The resultant waveform, shown in Figure 1.3(a), can be Fourier transformed to obtain its frequency components. Using the convolution theorem, $E(\omega)$ can be written as the convolution of the transforms of the two functions which, in the time domain, were multiplied. This is simply

$$E(\omega) = \mathscr{F}\left\{|\mathbf{E}(t)|\right\} = E_0\ \delta(\omega_0) \circledast \frac{t_p}{2\pi} \operatorname{sinc}\left(\frac{t_p \omega}{2}\right) \quad : \tag{1.8}$$

a sinc function shifted to be centred around ω_0 by convolution with the Dirac delta function.

The square of this field gives the intensity of the probe light at the ion: proportional to the Rabi frequency Ω_0 and, for weak excitations where $|\langle g|\Psi\rangle| \approx 1$ throughout, to the excitation probability [65, 66]. This is the blue line in Figure 1.3(b), and results in a linewidth of $\delta\nu_{\text{weak}} = 0.8859/t_p$. For the more interesting case where the probe light significantly affects the population of the initial state, solution of the time-dependent Schrödinger equation (TDSE) gives the Fourier-limited linewidth as [§7.3 65]

$$\delta\nu_{\mathcal{F}} = \frac{0.7987}{t_p} \quad . \tag{1.9}$$

If we assume that the clock cycle has negligible dead-time (a good approximation for ion clocks), insertion of this expression into Equation 1.3 shows that

$$\sigma_y(\tau) \propto \frac{1}{\sqrt{t_m}} \quad , \tag{1.10}$$

an important incentive to keep the coherence time of your local oscillator as high as possible (see Chapter 6).

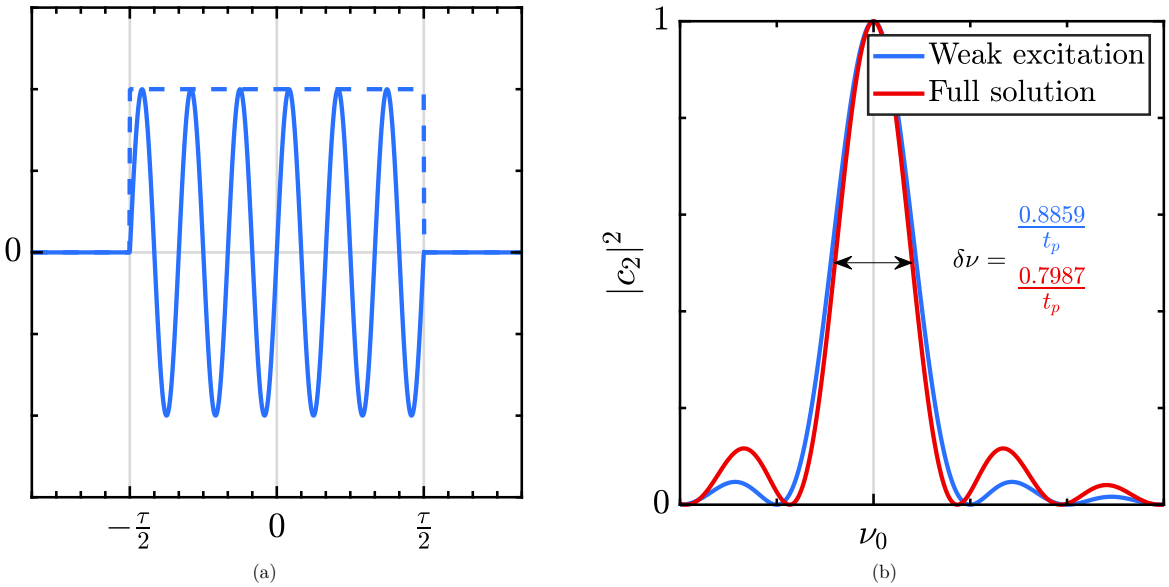

FIGURE 1.3: Excitation of an atomic resonance with a Fourier-limited π-pulse. *(left)* A sinusoidal waveform truncated by a Heaviside envelope: the form taken by a laser pulse used to excite an atomic transition. *(right)* The excitation fraction where $c_2 = \langle e|\Psi\rangle$ for a pulse of length $t_p = \pi/\Omega$ (Ω is the transition's Rabi frequency) detuned from the transition's centre frequency ν_0. The blue line shows the Fourier spectrum of the pulse shown in (a), equal to the atomic excitation under the assumption that the system remains mostly in the ground state (an invalid assumption for most of this plot). The red line shows the excitation profile calculated without this simplifying assumption. Due to the similarity of these two profiles, frequency metrologists often refer to the "Fourier limit" for the minimum linewidth observable with a given pulse time t_p.

1.2 The Why?

Now we know roughly how a clock works, we may ask "why bother?" Certainly that is the question that guests in our laboratory are often too polite to voice when told how much work it takes to go from the 17$^{\text{th}}$ decimal place to the 18$^{\text{th}}$. But we are far from alone in our efforts, as Figure 1.4 shows. There are many answers to that question, ranging from fundamental physics to technological applications: by the end of this section I hope you will agree that clocks are no longer just about timekeeping.

1.2.1 Technological applications

Maybe the most common use cited in answer to the above question relates to Global Navigation Satellite Systems (GNSSs). GNSSs, or most commonly the US's Global Positioning System (GPS), consist of a constellation of clocks in space that regularly beam out the time: small differences in the time received from the satellites reveal the user's distance from them, allowing their local position to be determined anywhere on the world with 4 m accuracy [14]. These satellites contain rubidium-based oscillators with a fractional stability of around $1.6 \times 10^{-13}\,(\tau/1\,\mathrm{s})^{-1/2}$: it is not hard to imagine that replacing these with clocks of up to three orders of magnitude better stability could one day improve the system [15].

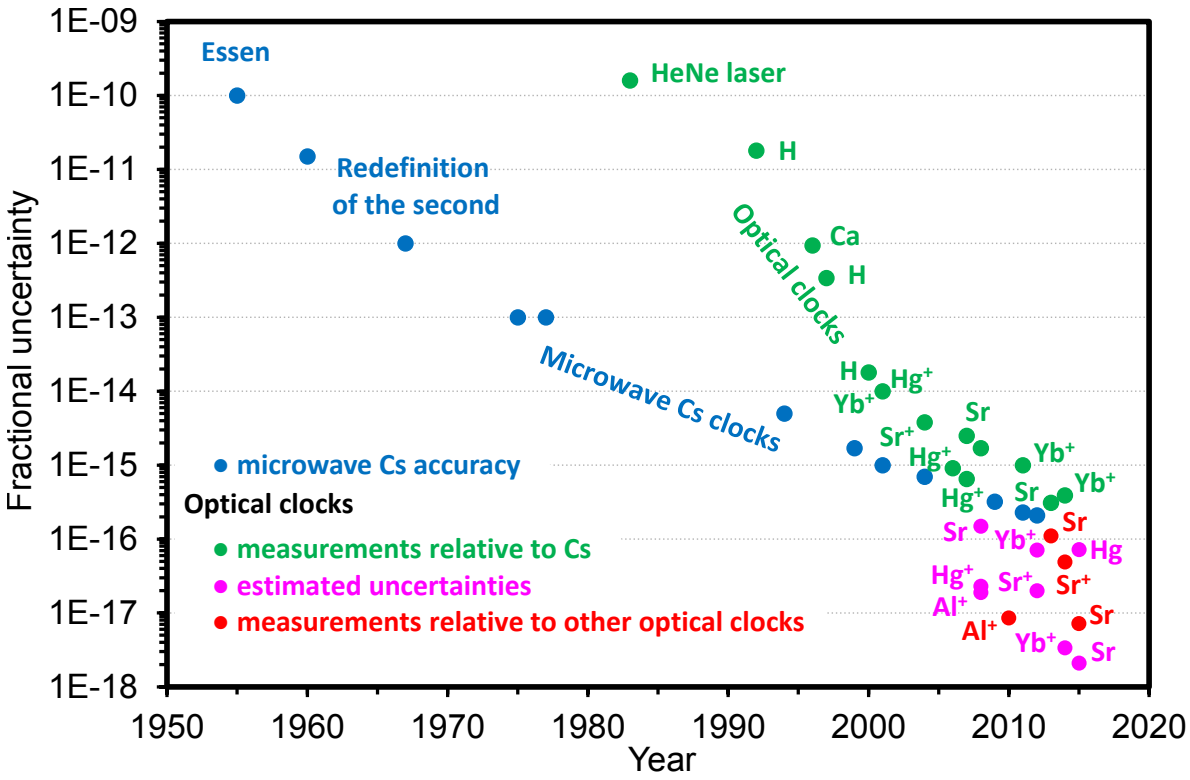

Figure 1.4: Improvement in atomic clocks over time. Red and pink points represent optical clocks whose accuracy has surpassed that of caesium devices. Red points are experimental demonstrations of this fact, whereas pink points are estimated uncertainties. This plot is courtesy of Dr Rachel Godun.

Another application of clocks is opening up at the moment. Relativistic time-dilation means that any clock is sensitive to the absolute value of gravitational potential (and centrifugal effects due to the Earth's rotation). This tiny effect is now measurable [67, 68], and relevant at the $\sim 10^{-18}\,\mathrm{cm}^{-1}$ level. As clocks fast approach this accuracy (see Figure 1.4) the prospects for geodesy are transformative [69, 70].

But the story of GPS serves to illustrate a common theme in science. When the atomic clock was invented, no-one imagined that it could one day birth a technology that underpins so much of the modern economy (GPS adds an annual estimated minimum of £6.7bn to the UK economy [71]). The accelerating pace of development in atomic clocks (shown in Figure 1.4) is driven by and itself helps to drive developments in modern ultracold atom manipulation. The "second quantum revolution" has long been predicted [72, 73] and optical clocks are at the forefront, but the technology is still young. Perhaps there are yet undiscovered applications that in 50 years' time will prove just as significant.

1.2.2 Fundamental physics

At the other end of the spectrum, optical atomic clocks now measure to extreme accuracies a frequency whose value is set by fundamental physics. An atomic clock is a place where an atom is allowed to evolve under the laws of physics, free from the effects of external distractions. If that evolution is not as identical as the standard model predicts, that tells us something profound about the universe.

Relativity was formulated using the concept of a perfect clock, so naturally atomic clocks have something to contribute in this field. General Relativity is founded on the Einstein equivalence principle (EEP) which includes the principles of local position invariance (LPI) and local Lorentz invariance (LLI). LPI asserts that the outcome of any local experiment does not depend on its location, whereas LLI asserts the same

for an experiment's orientation and velocity in space. An atomic clock is such a local experiment, and as such is sensitive to violations of both these principles.

Temporal variation of fundamental constants is predicted by various theories that go beyond the Standard Model [74–81]. Optical atomic clocks are primarily sensitive to variation in α, the fine-structure constant, and $\mu = m_p/m_e$, the proton to electron mass ratio [81]. Ytterbium in particular is well-suited to this test for two reasons [82, 83]. Firstly, excitation of the E3 transition results in the promotion of a core electron from a 4 f shell to the outer 6 s shell. The resultant hole is subject to large spin-orbit corrections, producing a large, inverted fine-structure for the ^{2}F term. Secondly, it possesses two clock transitions (E2 $^2\mathrm{S}_{1/2} \rightarrow {}^2\mathrm{D}_{3/2}$ and E3 $^2\mathrm{S}_{1/2} \rightarrow {}^2\mathrm{F}_{7/2}$) and the E2 transition has a non-inverted fine-structure. By comparing the frequencies of these two transitions in the same ion, a ratio with high sensitivity to the fine-structure constant and therefore to $\dot{\alpha}$ can be derived, free from many systematic effects. Following this method, $^{171}\mathrm{Yb}^+$-based optical clocks have produced the most stringent tests of fine-structure variation so far: $\dot{\alpha}/\alpha = (-0.7 \pm 2.1) \times 10^{-17}\,\mathrm{yr}^{-1}$ [18, 19].[‡‡] The same experiment yields values for $\dot{\mu}/\mu = (0.2 \pm 1.1) \times 10^{-16}\,\mathrm{yr}^{-1}$ through the caesium hyperfine transition's sensitivity.

The presence of local Lorentz invariance can be tested for by searching for variation in atomic energy levels with respect to changes in the electronic wave function's orientation [17, 84]. The comparatively large relativistic corrections required for the 4 f electrons (or rather, hole) and responsible for the ^{2}F state's large splitting help us again, since this amplifies the effect of Lorentz invariance violation. By measuring the difference in energy of magnetic sub-levels of the $^2\mathrm{F}_{7/2}$ state as the Earth rotates the laboratory frame, it should be possible to measure the LLI violating parameters $C_0^{(2)}$[§§]

[‡‡] To go further than this, we may find ourselves limited by the stability of the E2 transition. We may therefore find it more efficient to compare instead against a high-stability neutral atom system such as the Sr-lattice at the NPL; even though it has no sensitivity to the fine structure constant, by not measuring the E2 transition we can increase the stability of the E3 by a factor of 2.

[§§] If violations of Lorentz invariance cause a small shift to atomic energy levels, $C_0^{(2)}$ is a parameter

with a stability of $1.7 \times 10^{-19}(\tau/1\,\mathrm{s})^{-1/2}$: a 2400-fold improvement compared to the best measurement with Ca^+ [17, 85]. This method works best with a decoherence free subspace (DFS) to shield against magnetic field noise, and so two ions must be compared: this is one of the motivating factors behind work on a linear trap (see §8.2.1.5).

A different direction for a $^{171}Yb^+$ experiment to take could involve measurement of the Higgs boson's coupling to the electron. This quantity is important since it is predicted to be very small ($y_e \sim 2 \times 10^{-6}$ evaluated at the Higgs mass scale) [22], but the best measurements possible at the LHC can only constrain it at the 1.3×10^{-3} level [86, 87]. If the particle detected in 2012 was not the Higgs boson that the Standard Model predicts it will point to a new direction for particle physics.

To measure this with atomic clocks, one looks for the coupling to an atomic transition. The Higgs contributions to atomic clock frequencies could cause a constant offset as large as 100 Hz [22]: easily within the resolution of atomic clocks. The correction is particularly large for Yb^+ due to its large number of nucleons. However, theoretical predictions of the clock transition's frequency are not sufficiently accurate to allow this shift to be determined. Instead, one may measure the change in frequency from isotope to isotope, looking for non-linearity in a King plot. Here, again, ytterbium is the candidate of choice with 7 stable isotopes. Driving all these different isotopes will require a flexible laser system, and is the motivation behind the new cooling laser system planned in Section 2.7.

1.3 Conclusion and outline

This chapter has introduced the atomic clock as a means for producing a stable, repeatable and universal measure of time. It has outlined the three ingredients of any

governing the size of the contribution of the LLI-violating operator $\tilde{T}_0^{(2)} = \tilde{\mathbf{p}}^2 - 3\tilde{p}_z^2$ to the perturbing Hamiltonian, where the ion's quantization axis lies along $\hat{\mathbf{z}}$. See Ref. [17] for more information.

frequency standard: the reference which sets the frequency, the local oscillator which is steered to it, and the counter that measures it. The benefits of a move to the optical such as the large increase in $\mathcal{Q}$-factor were outlined and the implementation of the three ingredients in the optical regime were described.

Section 1.2 outlined some of the motivations behind building an optical atomic clock, but there are many more. Clocks could pop up in places that most people would not expect: they already help us navigate here on Earth [14, 15], but could one day do the same for deep-space missions [88]. They could measure the ground beneath our feet [70, 89] and act as metronomes for the next generation of communication networks [16]. In late 2018 / early 2019, an atomic clock ensemble will be launched into space to run on the International Space Station (ISS) enabling a step-change in international clock comparisons, as well as various fundamental physics experiments. [90, 91]

For the physicist, optical clocks are now bearing fruit. We have discussed their application to detection of LLI and LPI, to measurement of the Higgs boson, and to variation of physical constants. Not mentioned were tests of special relativity [1, 92], searches for dilaton dark matter [93] and topological dark matter [2, 20, 21]. The future is bright.

This thesis will begin by outlining in more detail some of the sub-systems that go into the $^{171}Yb^{+}$ optical atomic clock in Chapter 2. In Chapter 3 it will go into much more detail on one of those sub-systems in particular: the ion trap that is the experiment's heart. Chapter 4 will present a measurement of one of the ion's properties: its response to thermal radiation. This number is of importance for anyone building a clock based on $^{171}Yb^{+}$ and is used in Chapter 5 where this effect and all the other systematic effects which perturb the ion's transition are analysed. Chapter 6 will take a close look at the improvements made to the second ingredient of the clock, its local oscillator, making the uncertainties achieved in Chapter 5 realisable. Finally, Chapter 7

will demonstrate what can be done with a network of these clocks, presenting the result of an international collaboration between European NMIs.

Experimental setup 2

> Big fleas have little fleas upon their backs to bite 'em,
> And little fleas have lesser fleas, and so, ad infinitum.
>
> — *Augustus De Morgan*

The phrase "optical atomic clock" summons a picture of a self-contained device, perhaps a large black box, that sits in a corner and diligently counts away the femtoseconds. This idea is a worthy goal, and several teams around the world are indeed working to make it a reality [94–96]. However the current state of the art is somewhat different.

Our clock consists of several sub-systems, all of which must work simultaneously. These sub-systems entirely fill one (fairly large) laboratory, and are distributed across two others. Chapter 1 referred to the three parts of a clock, but in truth there are far more. For a full appreciation of the big-picture view of frequency metrology, it is important to have at least the flavour of the components which make up the whole.

This chapter will introduce a few more pieces of the puzzle. The experiment's heart, the ion trap, will be presented later in Chapter 3, but Section 2.2 will discuss

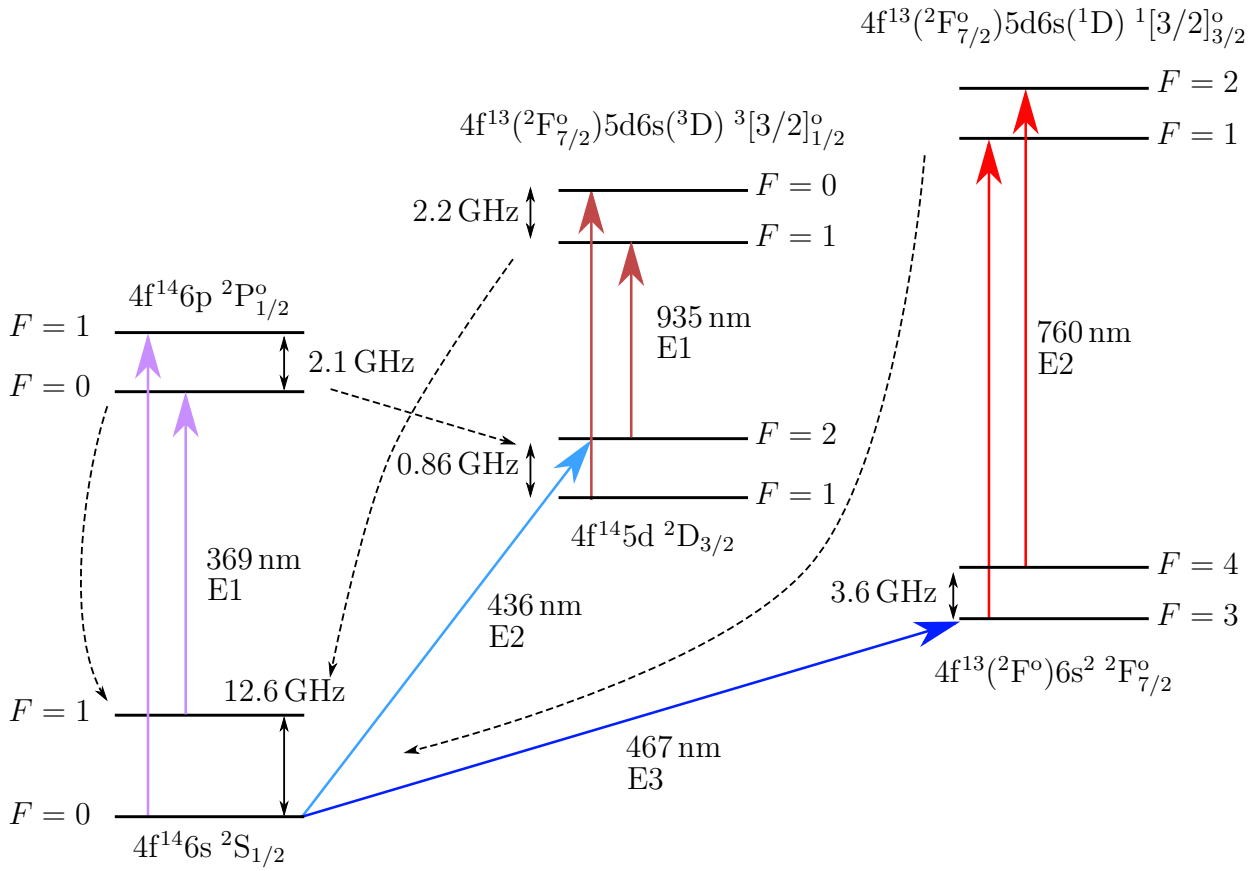

Figure 2.1: Term scheme diagram of $^{171}Yb^+$. The branching ratio for the $^2P_{1/2} \rightarrow {}^2D_{3/2}$ decay is 0.005 01(15) [97], with the $^2P_{1/2}$ state's lifetime 8.07(9) ns [98]. The decay constants for decay to the ground state of the $^3[3/2]^o_{1/2}$ and $^1[3/2]^o_{3/2}$ excited states are, respectivly, 42(3) ns [99] and 28.6(4) ns [100]. The 369 nm, $F = 1 \rightarrow 0$ transition is used for Doppler cooling of the trapped ion, the 436 nm and 467 nm transitions are the quadrupole and octupole clock transitions and the other transitions shown are used for repumping of the ion into the cooling cycle.

the techniques used to load and cool trapped ions. The business of exciting forbidden transitions, from the production of clock-light to the algorithm used to lock to the clock transition, is treated in Section 2.3. Control over the ion's environment in terms of magnetic field is described in Section 2.4, and Section 2.6 will briefly describe the workings of an optical frequency comb, the third key part of an optical clock, whose development could be said to have kicked it all off in earnest.

2.1 Trapping

All optical atomic clocks must confine their atoms in some way, so that they may be addressed and interrogated as a frequency reference. Our experiment uses a charged ion instead of a neutral atom in order that it may be stored using a time-varying electric field: a Paul ion trap.

The trap used for our experiment is of the Schrama end-cap design [6, 101] and is used to trap a single ion of $^{171}Yb^{+}$, treated in detail in Chapter 3. On a day-to-day basis, the trap needs little adjustment. The only parameters that (infrequently) change are the compensation voltages, required to avoid excess micromotion of the ion, whose determination is described in Section 3.5.

2.2 Loading and cooling

2.2.1 Loading

In the trap described in Chapter 3, single ions can be trapped and cooled for periods of several weeks. Nevertheless, it is sometimes necessary to load new ones. To do this, a thermal beam of atomic ytterbium is passed through the centre of the trapping region. This is produced by an ytterbium oven: a 1 mm diameter tantalum tube loaded with enriched ytterbium which can be heated by passing an electrical current through it, and is long enough to collimate the beam.

This beam passes through trap-centre where the ytterbium atoms are photo-ionised in a two photon process. Ytterbium possesses a dipole-allowed $^1S_0 \rightarrow {}^1P_1$ transition at 399 nm [102, 103]. From the top of this transition ($^1P_1$) the atom is ionised via non-resonant excitation to the continuum, with energy provided by a 369 nm photon from our cooling laser.

The RF trap is turned on throughout this process, and the ions produced therefore appear in the pseudo-potential with significant energy, both potential and kinetic, i.e. a high temperature. Doppler cooling efficiency relates to the spectral density in the frequency modulation (FM) sidebands [104] and so, for fast-moving ions, the higher-order Bessel functions are non-negligible.* To improve capture, we therefore apply an additional cooling beam 220 MHz red-detuned† from our usual cooling light during loading only. Note that a Doppler shift of 220 MHz corresponds to an ion temperature of only 70 K, whereas our ions are certainly at >300 K and probably much more. It's therefore likely that even with this additional detuning, a great many ions are wasted during the loading process.

Control of ion loading rate is effected by varying the flux of neutral atoms. We find that oven currents of around 5 A for 60 s with both the 369 nm and 399 nm light at saturation result, on average, in 1 ion loaded.

Our 399 nm source was previously a home-made external-cavity diode laser (ECDL). However, we found this laser to be fairly non-deterministic in behaviour, exhibiting significant hysteresis and mode-competition. Our replacement photo-ionisation laser is a commercial Sacher Micron ECDL [106] lasing at 798 nm, frequency doubled by an SHG wavelength conversion module by NTT Electronics [107]. This modular system, shown in Figure 2.2, fills a volume of less than $30 \times 10 \times 10\,\mathrm{cm}^3$ and couples the generated light into a fibre for later integration with the rest of the clock system. The Sacher Micron laser has a 1 ms bandwidth of around 18 kHz, frequency doubled to 36 kHz [106]. This is easily narrow enough both to drive the transition—whose natural linewidth is on the order of 10 MHz—and to perform isotope selection.‡

*See §3.4.1 for a discussion of frequency modulation of incident light by a moving ion.
†Approximately 20 linewidths of the unbroadened cooling transition.
‡Isotope shifts between neutral ytterbium isotopes typically range from 200 to 600 MHz [110].

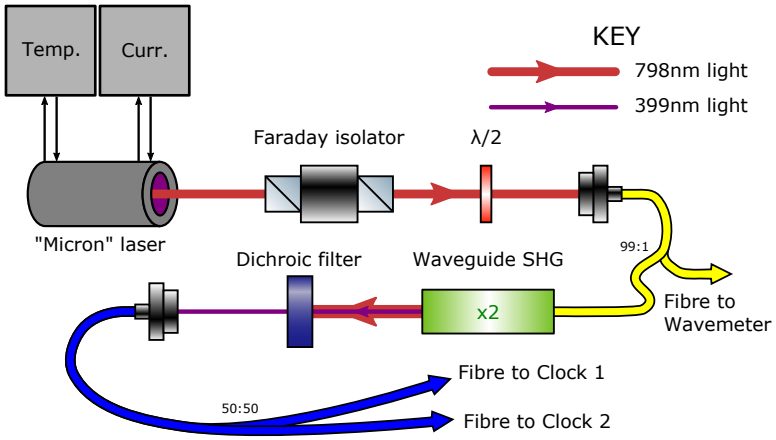

FIGURE 2.2: Schematic of the 399 nm laser system used for photo-ionisation of neutral ytterbium. Temperature control is provided by the same unit as described in Appendix C and §6.3.2, current control is done using a Thorlabs T-Cube constant current source [105]. The laser is a Sacher Micron external-cavity diode laser (ECDL) [106], the SHG unit is a wave-guide frequency conversion module from NTT Electronics [107] and the dichroic filter is a low-pass model from Semrock [108]. The waveplate is for aligning the IR beam's polarisation with the single mode, polarisation maintaining fibre's axis. Note that this is factory aligned with the doubling crystal's axis.
Many of the figures throughout this thesis, including this one, have made use of the SVG ComponentLibrary by Alexander Franzen [109].

Although schemes exist that can load ions at rates of up to 125 Hz using laser ablation [111–114], the long lifetime of ions in our trap (see Chapter 3) makes loading an infrequent occurrence and so the simplicity of our current setup was a more important concern for our application.

2.2.2 Cooling

Doppler cooling is a well known technique for reducing the momenta of atoms that works by exploiting the Doppler effect to cause atoms to preferentially absorb photons whose momenta oppose the atoms' movement [58, 104]. In an ion trap, confinement is provided by the trapping RF field so laser cooling is used not to confine the ions (as in optical molasses) but just to reduce their energy (temperature) within the trap.

In order to do this in $^{171}Yb^{+}$, an ultra-violet ECDL at 369 nm is red-detuned to

the full-width half-maximum (FWHM) of a dipole-allowed transition: $^2S_{1/2}(F = 1) \rightarrow {}^2P_{1/2}(F = 0)$ with a natural linewidth of 19.60(5) MHz [115]. Saturation of the cooling transition is observed with powers of ∼1 µW, suggesting a beat waist of ∼35 µm. For normal usage, we operate at ∼25 % of this level.

The Doppler shift experienced by the ion as it moves towards the light source moves the laser closer to the ion's resonance, causing it to absorb more (counter-propagating) photons than it does as it moves away. This means that the net force due to photon absorption serves to counteract movement parallel to the beam, whereas the net force from photon emission averages to zero. For fuller treatments of this topic, see [58, 65, 104, 116].

In our setup, shown in detail in Figure 2.3, a Toptica DL Pro ECDL with a custom Nichia 371 nm diode is used as the laser source that can be cooled to lase at 369.5 nm.[§] This is locked to a low-drift cavity with $\mathcal{F} \approx 150$ using the side of fringe method.

The side of fringe method works by stabilising the laser frequency to keep a constant transmission fraction through the cavity, chosen to sit on the steepest part of the Fabry–Pérot transmission curve for greatest frequency discrimination. By stabilising the difference between intensities measured before and after the cavity, fluctuations in laser intensity that would otherwise become frequency-noise can be rejected. If $F_A(F_B)$ is the fraction of light that is split towards (away from) the cavity, $G_A(G_B)$ is the gain of the trans-impedance amplifier for the photodiode after (before) the cavity and $T(\nu)$ is the frequency dependent transmission fraction through the cavity, engaging a frequency servo to drive the voltage difference between the two amplifiers' outputs to

[§]Diodes operating at 369.5 nm are few and far between. Our 371 nm diode is an outlier from a manufacturing process designed for 375 nm diodes. Unfortunately (for us), diode manufacturing techniques have advanced and few such outliers are now created. There is yet hope however: at time of writing, I have been assured that various companies are close to releasing frequency doublers that can reliably produce light this far into the UV. Future $^{171}Yb^+$ clocks will probably take advantage of these systems to avoid working with lossy UV optics until the last stages of the optical system.

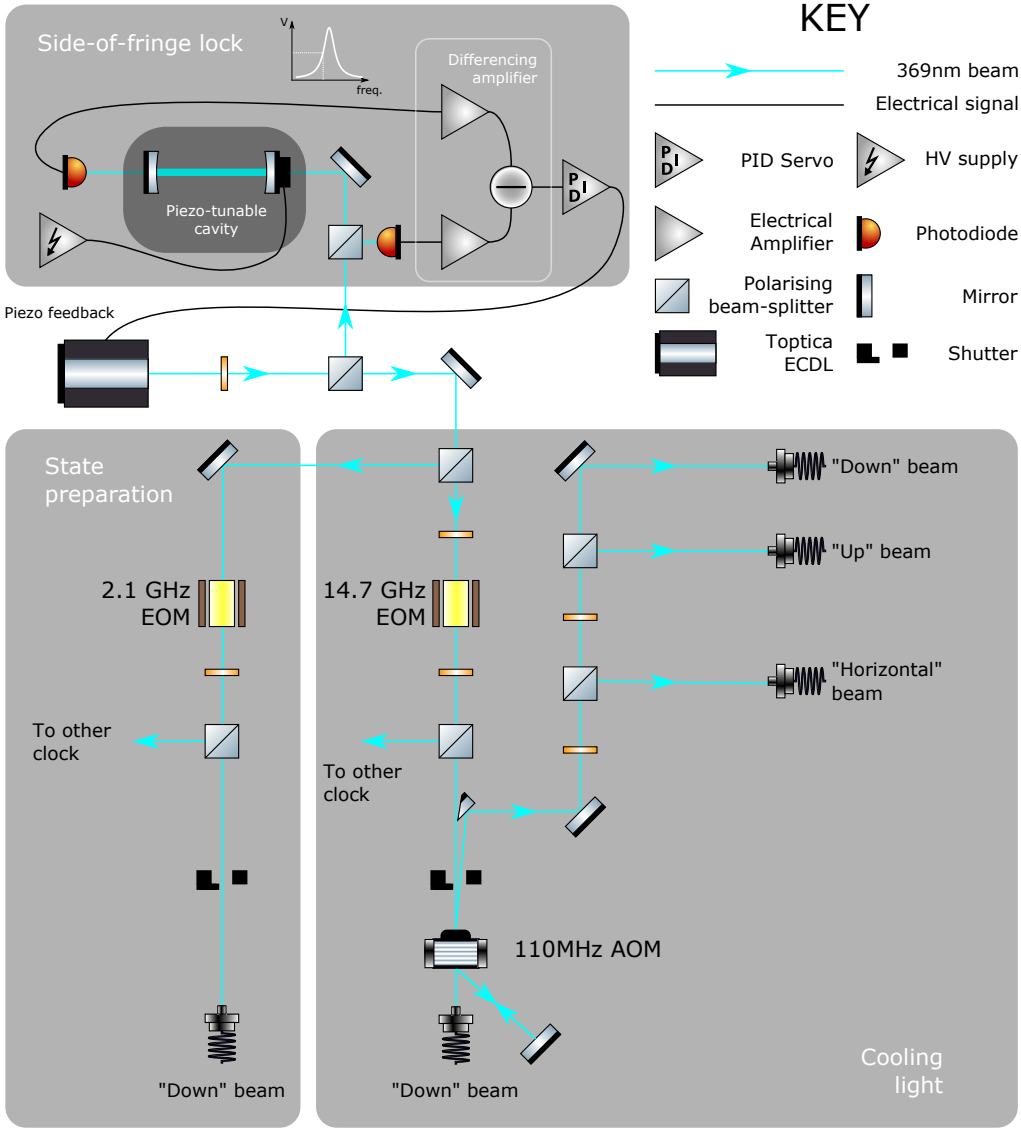

FIGURE 2.3: Diagram of the 369 nm cooling and state-preparation laser setup. Most mirrors and all lenses are omitted for clarity. The laser is locked to a piezo-adjustable cavity via the side-of-fringe method. The cavity's length is set using a high voltage (HV) supply, by reference to the ion's fluorescence (an additional pick-off to a Wavemeter is not shown). We find that our cavity is sufficiently stable that this correction need only be adjusted every few days. Feedback is performed by altering the length of the ECDL's laser cavity; diode current and temperature are kept constant. The differencing amplifier setup rejects intensity noise on the laser light. A digitally synthesised 2×110 MHz offset is applied to the light using an Acousto-optic Modulator (AOM) so that the cooling light's frequency can be computer-controlled. Two resonant electro-optic modulators (EOMs) create sidebands on the light to address the ion's hyperfine structure—see text. All fibre docks with the same label are, in reality, the same dock: beam routing optics to merge these beams have been omitted for clarity.

zero ensures that

$$\begin{aligned} V_A(I,\nu) - V_B(I) &= 0 \\ F_A G_A\, T(\nu)\, I &= F_B G_B\, I \\ \implies T(\nu) &= \frac{F_A G_A}{F_B G_B} \quad , \end{aligned} \tag{2.1}$$

where the lock-point for the transmission fraction T is now independent of laser intensity.

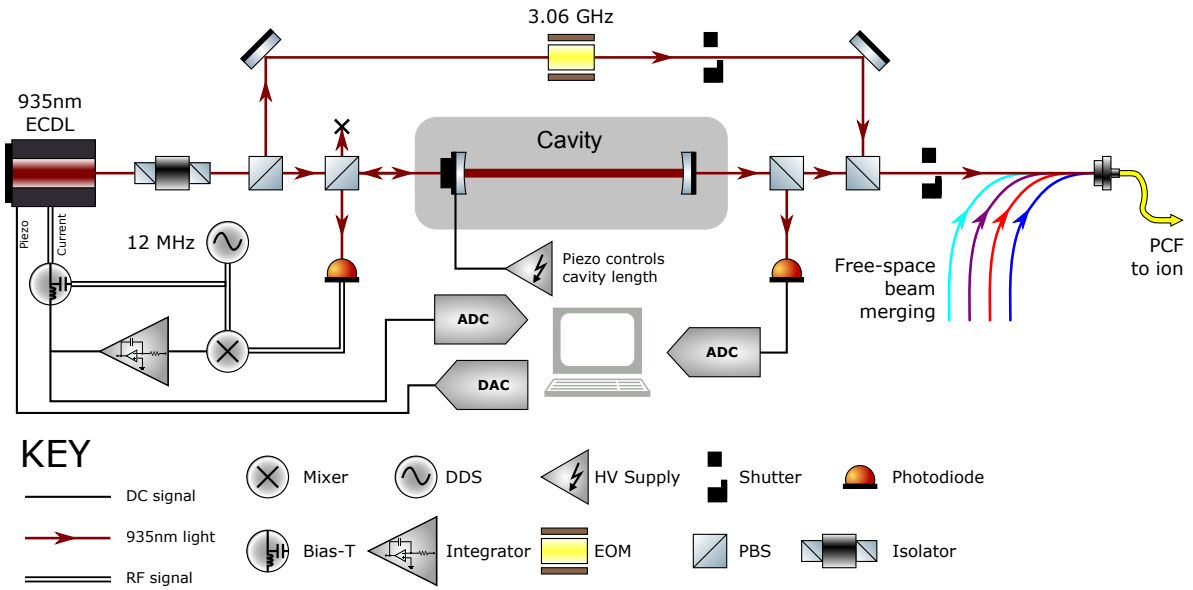

FIGURE 2.4: Diagram of the repumping 935 nm laser setup. Mirrors, lenses and wave-plates have been omitted for clarity. The diode's current is modulated at 12 MHz so that the Pound-Drever-Hall (PDH) technique can be used for locking to a low-drift, piezo-adjustable etalon. For more information on this technique see Section 6.1.¶ A fast lock to the cavity resonance feeds back to the diode current, while a computer monitors the output of this servo, slowly driving it to zero by altering the laser-cavity length through an integrated piezo. The computer also monitors the cavity transmission to detect unlock events and attempt a relock based on past history. We find that this setup routinely stays in lock for months at a time. The cavity used here is of the same design as that of the 369 nm system (Figure 2.3), and we similarly find that the cavity length need only be tuned every few days or weeks.
The 935 nm light is split into two paths and a 3.06 GHz sideband is added to one. This repumps from the $^2D_{3/2}(F = 2)$ state: the top of the E2 clock transition. The main beam is set to repump from the $(F = 1)$ state, occasionally populated during the cooling cycle. During state-readout for the E2 clock, we do not want to repump from the $(F = 2)$ state, so a shutter can be used to block this beam. The light used to repump the $(F = 1)$ state is the cavity transmission and so the cavity acts as a notch filter to prevent accidental off-resonant repumping.

The EOMs shown in Figure 2.3 serve to address the hyperfine sub-levels of $^{171}Yb^{+}$. Recalling the energy level structure shown in Figure 2.1, the cooling cycle involves excitation from $^{2}S_{1/2}(F = 1) \rightarrow {}^{2}P_{1/2}(F = 0)$ and decay along the same path. From the upper state, there is a $5.01(15) \times 10^{-3}$ branching ratio to the long-lived $^{2}D_{3/2}$ state [97]. For this reason (and also to repump from the E2 clock state) a 935 nm ECDL—shown in Figure 2.4—is used to repump the ion to the $^{3}[3/2]_{1/2}$ state, from which it can decay back into the cooling cycle. This state has $\tau = 42(3)$ ns [99] so, assuming a similar beam waist as calculated for the 369 nm beam (a reasonable assumption since all beams are delivered through the same fibre and focussed using parabolic mirrors — see Chapter 3), 10 µW of power is easily enough to ensure saturation of the transition.

A yet more unlikely route that the ion can take results in it leaving the cooling cycle and returning to the $F = 0$ ground state, or starting there after a failed clock excitation attempt. This can occur via off-resonant excitation from $^{2}S_{1/2}(F = 1) \rightarrow {}^{2}P_{1/2}(F = 1)$ followed by decay, or by decay from the $^{2}D_{3/2}$ state before the 935 nm does its job. For all of these scenarios, a 14.7 GHz EOM adds a sideband to the 369 nm light allowing repumping from $^{2}S_{1/2}(F = 0) \rightarrow {}^{2}P_{1/2}(F = 1)$ and decay back into the cooling cycle.[‖]

Similarly, the 935 nm light has an EOM operating at 3.06 GHz to repump from the $^{2}D_{3/2}(F = 1)$ state, resulting either from excitation of the E2 clock transition or from decay following off-resonant excitation to the $^{2}P_{1/2}(F = 1)$ state. See Figure 2.4 for more detail.

[‖]For cost and availability reasons, this is actually implemented as a 7.4 GHz EOM whose second order sideband does the work. This EOM is driven at far less than its half-wave voltage V_{π}, so the spectral density in the second order sideband is very low. Nevertheless, accidental population of the ion's ground state occurs so infrequently that increases to drive power of this EOM are not observed to affect fluorescence rates.

2.2.3 State preparation

In order to make an attempt at exciting either clock transition (the E2 or E3), the ion must be prepared into its ground state. Doing this is fairly easy: the 14.7 GHz is designed to depopulate the ground state, so simply turning off this EOM will eventually result in state preparation. However, this process relies on either off-resonant excitation or an unusual decay as described above, and so can take many milliseconds. To hurry the process along, a 2.1 GHz EOM adds another sideband to the light, allowing resonant pumping from $^2S_{1/2}(F = 1) \rightarrow {}^2P_{1/2}(F = 1)$. The ion is therefore quickly pumped into the $(F = 0)$ dark ground state, where it remains.

2.2.4 Readout and repumping

After a clock pulse, readout of the ion state is done simply by turning on the cooling light (369 nm + 935 nm): observed fluorescence indicates that the ion is still in the ground state whereas darkness indicates a successful excitation. For the E2 clock, it is necessary to block the 935 nm light with the additional 3.06 GHz sideband using the shutter shown in Figure 2.4.

To repump from the E2 upper metastable state, the additional 935 nm light is turned back on. To repump from the upper state of the E3 transition ($^2F_{7/2}$ (F=3)), it is necessary to excite a quadrupole transition using another laser at 760 nm. This excites the ion to the $^1[3/2]_{3/2}$ state from which it rapidly decays back to the cooling cycle (see Figure 2.1). To avoid needing high frequency selectivity on this laser, ∼10 mW of light are used, focussed to a spot size of ∼100 µm. This high intensity rapidly repumps even when imperfectly tuned to the transition frequency, allowing us to simply tune this laser using a Wavemeter with no need to lock its frequency.

Finally, an additional 760 nm laser is used to repump from the $^2F_{7/2}$ (F=4) state. This state is equally long-lived as the E3 upper clock state and is very infrequently

populated, possibly through collisional processes with atoms in the vacuum chamber. We find that the ion ends up in this state roughly once per day if this laser is disabled.

2.2.5 Detection of single ions

A commonly asked question in lab tours is "how do you know how many ions you have loaded?" To detect the number of ions in the trap, we make use of *electron shelving*. As mentioned above, the 935 nm light has a sideband added to enable it to address the $^2D_{3/2}(F = 2)$ state in addition to the $(F = 1)$. The $(F = 1)$ state is often populated through decay from the upper cooling state ($^2P_{1/2}(F = 0)$) but the $(F = 2)$ state is only rarely populated following off-resonant excitation by the cooling laser. By turning off the -3.06 GHz shifted light, we do not repump from this state, allowing the ion to decay naturally to the ground state with a lifetime of 52.7(24) ms [117]. Like this, the ion cycles through light and dark states with the dark states lasting on average 50 ms and off-resonant pumping into this dark state happening at roughly similar rates. By measuring the observed fluorescence and plotting this as a histogram with suitable chosen bin-sizes, two clear fluorescence levels are visible, corresponding to the dark and light states, shown in Figure 2.5. If more than one ion is present in the trap there are now more possible fluorescence levels, corresponding to 0, 1, or 2 ions fluorescing.

2.3 Excitation of clock states

2.3.1 Laser stabilisation

Production of high stability light is a key step in building an atomic clock; without sufficient spectral density you will never excite a clock transition whose linewidth is on the order of 1 nHz. Our setup uses a multi-stage stabilisation scheme based on Fabry-Perot cavities to provide short- and medium-term stability. This topic deserves its own

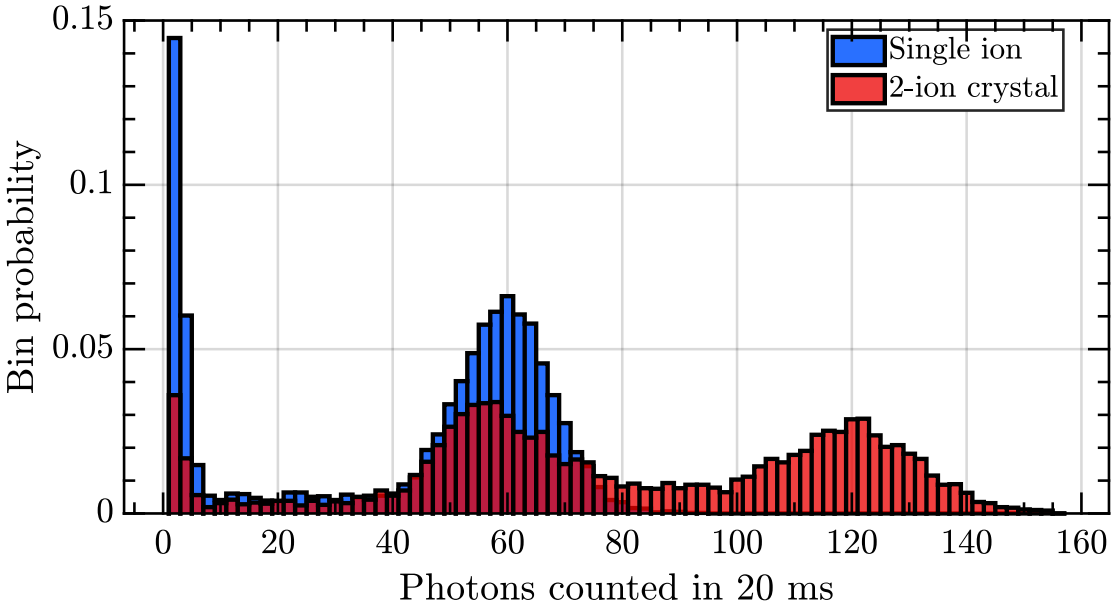

FIGURE 2.5: Histogram of photon counts detected from an ion / ions shelving into the $^2D_{3/2}(F = 2)$ state. When two ions are loaded three levels of fluorescence are clearly visible, corresponding to 0, 1, or 2 ions fluorescing simultaneously.

space, and is described in Chapter 6. Long-term stability and, importantly, accuracy is provided in the final stages by feedback to the ion's clock transition, described here.

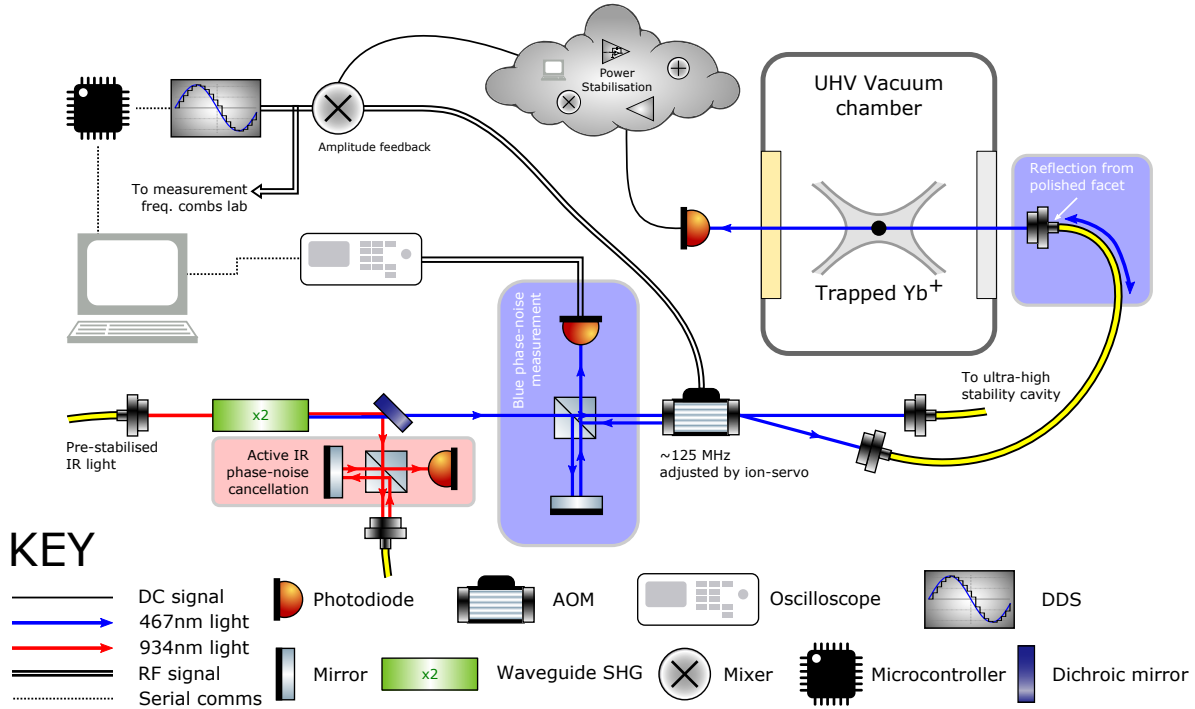

Figure 2.6: Diagram of the clock probe light production.
The IR light is pre-stabilised to high-stability cavities as detailed in Chapter 6 and Figure 6.1. A SHG crystal produces frequency-doubled light at 467 nm. The remaining IR light (∼5 mW per comb) is sent to the measurement frequency combs while the blue light has an additional frequency of Δf_B added to it to bring it into resonance with the ion's clock transition. The red- and blue-shaded areas are involved in phase-noise measurement of the light. The "power stabilisation" setup is described in §5.2.2. Beam offsets at reflections are for legibility only. The active phase noise cancellation of the IR light is actuated by an AOM at the other end of the fibre (see Section 2.6).

2.3.2 Probe light production

The blue light at 436 nm and 467 nm used to excite the E2 and E3 transitions is produced in each case by doubling light in the IR from a Toptica DL Pro ECDL. In the case of the octupole, since the transition's natural linewidth is so small, a tapered amplifier (TA) is used to boost power levels and achieve higher spectral density. In both cases the IR light is subjected to extreme frequency stabilisation before it reaches the doubler (see Chapter 6).

Figure 2.6 shows the conversion of 934 nm light to 467 nm light for the E3 transition, but the situation is similar for the E2 with 436 nm and 871 nm light instead. The rest of this Section will refer to 467 nm light only, but should be understood to be applicable to both transitions.

The frequency at which the IR light is locked depends on the cavity mode chosen and will not be exactly equal to half the clock transition's frequency. Therefore an AOM to bridge this gap is required—shown in Figure 2.6. The frequency sent to this AOM is altered by the computer to keep the blue light resonant with the ion's transition as described in §2.3.4. The amplitude of the RF signal used to drive this AOM is used to actuate a power servo, controlling the intensity of light experienced by the ion and described in §5.2.2. Control of the direct digital synthesis unit (DDS) responsible for pulse shaping is done by a standalone, on-board microcontroller to take advantage of deterministic hardware timings [119].

§5.2.2 will discuss how any residual amplitude instability of the power servo affects the clock's systematic performance via the AC Stark effect, and Section 5.6 will discuss the effect of frequency chirp caused by heating in the AOM.

2.3.3 Pulse shape

Our current configuration uses simple Rabi excitation to excite the clock states. Pulse shaping is therefore minimal: the microcontroller in Figure 2.6 applies a timed pulse with a square envelope for a time $t_\pi = \pi/\Omega_{\text{Rabi}}$. Section 5.2 describes how two different power levels are used in order to compensate for the probe-induced AC Stark shift.

This scheme was chosen for its simplicity and its immunity to perturbations such as heating of the ion during excitation. However other schemes have now been developed which can deal with these problems and will be discussed in §8.2.1.3.

2.3.4 Servo algorithm

To obtain information about the clock transition's frequency, we do not probe exactly on-resonance at ν_{E3}, our best-guess clock frequency. Instead, our clock interrogation scheme alternates between probing at the positive and negative sides of the observed line-shape, separated by the Fourier linewidth for a given probe-length. The excitation measured on both sides can be subtracted to form an error signal whose mean value is zero when on resonance, shown in Figure 2.7.

Since multiple probes must be taken to form one measurement of excitation probability, local-oscillator drift from shot-to-shot must be considered. To reduce sensitivity to this low-frequency noise, pulses are ordered using the Thue-Morse sequence. This sequence provides rejection of nth-order drift for a sequence of length $N = 2^n$ [120, 121]. In our application we must balance drift-rejection with remaining on-resonance long enough to excite the transition successfully for a significant fraction of probe attempts. We therefore choose $N = 8$, resulting in a sequence of 01101001 where 0(1) represent a probe on the low(high) side of the transition.

The frequency correction applied to the AOM is calculated by the control software running on a lab PC after a full sequence of 8 probes has taken place. This algo-

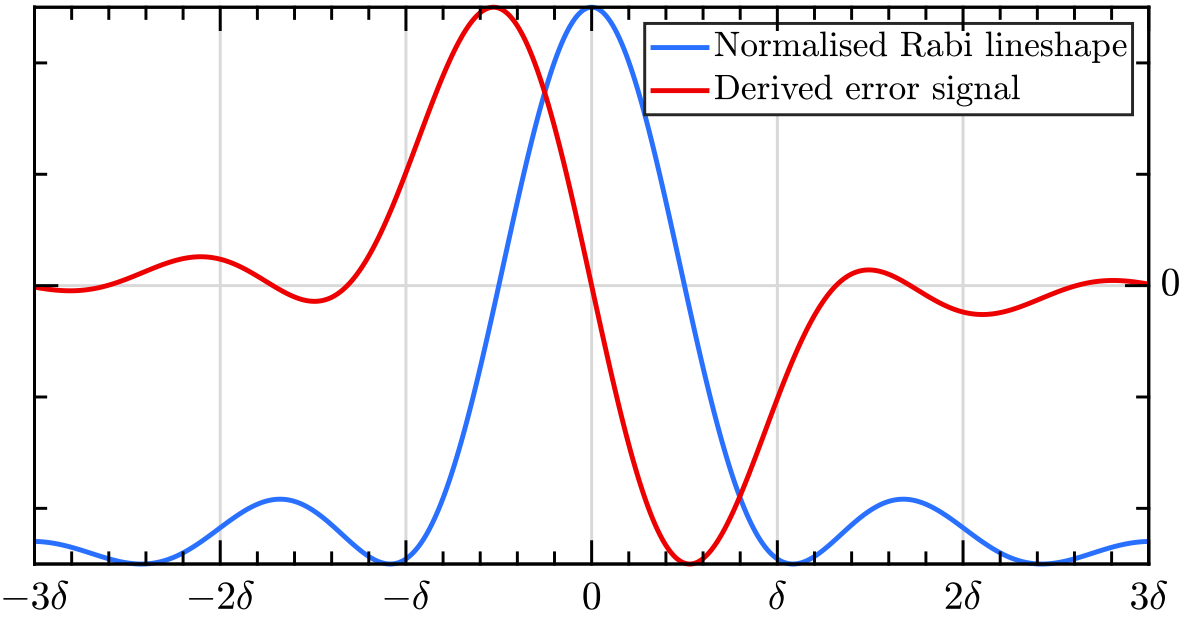

FIGURE 2.7: Rabi lineshape and error signal derived by subtracting measurements taken at $\pm\delta/2$ where δ is the FWHM of the spectral line.

rithm seeks to minimise the error signal by applying corrections proportional to the integral and second integral of the error signal. Specifically, the error signal e_i and the subsequent new centre frequency f_i are calculated using

$$e_i = \frac{n_i^{\text{high}} - n_i^{\text{low}}}{n_i^{\text{high}} + n_i^{\text{low}}} \tag{2.2}$$

$$f_i = f_{i-1} + G_{\text{I}}\, e_i + G_{2\text{I}}\, \delta t_i \sum_{i'=0}^{i} e_{i'} \quad , \tag{2.3}$$

where n_i^{high} and n_i^{low} are the number of jumps measured on the high and low sides of the transition in the ith cycle, G_{I} and $G_{2\text{I}}$ are the empirically found constants and δt_i is the duration of the ith cycle.

These servo tuning constants are found empirically. We judge the effectiveness of this algorithm by comparing the stability of the frequency difference between two locks to the theoretical limit set by QPN: we find that our clock performs at the QPN limit for a dual-servo configuration with $\sigma_{QPN}(\tau)/\nu_0 = 2.3 \times 10^{-15}\,(\tau/1\,\text{s})^{-1/2}$ (suggesting a

single-servo performance of $1.7 \times 10^{-15}\,(\tau/1\,\mathrm{s})^{-1/2}$) demonstrating that the instability added by inefficiency in the locking algorithm is below this level.

2.4 Control of magnetic field

The magnetic field experienced by the ion can be controlled using the 3-axis Helmholtz coils fitted to the trap. However, in order to determine the correct current to apply, we require a method of measuring the field at the ion. This is provided by the ion itself: although we drive the $m_F = 0 \rightarrow 0$ transitions when operating the clock, both the E2 and E3 transitions have other Zeeman sub-levels available. By driving instead the $\Delta m_F = \pm 1, \pm 2$ transitions, we can measure the external magnetic field spectroscopically, using the ion as a probe.

The E2 transition is the most appropriate for this measurement: given that we expect AC magnetic field noise at a significant level, the extreme linewidth of the E3 transition would make obtaining the necessary spectral density very difficult.**

The magnetic field experienced by the ion depends on both the background magnetic field and the current through the three coil pairs. The geometry of the trap determines how current applied to a particular coil affects the field experienced by the ion. The current in the coils is under our control, however the background field varies over time and the coil coupling coefficients are hard to calculate. We therefore determine these values experimentally.

2.4.1 Measuring the fields

In order to determine the magnitude of the magnetic field experienced by the ion, the $\Delta m_F = \pm 1, \pm 2$ Zeeman components of the E2 transition are observed. By observing

**Modulation of the transition frequency during the pulse by AC fields has the same effect on the Rabi frequency as adding frequency noise to your laser.

the splitting of the positive and negative components, a value for the magnetic field's magnitude at the ion can be deduced.

For the E2's $^2\mathrm{D}_{3/2}(F=2)$ transition we have, for the upper state, $S=\frac{1}{2}$, $L=2$, $J=\frac{3}{2}$, $F=2$. The Landé g-factor can therefore be calculated as [65, 122]

$$\begin{aligned} g_J &= \frac{J(J+1)-S(S+1)+L(L+1)}{2J(J+1)}\, g_L \\ &\quad + \frac{J(J+1)+S(S+1)-L(L+1)}{2J(J+1)}\, g_S \\ g_F &= \frac{F(F+1)-I(I+1)+J(J+1)}{2F(F+1)}\, g_J \\ &= 0.60 \quad , \end{aligned} \tag{2.4}$$

where $g_L = 1$, $g_S = 2.002\,319$[123] and the nuclear g-factor g_I has been neglected. Since the $^2\mathrm{S}_{1/2}(F=0)$ lower state of the E2 transition has $F = m_F = 0$, it does not contribute to the observed Zeeman splitting of the spectral line. The splitting observed for the Zeeman components of the E2 transition is therefore

$$\begin{aligned} \Delta\nu/B &= \frac{g_F \mu_B}{h} \Delta m_F \\ &= \Delta m_F \times 8.393\,\mathrm{kHz\,\mu T^{-1}} \end{aligned} \tag{2.5}$$

2.4.2 Magnetic field model

The field experienced by the ion is modelled by the following:

$$\begin{aligned} \mathbf{B}(\mathbf{I}) &= \boldsymbol{A}\mathbf{I} + \mathbf{B_0} \\ &\equiv \begin{bmatrix} \frac{\partial \mathrm{B_x}}{\partial \mathrm{I_1}} & \frac{\partial \mathrm{B_x}}{\partial \mathrm{I_2}} & \frac{\partial \mathrm{B_x}}{\partial \mathrm{I_3}} \\ \frac{\partial \mathrm{B_y}}{\partial \mathrm{I_1}} & \frac{\partial \mathrm{B_y}}{\partial \mathrm{I_2}} & \frac{\partial \mathrm{B_y}}{\partial \mathrm{I_3}} \\ \frac{\partial \mathrm{B_z}}{\partial \mathrm{I_1}} & \frac{\partial \mathrm{B_z}}{\partial \mathrm{I_2}} & \frac{\partial \mathrm{B_z}}{\partial \mathrm{I_3}} \end{bmatrix} \begin{bmatrix} \mathrm{I_1} \\ \mathrm{I_2} \\ \mathrm{I_3} \end{bmatrix} + \begin{bmatrix} \mathrm{B_{0,x}} \\ \mathrm{B_{0,y}} \\ \mathrm{B_{0,z}} \end{bmatrix} \end{aligned} \tag{2.6}$$

where $\mathbf{B_0}$ is the background magnetic field and $\mathbf{I}$ is a vector of currents (although we hope that current coil 1 produces exclusively field in direction $\hat{\mathbf{x}}$, this is not true

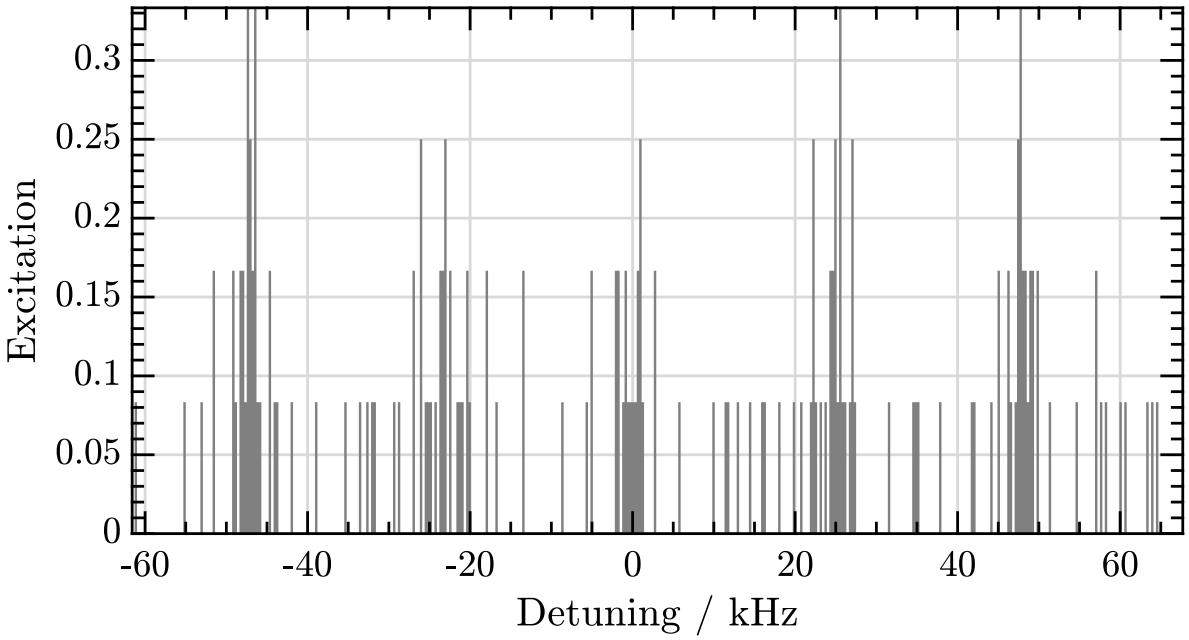

Figure 2.8: A typical run of data showing the $\Delta m_F = 0, \pm 1, \pm 2$ Zeeman sidebands of the E2 transition. The $\Delta m_F = \pm 2$ splitting of 95.0(2) kHz corresponds to a field of 2.828(5) µT. This scan was taken with 2 ms probe times, Fourier broadening the lines to 400 Hz. Further broadening is due to AC magnetic field noise: 2 kHz for the $\Delta m_F = \pm 2$ pair. Note that in a usual B field compensation routine, only the strongest pair of Zeeman components is scanned: the ± 2 pair for this field orientation.

in general: the subscripts are therefore distinct). The Jacobian matrix element $A_{i,j}$ quantifies the effect of current in coil j on the magnetic field in direction $\hat{\mathbf{i}}$.

This model contains 12 coefficients. However, there is a subtlety here: inspection of the model so far will reveal that we have not defined the axes of the system. Attempting to fit all 12 parameters therefore would result in an indeterminate coordinate system, mostly dependent on the choice of initial guess for $\boldsymbol{A}$ and $\mathbf{B_0}$. Fortunately this problem is easy to resolve: we choose to define our unit system using the effect of the coils themselves.

If we define the vectors $\hat{\mathbf{n}}_\mathbf{1}$, $\hat{\mathbf{n}}_\mathbf{2}$ and $\hat{\mathbf{n}}_\mathbf{3}$ according to the direction of the magnetic fields induced by coils 1, 2 and 3, we can create a right-handed, orthogonal coordinate

basis by using:

$$\hat{\mathbf{x}} = \hat{\mathbf{n}}_\mathbf{1}, \quad \hat{\mathbf{y}} = \hat{\mathbf{z}} \times \hat{\mathbf{n}}_\mathbf{1}, \quad \hat{\mathbf{z}} = \frac{\hat{\mathbf{n}}_\mathbf{1} \times \hat{\mathbf{n}}_\mathbf{2}}{|\hat{\mathbf{n}}_\mathbf{1} \times \hat{\mathbf{n}}_\mathbf{2}|} \tag{2.7}$$

The effect of this choice is felt for the Jacobian $\boldsymbol{A}$. By construction, we have ensured that $\frac{\partial \mathrm{B_y}}{\partial \mathrm{I_1}} = \frac{\partial \mathrm{B_z}}{\partial \mathrm{I_1}} = \frac{\partial \mathrm{B_z}}{\partial \mathrm{I_2}} = 0$, so

$$\boldsymbol{A} = \begin{bmatrix} \frac{\partial \mathrm{B_x}}{\partial \mathrm{I_1}} & \frac{\partial \mathrm{B_x}}{\partial \mathrm{I_2}} & \frac{\partial \mathrm{B_x}}{\partial \mathrm{I_3}} \\ 0 & \frac{\partial \mathrm{B_y}}{\partial \mathrm{I_2}} & \frac{\partial \mathrm{B_y}}{\partial \mathrm{I_3}} \\ 0 & 0 & \frac{\partial \mathrm{B_z}}{\partial \mathrm{I_3}} \end{bmatrix} \tag{2.8}$$

There are therefore only 9 coefficients required to fully parameterize the magnetic field in the trap. Since every measurement only reveals the magnitude of the field and not its direction, we require at least 9 measurements to fully characterize the system, and preferably much more.

2.4.3 Fitting the fields

For a single measurement of the field B_μ caused by the current $\mathbf{I}_\mu$, a residual can be constructed:

$$R_\mu = (\boldsymbol{A}\mathbf{I}_\mu + \mathbf{B_0})^2 - B_\mu^2 \quad . \tag{2.9}$$

Note that B_μ is a scalar quantity since each scan reveals only the magnitude of the magnetic field.

The sum-squared residual, $\mathbf{R} \cdot \mathbf{R} = \sum_\mu R_\mu^2$ is then minimized by a Trust-Region-Reflective Least Squares algorithm [124, 125].

With this fit performed, the currents required to construct an arbitrary magnetic field can be calculated simply by considering the inverse of $\boldsymbol{A}$:

$$\mathbf{I} = \boldsymbol{A}^{-1}(\mathbf{B} - \mathbf{B_0}) \tag{2.10}$$

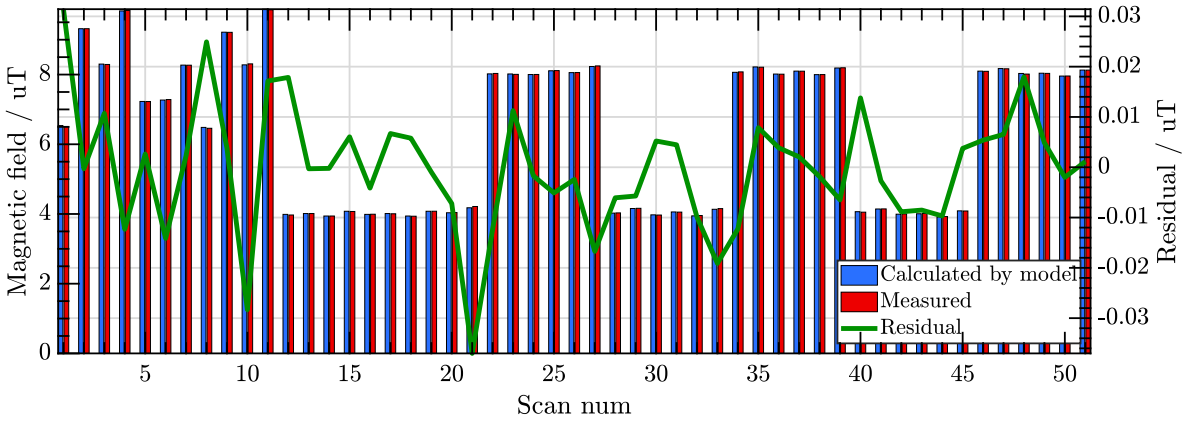

Figure 2.9: Agreement between magnetic field model and 51 scans of the E2 Zeeman components carried out with different coil currents $\mathbf{I}_\mu$. The RMS error of the model is 0.012. Typical operating fields are between 3 µT and 10 µT.

2.4.4 Typical results

The model outlined above was applied to a set of 51 scans with different coil currents $\mathbf{I}_\mu$, shown in Figure 2.9. The background magnetic field was found to be

$$\mathbf{B_0} = (-3.775(2), 2.377(4), 1.866(3))\ \mu\mathrm{T}$$

and the coil coupling coefficients were found to be

$$\boldsymbol{A} = \begin{bmatrix} -60.26(2) & 0(0) & 0(0) \\ -0.21(5) & -162.16(5) & 0(0) \\ -0.18(4) & 1.72(10) & -62.17(2) \end{bmatrix} \mu\mathrm{T\,A^{-1}} \tag{2.11}$$

Considering $\boldsymbol{A}$, we see that our coils are operating mostly orthogonally to each other but with cross-coupling terms at the $\sim$5 % level. For e.g. a typical magnetic field of 5 µT in the $\hat{y}$ direction, Equation 2.10 gives $\mathbf{I} = (-64.8, -16.0, 25.8)$ mA.

Although this fitting procedure is instructive, the values of $\boldsymbol{A}$ depend on the trap geometry and do not typically change. However, $\mathbf{B_0}$ does vary on a day-to-day basis according to the trap's surroundings in the laboratory and the Earth's normal variation in local field strength. For daily operation therefore, we can fix the values of $\boldsymbol{A}$ leaving

only the 3 free parameters of $\mathbf{B_0}$. This means that a magnetic field compensation routine can be carried out much quicker: requiring a minimum of 3 scans to form a fully constrained problem. We typically perform 6, corresponding to field directions $\pm\hat{\mathbf{x}}, \pm\hat{\mathbf{y}}, \pm\hat{\mathbf{z}}$ or another orthogonal basis. This choice of field orientations maximizes the sensitivity $\partial B_\mu / \partial \mathrm{B}_{0,\mathrm{i}}$ to changes in the 3 underlying field components.

The requirements for the coil current drivers are fairly relaxed. Based on the sensitivities found in Equation 2.11, to achieve a field noise of 1 nT in the most sensitive direction only a current stability of 0.58 mA is needed. This is easily supplied by standard off-the-shelf equipment: we use TTi QL564P current supplies whose noise spec. is typically 20 µA RMS [126].

2.4.4.1 Coil switching

To investigate the time required for the magnetic field created by the coils to stabilize, a Bartington 3-axis magnetic field sensor [127] was used to measure the field produced by one of the trap coils. This sensor has a bandwidth of ∼3 kHz, ∼1× faster than the coil switching times.

In fact, one of the trap's compensation coils has many more coils than the others, allowing us to create larger magnetic fields. We therefore expect this coil to have a larger self-impedance, and to exhibit the slowest dynamics: the measurement of this coil is therefore an upper bound of the switching time of the others.

The current in this coil was switched from 0 mA to 200 mA and the magnetic field was monitored. Results are shown in Figure 2.10, where the characteristic decay constant of the induced field is found to be $\tau_{\mathrm{on}} = 2.643(2)$ ms. We must ensure therefore that our magnetic field scans are separated by at least several multiples of this lifetime. In practice, successive scans of the Zeeman components are separated by many seconds, so this is not a concern.

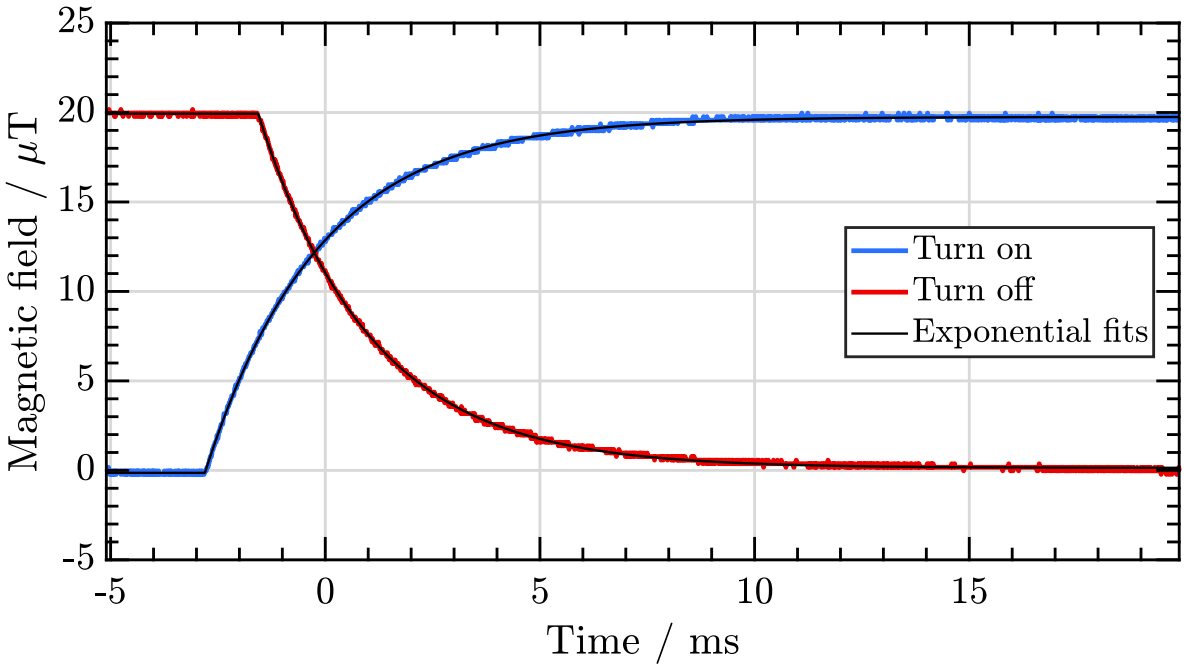

Figure 2.10: Magnetic field induced outside the chamber by the largest compensation coil, monitored by a 3-axis field sensor [127] as the coils are turned on and off. The exponential fits shown have decay constants $\tau_{on} = 2.643(2)$ ms and $\tau_{off} = 2.624(2)$ ms.

2.5 Optical phase-noise due to path-length variation

2.5.1 Active cancellation

There are many parts of our experiment that rely on the faithful delivery of an optical frequency from one place to another. Figure 6.1 in Chapter 6 will show how light produced in one laboratory ultimately ends up in three.[††] However this deliver process has the potential to introduce noise. Temperature variations or vibrations can alter the effective optical path-length for fibres or free-space beams, resulting in frequency offsets if unchecked.

To detect and compensate for this noise, we measure a heterodyne optical beat of

[††] In fact, for consistency checks, our light is measured simultaneously on two optical frequency combs in separate laboratories, for a total of four labs.

retro-reflected light that has sampled the noisy path twice[‡‡] [128, 129]. Light passes through an AOM, receiving a frequency boost of $f^{\mathrm{AOM}}(t)$. This light then passes through free-space and polarisation maintaining (PM) optical fibres until it arrives at its destination. Along the way, it experiences phase noise due to the conditions of its path, resulting in a change to its momentary frequency of $\delta f^{\mathrm{noise}}(t)$. A fraction of this light is retro-reflected and travels back along the same optical path, receiving the noise and AOM boost again, for a total change in frequency of

$$f(t) = 2 \times \left(f^{\mathrm{AOM}}(t) + \delta f^{\mathrm{noise}}(t) \right) \tag{2.12}$$

$$= 2 \times \left(f_0^{\mathrm{AOM}} + \delta f_{\mathrm{mod}}^{\mathrm{AOM}}(t) + \delta f^{\mathrm{noise}}(t) \right) \quad . \tag{2.13}$$

By combining the outgoing and returning beams on a fast photodiode, an optical heterodyne beat frequency can be measured at $f(t)$. In the noise-free case this frequency is at exactly twice the AOM's frequency, so to cancel the path-length variations we mix this beat note with an accurate reference frequency $f_{\mathrm{ref}} = 2f_0^{\mathrm{AOM}}$. The resultant DC signal is used to perform a phase-lock, actuating by modulating the drive frequency of the AOM $f^{\mathrm{AOM}}(t)$ such that $\delta f_{\mathrm{mod}}^{\mathrm{AOM}}(t) = -\delta f^{\mathrm{noise}}(t)$. Refs. [128, 129] contain more detail about this technique.

The bandwidth of this method is fundamentally limited by the travel time of light through the fibre. For e.g. a 50 m fibre, this restricts the loop-bandwidth to 3 MHz. This is typically slightly larger than the modulation bandwidth of an AOM, limited by acoustic propagation in its crystal to ∼1 MHz [130], and so does not present a problem. More importantly, path-length variation typically results from thermal or acoustic effects, both of which occur at frequencies significantly lower than this. In practice, our locks do not need to be anywhere near so fast to accurately remove phase noise at timescales longer a few periods of f_{ref}, typically ∼200 MHz in our laboratory.

[‡‡] We assume that the phase noise for the forward- and counter-propagating light is the same.

We use this technique for the IR light delivered from our laboratory to remote laboratories containing both frequency combs (see Section 2.6) and our remote high-finesse optical cavity (see Chapter 6). By placing the actuating AOMs at the remote ends of the fibre and using different modulation frequencies f_0^{AOM} for each we can measure all three phase noise signals on the same photo-detector, demodulating at the appropriate frequencies.

2.5.2 Effect of uncompensated path

The delivery of blue clock light to the ion, as shown in Figure 2.6, is not currently actively stabilised due to technical difficulties regarding its pulsed nature. This is an upgrade that we intend to make soon, however in the mean time, we can measure the effect of this uncompensated path.

The first order mode of the AOM in Figure 2.6 is sent to the trap via a photonic-crystal fibre (PCF).[§§] The end of the fibre has a flat facet, reflecting a fraction of the beam. This reflected light is then directed onto a fast photodiode where it beats with the original, unaltered light, producing the noise-dependent beat note $\Delta f(t)$ of Equation 2.12. Note that here $\delta f_{\mathrm{mod}}^{\mathrm{AOM}}(t) = 0$ because there is no feedback to the AOM: it always runs at f_0^{AOM}.

When used for a phase lock, this beat is mixed with a reference frequency at $2f_0^{\mathrm{AOM}}$ to produce a DC signal proportional to the phase deviation (for small deviations). However, in order to reduce sensitivity to $1/f$ noise, we actually perform measurement at a higher frequency by using $f_{\mathrm{ref}} = 2f_0^{\mathrm{AOM}} + f_{\mathrm{M}}$, where $f_{\mathrm{M}} = 1.2\,\mathrm{MHz}$, chosen for immunity to low-bandwidth noise and compatibility with frequency counters.

[§§] The choice of a PDF was motivated by the need to carry several wavelengths simultaneously: this fibre delivers our ionization, cooling and repumping light as well as the two clock beams. However, PCFs also enjoy reduced sensitivity to thermal variation (as well as reduced non-linear effects).

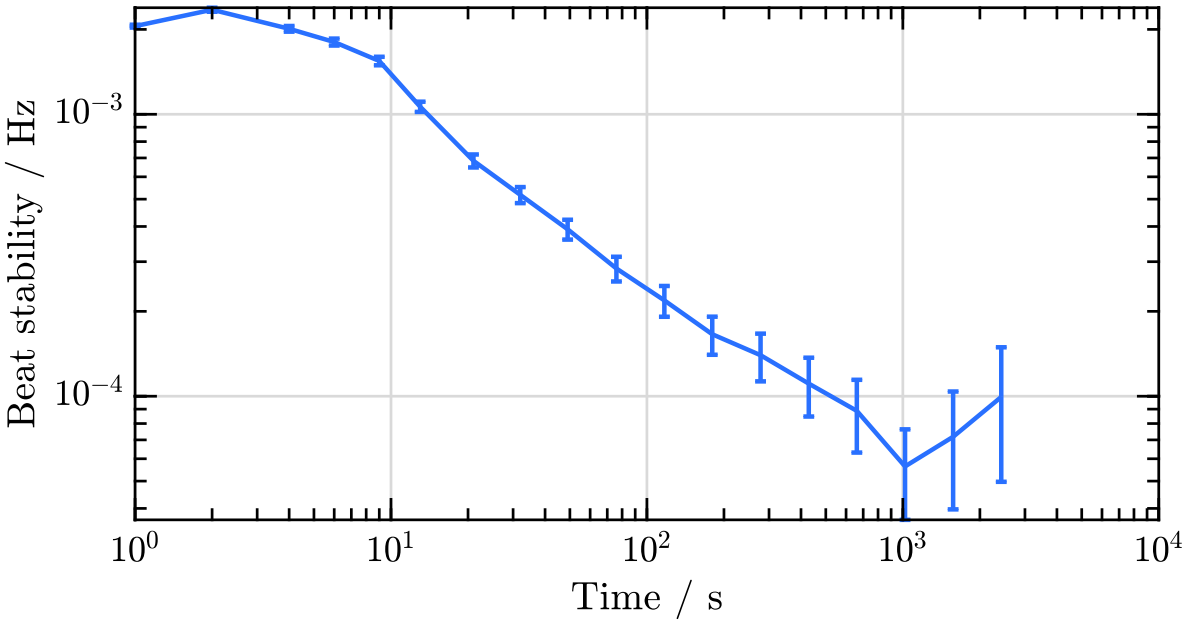

FIGURE 2.11: Phase noise stability of the free-space and fibre link to the ion. This stability is assessed by using the apparatus shown in Figure 2.6 and described in the text.

This beat frequency was counted using a frequency counter in lambda mode, clocked by the local time-scale reference. The Allan deviation of this beat is divided by 2 to recover δf^{noise} and plotted in Figure 2.11.[¶¶] The mean of the beat signal measured was $f_M + 2\delta f^{\text{noise}} = 1\,200\,000.000\,090\,\text{Hz}$ and an uncertainty of 0.1 mHz was measured at $\tau = 1000\,\text{s}$.

2.6 Optical frequency measurements

Chapter 3 covers the atomic reference, Chapter 6 the local oscillator—this Section will briefly treat the third and final part of an optical atomic clock: the frequency comb.

The significance of John Hall and Theodor Hänsch's invention for the field of frequency metrology can hardly be overstated [131, 132]. I began my DPhil well after the frequency comb had become an established part of the clock operator's life but, before

[¶¶] The instability of the maser reference can be neglected at this level.

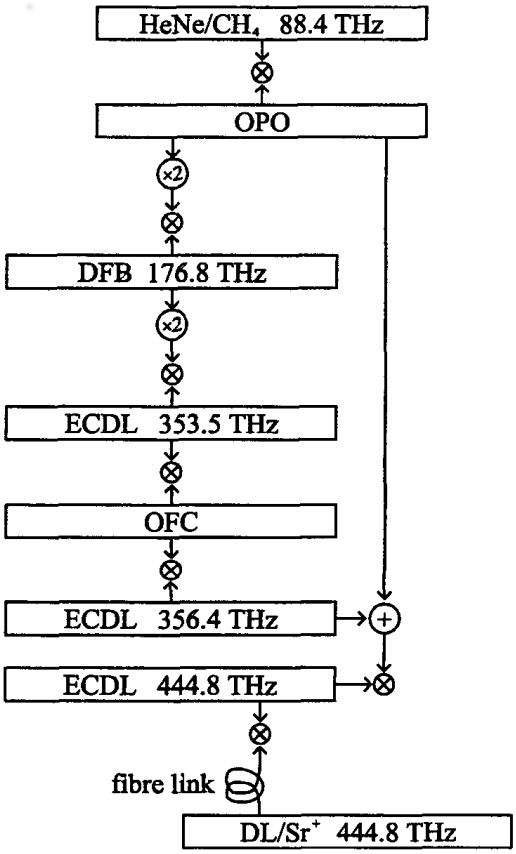

Figure 2.12: A figure reproduced from [133] showing the chain required to link the transition frequency of $^{88}Sr^{+}$ at 444.8 THz back to a reference transition in methane at 88.4 THz. Modern optical frequency combs allow linkage of high optical frequencies (e.g. our E3 transition at 642 THz) all the way to a 10 MHz reference frequency in a single step, whilst simultaneously measuring several other optical frequencies.

their advent, optical frequency measurements involved painstakingly linking from your laser frequency back to a known reference via complex and fragile *frequency chains* [133, 134].

The femtosecond frequency comb is based on a pulse train of "ultrashort" pulses, typically generated by a mode-locked laser. Viewed in the frequency domain, these pulses form a Dirac comb spaced by the pulse repetition rate f_R, convoluted with a Gaussian profile due to the pulses' finite length. The frequency of any tooth can then

be clearly identified as

$$v = f_0 + nf_R \tag{2.14}$$

where n is the mode number and f_0 is the carrier-envelope offset (CEO) frequency: the offset between the theoretical position of the zeroth mode and 0 Hz. f_R is under our control, so all that remains to be done to create a stable optical ruler is to bring f_0 under active control. This is done by creating an octave spanning comb and using SHG to double the frequency of a lower tooth. This doubled tooth is then compared to its upper partner: the *heterodyne beat* frequency*** between these is f_0.

Measuring an arbitrary optical frequency is now as simple as combining the light to be measured with the frequency comb on a fast photodiode, producing another heterodyne beat. This beat frequency (f_i) combined with knowledge of n, f_0 and f_R uniquely defines the light's frequency. The counters used to count these frequencies, all of which are in the RF spectrum and typically range from 10 to 200 MHz, are clocked to the local realization of Coordinated Universal Time (UTC): UTC(NPL). This provides traceability to TAI (exploited in Section 7.2) and a means of linking to the local caesium fountain, as well as other local optical references (see Section 6.4). For more information on the NPL frequency comb setup, see refs [5, 135].

The NPL frequency comb used for measurement is housed in a separate laboratory, rarely accessed and isolated from disturbance. All optical connections are made via fibre with active phase-noise cancellation applied, actuated via AOMs housed in the quiet comb laboratory. For a description of this technique, see Section 2.5.

***The term *heterodyne* refers to the creation of new frequencies, usually the sum and difference, by mixing together two others via some non-linear process. In electronics, this is performed with non-linear devices, most commonly diode mixers. In optics, however, physics is kind: since the observed quantity of light is invariably its intensity, the underlying electric fields must be squared. In the addition of two sinusoidal fields, $[E_1 \sin(\omega_1 t) + E_2 \sin(\omega_2 t)]^2$, it is the cross term $2E_1E_2 \sin(\omega_1 t)\sin(\omega_2 t) \equiv E_1E_2[\cos(\omega_1 - \omega_2)t - \cos(\omega_1 + \omega_2)t]$ which does the magic, requiring us simply to spatially overlap our beams to produce a signal containing their frequency difference.

Although the set-points of all AOM frequencies required to reconstruct the frequency of the light at the ion are logged on a 1-second grid, the RF drive signals for these AOMs are also sent to the comb laboratory and counted using counters gated identically to those measuring the optical beat to guarantee correct frequency synthesis and avoid problems introduced by misaligned timestamps.

2.7 Future upgrades to optical system

With advances in optical technology comes the opportunity to make our system more robust and compact. Robustness is a key concern: advances in stability are pointless if your clock spends much of its time offline and far more data can be gathered when researchers are not required to burn the candle at both ends to get it. As we will see in Chapter 7 the International Timescales with Optical Clocks (ITOC) campaign benefited from this, with several clocks around Europe showing up-times greater than 75 %. With a bit more work, we hope to push our system closer to 100 %, with full automation of all processes.

Key to any atomic physics experiment is the laser setup, presented earlier in this chapter. Given the success of our ion trap (see Chapter 3) our main failure modes are now laser-related. Our current setup involves 5 lasers aside from the clock lasers at wavelengths (935, 369, 399, 760) nm (we have two lasers at 760 nm). These are variously locked either to individual cavities or steered w.r.t. a Wavemeter. The ytterbium ion's hyperfine structure necessitates various sidebands each of several gigahertz (see Section 2.2) which are currently applied via resonant EOMs.

A future solution which I hope to adopt in the development of the new system could involve a *transfer cavity* used to transfer some of the stability of a clock laser to the other lasers. Obviously, hertz-level stability is unnecessary for repumping a dipole

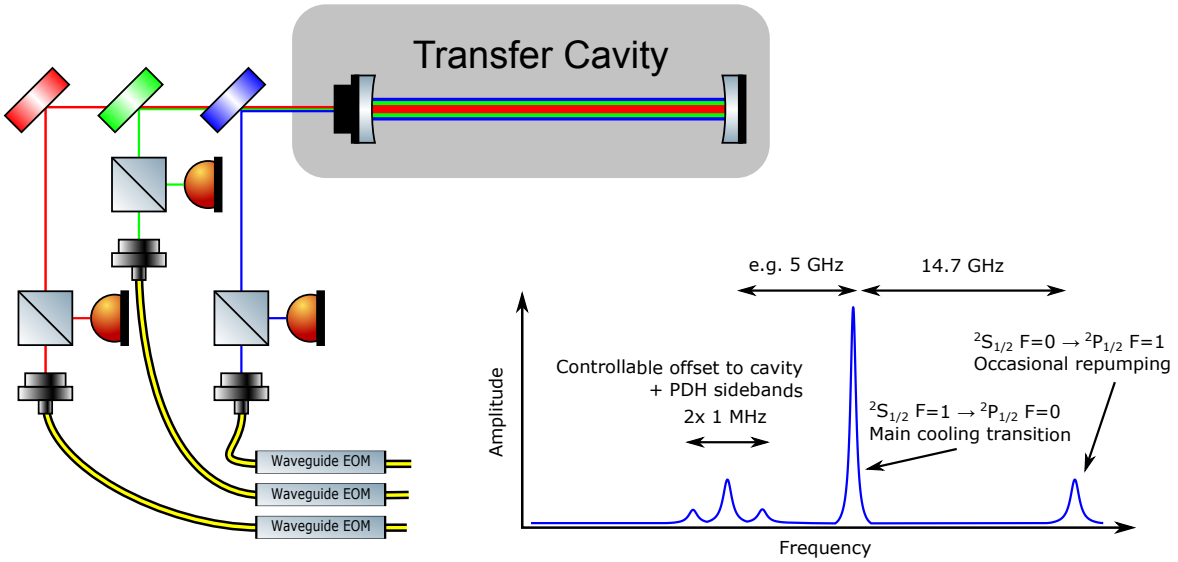

FIGURE 2.13: *(left)* A possible setup for future laser stabilisation. A *transfer cavity* is used to lock several lasers simultaneously using the PDH method. The sidebands for this technique are added using in-line waveguide EOMs which also add configurable offsets to control the frequency of the locked laser. Any desired hyperfine structure related sidebands can be added in the same step, making the setup highly flexible. *(right)* An example of how this could work for the 369 nm cooling laser. A 5 GHz frequency is phase-modulated at 1 MHz: this offsets the carrier by 5 GHz from the cavity mode and provides a PDH error signal. Another sideband at 14.7 GHz is also added to perform repumping from the otherwise dark F=0 state (see §2.2.2). The 2.2 GHz sidebands for state preparation could be added in the same manner as and when desired, removing the need for the separate beam path shown in Figure 2.3.

transition. However, use of waveguide EOMs would allow a fully in-fibre solution to (a) providing an adjustable offset to the transfer cavity and (b) applying sidebands to the light, both for state addressing and locking via the PDH method. Figure 2.13 shows how this could work for the 369 nm laser, where the 14.7 GHz sideband is now provided by the same unit that also adds a 5 GHz offset frequency, complete with PDH sidebands for locking. This approach can be simply extended to multiple lasers by using dichroic filters, also shown.

Aside from its low-maintenance nature, a key advantage of this setup is its flexibility. Ytterbium has many stable isotopes and some interesting experiments [22] involve comparison between their properties. Until now, driving isotopes with a different hyperfine

structure was impractical since it would require a whole new set of expensive resonant EOMs and realignment of the entire system each time we switch ions. With this design, changing repumping structure is as simple as reprogramming a DDS.

A new end-cap trap 3

> Time flies like an arrow; fruit flies like a banana.
>
> — *Anthony G. Oettinger*

There are two broad categories of optical atomic clocks in circulation. Both trap either one or many atoms, chosen for an ultra-narrow "clock" transition that is to be interrogated. Lattice clocks use neutral atoms, trapped in an optical lattice structure. Ion clocks, such as ours, charge their atoms by ionization and then exploit their subsequent interaction with electric fields to confine them. In both types, any and all environmental effects that could alter the transition's frequency must be carefully minimised and/or characterised.

While Chapter 1 described the three elements of an atomic clock, it could be argued that the ion trap is really its heart. Our job as metrologists is to create an atomic reference whose isolation from the external world is as near complete as we can make it. A well-built ion trap allows us to tailor every aspect of the atom's environment repeatably and accurately.

This chapter will build on the work reported in [6]. It will describe the obstacles encountered when building an ion trap designed for high-precision frequency metrology and how designers must choose compromises between sometimes conflicting requirements. Section 3.2 will describe our new ion trap, and characterisation of its most important properties will be reported in Sections 3.3 to 3.5. Finally, the improvements made to this design that are being incorporated into the next trap will be summarised in Section 3.6, designed both to solve bugs encountered with the previous build and to enable new physics with the $^{171}Yb^{+}$ frequency standard.

3.1 Requirements for high-precision spectroscopy

Quadrupole ion traps are widely used in fields varying from quantum computing [136] to mass spectrometry [137]. As such, a wide range of solutions to the different challenges posed by these fields have been found. The requirements for a trap suitable for high-precision frequency spectroscopy are different again, and can be summarised as follows:

1. At the ion's position, environmental Black-Body Radiation (BBR) must be very well defined. In practice, this means that thermal emissions from the trap must be minimised so that the well-controlled ambient field dominates the ion's thermal environment.

2. The anomalous *phonon heating rate* Γ_H of the ion must be minimised.

3. Stray electric fields capable of producing RF-induced micromotion must be eliminated.

4. Collisions with background gas must be minimised.

5. Fluorescence collection from the ion must be maximised.

The first two of these requirements are in conflict. The dominant mechanism for thermal heating of the trap is dielectric loss in the insulating components of the structure, primarily the spacers shown in Figure 3.1 that separate the confining RF potential from DC compensation electrodes. This loss takes the form

$$P = V\epsilon_r'\epsilon_0 \tan(\delta)\, \Omega_{RF}\, E^2 \quad , \tag{3.1}$$

where the power P dissipated into the dielectric of volume V depends on the dielectric's relative permittivity ϵ_r' and loss tangent $\tan(\delta)$ when an oscillating electric field E of frequency Ω_{RF} is applied across it. The obvious way to reduce thermal heating of the trap structure is therefore to reduce the frequency and amplitude of the confining electric field: Ω_{RF} and E.

However, low phonon heating rates Γ_H are achieved through tight confinement of the ion in the centre of the trap, where the anharmonic terms of the confining potential are minimised. To accomplish this, your trap requires high radial and secular frequencies $\omega_{r,z}$ which are obtained through high amplitude and frequency of the trapping RF drive.

Another process that affects the anomalous heating rate of a trapped ion is electrical field noise due to impurities and irregularities in the electrode surfaces. The exact cause of this effect is still uncertain, but empirical studies have shown the heating rate to have a $z_0^{-\alpha}$ dependence on the electrode separation, z_0 with $\alpha = 3.5(1)$ [138, 139]. This makes large electrode separations beneficial, but maintaining a given secular frequency $\omega_{r,z}$ while changing z_0 requires E to be increased as z_0^2.

Taken together, these conflicting considerations necessitate a careful design which finds a compromise suitable for operation of the trap as a high-precision optical frequency reference.

The other requirements are more straightforward to meet. Relative phase delays between the RF voltage on the two end-caps will result in micromotion that cannot

be compensated using only DC fields. The trap structure must therefore be totally symmetric to ensure that the effective path length between the end-caps and the RF feed, including all possible capacitive and inductive delays, is equal. Likewise the ion must be shielded from any RF field that does not come from the end-caps. The ion trap must be contained within an UHV / XHV environment to reduce pressure-dependent shifts on the order of $\sim 1 \times 10^5\,\mathrm{Hz\,Pa^{-1}}$ [140].

Finally, any apertures in the imaging setup should be placed as close to the ion as possible to increase the numerical aperture (NA) and hence fluorescence collection efficiency. Fast state detection is necessary for transitions with short excited state lifetimes to avoid losing excitation probability [141], decreasing the clock stability through increased dead-time fraction or introducing the Dick effect from the resulting undersampling of the local oscillator noise. A high signal-to-noise ratio (SNR) also permits easy use of photon correlation spectroscopy to minimize the excess micromotion, as is discussed in §3.5.1.

3.2 Design decisions

Our trap is based on the end-cap design [101] consisting of two cylindrical electrodes held at the same RF potential, contained within a pair of DC electrodes. This type of ion trap is used in multiple laboratories [5, 45, 142] and offers excellent optical access in the radial plane. Recent experiments with fibre-optics contained within the end-cap electrodes have extended this access into the axial direction [142].

A schematic of the trap is shown in Figure 3.1. The support structure for the trap, which also acts as the high voltage RF feed, is made of oxygen-free, high thermal conductivity (OFHC) copper. OFHC copper has both high electrical and thermal conductivity, and exhibits low out-gassing which will reduce ion loss via chemical reactions

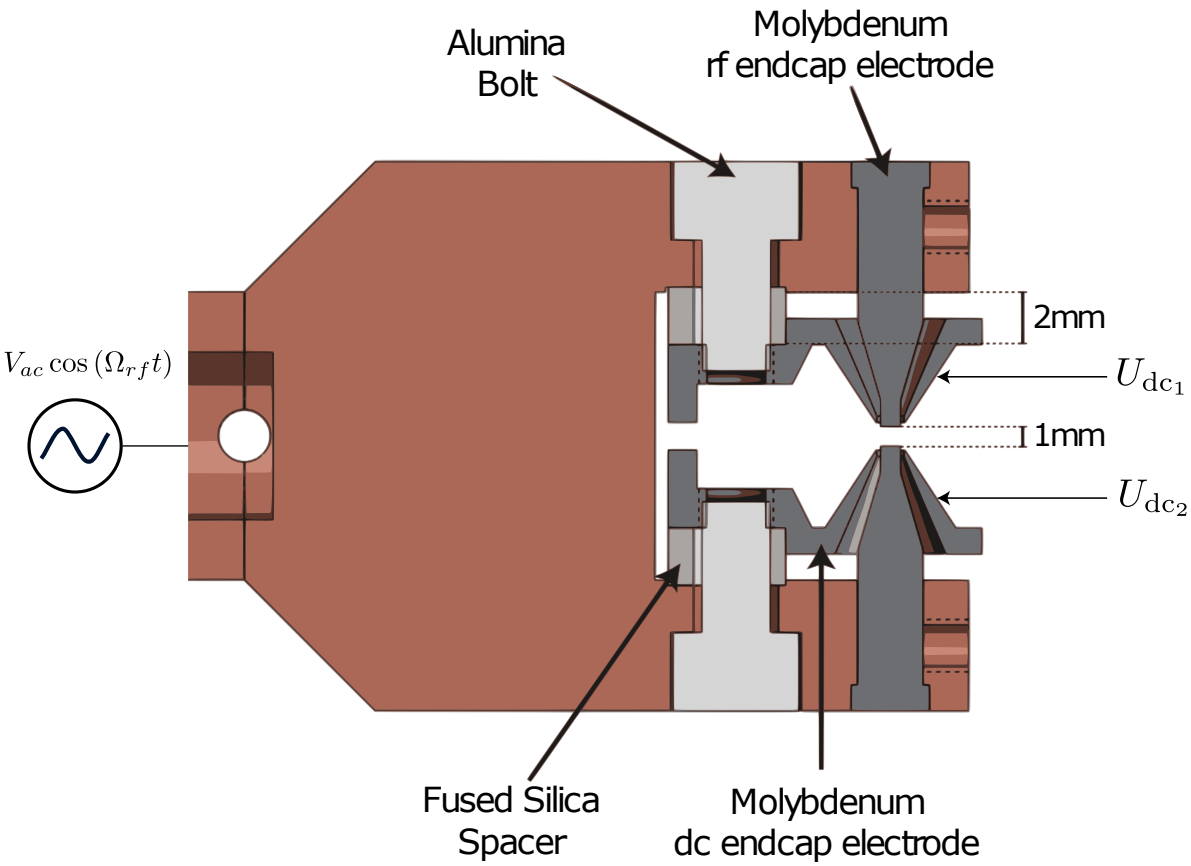

FIGURE 3.1: Vertical cross-section through the trap structure. The RF end-caps are secured into the oxygen-free, high thermal conductivity (OFHC) copper with M2 set-screws and sit within hollow DC end-cap electrodes, supported by fused silica spacers and recessed alumina bolts.

of the ion with oxygen. The two 99.9 % purity molybdenum RF end-cap electrodes are secured into the copper mount using M2 set-screws. Molybdenum has good electrical and thermal conductivity, is non-magnetic, and can be polished to a high surface quality. Material properties are also thought to contribute to Γ_H and, whilst the mechanism behind this is unclear, traps with cleaned molybdenum electrodes have demonstrated excellent results [143]. The faces of the RF electrodes which dominate the ion's field of view were mechanically polished to achieve a mirror quality finish as shown in Figure 3.2. The mean surface roughness was measured via focal-variation microscopy to be 20 nm, resulting in an emissivity of $\epsilon \approx 0.02$ at 300 K.

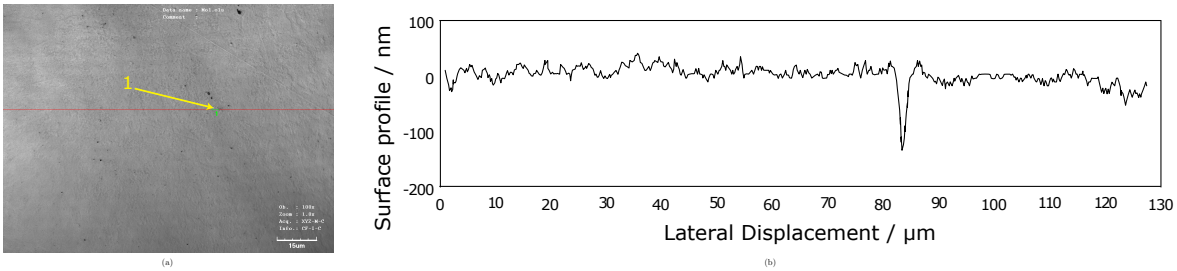

Figure 3.2: *(left)* Focal variation microscopy image of the polished surface of the upper RF end-cap electrode.
(right) Surface profile along the red line. The 150 nm pit highlighted by the yellow marker (1) is typical of the other imperfections which are visible as black dots in this image, although on a larger scale.

As the inner end-cap electrodes represent the largest solid angle contribution to the ion's field of view, their low emissivity reduces the thermal radiation that the ion will experience from any temperature rise of these end-caps. The polished surface may also reduce Γ_H as it removes any possible points for field emission of electrons and ensures a uniform surface free from adsorbates which have been proposed as a source of electric field noise [138]. The electrode tips have a diameter of 750 µm and a separation of 1000 µm.

3.2.1 Construction

Two molybdenum DC electrodes surround the RF end-caps and form the ground reference for the RF potential in the trapping region. The gap between the RF and DC electrodes in the trapping region is 135 µm to ensure a good quadrupole potential. This gap increases to 1 mm at the base to reduce the capacitance between the end-caps and thus reduce the RF current required to drive the trap. This also allows the RF electrodes to increase in thickness near the base increasing their mechanical rigidity. The DC electrodes are positioned using a pair of fused silica spacers and are secured with 99.9 % purity alumina bolts. By placing the dielectrics in a non-critical region away from the trap centre, it is possible to have a large separation between the high voltage

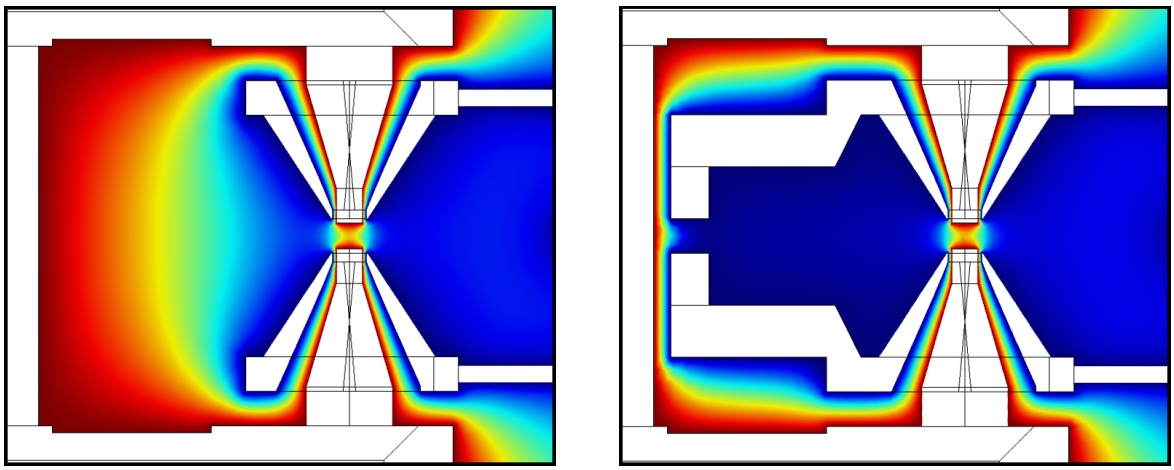

(a) (b)

FIGURE 3.3: finite-element method (FEM) simulation of the electrical potential in the trap, induced by the electrodes: (a) shows the potential if the DC end-caps were not extended to shield from the copper C, and (b) shows the trap as it was constructed. Simulation of the electric potential was performed using the COMSOL software package. With the copper C-shaped mount unshielded, the RF potential asymmetrically distorts the quadrupole potential in the trapping region. The phase difference between the RF wave at the end-caps and on the C could cause uncompensatable micromotion if not avoided.

and DC electrodes greatly reducing E^2 across the lossy dielectric and therefore reducing the thermal heating in the dielectric due to its non-zero loss-tangent. Positioning the high emissivity dielectric behind the DC end-cap also removes any direct line of sight between it and the ion.

The C-shape of the copper mount breaks the trap's cylindrical symmetry (Figure 3.3(a)). To correct this, the asymmetric mounting protrusions on the DC end-caps effectively shield the ion from the copper mount, restoring the surrounding ground potential as shown in Figure 3.3(b). Without the extra shielding the RF minimum would be shifted from the geometric centre of the trap, and there would no longer be a true micromotion zero due to the phase delay between the RF potential from the electrode tips and the centre of the C.

The DC electric field in the trapping region is controlled by applying static voltages

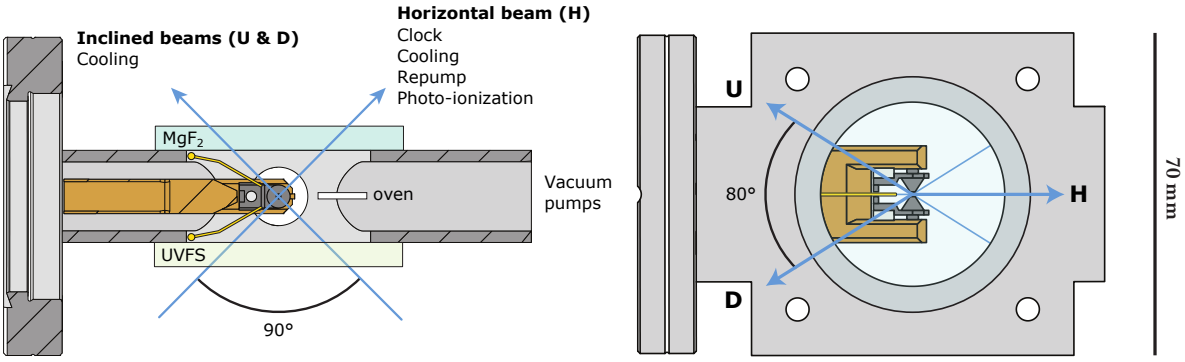

FIGURE 3.4: Schematic diagram of the trap and vacuum chamber. The compensation electrodes are shown in yellow and the paths of the named collinear laser beams (**H**orizontal, **U**p and **D**own) are shown as blue lines.
(left) Cross-section in the horizontal plane taken through the trap centre. *(right)* Front view.

to the DC electrodes (axial direction) and to two fixed compensation electrodes set back from trap centre by 5 mm in the radial plane (Figure 3.4) with a separation of 60° to maximize optical access in the radial plane. The DC electrodes are capacitively shorted to ground via 1 µF capacitors* to prevent any RF pickup on the DC electrodes that could be re-radiated with a phase offset. These capacitors are located 50 mm from trap centre on the air-side of the DC feed-through. The applied DC voltages are filtered close to the feed-through using a combination of passive RC and LC π-filters.†

Isotopically enriched neutral ytterbium is contained within a resistively heated tantalum tube oven. The atomic beam is slightly collimated (opening angle of 10°) reducing the amount of ytterbium deposited on the trap structure during loading. Ytterbium deposits can cause patch potentials leading to changes in the necessary compensation voltages and might also affect the phonon heating rate of the ion.

*High series resonant frequency (SRF) SMD components (X7R dielectric) ensure good performance in the 1 to 10 MHz frequency range.
†10 Hz and 100 kHz respectively.

3.2.2 Vacuum system

The vacuum system maximizes the optical access to the trap whilst maintaining a small, light-weight package. The chamber was machined out of a single aluminium block and is fitted with non-magnetic ConFlat vacuum flanges (CF) mounting flanges. The trap region of the chamber takes the form of a $70 \times 70 \times 20\,\mathrm{mm}^3$ cuboid with a central $\varnothing = 40\,\mathrm{mm}$ cylindrical opening (Figure 3.4). This opening is sealed using two $\varnothing = 50\,\mathrm{mm}$ view-ports. The laser access and ion imaging window is anti-reflection coated UV-grade fused silica (UVFS). The other window is magnesium fluoride (MgF_2), which is transparent for radiation up to $\lambda = 8\,\mu\mathrm{m}$ to allow (a) direct thermal imaging of the trap structure during operation (Figure 3.6) and (b) entry of a $7\,\mu\mathrm{m}$ laser (see Chapter 4). Both windows are cold-welded to the chamber with $\varnothing = 1\,\mathrm{mm}$ indium wire, achieving undetectable helium leak rates.

The indium sealed windows allow a maximum optical access opening angle of 112°, compared to the 80° from a traditional CF optic, and allows us to probe and cool the ion in two perpendicular radial directions. This also maximizes the effectiveness of the polarization spinning technique [144] and ensures a high fluorescence rate. Optical access in the axial direction is limited by the trap structure itself at 103°.

Ultra-high vacuum is maintained by a SAES NexTorr D100-5 combination non-evaporable getter (NEG) and ion-getter pump. The NEG provides a pumping speed of up to $100\,\mathrm{L\,s^{-1}}$ for active gases (H_2, H_2O, N_2, O_2, etc.), while inert gases are pumped by the ion getter pump at a rate of $6\,\mathrm{L\,s^{-1}}$.

After final assembly, a bakeout at $125\,^{\circ}\mathrm{C}$ roughed by a turbo-molecular pump achieved a base pressure of $< 1 \times 10^{-9}\,\mathrm{Pa}$ ($1 \times 10^{-11}\,\mathrm{mbar}$) determined by the current draw of the ion pump. For a Langevin-approximated sensitivity of $1 \times 10^5\,\mathrm{Hz\,Pa^{-1}}$ [140] this corresponds to a shift of about $100\,\mu\mathrm{Hz}$.

3.2.3 Light delivery and collection

The ion is illuminated along three optical axes H, U and D (see Figure 3.4). H samples motion in the radial plane only, and is almost perpendicular to the projections of both U and D on this plane. U and D both also sample the axial motion of the ion at inclines of $\pm 40°$ to the radial plane.

The H beam contains all the wavelengths that are used in the experiment which range from the UV (369 nm for cooling) to the IR (935 nm for repumping). These wavelengths are combined using dichroic beam-splitters and coupled into an endlessly-single-mode photonic crystal fibre [145]. The fibre output is brought to an achromatic focus of waist $w = 19\,\mu\text{m}$ at the ion's position using a pair of off-axis parabolic mirrors, ensuring perfect overlap of all lasers onto the ion. The two beams that are raised out of the horizontal plane (U and D) only supply cooling light.

Atomic fluorescence is collected through the UVFS view-port using an aspheric lens pair in a 2.6:1 telescope. After spatial and spectral filtering an on-resonance fluorescence signal of $20\,000\,\text{s}^{-1}$ is obtained for a single $^{171}\text{Yb}^+$ ion at I_{sat} for its 369 nm $^2\text{S}_{1/2} \rightarrow {}^2\text{P}_{1/2}$ dipole transition ($\tau = 8.12(2)$ ns [115]). For a typical background count rate of $50\,\text{s}^{-1}$ due to stray scatter from the 369 nm cooling beam this results in a signal to noise ratio of SNR $= 400$.

3.3 Thermal evaluation

One of the dominant causes of uncertainty in state-of-the-art optical atomic clocks is the Stark shift caused by the emission of black-body radiation from the trap and vacuum chamber apparatus (see Chapter 4). It is therefore essential that the trap is designed such that any temperature rise during operation is low, can be accurately determined, and can be kept stable.

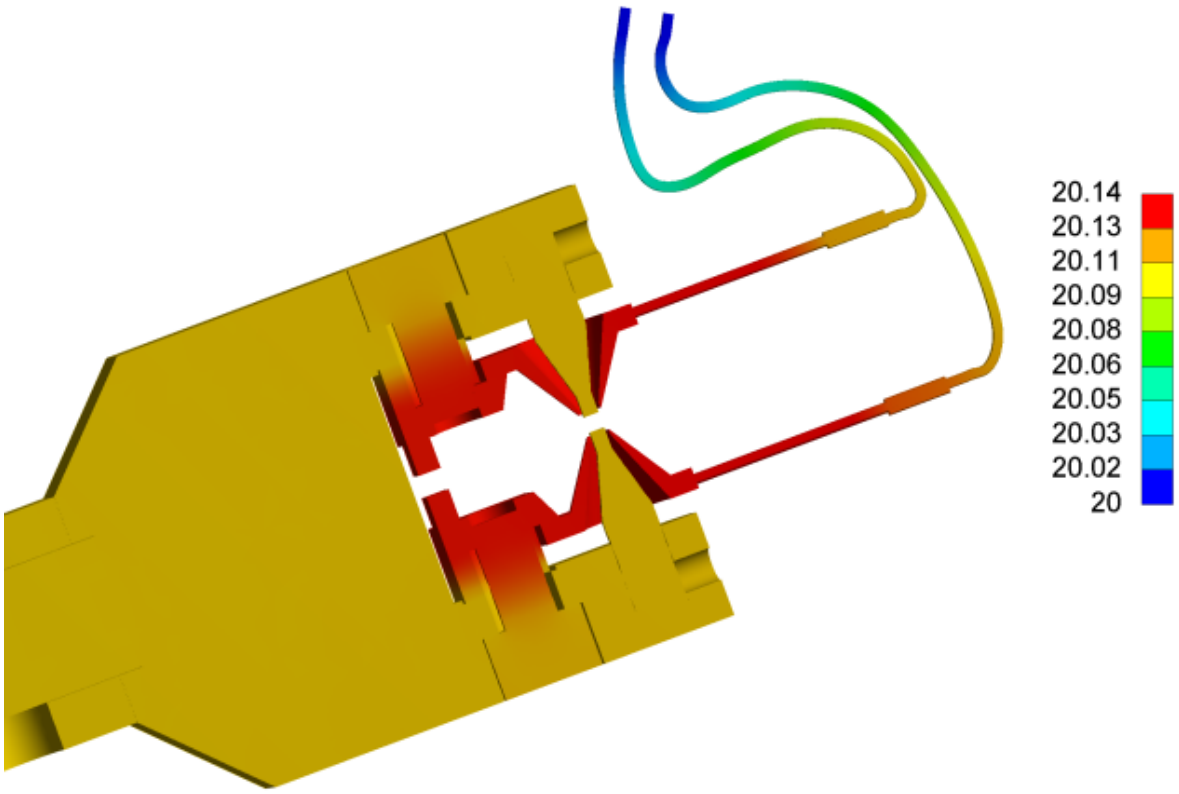

FIGURE 3.5: FEM simulation of the trap's temperature cross-section for an applied RF potential of $\Omega_{RF}/2\pi = 15\,\mathrm{MHz}$, chosen to give radial secular frequencies of $\omega_r/2\pi = 1\,\mathrm{MHz}$. The maximum temperature rise was determined to be 0.15 K. This figure is based on work published in [146].

Finite-element models (FEM) were developed by the Czech Metrology Institute (CMI) to calculate the changes in the temperature distribution across our ion trap caused by its operation, and thus the effective temperature of the total BBR environment seen by the ion [146]. These models find that the maximum temperature rise of any part of the trap structure should be 0.15 K under standard operating conditions, as shown in Figure 3.5. As the solid angle subtended by the hot regions of the trap is very small and the RF electrode, which has a very large solid angle, has been polished to a mirror finish, the effective temperature rise that should be seen by the ion is much lower than this; $\Delta T_{ion} = 0.02(2)\,\mathrm{K}$.

The thermal characteristics of the operating trap were measured in situ through the

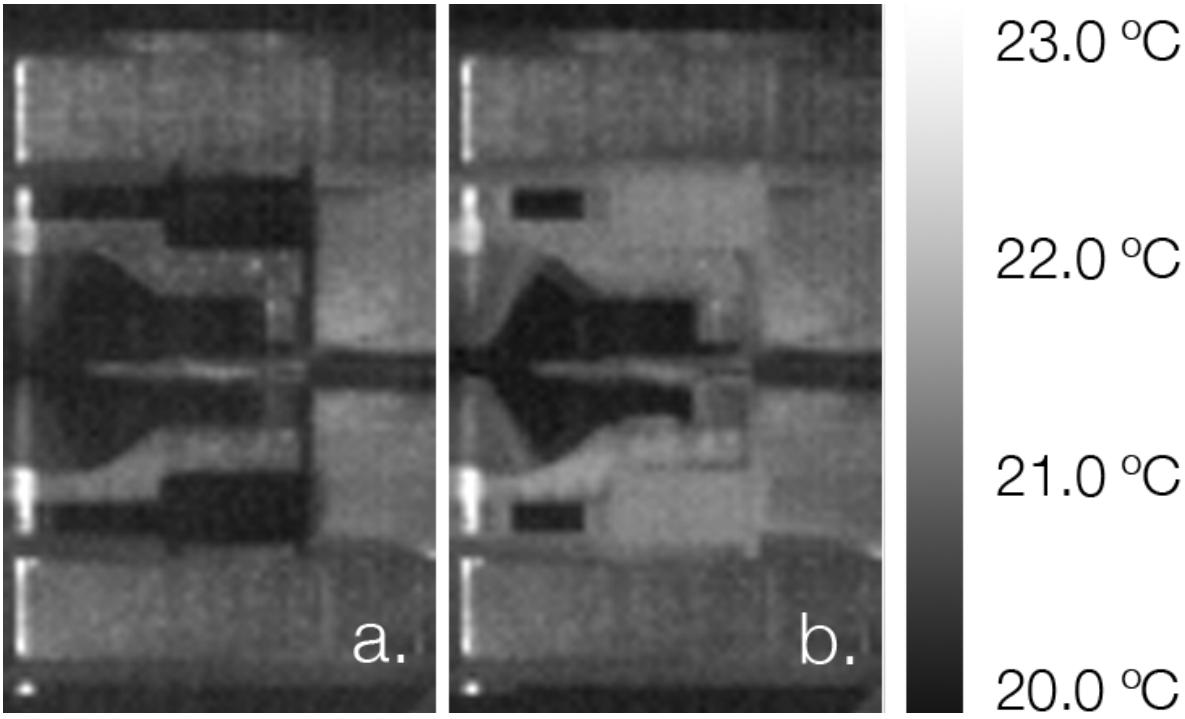

Figure 3.6: IR images of the trap structure taken in the $\lambda = 3$ to 5 µm range (a) without any applied RF trapping potential and (b) with $\Omega_{RF}/2\pi = 15$ MHz.
The IR images have not been corrected for emissivity and thus show the effective temperature that the ion experiences rather than the actual temperature of the trap. The visible reflections (e.g. on the LHS) are due to ambient radiation in the laboratory which is shielded during normal operation. These measurements disagree with the FEM model shown in Figure 3.5, a difference we attribute to unexpected heating in the vacuum feed-through.

MgF_2 window using a Cedip Silver, thermal infrared camera in the 3 to 5 µm radiation band (Figure 3.6).

The imaging setup was pre-calibrated by measuring target samples at known temperatures. During initial characterization of the trap [146] it was found that dielectric heating in the ultra-high vacuum (UHV) feed-through completely dominated over heating from the trap structure itself, causing disagreement with the FEM model and a temperature rise of 6.5 K when the trap was driven at $\Omega_{RF}/2\pi = 21$ MHz. A simple heat sink made from a thermally conductive ceramic post (Shapal [147], $\varnothing = 13$ mm) reduced this temperature rise by a factor of two, and a further improvement in the feed-

through temperature was obtained by decreasing the drive frequency by 30 %. With these minor modifications, a temperature rise of 1.5 K was measured both with the thermal camera and calibrated PT100 sensors on the air-side of the feed-through, when an ion was trapped in a $\Omega_{RF}/2\pi = 14$ MHz field, chosen for radial secular frequencies of $\omega_R/2\pi = 1$ MHz. This results in an effective temperature rise at the ion of $\Delta T_{ion} = 0.14(14)$ K according to modeling.

3.4 Ion motional heating rate

Evaluation of the trap was done using a trapped single ion of $^{171}Yb^+$, however conclusions drawn about its performance should be transferable to other species. Ions have been loaded and trapped at RF frequencies from $\Omega_{RF}/2\pi = 3$ to 21 MHz.

The secular frequencies of trapped single ions were measured by 'tickling' the ion with a low-power RF field applied to one of the DC end-caps, as examined further in §3.4.3. Secular frequencies have been arbitrarily set from the kHz to the MHz range up to a maximum of $\omega_{x,y,z} = 2\pi\times$ (1.02, 1.04, 2.04) MHz, obtained using a helical resonator with a loaded resonant frequency of 14 MHz at 1 W of forward power. Ion lifetimes on the order of a week are routinely observed at all frequencies. Uncooled ion lifetimes of up to 15 h have been observed on multiple occasions.

Collisions with background gas molecules can populate the long-lived F-state in $^{171}Yb^+$, causing loss of fluorescence and ultimately the ion [148]. We routinely observe > 24 h lifetimes without collisional transfer to this state (with repumping disabled) which supports the low vacuum pressure measured in §3.2.2.

To measure the ion motional heating rate, perhaps the most important figure of merit for an ion trap, several methods were used, roughly in order of ease. In [6] the anomalous phonon heating rate was first evaluated using the Doppler re-cooling method,

concluding that $\mathrm{d}\langle n\rangle/\mathrm{d}t = 50(100)\,\mathrm{s}^{-1}$. Observing the heating-induced dephasing of the E3 transition provided $\mathrm{d}\langle n\rangle/\mathrm{d}t = 24(30)\,\mathrm{s}^{-1}$. For more details of these methods, see [6].

In order to reduce the uncertainty on this important number further, we used the amplitude of the ion's *secular sidebands* as a measure of its temperature.

3.4.1 Secular sidebands

Movement of an atom within an incident laser beam has the effect of modulating the phase of the electric field sampled by the atom. Later in Section 3.5 we will treat the ion's movement in its quadrupole confining potential fully. For this section however, it suffices to consider the time-averaged RF potential as a harmonic *pseudo-potential*.

The electric field caused by an interrogating laser can be written:

$$\mathbf{E} = \mathbf{E_0} e^{-i(\omega_L t - \mathbf{k}\cdot\mathbf{x})} \tag{3.2}$$

where ω_L is the angular frequency of the laser's oscillation, $\mathbf{k}$ is its wave vector and E_0 is the maximum electric field induced.

Under the simplifying assumption that the ion experiences only 1D movement at a secular frequency ω_S in the direction of the probe beam $\mathbf{k}$ with maximum displacement X, the position-related phase of the beam sampled by the ion is[‡]

$$\mathbf{k}\cdot\mathbf{x} = kX\sin(\omega_S t) \tag{3.3}$$

where the quantity $\beta = kX$ is commonly defined as the modulation depth [149].

Using the Jacobi-Anger identity,

$$e^{iz\cos\theta} \equiv \sum_{n=-\infty}^{\infty} i^n\, J_n(z)\, e^{in\theta} \tag{3.4}$$

$$\implies \quad e^{iz\sin\theta} \equiv \sum_{n=-\infty}^{\infty} J_n(z)\, e^{in\theta} \tag{3.5}$$

[‡]This analysis treats the ion's movement as purely classical, an approximation that is valid when the average population in the quantum harmonic oscillator's ground state is close to zero.

we now expand the modulation component in terms of the Bessel functions J_n:

$$\mathbf{E}(t) = \mathbf{E_0} e^{-i\omega_L t}\ e^{i(\beta \sin(\omega_S t))} \tag{3.6}$$

$$\equiv \mathbf{E_0} e^{-i\omega_L t} \sum_{n=-\infty}^{\infty} J_n(\beta)\ e^{in\omega_S t} \tag{3.7}$$

Finally by considering the Fourier transform and recalling the convolution theorem $\mathscr{F}\{a.b\} = \mathscr{F}\{a\} \circledast \mathscr{F}\{b\}$[§], it is apparent that the radiation experienced by the ion contains components at $\omega_L \pm n\omega_S$ for all $n \in \mathbb{Z}^+$, whose amplitudes are given by $J_n(\beta)$. These components are called *secular sidebands*, given by

$$\begin{aligned}
\mathbf{E}(\omega) &= \mathscr{F}\{\mathbf{E}(t)\} \\
&= \mathbf{E_0} \sum_{n=-\infty}^{\infty} J_n(\beta)\ \left[\mathscr{F}\left\{e^{-i\omega_L t}\right\} \circledast \mathscr{F}\left\{e^{in\omega_S t}\right\}\right] \\
&= \mathbf{E_0} \sum_{n=-\infty}^{\infty} J_n(\beta)\ \ \delta(\omega - \omega_L) \circledast \delta(\omega - n\omega_S) \quad .
\end{aligned} \tag{3.8}$$

The treatment above neglected both the finite frequency width of the interrogating laser and the natural linewidth of the transition. In practice, in order to resolve the secular sidebands it is necessary to choose a transition where the transition's natural linewidth $\gamma \ll \omega_S$, known as the "strong binding regime."

This rules out most Doppler-cooling transitions, whose linewidths are on the order of 10 MHz versus a typical $\omega_S = 1\,\text{MHz}$. The two most common solutions to this problem are either to interrogate a dipole-forbidden transition or to manufacture a low linewidth transition by inducing a Raman transition between two hyperfine or Zeeman sub-levels of the ground state. $^{171}\text{Yb}^+$ of course has an E2 clock transition, and we use this to resolve our secular sidebands.

By comparing the excitation of the carrier versus the first resolved sideband in the low saturation regime where the atom's response is proportional to the squared Rabi

[§]Where . denotes point-wise multiplication and $\circledast$ is the convolution operator.

frequency Ω_0^2 and therefore the intensity of the probing light, it is possible to measure the ratio

$$R = |J_1(\beta)|^2 / |J_0(\beta)|^2 \quad . \tag{3.9}$$

For the small values of β typical of a well-designed ion trap, this ratio is well approximated by $R \approx \frac{\beta^2}{4}$ [150].

Finally, we relate the ion's temperature to the modulation depth by linking the ion's maximum velocity $v_{max} = \omega_S X$ to the energy in a 1D harmonic oscillator $k_B T = \frac{1}{2} m v_{max}^2$, and obtain [140]:

$$\begin{aligned} k_B T &= \frac{1}{2} m \beta^2 c^2 \left(\frac{\omega_S}{\omega_0}\right)^2 \\ &\approx 2mc^2 \quad \left(\frac{\omega_S}{\omega_0}\right)^2 R \quad . \end{aligned} \tag{3.10}$$

3.4.2 Extension to 3D

To model a real trap we must now revisit the assumptions made in Equation 3.3. More generally, for a trap with secular modes in the directions $\hat{\mathbf{n}}_i$, we can write $\mathbf{E}(t) \propto e^{i\mathbf{k}\cdot\mathbf{x}(t)}$ with

$$\mathbf{k} \cdot \mathbf{x}(t) = \sum_i \mathbf{k} \cdot \hat{\mathbf{n}}_i \, \mathrm{X_i} \sin(\omega_i t) \tag{3.11}$$

where $\mathrm{X_i}$ and ω_i are the oscillation amplitude and secular frequency of the ith mode.

Since in our trap geometry the probe beam is in the radial plane, for the axial mode $\mathbf{k} \cdot \hat{\mathbf{n}}_3 \approx 0$ and we can write

$$\beta_i = \begin{cases} \mathbf{k} \cdot \hat{\mathbf{n}}_i \, X_i = k \cos\phi_i \, X_i, & i = 1, 2 \\ 0, & i = 3 \end{cases}$$

where ϕ is the angle between the probe beam and the mode, and $k = |\mathbf{k}|$.

Then, by substitution of Equation 3.11 into Equation 3.2, we obtain:

$$\begin{aligned}\mathbf{E}(t) &= \mathbf{E_0} e^{-i\omega_L t} \left[\sum_{n=-\infty}^{\infty} J_n(\beta_1)\, e^{in\omega_1 t}\right]\left[\sum_{n=-\infty}^{\infty} J_n(\beta_2)\, e^{in\omega_2 t}\right] \\ &\approx \mathbf{E_0} e^{-i\omega_L t} \left[1 + \frac{\mathrm{X}_1 k}{2}\cos\phi_1\, e^{\pm i\omega_1 t} + \frac{\mathrm{X}_2 k}{2}\cos\phi_2\, e^{\pm i\omega_2 t}\right]\end{aligned} \tag{3.12}$$

Since the directions of the three modes are in general unknown, the best approach would be to probe from several different directions on each sideband. However, in our trap the probe beam's direction is fixed w.r.t. the trap geometry. In these conditions, it is still possible to obtain an estimate for the ion's temperature by making the following assumptions:

1. The energy in all three modes is the same ($\omega_i X_i = const.$),
2. All modes are orthogonal ($\phi_1 = \phi_2 + \frac{\pi}{2}$).

If the above assumptions hold, the ratios between the excitation of the carrier and the first sidebands of the 2 radial secular modes are

$$\begin{aligned}R_1 &\approx \left(\frac{kX_1}{2}\right)^2 \cos^2\phi_1 \\ R_2 &\approx \left(\frac{kX_1}{2}\right)^2 \left(\frac{\omega_1}{\omega_2}\right)^2 \sin^2\phi_1\end{aligned} \tag{3.13}$$

The quantity X_1 is therefore

$$X_1^2 = \frac{4}{k^2}\left[R_1 + \left(\frac{\omega_2}{\omega_1}\right)^2 R_2\right] \tag{3.14}$$

Using Equation 3.10 with $\beta_{1D} = \beta_1/\cos\phi_i = kX_1$ to calculate the energy in the first mode, and remembering assumption 1 allows us to estimate the ion's total energy as:

$$k_B T_{total} = 6mc^2\, \frac{\omega_1^2 R_1 + \omega_2^2 R_2}{\omega_L^2} \tag{3.15}$$

3.4.3 Locating the sidebands

As mentioned above, the secular sidebands were driven using the E2 clock transition. Since this transition is typically ∼30 Hz wide, locating sidebands with a splitting on the order of 1 MHz would have taken a long time. We therefore use a technique known as *tickling* to identify the secular frequencies approximately.

The oven of the ion trap is used as an electrode since, unlike the DC compensation electrodes, the oven has no passive electrical filtering and is not needed for excess micromotion compensation (see Section 3.5). The cooling 369 nm $^2S_{1/2} \rightarrow {}^2P_{1/2}$ light is red-detuned to $\delta\omega \approx \Gamma_{FWHM} = 2\pi \times 19.7$ MHz [98, 115].

A $V_{max} = 9$ V RF signal is then applied to the oven and its frequency is slowly swept from 0 to 1 MHz while the ion's fluorescence is observed.

As the frequency passes through the secular resonances, the increased phonon heating rate results in an increased RMS velocity of the ion, and therefore an increased mean Doppler shift. At low voltages this results in an increase in fluorescence as the light is shifted closer to resonance. For the 9 V perturbing voltage used and with our particular trap geometry, the ion is actually heated further until the light is now blue-detuned from the shifted resonance. Left in this condition for long the ion would be lost, but we find that our trap is sufficiently deep to recover the ion even after several minutes in this state.

Tickling in this manner allowed us to locate 3 resonances at 438 kHz, 462 kHz and 857 kHz. These correspond to the two secular modes in the radial plane and the one at twice the frequency in the axial direction, characteristic of an end-cap trap.[¶] Note

[¶]We are able to observe this axial sideband even though our probe beam is in the radial plane because the trap's oven, acting here as an electrode on which the perpetuating "tickling" potential is applied, is slightly out of this place. It therefore couples to all three modes and the trap's slight asymmetry causes heating in the axial mode to couple into the radial plane where we observe its effect on the ion's fluorescence.

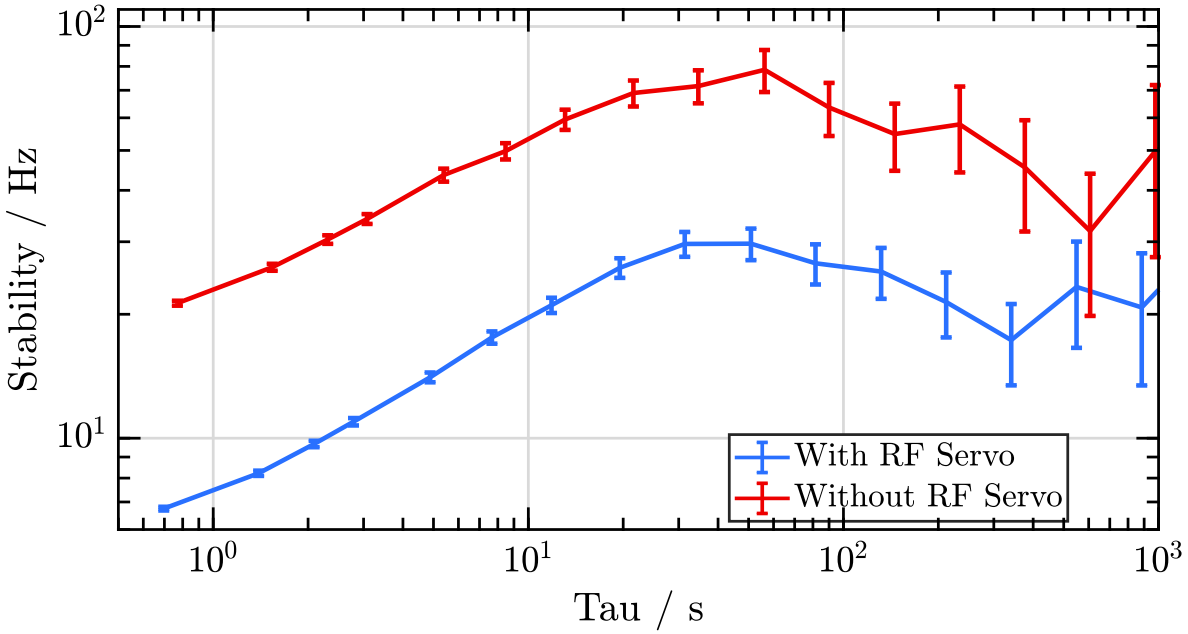

FIGURE 3.7: Allan deviation of stability in sideband frequency for the 446 kHz radial secular sideband. The two plots show a comparison between the sideband's frequency stability with (blue) and without (red) a servo controlling the RF power sent to the ion trap.

that these frequencies differ slightly from those measured later in this chapter due to the servo described in §3.4.4. The tickling was done without the servo engaged, and engaging the lock results in a small shift to the trap depth due to the small change in set-point.

3.4.4 Probing the sidebands

With the sidebands located, our task is now to measure the relative heights of each of them versus the carrier, giving us a measurement of R (Equation 3.9). We chose to probe the E2 transition with 2 ms long pulses, adjusting the power accordingly to maintain a π-pulse. The resultant Fourier broadening results in a minimum linewidth for both the carrier and the sidebands of 400 Hz. To assess the stability of the sidebands, we then ran a clock servo measuring their frequency separation from the carrier component (see Chapter 2 for details of the interrogation scheme). The instability of

the resultant data, shown in Figure 3.7, is the quadrature sum of noise due to changing power in the RF trapping field and Quantum Projection Noise (QPN). A low bandwidth ($\nu < 50\,\mathrm{kHz}$) digital servo was constructed that monitored a sample of the RF power sent to the filtering helical resonator via an Analogue to Digital Converter (ADC) monitoring the output of a low-passed, full-wave rectifying diode bridge. This feedback was intended to remove fluctuations in drive power due to changing gain of the RF amplifier[151], a category of device known to have significant temperature sensitivity.

Figure 3.7 indicates that with the servo in operation, the frequency instability of the secular sidebands is less than 30 Hz at all time-scales up to 1000 s.[‖]

With this assured, we then ran datasets where the carrier and sidebands were probed at their peaks to assess their excitation probabilities. This was done with the probe-beam's power significantly reduced from the level required for a $\pi/2$ pulse to ensure that we were in the low saturation regime for both features, where the excitation measured is proportional to the Rabi frequency and therefore to the intensity in the probe beam. These datasets were run with a pause between the state preparation and probing segments of the clock cycle of $\tau = (15,\ 70,\ 150,\ 600,\ 1000)\,\mathrm{ms}$, to allow time for the ion to heat. Datasets taking longer than 1000 s were stopped, re-centred and restarted to avoid the probe laser drifting away from the centre of the resonances.

Figure 3.8 shows the ion temperatures obtained for the two radial sidebands using measured values of R with Equation 3.10. The heating rates measured were $\frac{\mathrm{d}}{\mathrm{d}t}\langle n\rangle = (-4.9 \pm 5.2)\,\mathrm{s}^{-1}$ and $(-1.3 \pm 3.6)\,\mathrm{s}^{-1}$ where $\omega_S = 2\pi\times(446,\ 470)\,\mathrm{kHz}$ and the uncertainties quoted are standard errors.

[‖]The power servo acts to stabilize the power leaving the amplifier, but does not remove fluctuations due to changing coupling to the *helical resonator* used as a band-pass transformer to generate high trapping voltages. To remove these as well, it is necessary to monitor the amplitude of the high-voltage trap drive. A capacitive divider has been built to do this using a capacitance ratio of 0.2 pF : 20 pF with no measurable effect on the helical resonator's frequency resonance. This will in future be used to remove this source of fluctuations as well.

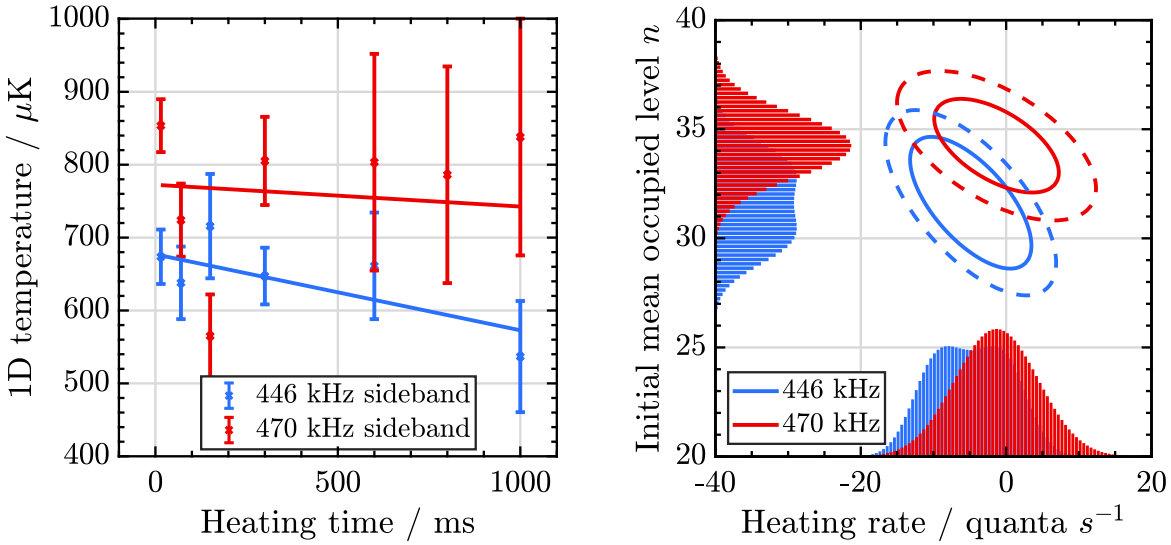

FIGURE 3.8: (a) 1-dimensional temperature of the ion determined by secular sideband–carrier ratio measurements for the two radial secular modes. No correction for the ion-motion projection onto the probing beams' directions has been applied.
(b) Confidence intervals and PDF histograms of the heating rate *(x axis)* and initial mean occupancy of trapping quantum harmonic oscillator (QHO) *(y axis)*. Solid (dashed) lines outline the 68 % (99 %) confidence regions. The heating rates determined by least-squares fitting were $\frac{\mathrm{d}}{\mathrm{d}t}\langle n\rangle = (-4.9 \pm 5.2)\,\mathrm{s}^{-1}$ and $(-1.3 \pm 3.6)\,\mathrm{s}^{-1}$ for the lower and upper sidebands respectively, where $\omega_S = 2\pi\times(446, 470)\,\mathrm{kHz}$ with all quoted uncertainties at the 1-sigma confidence level.

The 3-dimensional ion temperature can be estimated from the sideband ratio measurements with no additional heating time using Equation 3.15, under the assumptions listed in §3.4.2, as

$$T_{total} = 4.58(16)\,\mathrm{mK} \quad . \tag{3.16}$$

Comparing this to the Doppler temperature of [98, 115, 152]

$$T_D = \hbar\gamma/(2k_B) = 0.47\,\mathrm{mK} \tag{3.17}$$

reveals a problem with our cooling. Since the measured heating rate is low, the issue lies not with the trap but with the laser system used to effect Doppler cooling. This problem is under active investigation at time of writing. Note that this high ion temperature invalidates the approximations made in Equations 3.9 and 3.10, causing an overestimate

of the temperature / heating rate by ∼50 %. Still though, the ion is far too hot and this experiment will be repeated once the culprit has been found.

3.5 Micromotion

The picture of 1D ion motion presented in §3.4.1 or even of 3D motion in §3.4.2 is a simplification. Ion movement is relevant to frequency metrologists due to its effect on the clock transition via both special relativity and the Stark effect from the RF confining potential (see Section 5.1). To understand these dynamics, it is helpful to consider the quadrupole field produced by the trap's electrodes.

In a quadrupole field, the electric potential Φ can be written [153]

$$\Phi(\mathbf{r}) = \frac{\Phi_0}{2r_0^2}(\gamma_x x^2 + \gamma_y y^2 + \gamma_z z^2) \tag{3.18}$$

and the Laplace condition $\nabla^2\Phi = 0$ imposes $\sum_{i=\{x,y,z\}} \gamma_i = 0$.

For an end-cap trap with electrodes at potential Φ_0 separated by $2r_0$, one obtains $\gamma_x = \gamma_y = 1$, $\gamma_z = -2$. If the trapping potential is now allowed to vary sinusoidally in time as

$$\Phi_0 = U_0 + U_1 \cos(\Omega t) \quad , \tag{3.19}$$

the equation of motion in the direction of $x_i = \{x, y, z\}$ is

$$\ddot{x_i} + \gamma_i \frac{Q}{mr_0^2}[U_0 + U_1 \cos(\Omega t)]\, x_i = 0 \tag{3.20}$$

with Q, m the ion's charge and mass. Note that motion in the three dimensions is decoupled.

As lucky physicists often find, an equation of this form has already been studied by mathematicians. The Mathieu equation, originally proposed for the description of

vibration in elliptical drums, can be transformed to find the ion's movement [154, 155]. This equation is written in terms of dimensionless constants a_i, q_i and τ as [153]

$$\frac{\mathrm{d}^2}{\mathrm{d}\tau^2}x_i + [a_i + 2q_i\ \cos(2\tau)]\ x_i = 0 \tag{3.21}$$

where, by inspection of Equation 3.20, the dimensionless constants are defined as

$$a_i = \gamma_i \frac{4Q\kappa_{0i}U_0}{mr_0^2\Omega^2}, \quad q_i = \gamma_i \frac{2Q\kappa_{1i}U_1}{mr_0^2\Omega^2}, \quad \tau = \frac{\Omega t}{2} \tag{3.22}$$

and geometrical correction factors κ_{0i} and κ_{1i} of order 1 have been added.

The solution of this equation to first order in q_i and a_i is [149, 150]

$$x_i(t) = \Big(x_{0,i} + x_{1,i}\cos(\omega_i t)\Big)\Big(1 + \frac{q_i}{2}\cos(\Omega t + \phi_i)\Big), \tag{3.23}$$

$$\text{with} \quad \omega_i = \frac{\Omega}{2}\sqrt{a_i + \frac{q_i^2}{2}}\ . \tag{3.24}$$

$x_{0,i}$ represents a displacement of the ion's equilibrium position from trap-centre and is proportional to the DC electric field experienced by the ion (not represented in Equation 3.18). $x_{1,i}$ is the amplitude of the ion's motion in the secular modes ω_i and depends on the ion's temperature (see Equation 3.10). Figure 5.1 demonstrates this movement.

From this equation, it can be seen that the ion undergoes movement at four frequencies. Motion at the three secular frequencies $\omega_{x,y,z}$[**] is that typical of a simple harmonic oscillator (SHO) in the pseudo-potential created by the confining field. Driven motion at Ω has itself two components: *intrinsic micromotion* caused by the ion's secular motion exposing it to the driving RF field and *excess micromotion* resulting from stray electric fields moving the ion away from its ideal position ($x_{0,i} \neq 0$).

Section 5.1 treats the consequences of this micromotion from the frequency metrologist's point of view. Here, however, we deal with the detection and prevention of excess micromotion.

[**]Generally non-equal due to small variations in the geometric correction factors κ_i.

3.5.1 Detecting micromotion with RF–photon correlation

In §3.4.1 & §3.4.2 we demonstrated the effect of ion movement in a probing laser beam. The conclusions drawn there for motion at the secular frequencies apply equally well here to driven motions at Ω, namely that [150]

$$\begin{aligned} E(\omega) \propto\ & J_0(\beta)\ \delta(\omega - \omega_L) \\ & + J_1(\beta)\ \Big(\delta(\omega - \omega_L - \Omega) - \delta(\omega - \omega_L + \Omega)\Big) \quad . \end{aligned} \tag{3.25}$$

where $\beta = \mathbf{k}\cdot\mathbf{v}/\Omega$, J_i are the Bessel functions, $\mathbf{k}$ is the interrogating laser's wave vector, and $\mathbf{v}$ is the velocity of the ion. Similar methods can therefore be applied to detect micromotion as were used in probing the ion's temperature. The *resolved sideband method* is exactly equivalent to the technique used for detecting the secular motion amplitudes, relying on the E2 transition's low linewidth ($\Gamma \ll \Omega$) to let us spectrally resolve sidebands at $\pm\Omega$.

However, it is also possible (and indeed quicker) to detect excess micromotion via a transition that does not fulfill the resolved sideband condition — i.e. the cooling $^2S_{1/2}$ (F=1) $\rightarrow$ $^2P_{1/2}$ (F=0) transition at $\lambda = 369\,\text{nm}$. This is done by monitoring the arrival times of photons emitted by the ion and comparing them to the phase of the RF trap drive. Since the probability of absorption / emission of photons depends on the Doppler-shifted frequency of the light—related to the ion's velocity—as the ion moves in the trap its photon emission rate S varies at Ω. This variation can be used to detect the amplitude of excess micromotion by taking a histogram of delays between photon arrival times and RF zero-crossings, which takes the form

$$S(t) = S_0 + \Delta S \cos(\Omega t - \phi) \quad , \tag{3.26}$$

where S_0 is proportional to the mean fluorescence and the micromotion detection signal consists of both the normalised modulation amplitude $\Delta S/S_0$ and the phase ϕ.

The key observation for the use of this method to detect *excess* micromotion is that the phase of this detected signal jumps by π as the ion moves past the RF node due to the trap's symmetry. Therefore, for low amplitudes of secular motion—low ion temperatures—the intrinsic micromotion at Ω does not contribute to the time-averaged correlation signal $\Delta S/S_0$ when Ω is not an integer multiple of the secular frequency, effectively because the ion spends half its time in a location where the intrinsic micromotion's contribution to ΔS has one phase, and half its time where it has the opposite phase. The phase and amplitude of ΔS therefore reflect only the excess micromotion projected onto the interrogating beam's axis. For a detailed look at this topic, see Ref. [150].

This method has been modeled by Berkeland et al. in Ref. [156] under the assumption that $\Gamma \gg \Omega$ and the ion reaches steady-state at each point in the micromotion oscillation. Keller et al. treat the case where $\Gamma \approx \Omega$ in Ref. [150], relevant for us since our trapping frequency and cooling transition linewidth are both on the order of 10 MHz.

3.5.1.1 A low cost time-to-digital converter

In order to obtain the signal in Equation 3.26, a circuit was built to measure time delays of the photon arrivals. Figure 3.9 shows the printed circuit board (PCB) developed. Details are available in Appendix D.

This device is designed for measuring time delays between up to 4 events whose arrival times range from 3.5 ns to 4 ms of the first, trigger event. The design features an on-board microcontroller, signal conditioning electronics, integrated TDC, buffering and distribution of the photon counter signal to other lab electronics and a high-speed photon counter. Interfacing to the experimental control system is possible either through a front-panel USB interface or RS-485 carried over an in-house backplane, both of which

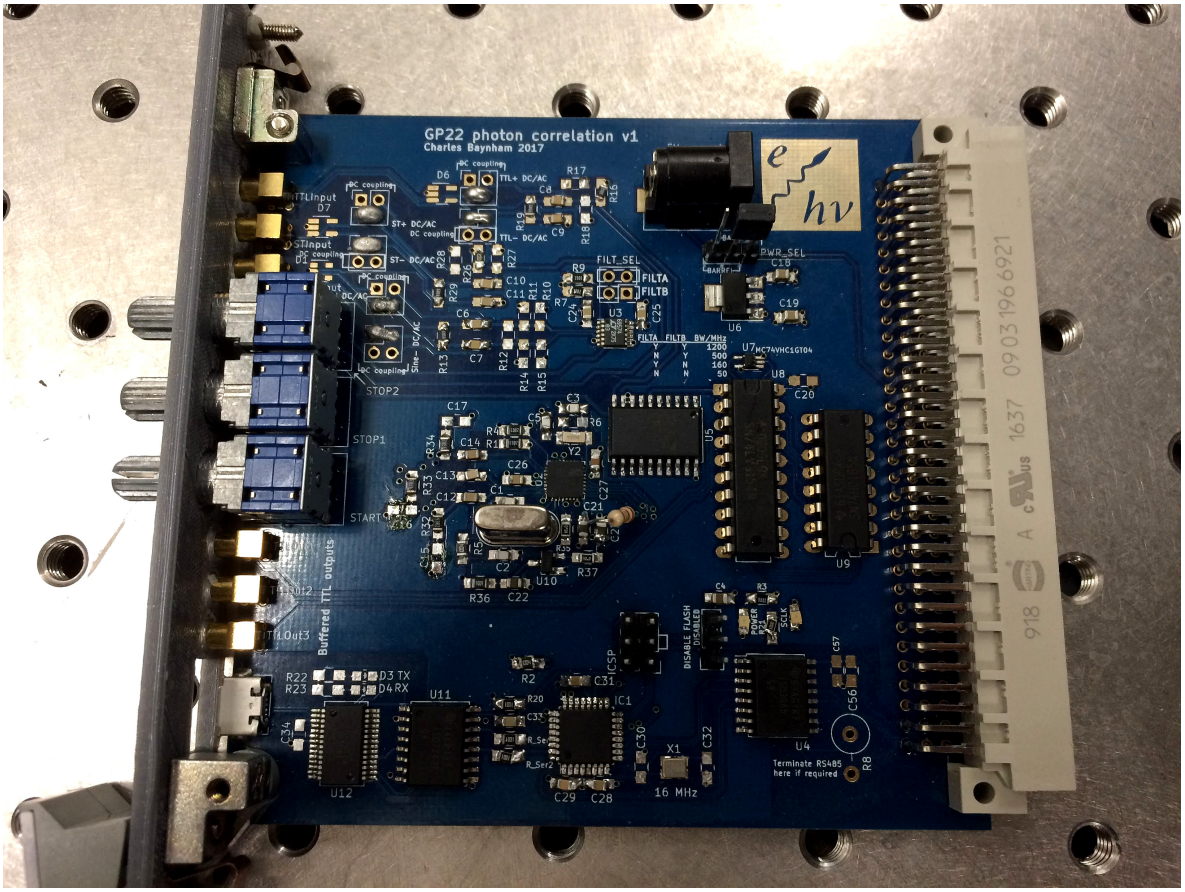

FIGURE 3.9: The TDC interface board built for the detection of excess micromotion. The board can measure time-delays with an least significant bit (LSB) resolution of 45 ps, minimum delay of 3.5 ns at a photon arrival rate of up to 15.6 kHz. It also counts photon arrivals in parallel and acts as a fast transistor–transistor logic (TTL) splitter for photon events.

are galvanically isolated to prevent ground-loops and other unexpected system coupling. The total per-unit cost of the complete system including bill of materials (BOM) + PCB was ∼£50 [157].

Characterisation of the device revealed that the data acquisition rate was limited by floating-point operations on the microcontroller to 15.6 kHz. This could have been improved by processing and detecting events in parallel, but was sufficient to capture every photon arriving at our photo multiplying tube (PMT) when the laser exciting the $^2S_{1/2} \rightarrow {}^2P_{1/2}$ cooling transition is detuned to the optimal point of $\delta\nu \approx \Omega$ as calculated

in [150]. For more information and full schematics of this device, see Appendix D.

3.5.2 Preventing micromotion with compensation voltages

Since excess micromotion is caused by a non-zero DC electric field at the RF nodal point, it can be prevented by applying a compensating electric field. For this reason, the trap incorporates 4 DC electrodes: the 2 conical end-caps and 2 other floating electrodes separated by 60° from the ion's position. With a combination of all these electrodes, an arbitrary electric field in any direction can be applied to the ion.

§3.2.1 described the heavy passive filtering applied externally to the DC compensation voltages. These voltages are produced by a digitally controlled supply unit which includes further passive and active filtering, particularly at frequencies typical of the ion's secular motion (0.1 to 2 MHz) to heating of the ion. The design and construction of this device was done by Jones and is described in Ref. [158]. Our goal, to effectively compensate for excess micromotion, will be to determine the set of voltages which results in zero DC electric field at the RF node.

According to [150], the micromotion signal $\Delta S/S_0$ is proportional to $J_1(\beta_i)/J_0(\beta_i)$ for small values of the modulation index β_i. β_i for a given beam direction i can be expressed as

$$\beta_i = \frac{kQ}{m\Omega^2}\mathrm{E}_{\mathrm{RF,i}} \quad . \tag{3.27}$$

By considering $\tilde{\nabla}\Phi(\mathbf{r})$ (from Equation 3.18), we find that $\mathbf{E}_{\mathrm{RF}} \propto \mathbf{r}$. We therefore make the assumption that, for small changes from the ideal set of electrode voltages $\mathrm{V}_{0,\mathrm{i}}$ ($i = 1 \rightarrow 4$), the coupling to the micromotion signal is linear. $\mathbf{E}_{\mathrm{RF}}$ here is the amplitude of any RF electric field present at the ion's mean position: non-zero if excess micromotion is present.[††]

[††]For the case we consider here, $\mathbf{E}_{\mathrm{RF}}$ is due to a DC electric field having offset the trapping potential's minimum from the RF node. However, it is possible for out-of-phase RF to cause the same effect even

We write the three micromotion signals $\Delta S/S_0$ for the three near-orthogonal beams (H, U and D) as a 3-dimensional vector $\mathbf{A} = \mathbf{A}(\mathbf{V})$ where the n-dimensional vector $\mathbf{V}$ contains the voltages on the $n = 4$ electrodes. If the above assumption holds true, the expected micromotion signal observed can be written as[‡‡]

$$\mathbf{A}(\mathbf{V}) = \boldsymbol{C}(\mathbf{V} - \mathbf{V_0}) \tag{3.28}$$

$$\text{where} \quad C_{ij} = \frac{\partial \mathrm{A_i}}{\partial \mathrm{V_j}} \tag{3.29}$$

In practice, one of the electrode values may be fixed and the others adjusted w.r.t. it in order to produce the desired field. Changing this extra voltage alters the quadrupole DC field experienced by the ion (see Section 5.5) but not its linear DC component. This leaves 12 free parameters for our fit: the Jacobian $\boldsymbol{C}$ has dimensions of 3 beams $\times(4-1)$ electrodes, and $\mathbf{V_0}$ has 3 components.

In a typical data run, ∼45 datasets are taken, corresponding to 15 different voltage configurations measured in the 3 different directions. The residual mean square error, weighted by the inverse of each data-point's experimental uncertainty, is minimised by using a Levenberg-Marquardt algorithm (LMA). Similarly to the approach used in §2.4.3, the LMA is an iterative approach to solving non-linear minimization problems, and can be considered as a trust-region adaptation of the Gauss-Newton method [159, 160]. Figure 3.11 shows a screenshot of the software developed to run this data collection / analysis. The software was designed in Labview and is built around the Actor Model [161] for increased UI–application logic decoupling and ease of reuse.

With one of our end-cap electrodes fixed at $-0.55\,\mathrm{V}$ (chosen for the resultant electric quadrupole shift, see Section 5.5) the ion's response when close to $\mathbf{V_0}$ is best modelled

with no DC field present. The micromotion caused by this effect would be uncompensatable, and so great care must be taken in the design of a trap to prevent it (see §3.2.1 and Figure 3.3).

[‡‡]See note about notation.

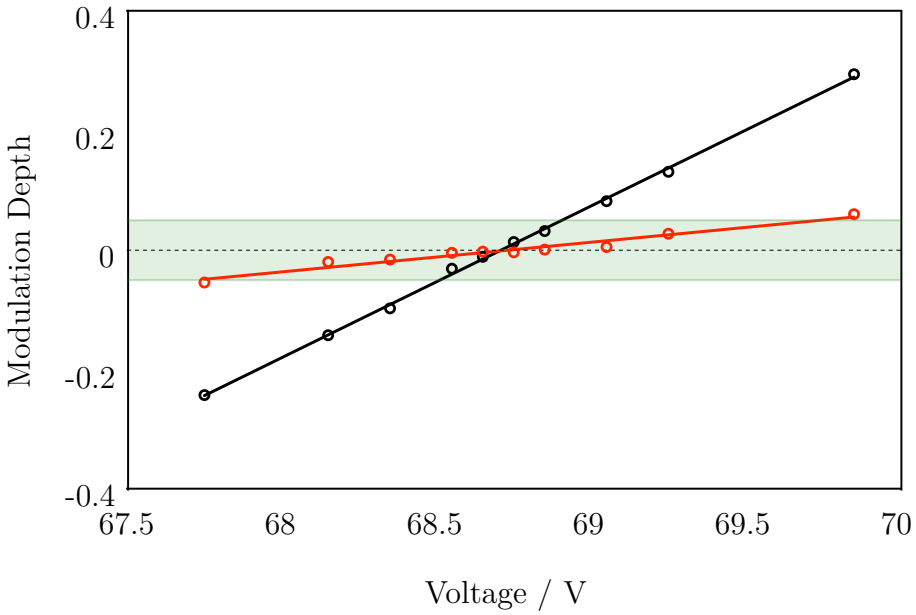

FIGURE 3.10: Modulation depth of the photon correlation signal A_i for variation of the voltage on an electrode in the radial plane shown in black (red) for a detection beam at an angle of 75° (15°) in the radial plane. The green shaded area represents the modulation depth below which the DC-Stark and time dilation shifts are below 1×10^{-18} (see Section 5.4 and §5.1.2). A sign change in the modulation depth corresponds to a π-phase shift in the correlation signal.

with

$$\boldsymbol{C} = \begin{pmatrix} -0.108 & -0.450 & -0.157 \\ 0.792 & -0.123 & -3.411 \\ 0.872 & -0.117 & -0.763 \end{pmatrix} \mathrm{V}^{-1}, \quad \mathbf{V_0} = \begin{pmatrix} 0.43 \\ 71.46 \\ -1.13 \end{pmatrix} \mathrm{V}\,. \tag{3.30}$$

Inspection of $\boldsymbol{C}$ reveals that our compensating electrodes are far from orthogonal at the ion's position. Nevertheless, we are still able to prevent excess micromotion effectively at the measurement resolution of our system, resulting in $|A_i| \leq 5 \times 10^{-3}$ for all beam directions. After micromotion minimization the trap has been consecutively reloaded up to twenty times over a 5 h period without noticeable changes in the micromotion at the $A_i = 0.01$ level. No long term drifts in the micromotion have been observed suggesting that vacuum windows are sufficiently far from the ion that

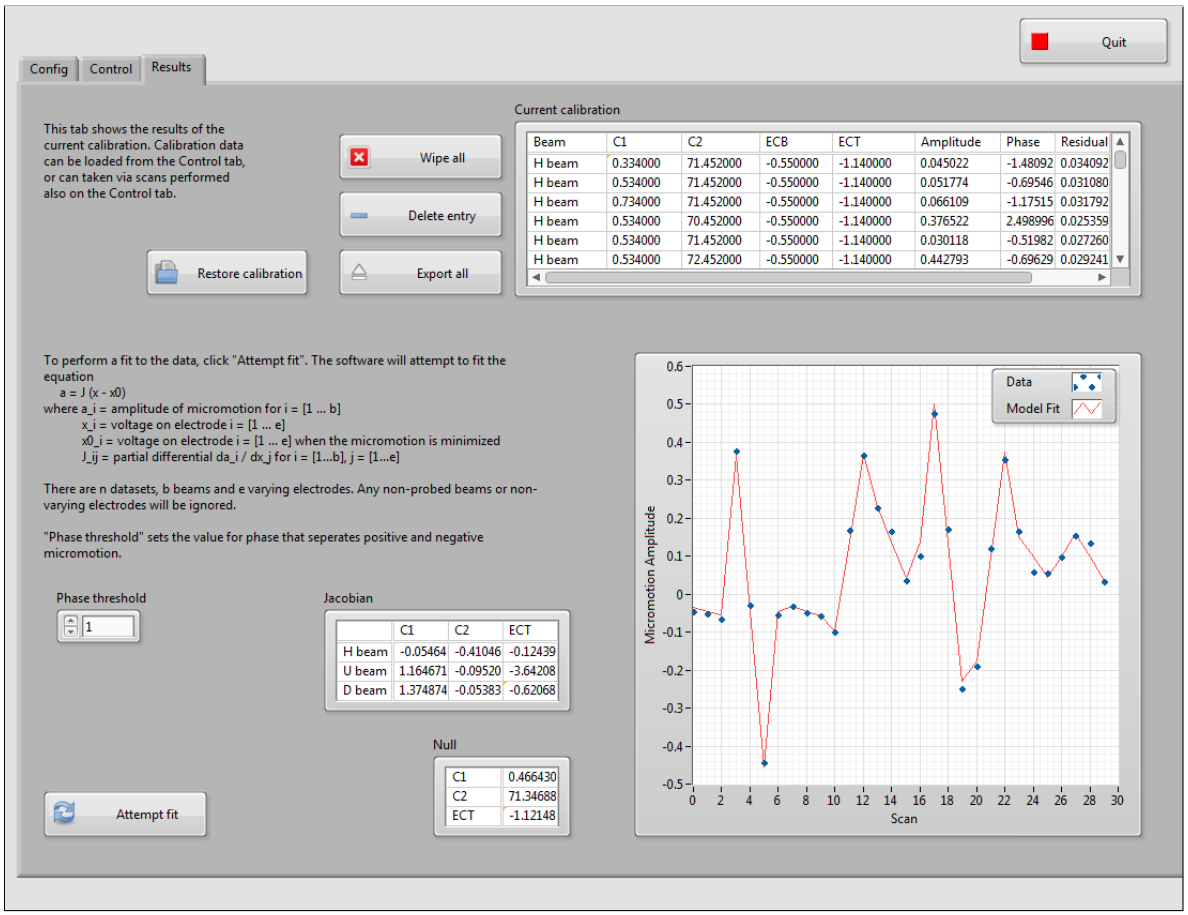

FIGURE 3.11: The LabView interface for micromotion minimization. Data are obtained and analysed automatically. The system has been designed around the Actor model to decouple the UI from the application code: this will allow the code to be reused asynchronously as the clock's software is upgraded to be fully autonomous in future.

dielectric charging from the UV laser beams is insignificant [162] and that the trap is electrically and mechanically stable.

3.6 The next iteration of the end-cap trap

According to our characterisation, this trap will allow us to operate with trap-related fractional uncertainties of less than 1×10^{-18}. However, we only have one! The only true test of an atomic clock's systematic budget is a comparison with a frequency standard of better or equal quality. We are therefore in the process of building another

trap of almost the same design, but with some improvements.

Firstly, we addressed the unexpected temperature rise reported in Section 3.3. This was caused by RF–dielectric heating in the vacuum feed-through. Dielectric heating occurs when the polarisation of molecules in a dielectric material is rapidly reversed, dissipating energy. The power dissipation is therefore proportional to the capacitance between the RF path and the nearest DC voltage. The heating in our feed-through was caused by the proximity of the high-voltage RF trap drive to the vacuum chamber, held at ground potential. In order to prevent this problem, the RF feed-through has been redesigned to reduce the capacitance between the RF electrode and the vacuum chamber by separating the RF voltage from the surrounding chamber, as shown in Figure 3.12.

Additionally, the new trap has been surrounded by three layers of mu-metal shielding. This is expected to provide shielding factors in excess of 1000 for low frequency magnetic fields. We intend to use this magnetic stability to investigate the feasibility of operating the E3 clock on the $m_F = 0 \rightarrow \pm 2$ Zeeman components, instead of the currently used $m_F = 0 \rightarrow 0$. The reason for this test relates to the electric quadrupole systematic shift, covered in Section 5.5. The shift due to this effect, $\Delta\nu_{quad}$, is related to the ion's quantum numbers by

$$\Delta\nu_{quad} \propto \left(\frac{F(F+1)}{3} - {m_F}^2 \right) \quad . \tag{3.31}$$

The upper state of the E3 transition has $F = 3$, so $\Delta\nu_{quad}$ becomes identically zero. This would be a very useful property if a $^{171}Yb^+$ clock were to be run in a linear trap, where ion–ion interaction must be considered. However it re-exposes us to the linear Zeeman shift, and so the unperturbed frequency would have to be derived from an average of the positive and negative Zeeman components. Drifting magnetic fields between these two probes would cause instability, or even inaccuracy, and so the effectiveness of magnetic shielding is key.

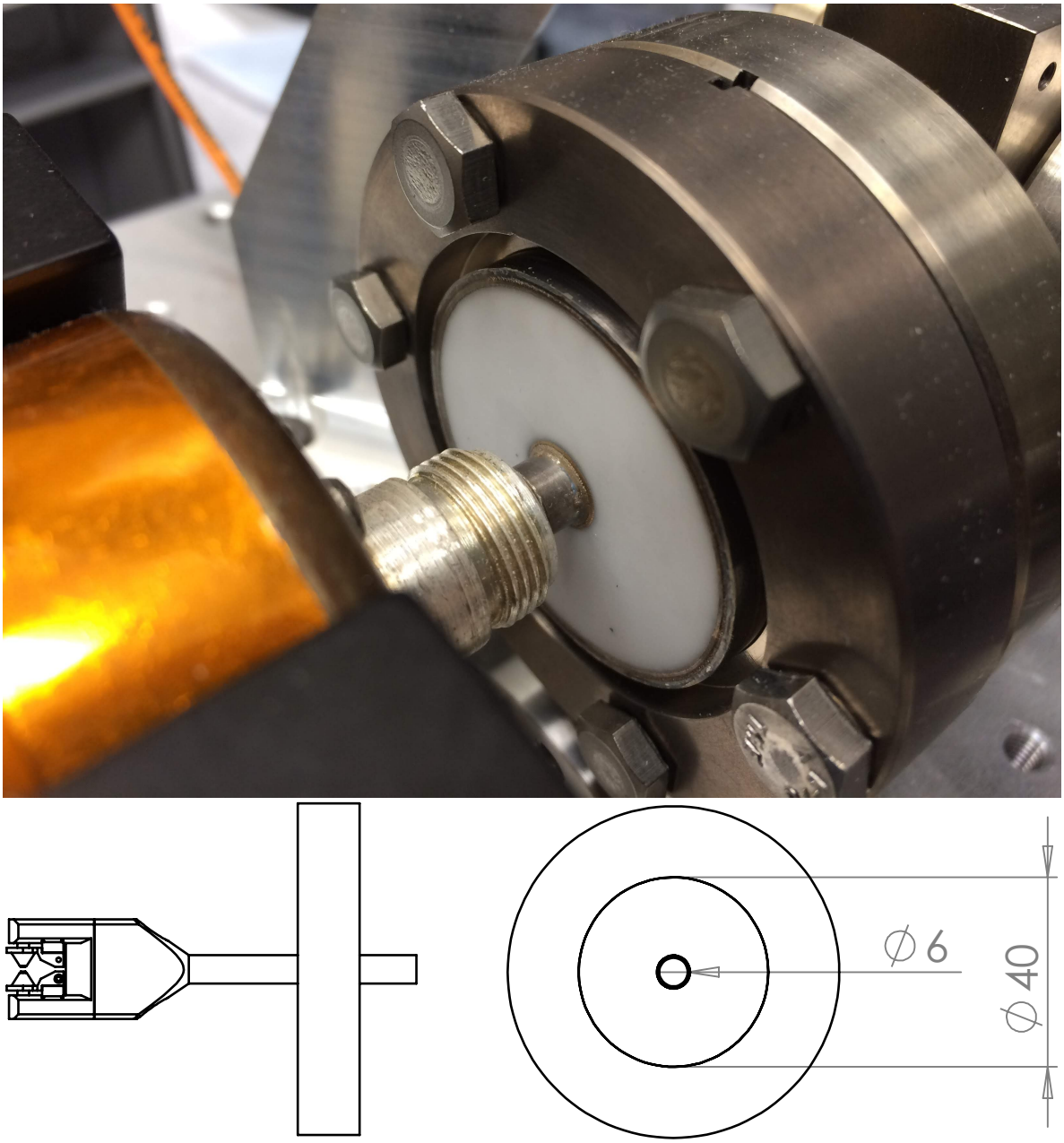

Figure 3.12: The redesigned RF feed-through with large separation between the centre conductor and the vacuum chamber to minimise capacitance and therefore dielectric heating.

Finally, the beam-delivery and fluorescence-collection optics have been mounted to computer-controlled, piezo-actuated translation stages for automated alignment. This usability upgrade will go a long way towards improving the robustness of the clock, an

oft-neglected metric of performance.

With these alterations, and other improvements to the supporting laser systems, we intend to operate two independent systems in a fully automatic configuration. The improved up-times that the clock robustness will bring will be of use in clock comparison campaigns (Section 7.1) and future contributions to UTC (Section 7.2). The magnetic shielding will pave the way towards operation of ytterbium-based clocks in a linear trap, a vital step if ion-clocks' stability is to keep pace with their accuracy. The independent systems will allow us not only to validate our calculated uncertainty budget and perform a local frequency comparison whose fractional agreement is anticipated to be at the low 10^{-18} level, but to take advantage of ytterbium's exotic atomic structure and investigate effects ranging from Lorentz invariance (§8.2.2.3) to quark–electron Higgs coupling (§8.2.2.2).

Determining the thermal Stark shift 4

A direct measurement of the response of $^{171}Yb^{+}$ to environmental Black-Body Radiation

In order to accurately realise an unperturbed atomic frequency standard, all sources of frequency shift must be carefully characterized and either compensated or subtracted. Chapter 5 will present a review of other pertinent systematic effects relevant to clock operation, but this chapter will examine the a.c. Stark shift due to environmental Black-Body Radiation (BBR).

Section 4.1 will go into detail about the cause of this shift and present the motivation for the measurement performed in the following sections of the atom's differential polarizabilities. Section 4.2 describes the experimental method used to quantify these properties.

The method used lends itself to a determination of the differential polarizabilities in two stages. Section 4.3 will therefore present measured ratios of components of the ion's

differential polarizabilities to other components. In Section 4.4 these ratios will be used to derive an absolute value for the ion's differential polarizability at 7 µm. Section 4.5 will deal with the extrapolation of this value to the BBR related frequency shift. And finally, in Section 4.7 these measurements will be placed in the context of the literature.

4.1 Introduction

The interaction of a trapped ion with an oscillating electric field gives rise to a Stark shift in the energy levels of the ion. This includes the electric field produced by the thermal background, i.e. environmental Black-Body Radiation (BBR). One of the favourable features of the E3 clock transition in $^{171}Yb^{+}$ is its small response to electric fields in the frequency range typical of BBR. Nevertheless, knowledge of the coefficient that characterizes this shift, the differential scalar polarizability, is an important term in our systematic budget, both for the E3 and E2 transitions.

The complex structure of the ytterbium ion makes theoretical calculations of these polarizabilities difficult [163–165]. We therefore performed direct measurements of the frequency shifts of the E2 and E3 transitions in $^{171}Yb^{+}$, induced by the electric field of a laser with a mid-IR wavelength of 7.17 µm, representative of a typical room-temperature thermal environment. From this we deduce values for the differential polarizabilities of both transitions that are of direct use in determining the BBR shifts of a $^{171}Yb^{+}$ frequency standard.

In the presence of an oscillating electric field $\mathbf{E}$, an energy level γ with quantum

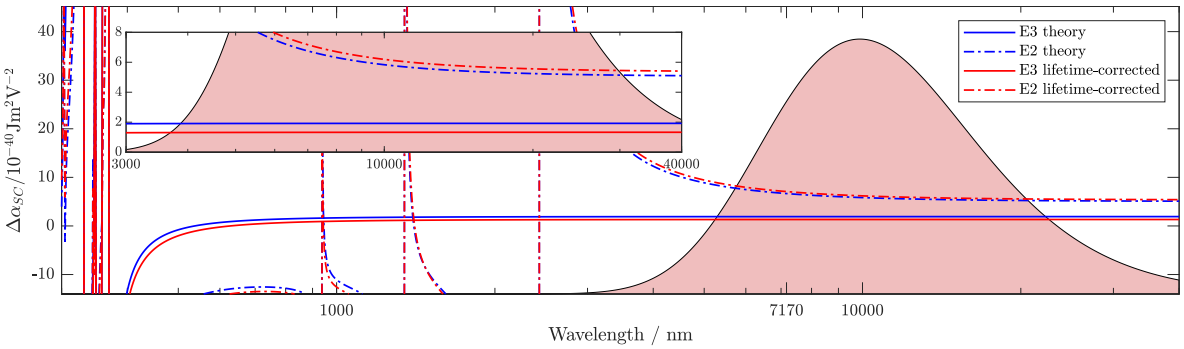

FIGURE 4.1: The solid and dotted lines show the theoretical differential polarizabilities of the E3 and E2 transitions respectively. The blue lines result from theoretical calculation [163] and the red lines from oscillator-strength corrections based on lifetime measurements [164]. The solid fill shows the spectrum of BBR radiation at 298 K in arbitrary units.
(inset) Zoomed in view of the region of interest, where the BBR interacts with the ion's differential polarizability. Note the extreme flatness of the E3 transition's differential polarizability in this region: a property that enables us to probe at a single wavelength yet obtain a good estimate over the whole region of interest.

numbers J and F in an atom is shifted by an amount δW, given by

$$\begin{aligned}\delta W(\gamma, J, F, \mathbf{E}, \theta) = & -\frac{1}{2}\alpha(\gamma, J, F, \theta)\,\langle \mathbf{E}^2 \rangle \\ = & -\frac{1}{2}\Big[\alpha^{SC}(\gamma, J) + \frac{3M_F^2 - F(F+1)}{2F(2F-1)}\times \\ & (3\cos^2\theta - 1)\,\alpha^{TEN}(\gamma, J, F)\Big]\langle \mathbf{E}^2 \rangle\,,\end{aligned} \tag{4.1}$$

where θ is the angle between the electric field and the atom's quantisation axis; α is the polarizability of the state and $\alpha^{SC}, \alpha^{TEN}$ are the polarizability's scalar and tensor components [166]. Note that the vector component of the polarizability is not present since both clock transitions involve states with $M_F = 0 \to 0$ [167, 168].

This perturbation to the atomic energy levels results in an observed frequency shift $\delta\nu$ given by

$$\begin{aligned} h\,\delta\nu(\mathbf{E}, \theta) &= \delta W_2 - \delta W_1 \\ &= -\frac{1}{2}\Delta\alpha_{21}(\theta)\,\langle \mathbf{E}^2 \rangle\,, \end{aligned} \tag{4.2}$$

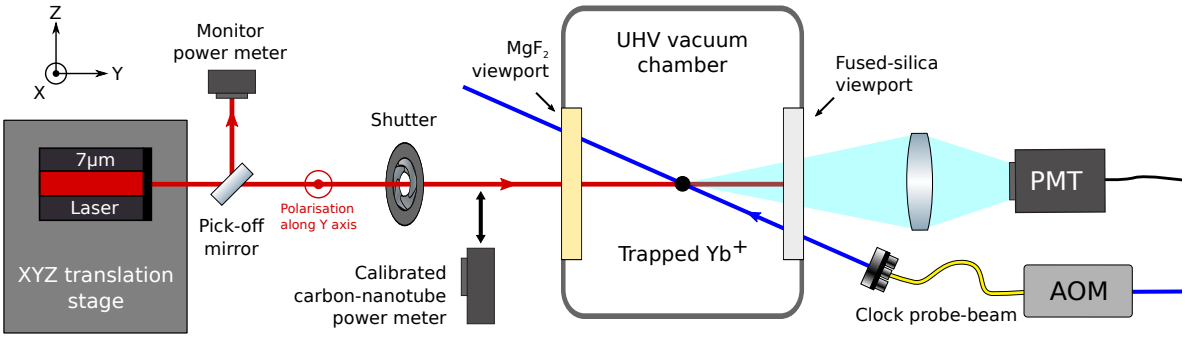

Figure 4.2: A trapped $^{171}Yb^{+}$ ion is interrogated by an ultra-stable probe laser at either 436 nm or 467 nm. The transition frequency is perturbed by the electric field created by an incident laser beam of $\lambda = 7.17\,\mu m$. The laser is mounted on a computer-controlled translation stage to allow the full intensity profile of the beam to be explored. The 7-µm beam is inclined by 4° clockwise in the horizontal x–y plane with respect to the y axis (which is perpendicular to the vacuum chamber window), with polarisation along the x axis. Total power in the beam is continuously monitored for stability, and can be measured with a calibrated carbon nanotube-based detector. The coordinate system shown is consistent with that used throughout this thesis.

where $\Delta\alpha_{21} = \alpha_2 - \alpha_1$ is the differential polarizability of the transition between states 1 and 2 and is independent of the magnitude of the electric field. The differential polarizability of a transition is frequency dependent but, for electric fields in the frequency range typical of room temperature BBR spectra, the two clock transitions' differential polarizabilities ($\Delta\alpha_{E2}$ and $\Delta\alpha_{E3}$) are smoothly varying and tend asymptotically to their DC values, as shown in Figure 4.1 [163].

4.2 Experimental method

In our experimental setup, as shown in Figure 4.2, a single ion of $^{171}Yb^{+}$ is trapped in an RF Paul trap. Its ultra-narrow E2 and E3 optical clock transitions are interrogated by one of two ultra stable lasers at 436 nm and 467 nm, as described in detail in Chapter 2 or [5, 7, 19].

In addition to this, a quantum cascade laser (QCL) [169] oscillating with $\lambda =$

7.17 µm was mounted to a NanoMover translation stage[170] and aligned onto the ion almost along the y-axis, offset by 4° to prevent any reflection from the rear window interacting with the ion. The vacuum chamber of the system was fitted with a window made from MgF_2, chosen for its transmissivity at this wavelength [6] (transmissivity requirements for other frequencies used in our experiment, particularly UV light at 369 nm, precluded use of e.g. a ZnSe window whose transmissivity at 7 µm would be slightly higher). The laser was linearly polarised with electric field always in the x-direction.

The 7-µm laser's electric field induces a frequency shift of the clock transition as described by Equation 4.2. This shift was measured by running two interleaved frequency locks to the atomic transition: one with the 7-µm light incident on the ion and another with it blocked by a shutter. All other experimental conditions were kept identical between the two servos so we attribute any observed frequency difference as entirely due to the Stark shift of the infrared light. Figure 4.3 shows data taken in this arrangement, as the translation stage was moved to scan the position of the 7-µm laser beam over the ion. The laser was typically in a given position for a period of 30 s to allow frequency data to be acquired, before stepping to the next position.

Control of the ion's quantisation axis was achieved by the application of an external magnetic field to set or vary the angle θ in Equation 4.1.

4.3 Polarizability ratios

Without characterising the absolute strength of the electric field at 7 µm, information can already be obtained about the relative polarizabilities between different transitions or between different orientations of the ion, by making measurements in a constant electric field. For these measurements the intensity maximum of the 7-µm beam was

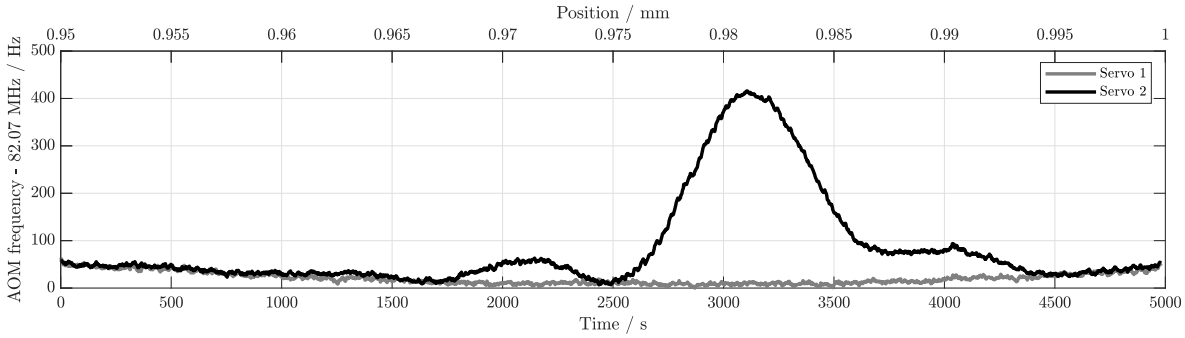

Figure 4.3: Typical E2 data taken as the 7 µm laser is translated over the ion's position. The y axis shows the frequency offset applied by the AOM in Figure 4.2 to keep the light on resonance with the clock transition. Servo 1 shows the unperturbed clock frequency, while servo 2 samples the shift of the clock transition due to the presence of the 7 µm radiation. The intensity of the perturbing electric field experienced by the ion changes as the 7 µm beam is translated. The change in servo 1's frequency is due to non-linear drift of the local reference cavity for the clock laser.

positioned onto the ion by maximizing shifts to the clock transitions, increasing our signal-to-noise ratio, while also minimising sensitivity to small excursions in the beam position.

By monitoring the power at the beam pick-off shown in Figure 4.2, we determined that the total power of IR light produced by the 7-µm laser in the plane of the ion was stable at the $\delta P/P \leq 6 \times 10^{-5}$ level over time-scales of 10^3 to 10^4 seconds. Note that this stability refers to the total power in the beam, not the intensity experienced by the ion which is subject to further uncertainties such as beam pointing which will be addressed in Section 4.4. We attribute this surprisingly high power stability to the inherent stability of Quantum Cascade Lasers (QCLs)[171] and note that even if this stability were to be degraded by a factor of 100 this would not affect the results presented here.

We will first discuss the ratio of the differential scalar polarizabilities between the E3 and E2 clock transitions, $\Delta\alpha^{SC}_{E3}/\Delta\alpha^{SC}_{E2}$. The frequency shifts from the incident 7-µm light were measured for each clock transition in turn, in a set of orthogonal mag-

Quantity	Ratio
Quadrupole : Octupole	
$\Delta\alpha_{E2}^{SC}/\Delta\alpha_{E3}^{SC}$	9.13(14)
Scalar : Tensor	
$\Delta\alpha_{E3}^{SC}/\Delta\alpha_{E3}^{TEN}$	-4.13(10)
$\Delta\alpha_{E2}^{SC}/\Delta\alpha_{E2}^{TEN}$	-0.656(19)
Scalar : Probe field (B_y)	
$\Delta\alpha_{E3}^{SC}/\Delta\alpha_{E2}^{B_y}$	0.471(6)

Table 4.1: Observed ratios between the scalar and tensor differential polarizabilities of the two clock transitions in $^{171}Yb^{+}$ measured at $\lambda = 7\,\mu m$. Also included is the ratio of the E3 scalar differential polarizability vs. the E2 differential polarizability in a particular magnetic field, B_y, used in Section 4.4 to establish an absolute value for the differential polarizability. The values shown here for each ratio result from data taken on 3 separate occasions using 2 independent orthogonal sets of fields.

netic field directions chosen to simultaneously maximise the three Rabi frequencies for the clock probe-beam's fixed direction. By taking the average of the frequency shifts across three orthogonal directions of the ion's quantization axis, the tensor term in Equation 4.1 averages to zero, revealing the contribution from the differential scalar polarizability component for each transition [166]. Taking the ratio of these average frequency shifts for the two transitions, recorded in equal 7-µm electric field strengths, gives the ratio $\Delta\alpha_{E3}^{SC}/\Delta\alpha_{E2}^{SC}$, as shown in Table 4.1. Evaluating the uncertainty required consideration of both statistical uncertainties in the measured frequency shifts, and also non-orthogonalities in the applied magnetic field directions. Both these uncertainties dominated over any changes in the field strength or direction of the 7-µm electric field during the measurements. To evaluate the uncertainty due to non-orthogonality of the magnetic fields, a simulation was performed based on measurements of the field strength taken via the Zeeman components of the E2 transition. For the details of this method, see Appendix B.

The ratio of differential scalar to tensor polarizabilities was also measured for both

the E2 and E3 clock transitions, $\Delta\alpha^{SC}_{E2}/\Delta\alpha^{TEN}_{E2}$ and $\Delta\alpha^{SC}_{E3}/\Delta\alpha^{TEN}_{E3}$. As above, the frequency shift arising from the differential scalar polarizability was determined by averaging over the frequency shifts recorded in three orthogonal directions. For the E2 transition, with its large tensor polarizability, the frequency shifts in the orthogonal directions were well separated and it was possible to derive $\Delta\alpha^{SC}_{E2}/\Delta\alpha^{TEN}_{E2}$ directly from these shifts, using Equation 4.1. Once again, simulations based on observed deviations in the magnitudes of test magnetic fields were used to derive the uncertainties arising from non-orthogonality in the fields of the experiment, as in Appendix B. These frequency uncertainties, arising from uncertainties in direction, dominated over the statistical uncertainties for the E2 transition.

For the E3 transition however, the scalar and tensor shifts were both much smaller leading to a higher fractional uncertainty for their statistical noise. To resolve the tensor shift more clearly the frequency shift in B_x was measured, corresponding to $\theta = 0$ in Equations 4.1 and 4.2, to give an extreme value for the induced tensor shift. The tensor shift in B_x and the scalar shift from the average over three orthogonal directions were therefore used in Equation 4.1 to establish $\Delta\alpha^{SC}_{E3}/\Delta\alpha^{TEN}_{E3}$.

For the tensor shifts, the polarization of the 7-µm beam was also relevant. Observation of the tensor shift magnitude in all the fields (shown in Table B.1) allowed us to determine that the polarization of the 7-µm beam at the ion was aligned along the x axis to within $\pm 1°$. This level of uncertainty in the polarisation resulted in additional fractional uncertainties for the E2 and E3 tensor : scalar ratios of 5.2×10^{-3} and 8.3×10^{-4} respectively: negligible when compared with that due to magnetic field non-orthogonality and quantum projection noise.

4.4 Absolute polarizabilities

In order to determine the absolute value of a transition's differential polarizability, knowledge of the strength of electric field from the 7 µm laser at the ion is necessary. Since the electric field $\mathbf{E}$ from the applied laser was position dependent across the spatial extent of the beam (S), the induced shift $\delta\nu(\mathbf{x}, \theta)$ was measured in a 2D grid of positions, $\mathbf{x} = (x, z)$, across the beam.*

Starting from Equation 4.2:

$$\begin{aligned} h\,\delta\nu(\mathbf{x},\theta) &= -\frac{1}{2}\Delta\alpha_{21}(\theta)\,\langle\mathbf{E}(\mathbf{x})^2\rangle \\ h\int \delta\nu(\mathbf{x},\theta)\,dS &= -\frac{1}{2\epsilon_0 c}\Delta\alpha_{21}(\theta)\int I(\mathbf{x})\,dS\,, \end{aligned} \tag{4.3}$$

where $I(\mathbf{x}) = \epsilon_0 c\,\langle\mathbf{E}(\mathbf{x})^2\rangle$ is the position-dependent intensity of the 7-µm radiation. The beam produced by the 7-µm QCL contained high-order components making a Gaussian fit untenable, demonstrated by the 1D slices through the frequency shift profile shown in Figure 4.4. For this reason, we chose to measure and sum the frequency shifts over the entire extent of the beam. By approximating the LHS integral in Equation 4.3 by a sum over pixels each of area A, and noting that the RHS integral is simply equal to the total power in the beam, P,

$$\Delta\alpha_{21}(\theta) = -\frac{2\epsilon_0 hc}{P}\sum_{x,z} A\;\delta\nu(\mathbf{x},\theta)\,. \tag{4.4}$$

The polarizability can thus be derived by summing the frequency shifts measured across an entire grid, such as that shown in Figure 4.5. Having measured this quantity for one transition in a known quantisation direction θ, the value of any other differential polarizability component can be deduced by means of the ratios given in Section 4.3.

*Using the coordinate system followed throughout this thesis, unit vectors $\hat{x}$ and $\hat{z}$ are perpendicular to the 7 µm beam's direction of propagation.

The profiles obtained using this method showed good agreement with optical profiles taken of the beam by scanning over a pinhole and measuring a chopped signal with a photo-detector and lock-in amplifier. Unfortunately, however, uncertainty of the ion's distance from the focal point prevented a quantitative comparison.

4.4.1 Setup

As shown by Equation 4.4, knowledge of four quantities is essential in order to evaluate any component of the ion's differential polarizability: the area of each pixel in a 2D scan, the total power in the beam used to perturb the clock transition and the sum of the resultant shifts across the whole beam, as well as the ratio linking the polarizability component in the measured direction to the direction of interest. The following sections will detail how each of those quantities was controlled and measured.

4.4.1.1 Sum of frequency shifts over laser profile : $\sum_{x,z} \delta\nu(\mathbf{x}, \theta)$

The spatial profile of the beam was mapped out by translating the 7-µm beam across the ion and recording the frequency shifts induced at each (x, z) position, as shown in Figure 4.5. This was done using the E2 transition since its polarizability is $\sim 10\times$ greater than that of the E3 transition, allowing the shift to be resolved more quickly. The large number of points required to cover the entire transverse beam profile meant that each scan could take around two days. By operating in a magnetic field such that $\theta = \pi/2$ (field B_y in Figure 4.2) we minimised our sensitivity to changes in the background field affecting the tensor shift during this time.

Figure 4.5 shows the shift induced at a range of positions of the translation stage for fixed y-position, covering a large area across the beam.

Summing uncertainty In order to approximate the integral over all (x, z) points in the beam, we used the simple method of summing all the measured shifts in a 2D grid,

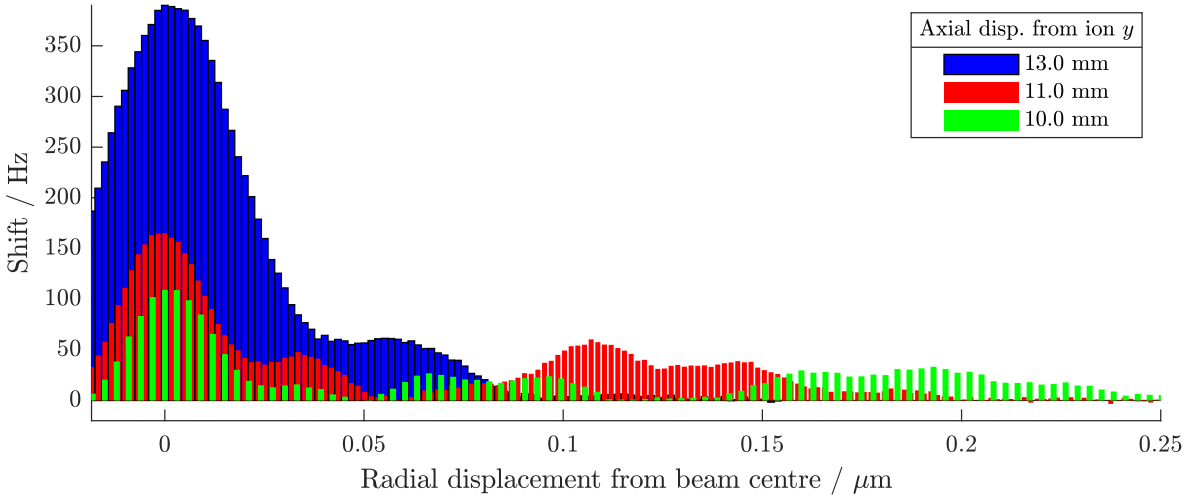

FIGURE 4.4: Shift induced by the 7-µm beam for various axial positions of the translation stage. Note that as y nears the focal point of the optical setup *(blue)* the peak shift increases and the power far from beam-centre (visible in these slices as deviations from the Gaussian lineshape) is reduced.

weighted by their corresponding grid square areas (described by Equation 4.4), since the inner region of the grid was scanned using smaller position steps on the NanoMover stage than the outer.

Simulations of the error in the summed shift deduced by this simple method were performed, by assuming a beam profile with either a Gaussian shape or an analytical function that closely approximated the observed profile in Figure 4.5 and mathematically sampling it on a regular spaced grid with variable orientation, offset and grid spacing. The results in both cases indicate that the penalty incurred by using the sum of pixelated shifts instead of the complete, smooth beam integral is surprisingly small even for large (i.e. approaching the beam-waist) grid spacings and also for off-centre grids. The contribution of the grid summing method to our total uncertainty can therefore be neglected at the 10^{-4} level.

Statistical Each point in Figure 4.5 was typically scanned for 30 s. At this timescale, the quantum projection noise of the interleaved E2 clock transition is around

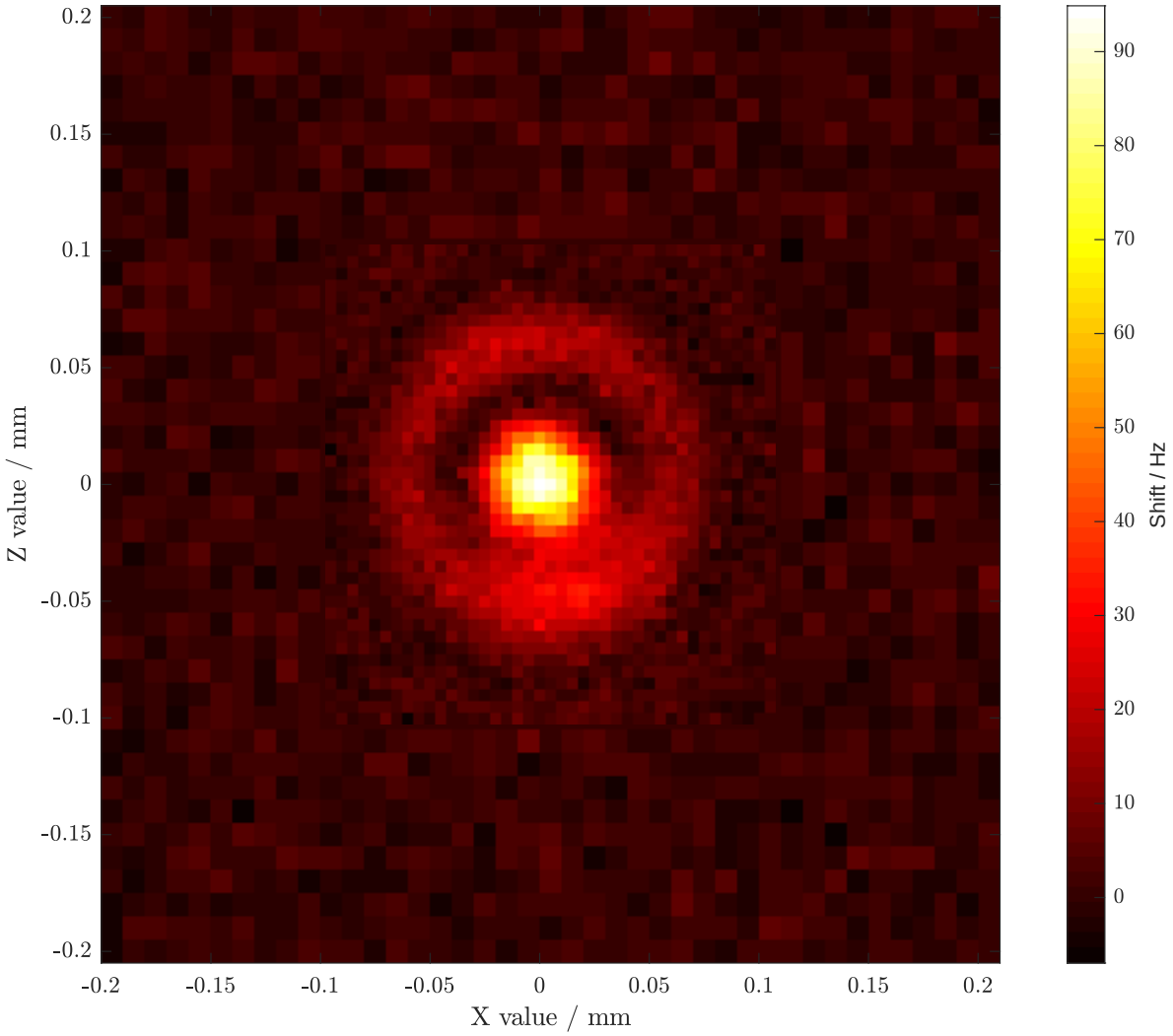

Figure 4.5: Colour map of the induced frequency shift at a large range of (x, z) positions. Each data point represents the average differential shift observed between 30 s interleaved locks to both the shifted and unshifted quadrupole clock transition in Yb^+ with the ion's quantization axis in the $\hat{y}$ direction and the electric field in the $\hat{x}$ direction. The scan was performed in a spiral manner outwards and then inwards. The axial displacement from the ion was 12.75 mm (see Figure 4.4).

3 Hz. Including this per-point uncertainty results in a fractional statistical uncertainty of 0.8 % on the sum of shifts over the whole grid.

Beam capture The method of considering the sum of shifts in Equation 4.4 relies on probing the beam over its entire extent; power missed by the 2D grid would cause an

underestimate of the differential polarizabilities. To judge how well all the frequency shifts have been captured, Figure 4.6 shows the shifts and their mean, as a function of distance from the beam centre. The plot is derived from the data in Figure 4.5 and the standard error on the mean shifts comes from the 3 Hz statistical noise on each of the points in the average mentioned above. At large radii, the standard errors are larger simply because there are fewer points contributing to the mean. The shifts at large radii are consistent with zero and we assume that there is no further power in the beam beyond the maximum radius measured.

This does not necessarily mean that our experiment captured all the shifts, however, as we took data in a square grid that only went out to the highest radii in the corners of the grid. We therefore need to estimate the total sum of shifts that would have been measured if we had sampled out to the highest radii across the full circular area. We do this by treating the circular area as a series of annular rings around the beam centre, each of which is assigned the mean shift at that radius around the whole ring. Note that this does not assume that the beam itself is circularly symmetric, only that the data contributing to the mean shift at each radius was sampled evenly around that ring.

The cumulative sum of shifts is plotted as a function of radius in Figure 4.6 and is seen to level off beyond a radius of 220 µm. The cumulative sum of shifts is then estimated from a weighted fit over the last few points in the plot to be 18 931(43) Hz across the whole circular area. This number has been scaled by area to correspond to a grid-sum over 5 µm pixels so that it can be readily compared to the actual sum of shifts, 18 712 Hz, measured over the square grid in Figure 4.5. This implies that a correction factor of 1.012(2) is required in our cumulative sum to account for shifts occurring beyond the square area sampled by our experiment.

However, in order to reach this conclusion we needed to make assumptions about

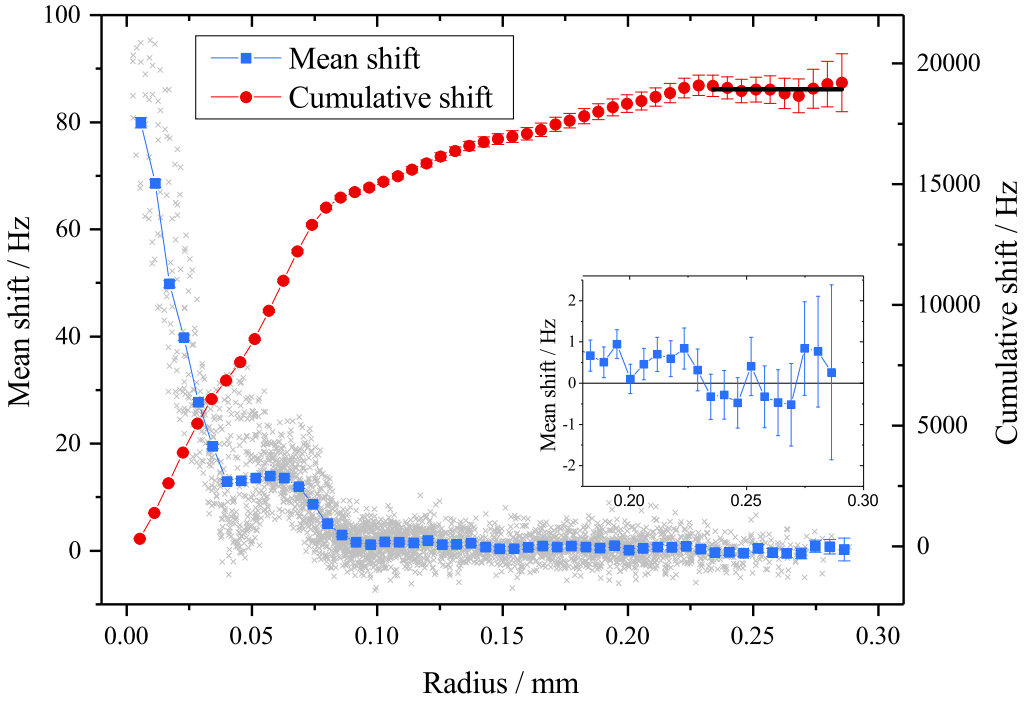

Figure 4.6: *(blue)* Mean shift of data in Figure 4.5 at $y = 12.75\,\text{mm}$ (see Figure 4.4), for circular bins spaced by $\delta r = 6\,\mu\text{m}$. The gray crosses represent the individual data points that contributed to this mean. The inset shows a close-up view of the measurements at the largest radii, consistent with no power in the 7-µm beam being present. *(red)* Cumulative sum of the binned shifts, with black line showing the weighted mean of the last few points.

the beam's behavior beyond the regions in which it was measured. Section 4.6 will highlight the limitations of this method, which unfortunately mean that the absolute measurements outlined in this chapter cannot be considered definitive.

4.4.1.2 Area : A

To determine the area, A, of the grid squares used in Equation 4.4, a Michelson interferometer setup with $\lambda = 935\,\text{nm}$ was used to monitor the step size of the NanoMover translation stage and its repeatability.

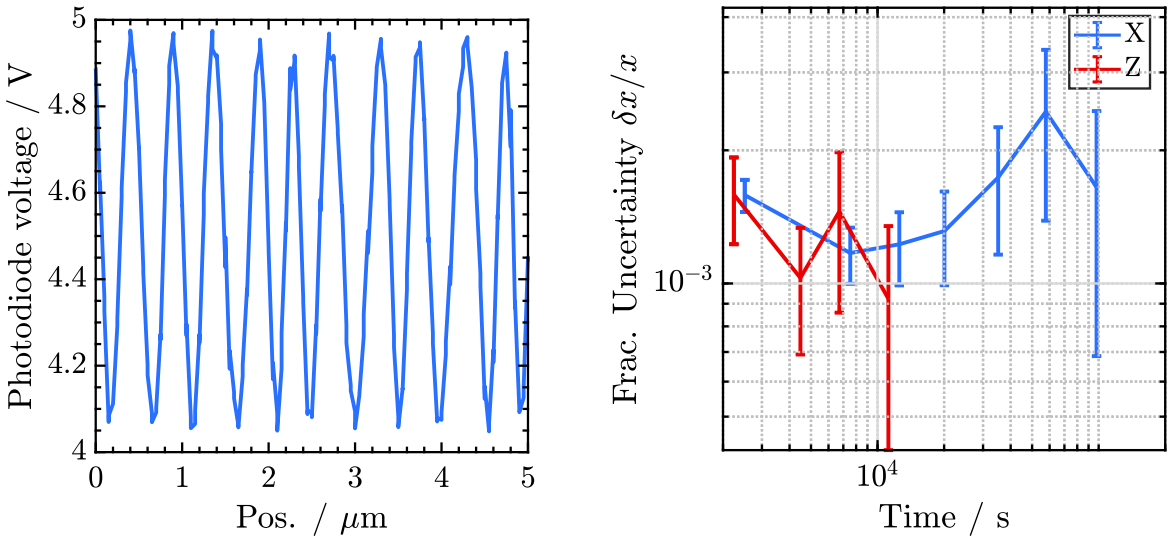

FIGURE 4.7: *(left)* Typical data for a single run of a Michelson interferometer setup with 935 nm light, for translation-stage movement in the X or Z directions. Each run took 2200 s: 58 h of data were taken for the X direction and 7.5 h for the Z. *(right)* Allan deviation of fractional uncertainty in translation-stage step size over time.

The fringes produced by changes in one arm of the interferometer due to movement of the translation stage were measured by a photodiode and analog–digital converter to be analysed digitally.

We ran datasets in the same conditions as when probing the ion with the interferometer set up for monitoring either x or z step sizes: see Figure 4.7. The fractional instability in step sizes produced by the NanoMover was below 2×10^{-3} over more than 8 hours: the time-scale of the 7-µm laser scans. We found that nominal 10 µm steps in the x and z directions, as programmed in the control software, produced 9.95(2) µm and 9.78(2) µm steps respectively.

4.4.1.3 Beam power : P

In order to determine the beam power at the ion, knowledge of two elements is necessary: firstly, its power before entering the trap and, secondly, the attenuation caused by the

windows of the vacuum chamber. In addition, an understanding of the stability of the power over the time between the polarizability scans and the power measurement is also required.

Traceability A pick-off mirror in the 7-µm beam path enabled continuous monitoring of laser power stability and a National Institute of Standards and Technology (NIST)-calibrated optical power transfer standard could be inserted into the main beam to measure its power with high accuracy. As optical power instrumentation suffers errors introduced by spectral non-uniformity, accurate measurement of laser power typically requires instrumentation calibrated against a primary standard at the wavelength to be studied. Due to power non-linearities, it is also necessary to calibrate near the power to be measured, typically within one-two decades depending on instrument performance. Direct calibrations of laser power instrumentation at the 20 mW level at 7 µm are not presently available from any calibration lab and, while spectrometer "bridging" measurements of the device or its coating are possible, this would introduce an unacceptably high uncertainty for the present application.

As such, a device coated with a Vertically Aligned Nanotube Array (VANTA) developed at NIST was used as the optical power standard. VANTA coatings show superior spectral uniformity in the VIS-FIR regime[172] and thereby permit a calibration performed against a primary laboratory standard at an arbitrary wavelength to serve as a standard at another arbitrary wavelength, with corrections for the small spectral variation and uncertainty contribution of the VANTA coating measurement—see Figure 4.8.

Use of this device allowed the power in the 7-µm beam to be measured as 17.52(16) mW. The uncertainty here refers to traceability to primary standards: the short-timescale instability of the device is much lower.

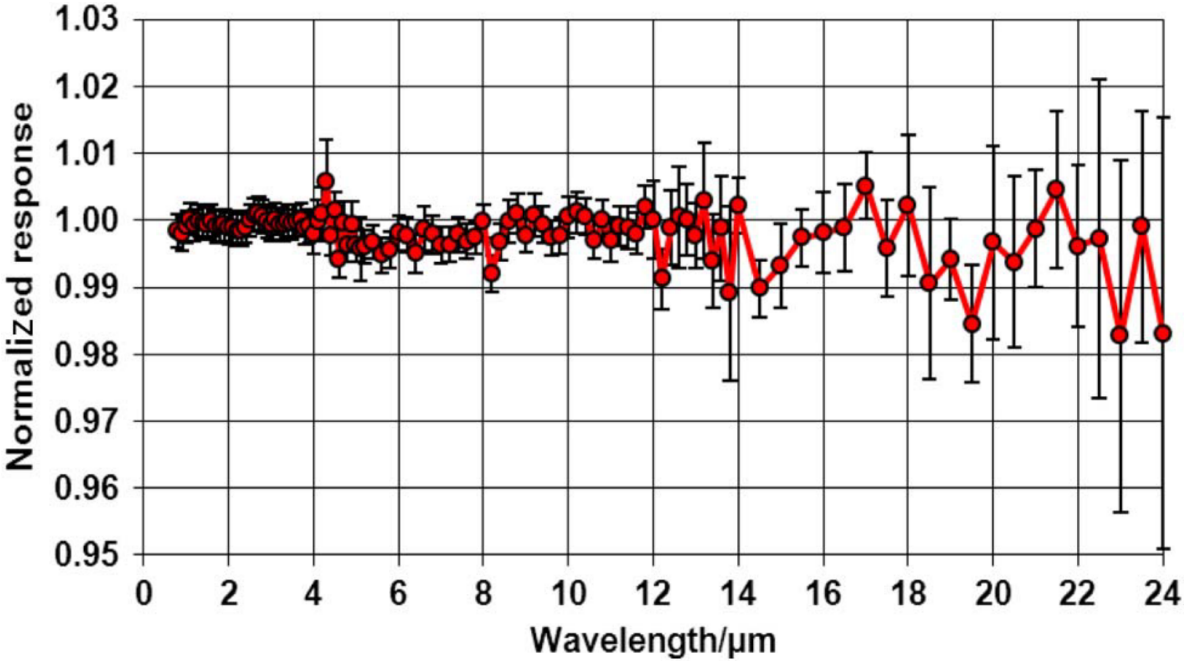

FIGURE 4.8: Flat spectral response of the calibrated carbon nanotube-based detector used for power measurement of the 7 µm beam. This figure is reproduced from [172].

Window attenuation To know the power in the plane of the ion, it was necessary to measure the attenuation experienced by the 7-µm beam as it passed through the MgF_2 window of the vacuum chamber.

Since access to the in-vacuum side of the trap window was impractical, an identically manufactured window from the same batch as that mounted to the chamber was used to characterise absorption. The 7-µm beam was aligned such that it passed through the test window at the same angle and with the same beam waist as in the main experiment. The attenuation through the window was measured using an IR power meter. This test was then repeated for different beam positions on the window.

The attenuation caused by the window was found to be insensitive to position at the 0.2 % level. Taking this into account, the transmission of the MgF_2 window at 7 µm was found to be 0.5101(14).

Stability Although we stated the surprisingly impressive fractional power stability of the 7-µm beam of 6×10^{-5} at timescales of 1000 to 10 000 s, this was not the number used here because it is not the most relevant timescale for the absolute polarizability experiment. Each grid scan took around 30 hours, and 2 separate grids were taken. To combine the data and treat it as a single dataset (as shown in Figure 4.5), we needed to consider any power fluctuations over the total time of measuring and until the calibrated power meter could be inserted at the ion's position.

The monitored power showed fluctuations at a level of 0.5 % over several days: to be conservative, we therefore used 1 % for the power fluctuations in our uncertainty analysis of the power at the ion.

4.4.1.4 Ratio : $\Delta\alpha^{SC}/\Delta\alpha^{\mathrm{B_y}}_{E2}$

The previous sections have described the measurements undertaken to derive the absolute differential polarizability in the field $\mathrm{B_y}$ where $\theta = \pi/2$. To link this measurement to the scalar and tensor components of the two transitions requires knowledge of the ratio between these components and the differential polarizability in $\mathrm{B_y}$.

The determination of these ratios was subject to the same considerations as those required when evaluating the ratios presented in Section 4.3. For the scalar components of the E2 / E3 transition, the fractional uncertainty contribution was 2.0 % / 1.3 %. In order to derive the absolute values of the tensor shifts of the two transitions, the scalar : tensor ratio measurements previously presented in Table 4.1 were used.

4.4.2 Results

The results of the measurements described in Section 4.4 are shown in Table 4.2. These data, in combination with Equation 4.4, are used to calculate the absolute values of the scalar and tensor components of the differential polarizabilities of the two transitions.

Contribution		Value	Fractional uncertainty (10^{-3})	
Area of pixels / µm^2		24.3		3
Power at ion / mW		8.94		14
Sum of shifts / Hz		-18712		8
Correction to sum of shifts		1.012		*2**
$\Delta\alpha^{SC}_{E3}/\Delta\alpha^{B_z}_{E2}$		0.471		13
$\Delta\alpha^{SC}_{E2}/\Delta\alpha^{SC}_{E3}$ *(used for E2 only)*		9.13		15
			Quadrupole	*Octupole*
Differential polarizability @ 7 µm / J m^2 V^{-2} $\times 10^{-40}$	scalar		7.79*(20)*	0.854*(18)*
	tensor		-11.88*(46)*	-0.2067*(67)*
				* *but see Section 4.6*

Table 4.2: Uncertainty budget and result of the determination of the absolute differential polarizabilities at 7 µm of the two clock transitions. Tensor components are derived from the scalar components using the ratios presented in Table 4.1. Uncertainties marked in *italics* are subject to the caveats discussed in Section 4.6.

4.5 Estimating BBR frequency shift

The differential scalar polarizability at 7 µm allows the atomic frequency shift to be deduced close to the peak of the room-temperature black-body radiation spectrum. The radiation spectrum, however, extends to both higher and lower wavelengths, and so the total frequency shift from a black body at room temperature also depends on the polarizability's wavelength dependence.

A basic theoretical model can be used to estimate the scalar polarizability α of state $|\gamma J\rangle$ at different wavelengths by summing over the oscillator strengths f of all the electric dipole transitions connecting state $|\gamma J\rangle$ to states $|\gamma' J'\rangle$ using [173]:

$$\alpha(\gamma J) = \frac{e^2}{m_e} \sum_{\gamma' J'} \left(\frac{f(\gamma J; \gamma' J')}{\omega^2_{\gamma J:\gamma' J'} - \omega_L^2} \right) \tag{4.5}$$

where $\omega_{\gamma J:\gamma' J'}$ is the atomic transition frequency and ω_L is the frequency of the applied electric field. e and m_e are the electronic charge and mass. The oscillator strengths are taken from [98, 115, 163, 164, 174], except for the leading term in the summation for each state.

The oscillator strengths of the leading terms for the excited and ground states are allowed to vary around their theoretical values[†] and, for each combination of oscillator strengths, the differential polarizability at all wavelengths is calculated giving curves such as those shown in Figure 4.1. For the E2 transition, the line-strengths of transitions at wavelength $\lambda = (329,\ 2438)\,\mathrm{nm}$ were chosen to be varied. For the E3, the (329, 265, 3432) nm transitions' line-strengths were used. The (329, 265) nm transitions were chosen because their line-strengths have the largest contributions to the polarizability of the lower clock state, $^2S_{1/2}$, at 7 µm. The (2438, 3432) nm line-strengths have the largest contributions to the upper clock state polarizabilities for the E2 and E3 transitions respectively. The UV transitions are so far-detuned from 7 µm that their contribution to the differential polarizability is a near-constant offset at IR wavelengths. The transitions closer to IR however have a much larger effect on the shape of the differential polarizability in the BBR region.

The validity of each combination of oscillator strengths is judged by comparing the predicted polarizability at 7 µm to our experimental observations for each clock state. Each polarizability curve is thus assigned a weight, calculated from its probability of lying in a normal distribution centred at our measurement with our experimental uncertainty. A weighted mean of all these curves gives our predicted differential scalar polarizability as a function of wavelength, with its uncertainty their standard deviation.

The BBR frequency shift can then be estimated by integrating, across all wavelengths, the product of the predicted differential scalar polarizability and the electric field squared. We derive the frequency shift from a black body at 298 K for the E2 transition to be −338 mHz with a fractional uncertainty of 3.5 %, and for the E3 transition to be −43.4 mHz with a fractional uncertainty of 2.1 %. For comparison with other work,

[†]The range of these variations was chosen such that the weights assigned later were non-negligible or, for transitions with well-known, experimentally measured oscillator strengths, to cover a 3-sigma range.

the model also predicts the DC scalar differential polarizabilities (as shown in Table 4.3) to be $5.89(30) \times 10^{-40}\,\mathrm{J\,m^2\,V^{-2}}$ for the E2 transition and $0.859(18) \times 10^{-40}\,\mathrm{J\,m^2\,V^{-2}}$ for the E3 transition, and the dynamic corrections (using the definition from [175]) at 298 K to be +0.135(22) and -0.00245(16) for the E2 and E3 transitions respectively. Note that the frequency shifts written above already include the effect of the dynamic correction.

The oscillator strength combinations that best predict our experimental polarizabilities cannot be used to draw conclusions about the true oscillator strengths of transitions in the ion however. In the DC limit, the denominator in Equation 4.5 becomes constant so the contribution from each transition is a constant value. Varying any of these would simply lead to an increase or decrease in the value of the DC polarizability, and so it would not matter which you chose. This is approximately true for $\lambda = 7\,\mu\mathrm{m}$ when considering the UV transitions in $^{171}\mathrm{Yb}^+$, and so our analysis does not separately predict oscillator strengths of the individual transitions.

4.6 Limitations

§4.4.1.1 outlined the method for evaluating the beam profile of the 7-µm beam by considering the shift induced to the E2 transition at a large range of positions within a radius of $r = 283\,\mu\mathrm{m}$, the maximum deviation measured in Figure 4.5. However, the sum of shifts outlined in Section 4.4 must be performed over all space. In order to do this, we had to make assumptions about the behavior of the 7-µm beam beyond the regions where we measured it. Namely, we assumed that

1. There was no power present in the beam beyond the maximum radius measured (283 µm), and

2. Beyond $r = 200\,\mu\mathrm{m}$, the beam was circularly symmetric.

Whilst our data is consistent with these assumptions, it is also consistent with beam profiles that do not match these assumptions. One could imagine for example a beam that contains a second maximum beyond this radius; or a very non-Gaussian beam that has a low level of power, below our QPN-limited detection threshold, spread over a large area. Such beams would render the assumptions—and therefore the conclusions—of this work incorrect for the absolute polarizability measurements.

It is for this reason that we cannot quantifiably assign an uncertainty to the absolute values of the two transitions' polarizabilities. Although the ratio measurements presented in Table 4.1 are unaffected by this methodological drawback, the values in Tables 4.2 and 4.3 should therefore be considered a work in progress.

To avoid this problem, future experiments will probably take one or both of two routes. Either a carefully Gaussian beam could be procured, allowing for a fit of the observed profile to a superposition of some small number of low order Gaussian modes. Or, the beam could be physically blocked by a pin-hole of known size, and the scan could be performed over a region larger than this occluding zone, eliminating the possibility of power outsize the measured zone.

4.7 Conclusion

We have directly measured the differential polarizabilities for the E2 and E3 clock transitions in $^{171}Yb^{+}$ using a perturbing field at $\lambda = 7.17\,\mu m$, a wavelength in the region typical of room temperature BBR spectra.

We presented ratios between the tensor and scalar components of the differential polarizabilities of both transitions, all at the few percent level of uncertainty. We have characterized the 7-µm beam's intensity profile, allowing the absolute values of the

	Quadrupole	*Octupole*
	$\Delta\alpha_{DC}^{SC}$/ $\mathrm{J\,m^2\,V^{-2}} \times 10^{-40}$	
This work	$5.89 \pm \textit{0.30}$	$0.859 \pm \textit{0.018}$
Previous work	6.90 ± 1.40 [176]	0.888 ± 0.016 [7]
Total	5.93 ± 0.29	0.875 ± 0.012

Table 4.3: Values for the DC scalar differential polarizabilities of the E2 and E3 transitions extrapolated using the method described in Section 4.5, shown for comparison with previous work. Uncertainties marked in *italics* are subject to the caveats discussed in Section 4.6.

differential polarizabilities to be deduced. However, limitations of the method used mean that the uncertainty of these measurements cannot be well defined.

A basic theoretical model was used to predict the polarizabilities at other wavelengths, thus allowing the BBR shifts to be calculated. Further work with more sophisticated theoretical models may improve upon the values presented here. Nevertheless, our basic model already reveals that polarizability measurements at 7 µm could greatly reduce the uncertainty of the BBR frequency shift for the E2 transition. Disregarding the unquantified error associated with beam outside the measurement zone, the measurements taken in this work suggest a reduction in uncertainty from approximately 20 % [176] to 3.5 % to be possible. This is significant as the BBR shift dominates the uncertainty budget for the E2 transition frequency in $^{171}\mathrm{Yb}^{+}$. We note that our predicted DC differential scalar polarizability for the E2 transition is significantly different from a recent *ab initio* theoretical calculation [177] that predicts $\Delta\alpha_{DC}^{SC} = 7.8(5) \times 10^{-40}\,\mathrm{J\,m^2\,V^{-2}}$. Nevertheless, we note reasonable agreement with totally independent experimental results for the DC differential scalar polarizabilities for both the E2 and E3 transitions, as shown in Table 4.3, to the uncertainties tabulated in Table 4.2.

These new measurements show that limits on the fractional frequency uncertainty

caused by room-temperature black-body radiation can be reduced to low parts in 10^{17} on the E2 transition and low parts in 10^{18} for the E3 transition. These uncertainties assume a temperature uncertainty in the ion's environment of 1 K or better, commonly achieved experimentally [6, 146].

Systematic offsets 5

> Of course, the real test of the achieved performance can only be accomplished with a second, independent detector system. Disappointment is the experimenters' first reward for this measurement.
>
> — *J. L. Hall*

Atomic clocks are beasts of many parts. Chapter 2 gave an overview of some of those parts, although many more exist. This multitude of bits and pieces is needed to keep every aspect of the ion's environment under tight control: a necessary condition if all unwanted frequency shifts are to be eliminated. Chapter 3 presented another spinning plate that the metrologist must balance: the ion trap. However, the improvements made in those chapters make our lives easier: the trap's effect on the ion is now unprecedentedly small and our control over other aspects of the experiment is similarly improved. Chapter 4 addressed a shift that we cannot remove* and so must instead characterise: the AC Stark shift due to BBR.

*Easily...

However, as any good scientist knows, a measurement is of no use unless you know its limitations and nowhere is this as true as in the field of metrology. For the builders of optical atomic clocks, the uncertainty budget carries great importance. With the environment under as tight restrictions as we can manage, our attention must now turn to measuring the level of control that we achieve.

This chapter will review the mechanisms by which the external world can affect the measured transition frequency of our ion. It will focus on the E3 transition, however a similar analysis can be applied to the E2. For each effect, a model will be presented with which the shift to the transition can be estimated. Where possible, these shifts will be cancelled out and the uncertainty in this cancellation will be reported. Where this is not possible, the method by which each shift is measured will be presented and the uncertainty on the resultant number will enter the uncertainty budget in Section 5.8.

5.1 Trap related

In a perfect trap, the ion would sit stationary in the centre, experiencing no electric field. Unfortunately, this is not possible in reality; the ion is confined by an electric field, and so must sometimes interact with that field. Additionally, the ion's non-zero temperature causes it to oscillate in the pseudo-potential created by the trapping field at the trap's characteristic secular frequencies.

Section 3.5 discussed the motion of the ion in this field, and Equation 3.23 is the solution to the ion's equation of motion. It describes motions at four frequencies: Ω, the trapping electric field's frequency; and ω_i, the three secular frequencies.

This motion affects the transition frequency in two ways, through time dilation and through the Stark effect. We will now examine each in turn.

5.1.1 Time dilation — second order Doppler

Traditionally, ion-based frequency standards have neglected the first order Doppler shift due to their confinement of the ion in the Lamb-Dicke regime, where its movement is far less than 1 wavelength of the probing radiation. This is because the excitation probability of the first vibrational sideband scales according to the Lamb-Dicke parameter $\eta = \sqrt{\hbar k_L^2/(2m\omega_S)}$ where m is the mass of the trapped ion and k_L is the wave number of the probing laser so, for tight confinement, excitation of vibrational sidebands instead of the carrier becomes unlikely.

Ref. [178] treats this fully and finds, for typical experimental parameters, that the first order Doppler shift contributes an offset of $\sim$1 nHz, justifying this assumption (for now). We therefore consider the second order shift, caused by time-dilation in the ion's frame due to its motion.

For an ion moving at a speed v at an angle θ to the direction of a probing laser beam[†], the relativistic Doppler shift z is given by

$$\begin{aligned} z &= \frac{1}{\sqrt{1-\frac{v^2}{c^2}}} \times \left(1 - \frac{v\cos\theta}{c}\right) - 1 \\ &\approx -\frac{v}{c}\cos\theta + \frac{v^2}{2c^2} + \mathcal{O}\left(\frac{v^3}{c^3}\right) \quad , \end{aligned} \tag{5.1}$$

where the first term results from time dilation and the second from the usual Doppler shift.

Since the ion's movement is fast w.r.t. the ~ 100 ms pulses used to excite the clock transition, we should consider the time average of this shift. The linear term therefore vanishes, leaving the *second order Doppler* term proportional to v^2. This effect acts to slow the ion's clock w.r.t. the lab frame, decreasing the observed resonance frequency. Ion motion comes from two sources: motion at the secular frequencies governed by

[†]Measured in the laboratory frame.

the ion's temperature and motion at the RF drive frequency from intrinsic and excess micromotion.

Figure 5.1 shows how, for an ion with no excess micromotion (EMM), energy is apportioned equally between the secular and micromotion modes [179, 180]. For an end-cap trap such as ours with RF confinement in all three directions, we find that $m\langle v^2\rangle/2 = 3k_BT$, giving the fractional frequency shift due to secular and intrinsic micromotion (IMM) as [150]

$$\left\langle \frac{\Delta\nu}{\nu} \right\rangle_{\text{Dop.}}^{\text{IMM}} = -\frac{3k_BT}{mc^2} \quad . \tag{5.2}$$

If the ion also has excess micromotion at some level, this results in an additional oscillation of the ion position at Ω due to the residual RF field present at the trapping minimum, $\mathbf{E}_{\text{RF}}$. By considering the consequent force on the ion, $m\frac{\mathrm{d}}{\mathrm{d}t}\mathbf{v_{ex}} = e\mathbf{E}_{\text{RF}}\cos(\Omega t)$, the extra velocity due to excess micromotion can be found. This contributes[‡] to the determination of $\langle v^2\rangle$, giving the total Doppler shift as [150]

$$\left\langle \frac{\Delta\nu}{\nu} \right\rangle_{\text{Dop.}} = -\left(\frac{e}{2mc\Omega}\mathbf{E}_{\text{RF}}\right)^2 - \frac{3k_BT}{mc^2} \quad . \tag{5.3}$$

The numerical evaluation of this shift will be done in §5.1.2 since both the second order Doppler and the RF Stark shifts take the same functional form.

5.1.2 RF Stark shift

The other effect of the ion's movement is to expose it to the trapping field. This electric field affects the ion's energy levels according to the Stark effect.

For a trapped ion, nature ensures that $\langle\mathbf{E}\rangle = 0$. We therefore need only to consider the second order Stark shift, related to the mean-squared electric field experienced by

[‡]Adding the two velocities gives $\langle v^2\rangle = \langle v_{sec}^2 + v_{ex}^2 + 2v_{sec}v_{ex}\rangle$. Even though v_{sec} and v_{ex} both contain terms oscillating at Ω, the cross-term $\langle 2v_{sec}v_{ex}\rangle = 0$ because the uncorrelated secular oscillation scrambles their covariance.[§]

[§]Assuming that Ω is not an integer multiple of ω.

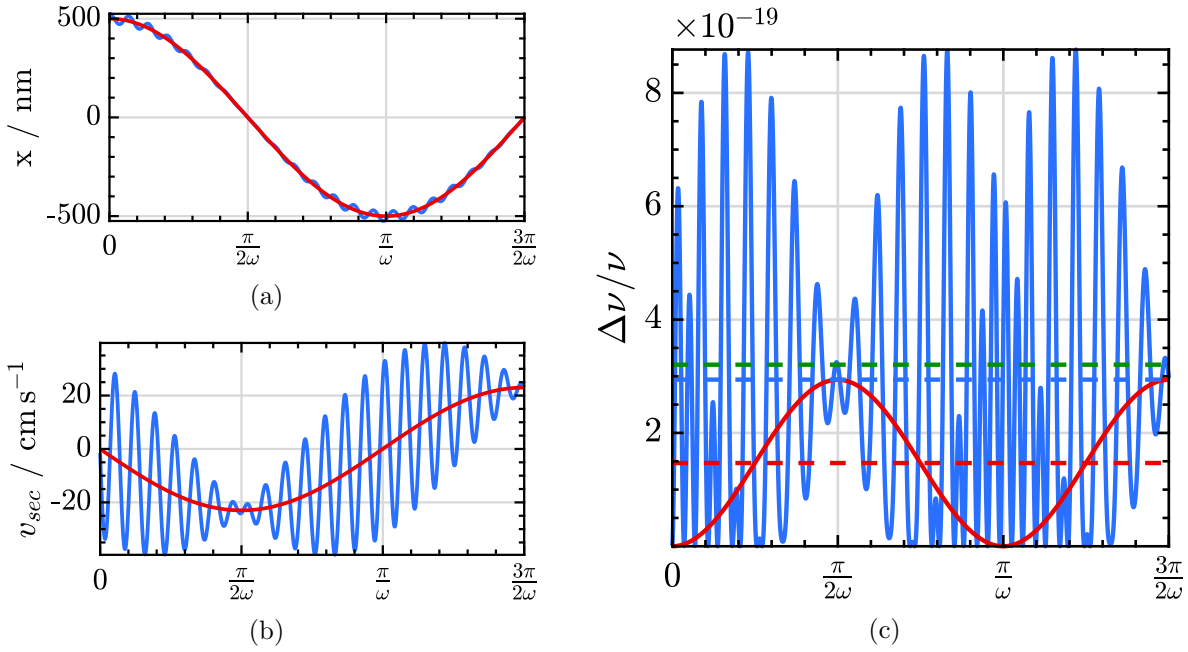

FIGURE 5.1: Ion motion in the trap. The blue line is the first order solution to the Mathieu equation and the red line is the pseudo-potential approximation. All plots are for a trap with $\Omega = 13\,\text{MHz}$, a strongly confining $q = 0.1$ and ion temperature at the Doppler limit.
(a) The ion's position.
(b) The ion's velocity.
(c) The transitions' fractional shift. Note that the mean value of the shift (denoted by dotted lines) is doubled when the kinetic energy stored in the micromotion is taken into account, as found in [179, eq. 2.19]. The green dotted line shows how the shift changes when excess micromotion is present, for an exaggerated offset of 150 nm.

the ion, $\langle \mathbf{E}^2 \rangle$. Since the ion's excursions from the trap-centre are small we may assume that

$$\mathbf{E}(t, \mathbf{x}) \approx \boldsymbol{G}(t)\ \mathbf{x} \tag{5.4}$$

$$\text{where} \quad G_{ij}(t) = \left.\frac{\partial \mathrm{E_i}(t)}{\partial \mathrm{x_j}}\right|_{\mathbf{x}=\mathbf{0}} . \tag{5.5}$$

This simplifies the calculation of $\langle \mathbf{E}^2 \rangle$, resulting in [140, eq. 23, 156]

$$\begin{aligned} \left\langle \frac{\Delta\nu}{\nu} \right\rangle_{\text{Stark}} &= \left\langle \frac{\Delta\nu}{\nu} \right\rangle_{\text{Stark}}^{\text{EMM}} + \left\langle \frac{\Delta\nu}{\nu} \right\rangle_{\text{Stark}}^{\text{IMM}} \\ &= \frac{\delta\alpha}{2h}\left(\frac{\mathbf{E}_{\text{RF}}^2}{2} + \frac{3m\Omega^2}{e^2} k_B T\right) \end{aligned} \tag{5.6}$$

where $\delta\alpha$ is the differential polarizability of the clock transition at DC. $\mathbf{E}_{\mathrm{RF}}$ can be found by measuring its projection onto the cooling beam vector $\mathbf{k}$ using Equation 3.27 and β, the modulation depth of the ion's movement, is proportional to the RF–photon correlation signal described in §3.5.1.

Micromotion in our trap can be minimised to the measurement resolution of our system, giving $\Delta S/S_0 = 0.00(1)$, where S is the micromotion signal explained in Section 3.5. Using Equation 3.27 to calculate E_{RF}, the second-order Doppler and RF Stark shifts due to excess micromotion (EMM) are

$$\left\langle \frac{\Delta\nu}{\nu} \right\rangle_{\mathrm{Dop.}}^{\mathrm{EMM}} = 0(2) \times 10^{-19}, \quad \left\langle \frac{\Delta\nu}{\nu} \right\rangle_{\mathrm{Stark}}^{\mathrm{EMM}} = 0(2) \times 10^{-19} \quad . \tag{5.7}$$

Section 3.4 described the measurement of ion temperature in our trap, and the discovery that it is surprisingly high. Nevertheless, the low heating rate measured implies that the problem lies not with the trap but with the cooling lasers, a system that is currently being rebuilt. When our Doppler cooling setup is fully debugged, we expect the ion to rest at the Doppler temperature (see Equation 3.17) of 0.47 mK. This will result in second-order Doppler and RF Stark shifts due to intrinsic micromotion and secular oscillation of

$$\left\langle \frac{\Delta\nu}{\nu} \right\rangle_{\mathrm{Dop.}}^{\mathrm{IMM}} = -7(1) \times 10^{-19}, \quad \left\langle \frac{\Delta\nu}{\nu} \right\rangle_{\mathrm{Stark}}^{\mathrm{IMM}} = -3(2) \times 10^{-19} \quad . \tag{5.8}$$

Under the current conditions, with $T_{total} = 4.58(16)\,\mathrm{mK}$, these numbers become $\langle \Delta\nu/\nu \rangle_{\mathrm{Dop.}}^{\mathrm{IMM}} = -6.8(2) \times 10^{-18}$ and $\langle \Delta\nu/\nu \rangle_{\mathrm{Stark}}^{\mathrm{IMM}} = -2.9(1) \times 10^{-18}$.

Note that both shifts in Equations 5.7 and 5.8 have the same sign. This is unfortunate, since other ions with differential polarizabilities of the opposite sign have the option of running their trap at a "magic frequency" such that these shifts cancel each other out [140]. Sadly this is not an option in $^{171}\mathrm{Yb}^{+}$, and so the careful characterisation presented above must be used instead.

5.1.3 Collisional shift

The trap's UHV environment is not perfect: a small amount of gas remains in the vacuum chamber and, occasionally, this gas will collide with the ion. If this occurs during an interrogation, this could alter the effective transition frequency.

To put an upper limit on this effect, we use the method in [47, 140]. The collision rate of background gas is estimated using the Langevin model for ion–neutral atom collisions [181, 182] and found to be approximately $1.5\,\mathrm{h}^{-1}$ for our trap pressure of $\sim 1 \times 10^{-11}$ mbar. We then take the worse case scenario where each collision results in a π phase change [47], giving a total shift of $\Delta\nu \sim 100\,\mu\mathrm{Hz}$. Given the hand-waviness of this method, we take the shift as zero but with an uncertainty equal to this predicted magnitude, giving

$$\left\langle \frac{\Delta\nu}{\nu} \right\rangle_{\text{coll.}} = (0.0 \pm 1.5) \times 10^{-19} \quad . \tag{5.9}$$

5.2 Probe-induced AC Stark shift

The extremely narrow linewidth of the E3 transition means that its spectral overlap with the probing laser is very low. This necessitates a very high probe intensity in order to drive the transition.

This high intensity of light couples to the other transitions in the term scheme, causing a probe-induced Stark shift to the clock transition. This shift is of considerable magnitude: with the power required to drive a π-pulse in 100 ms, the shift is 57 Hz. In order to realise the unperturbed E3 transition, it is necessary to compensate for this shift.

Just as in the thermal BBR case (see Chapter 4 and Equation 4.1), the presence of an oscillating electric field $\mathbf{E}$ induces a frequency shift to a transition γ of $\delta\nu_\gamma$, given

by [166]

$$h\,\delta\nu_\gamma(\mathbf{E},\omega,\theta) = -\frac{1}{2}\left\langle \mathbf{E}^2 \right\rangle \left[\Delta\alpha_\gamma^{SC}(\omega) + \frac{3M_F^2 - F(F+1)}{2F(2F-1)}(3\cos^2\theta - 1)\;\Delta\alpha_\gamma^{TEN}(\omega)\right] \tag{5.10}$$

where θ is the angle between the incident light's polarisation and the ion's quantization axis, $\mathbf{E}$ is the electric field caused by the probe light and $\Delta\alpha_\gamma^{SC}(\omega)$ and $\Delta\alpha_\gamma^{TEN}(\omega)$ are the frequency dependent scalar and tensor differential polarizabilities for transition γ.

The differential polarizabilities can be estimated by considering Equation 4.5, and this was the procedure followed in Section 4.5, but the important consideration here is that the shift is proportional to $\langle \mathbf{E}^2 \rangle$, the laser intensity. This feature allows the shift to be cancelled by operating at two different power levels P_1 and P_2 (assuming that the beam's spot size and position are unchanged on the timescale of 2 successive clock cycles, and subject to the uncertainty in the measurement of this ratio) and extrapolating the observed frequency to zero power.

5.2.1 Extrapolation

The unperturbed, extrapolated frequency f_0 can be written

$$f_0 = f_2 - \frac{f_2 - f_1}{P_2 - P_1}P_2 = f_2 - \frac{R}{R-1}(f_2 - f_1) \tag{5.11}$$

for two choices of probe intensities $P_1 \leq P_2$ in a ratio $R \stackrel{\text{def}}{=} P_2/P_1$, resulting in perturbed clock frequencies f_1, and f_2. Needing to operate a second servo in addition to the first results in additional dead time which impacts upon the stability of the clock according to Equation 1.3. However, assuming the experimenter alters the time spent probing at each power to maintain a π-pulse at each power, the second servo will have shorter probe pulses than the first.

Appendix A shows how the total uncertainty for the frequency of the unperturbed transition can be written in terms of the power ratio and the amount of dead time in

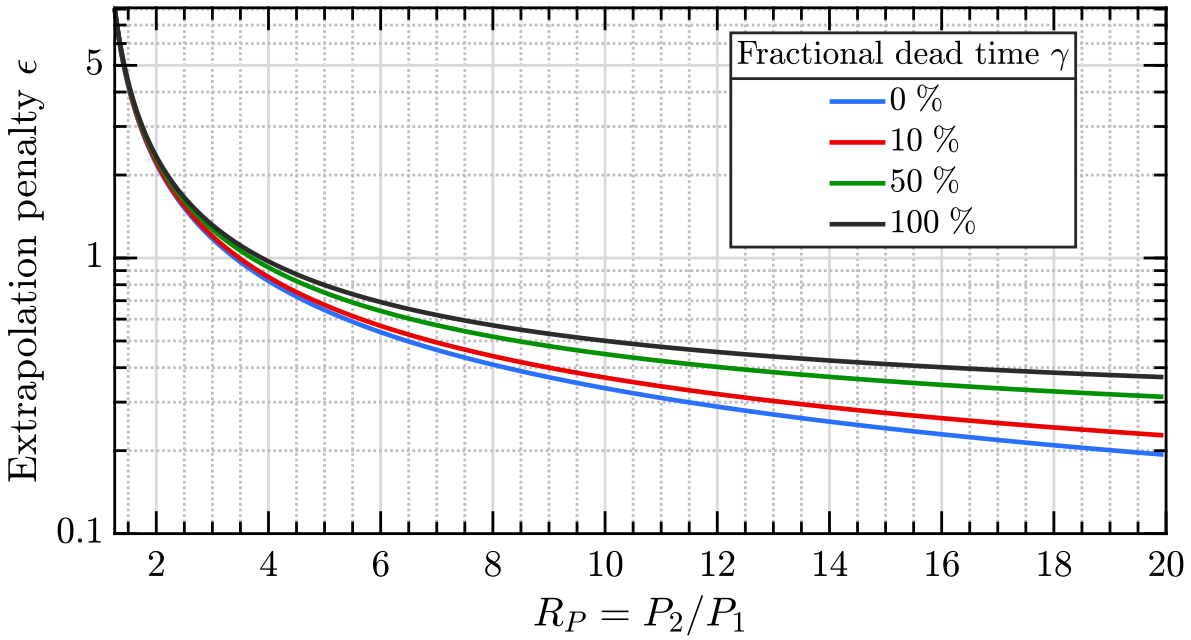

FIGURE 5.2: The degradation in stability caused by running two servos in extrapolation mode, for different proportions of probe pulse to dead time within each servo. See Equation 5.12 for definition of ϵ.

each servo loop compared to the length of the first probe pulse, $\gamma = t_{\text{dead}}/\tau_1$, as

$$\frac{\sigma_{\text{extrap}}}{\sigma_{\text{single}}} = \sqrt{\frac{R(R+1)}{(R-1)^2} \times \frac{1+2\gamma+R^{-1/2}}{1+\gamma}} \stackrel{\text{def}}{=} 1+\epsilon \quad . \tag{5.12}$$

where we compare the instability of our extrapolating servo (σ_{extrap}) against that of a single servo running at P_1 (σ_{single}).

Figure 5.2 shows how the quantity ϵ, the extrapolation penalty, depends on the power ratio chosen and the amount of dead time in the clock cycle. It is therefore desirable to operate your clock with large values of R, but any improvement beyond $R = 10$ becomes marginal.

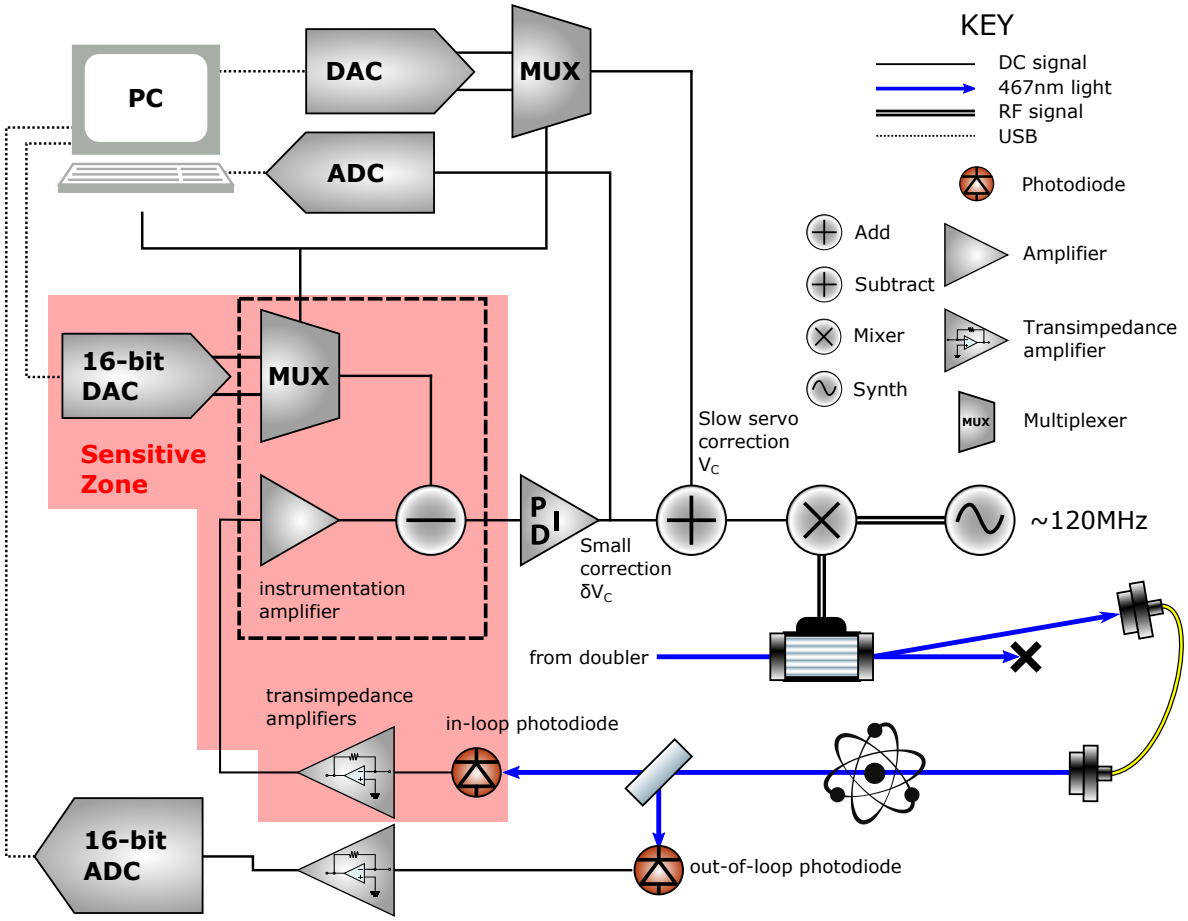

Figure 5.3: Block diagram of the power stabilization scheme. The red shaded area shows the parts of the system responsible for error-signal generation: electrical noise in this region will not be removed by the servo. Note that the method of considering the frequency *ratio* still provides immunity to most noise types even in this case. The dotted box indicates the circuit described in §5.2.2.2.

5.2.2 Power control

Equation 5.12 neglected the effect of power uncertainty on the final derived frequency. Including this (and neglecting frequency deviations this time) gives

$$\frac{\mathrm{d}f_0}{\mathrm{d}R} = \frac{f_2 - f_1}{(R-1)^2} \quad . \tag{5.13}$$

Since the level to which we can control the power ratio at the ion impacts directly upon the ultimate determination of the frequency, controlling this parameter strictly is of critical importance. Extrapolation is carried out for each servo cycle, each of which

which consists of 8 pairs of high / low power probes probing at the upper frequency and lower frequency sides of the Rabi profile. [¶] The ordering of high / low power probes is the same within cycle of 8 pairs, but is alternated from cycle to cycle. For a typical probe time of ∼200 ms, we therefore require good stability at the $\tau = 1 - 10$ s timescale.

Since our previous power stabilization setup did not achieve the required levels of power stability, we now use a two-stage power servo, where fast corrections are made by an integrator with bandwidth ≤ 500 kHz and slow drifts are corrected by a digital servo on the PC with bandwidth ∼1 Hz, as shown in Figure 5.3. A transimpedance amplifier provides the first gain stage to the detected photocurrent. In order to maximize the loop bandwidth (see §5.2.2.1) a subsequent amplification stage is performed using an instrumentation amplifier with 700 kHz bandwidth at $G = 10$.[‖] This minimizes the bandwidth required of the low-GBP transimpedance amplifier by allowing the instrumentation amplifier to provide the bulk of the gain. A reference voltage is subtracted from the amplified signal which defines the power level and can be toggled between two different levels. This error signal is fed to a fast integrator which produces a control signal with very limited range δV_c. This limited-range signal is then added to another control signal V_c produced by a computer-controlled DAC and used to set the amplitude of the RF frequency which powers an AOM in the 467 nm beam path. The computer controls the setpoints and slowly feeds back to V_c in order to drive δV_c to zero, so that the loop can benefit from a high gain while simultaneously minimizing the overshoot.

[¶] These pairs are interleaved using a Thue-Morse sequence to minimize sensitivity to low-order cavity drift. See §2.3.4 for more information.

[‖] Unlike opamps, instrumentation amplifiers do not typically have a constant Gain-Bandwidth Product (GBP), exhibiting higher performance at high frequencies than may be expected from their unity-gain bandwidth.

5.2.2.1 Overshoot

An added complication is created by the pulsed nature of our clock sequence; when the light is turned on the servo is initially railed. As the AOM turns on, the power increases until it surpasses the setpoint. The finite bandwidth of the feedback loop means that this increase continues for some time, until the integrator brings it under control. This process causes an undesirable overshoot in power at the start of each clock pulse, with the potential to cause a systematic bias as the clock transition is temporarily shifted.

The slow servo with fast-but-limited integrator correction architecture described above serves to limit the impact of this effect. In this configuration, the furthest the integrator can rail is set by the limited range of δV_c. By setting this range as small as possible while still leaving enough range to correct for typical deviations observed over 1 clock pulse the overshoot is greatly reduced.

Another solution to this problem could have been a sample-and-hold PID algorithm, gated by the TTL trigger controlling the AOM's incident RF power. However, although initially attractive, this solution suffers from a serious drawback: as the AOM turns on, the power coupled into the fibre jumps to an intermediate level before slowly increasing to its long-term value due to thermal effects in the AOM crystal affecting the beam-pointing. A sample-and-hold system would turn on the AOM with its long-term control setting, resulting in too little power at the ion. This would then be servoed away, however the power would spend more time in the "danger zone" where the erroneous light-shift is of the same order as the transition linewidth, increasing the pulling effect on the transition's observed centre-frequency. This effect will be discussed more fully in §5.2.3.2.

5.2.2.2 Prevention of electrical offsets

In order to achieve a high precision, high bandwidth lock the signal in Figure 5.3 cannot be amplified solely by the transimpedance amplifiers since their Gain-Bandwidth Product (GBP) would cause significant slowdown of the signal chain. Another amplification stage is therefore required to satisfy the constraints of high bandwidth (required for low overshoot) and to reduce the fractional impact of later added noise, but its DC performance is also critical since this will specify the ultimate noise floor of the probe-induced AC Stark shift.

Accurate DC measurements are notoriously tricky [183, 184], primarily due to unwanted effects such as 50 Hz noise[**] and ground loops. To mitigate and prevent these problems, all signals in the in-loop path are processed differentially. Distribution is by doubly shielded CAT6 cable with RJ45 termination:[††] these cables use twisted pairs for signal distribution to improve noise rejection from magnetic and capacitive coupling.

Use of instrumentation amplifiers[185] adds a 130 dB common-mode rejection ratio (CMRR) [186], while low-pass filtering at all transistor junctions prevents rectification of RF signals picked up from the lab[‡‡] by FET-coupled junctions and other non-linear processes internal to the instrumentation amplifier [187, 188]. The high input-impedance of the instrumentation amplifier circuit reduces the effect of $1/f$ Ohmic fluctuation in cable impedance and the gain is specified by a single high-precision resistor with low temperature coefficient of resistance (TCR), putting the total gain-response of the device at $25 \times 10^{-6}\,\mathrm{K}^{-1}$ [189]. Note that it is the ratio of the two power levels used in extrapolation that is important, so our system is inherently insensitive to this gain noise. References [184, 190–192] were invaluable in the design of this system.

[**] Or 60 Hz, to taste.

[††] A great deal of development by the electrical engineering community has gone into the design of these cables, making their performance disproportionately good considering their cost.

[‡‡] In particular the 13 MHz trapping frequency whose ∼300 V drive turns our trap into a frustratingly effective antenna.

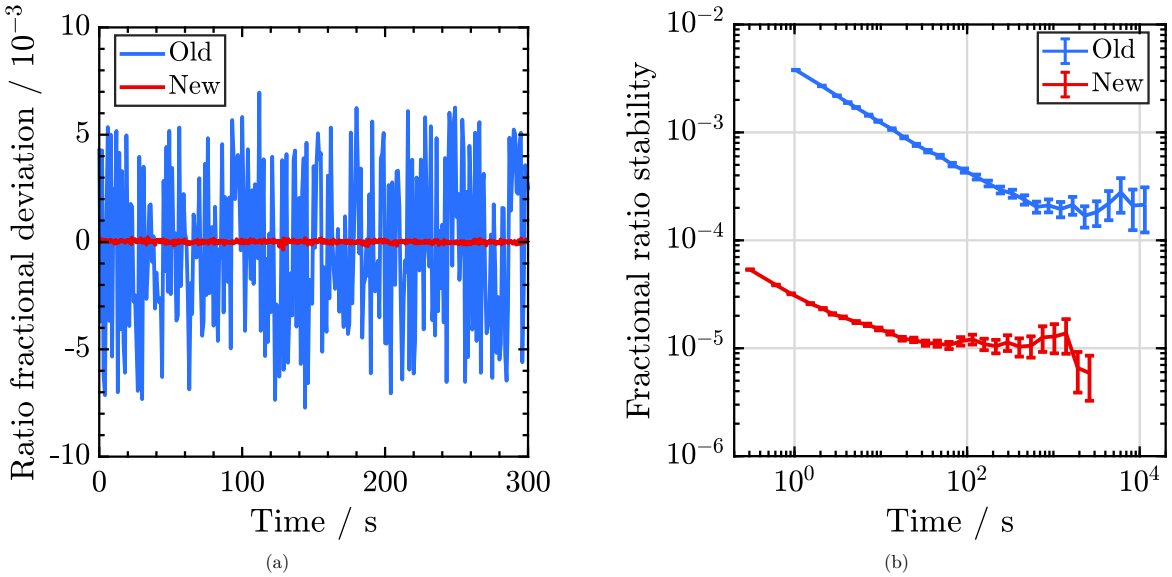

Figure 5.4: Long-term power stability of the clock light stabilisation setup.
(a) Time-domain comparison of out of loop (OOL) monitor traces of the ratio of two power levels at the ion's location, showing the improvements described in §5.2.2.
(b) Allan deviation of (a).

5.2.3 Results

5.2.3.1 Power stability

The long-term power stability of the probe power was assessed by monitoring the voltage measured by a separate, out of loop (OOL) photodiode (shown in Figure 5.3). This combines any noise in the light with noise introduced by the OOL measurement system, so the following figures are a worst-case scenario. Nevertheless, Figure 5.4 shows a ∼200-fold improvement in the short-term stability of the system and a ∼30-fold improvement in the long-term noise floor compared to our previous setup. The ratio of power delivered to the ion is now stable at the 10^{-5} level at timescales of 20 to 500 s.

By using Equation 5.13 with a power ratio of $R = 3$, chosen due to available optical power at 467 nm in our current setup, the ratio stability shown in Figure 5.4(b) produces

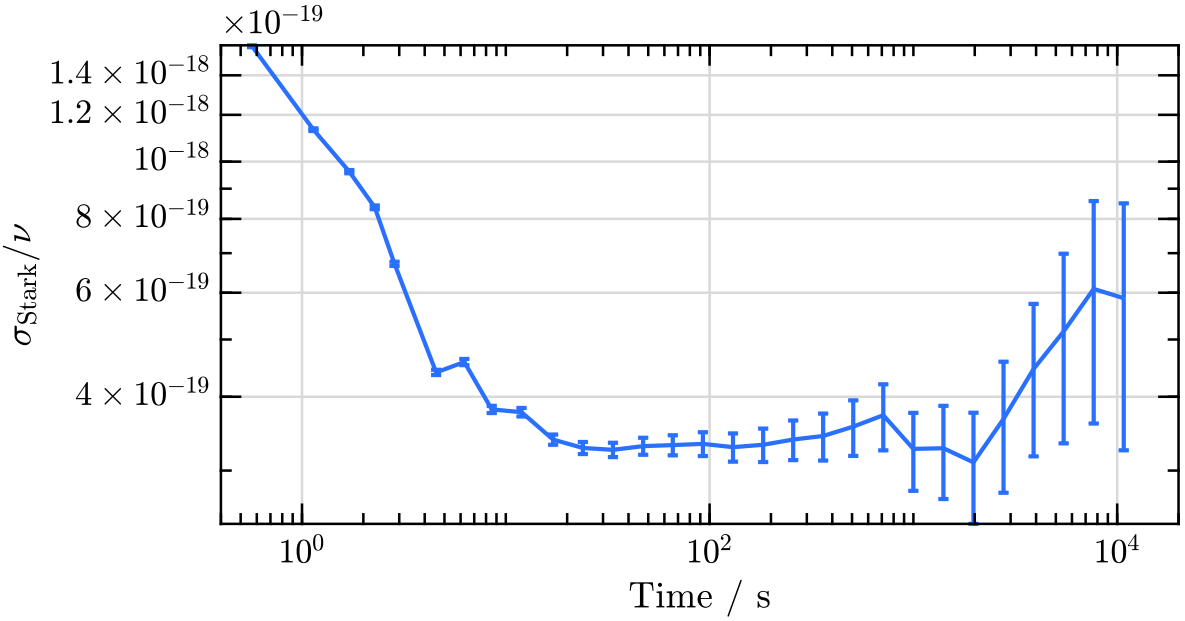

FIGURE 5.5: Allan deviation of the instability in a single power level (i.e. without considering a ratio, and therefore exposing us to common-mode noise). The instability in incident power has been converted to an instability in Stark shift, expressed as a fraction of the transition frequency.

a fractional shift to the low-power E3 transition's frequency of

$$\left.\frac{\Delta\nu}{\nu}\right|_{\text{AC Stark Extrap.}} = \sim 7.6 \times 10^{-15} \pm 5.4 \times 10^{-19} \quad . \tag{5.14}$$

The fractional shift of 7.6×10^{-15} quoted here is an illustrative value for the correction: the actual offset is determined by the ratio measured during clock operation by the OOL photodiode.

Since the power required for a π-pulse of length τ scales as $1/\tau^2$, the long probe times made possible by the developments in Chapter 6 have quadratically reduced the powers needed for a probe, and so the absolute value of the Stark shift is now significantly lower. Figure 5.5 shows the instability in power converted to fractional instability in the ion's AC Stark shift for a single servo operating at $\tau = 500\,\text{ms}$. This shows a fractional noise floor of $\sim 4 \times 10^{-19}$ for time-scales of up to $\sim 500\,\text{s}$, giving the possibility of operating the clock with only a single servo in scenarios where high

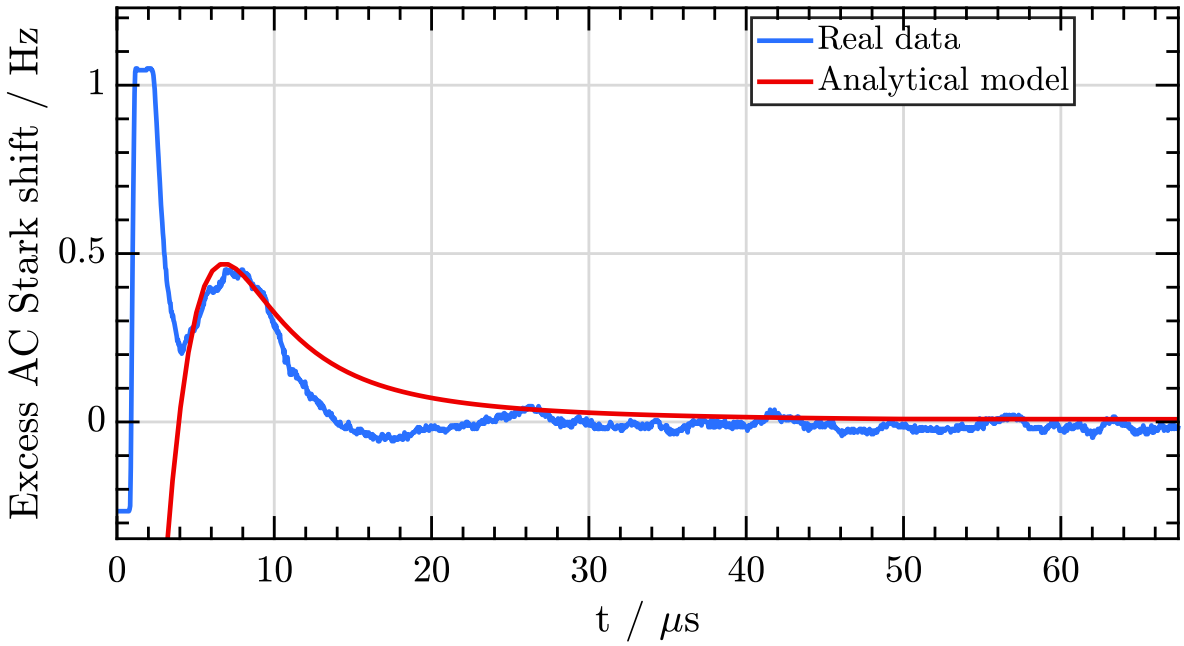

Figure 5.6: Capture of the power servo. This plot shows a comparison between the analytical model described in the text and the measured short-term response of the power servo. The excess power is reported according to its effect on the ion via the AC Stark shift.
The power servo captures and has completely removed the overshoot within 15 µs, suggesting a bandwidth of > 67 kHz. Note that the initial step in the data is believed to be an electrical artifact due to the finite bandwidth of the measuring equipment: it is present even with the servo disabled. The offset shown here is averaged over the whole pulse of $\tau = 500$ ms and results in a fractional offset to the lock-point of less than 10^{-20} compared to the stationary value of the Stark shift as $t \to \infty$ (see text for details).

stability instead of high accuracy is preferred.

5.2.3.2 Overshoot

Figure 5.6 shows the overshoot obtained with the new locking electronics. Whilst the bandwidth of ~ 70 kHz is not particularly large for an AOM-actuated feedback loop, it should be noted that this is the same system that must provide high DC accuracy for the previous sections. To obtain this bandwidth, the system must therefore exhibit good performance over 8 decades in its frequency response.

The coupling between power and frequency makes determining the effect of near-

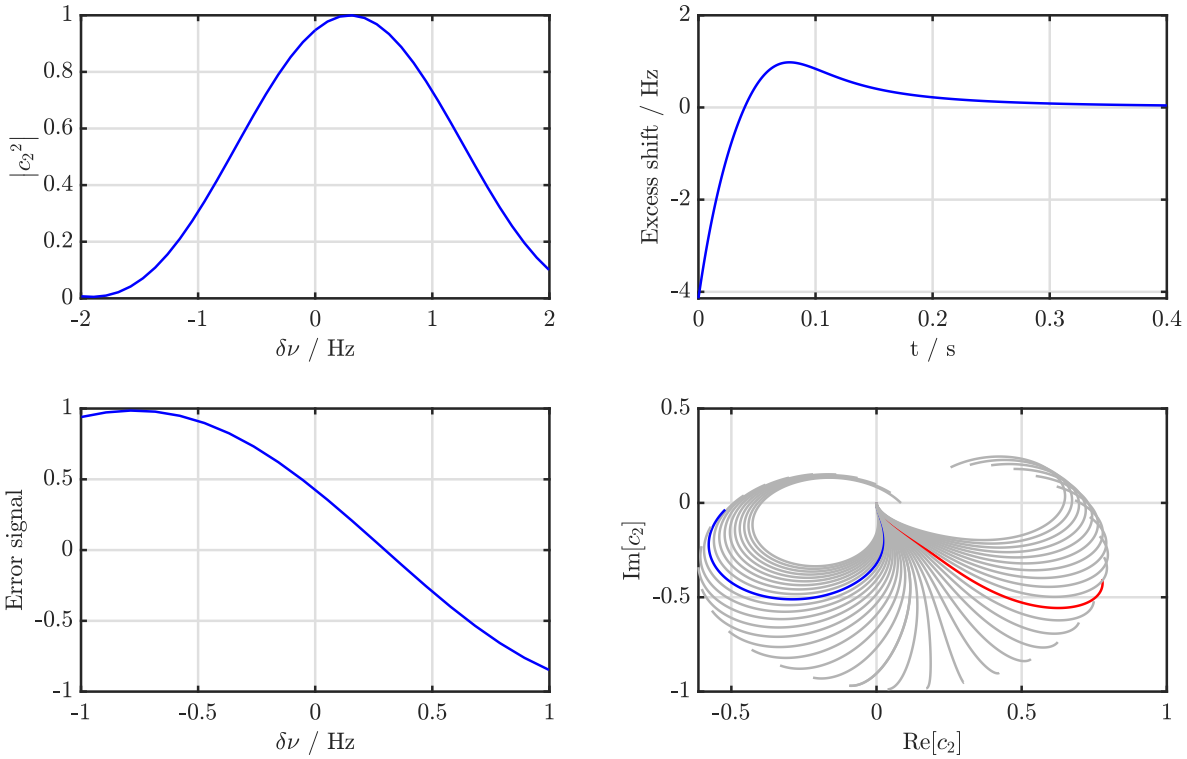

FIGURE 5.7: Example of the solution of Equation 5.16 for an exaggerated overshoot of $P_e = 0.3P_0$, $t_1 = 30\,\text{ms}$ and $t_0 = 60\,\text{ms}$, for a probe pulse of $\tau = 400\,\text{ms}$.
(top left) Perturbed excitation profile.
(top right) Power profile, showing overshoot according to Equation 5.17.
(bottom left) Error signal derived by probing the excitation profile at the positive and negative half-maximum points.
(bottom right) $\langle 2|\Psi(t)\rangle$ for various detuning values. The blue (red) line shows the path taken for the negative (positive) probe when $\delta\nu = 0$. The distortion of this manifold is the cause of the offset.

resonant light such as this a non-trivial problem. In order to evaluate this, a model of the ion as a two-level system was used. Adapting the method in [65], by considering the time-dependent Schrödinger equation (TDSE) in the presence of monochromatic light,

$$i\hbar\frac{\mathrm{d}}{\mathrm{dt}}\left|\Psi(t)\right\rangle = e\mathbf{r}\cdot\mathbf{E}(t)\cos(\omega_L t)\left|\Psi(t)\right\rangle \quad , \tag{5.15}$$

the linear system of equations

$$\begin{aligned} i\dot{c_1} &= \frac{\Omega(t)}{2}\ \exp\left[\ \ i\int_0^t \delta\omega\,\mathrm{d}t\right]\ c_2 \\ i\dot{c_2} &= \frac{\Omega(t)}{2}\ \exp\left[-i\int_0^t \delta\omega\,\mathrm{d}t\right]\ c_1 \end{aligned} \tag{5.16}$$

can be found by using the rotating wave approximation (RWA) and solved numerically to give the time-evolution of the system. Here $\delta\omega = \omega_L - \omega(P)$ is the laser's offset from the perturbed, intensity-dependent transition frequency $\omega(P)$ and $\Omega = \frac{e|\mathbf{E}(t)|}{\hbar}\langle 1|\mathbf{r}|2\rangle$ is the resonant Rabi frequency.

The red line in Figure 5.6 shows the fit of an analytical function to the overshoot. This function is of the form

$$P(t) = P_0(1 - \mathrm{e}^{-\frac{t}{t_1}}) + P_e\frac{t_0^2}{(t-t_0)^2 + t_0^2} \quad , \tag{5.17}$$

chosen for its qualitative resemblance to the overshoot and for the existence of an analytical integral. For the fit shown, $P_e = 0.147P_0$, $t_1 = 2\,\mu\mathrm{s}$ and $t_0 = 5\,\mu\mathrm{s}$. P_0 is the asymptotic value of the power in the beam, assumed to be chosen such that the probe over time τ results in a pi-pulse.

The solution of Equation 5.15 for an exaggerated overshoot is shown in Figure 5.7. Solving instead for the power profile shown in Figure 5.6 gives a total shift of $\delta\nu_{Overshoot} = 5.5\,\mathrm{nHz}$: a completely negligible amount. We can therefore neglect any offset due to the servo overshoot at below the 10^{-20} level.

$$\left.\frac{\Delta\nu}{\nu}\right|_{\text{AC Stark overshoot}} = 0(0) \times 10^{-20} \tag{5.18}$$

5.3 BBR Stark shift

The ion's environment is not at absolute zero, and so emits a spectrum of radiation according to Planck's law. This radiation interacts with the energy levels of an atom through their dipole moments [167, 168, 193] and so causes an AC Stark shift to the atom's transitions.

To find the value of this shift, two things must be well-known: the BBR environment defining the spectrum of radiation incident on the ion and the ion's response to this

radiation, known as the differential polarizability of a given transition. Section 3.3 details the determination of the first, whereas Chapter 4 is devoted to the latter.

The temperature rise measured in Section 3.3 of $\Delta T_{ion} = 0.14(14)\,\mathrm{K}$ results in an RMS electric field of [140, 194]

$$\left\langle E^2 \right\rangle = (831.9\,\mathrm{V\,m^{-1}})^2 \left(\frac{T}{300\,\mathrm{K}}\right)^4 \quad . \tag{5.19}$$

This interacts with the ion's differential polarizability (see Section 4.5) according to Equation 4.2 to give

$$\left.\frac{\Delta\nu}{\nu}\right|_{\mathrm{BBR}} = -\frac{\Delta\alpha_{21}}{2h\nu}\left\langle E^2 \right\rangle \tag{5.20}$$

$$= (-650.0 \pm 9.0) \times 10^{-19} \quad . \tag{5.21}$$

In this calculation, the fractional uncertainties for the two components (squared-field and differential polarizability) have been added in quadrature, contributing 1.2×10^{-19} and 8.9×10^{-19} respectively. This is assuming a negligible contribution from uncertainty in the temperature determination of the vacuum chamber.

5.4 Second order Zeeman

Both the clock transitions used in our experiment involve a transition between states with $m_F = 0 \rightarrow 0$, making them insensitive to the first order Zeeman effect. However, the Zeeman effect contains a small quadratic component that is nonetheless large enough that we must consider it. Non-zero magnetic fields cause mixing between the hyperfine sub-levels with equal values of m_F, given here for the ground $^2\mathrm{S}_{1/2}$ state as [eq. 6.34 in 65, 66]:

$$\left\langle F = 0, m_F = 0 \,|\, \mu \cdot \mathbf{B} \,|\, F = 1, m_F = 0 \right\rangle = -\zeta \mu_B B \tag{5.22}$$

with μ_B the Bohr magneton, μ the atomic magnetic moment and F, m_F having their usual meanings. ζ is a constant and A in the following equation is the hyperfine-structure constant.

This leads to eigenvalues of

$$\begin{aligned} E &= \pm\sqrt{\left(\frac{A}{2}\right)^2 + (\zeta\mu_B B)^2} \\ &\approx \pm\left[\frac{A}{2} + \frac{(\zeta\mu_B B)^2}{A}\right] \end{aligned} \tag{5.23}$$

where, in low fields, the induced shift is quadratic in B.

Determining the constants for a given transition can be done experimentally by varying the magnetic field the ion is exposed to and measuring the frequency difference compared to a fixed field. This was done in [19] and yielded quadratic Zeeman coefficients of $k_{E2} = 52.13(9)\,\mathrm{mHz\,\mu T^{-2}}$ and $k_{E3} = -2.08(1)\,\mathrm{mHz\,\mu T^{-2}}$ where $\Delta\nu = k_i B^2$. For the magnetic field scan shown in Figure 2.8 with a fractional fitting uncertainty of 1.7×10^{-3}, this results in an uncertainty for the E3 transition when operated in an intentional field of $3\,\mu\mathrm{T}$ of

$$\left.\frac{\Delta\nu}{\nu}\right|_{\text{second Zeeman}} = (-291.5 \pm 1.7) \times 10^{-19} \quad . \tag{5.24}$$

The shift for the E2 transition in these conditions can also be found and is $\Delta\nu_{E2}/\nu_{E2} = (681.6 \pm 2.5) \times 10^{-18}$.

In practice, the background magnetic field wanders over time as shown by Figure 5.8 and this dominates over uncertainty in its determination at long time-scales. This wander is characterised by regular measurements of the field during a measurement campaign: its half-range is taken as the 1-sigma uncertainty. This currently is done manually at roughly 12 h periods, but the improvements in Section 3.6 will eliminate this additional uncertainty by (a) automatically and continuously monitoring the magnetic field and (b) reducing the background field fluctuations by a factor of at least 100 by the addition of multi-layer mu-metal shielding.

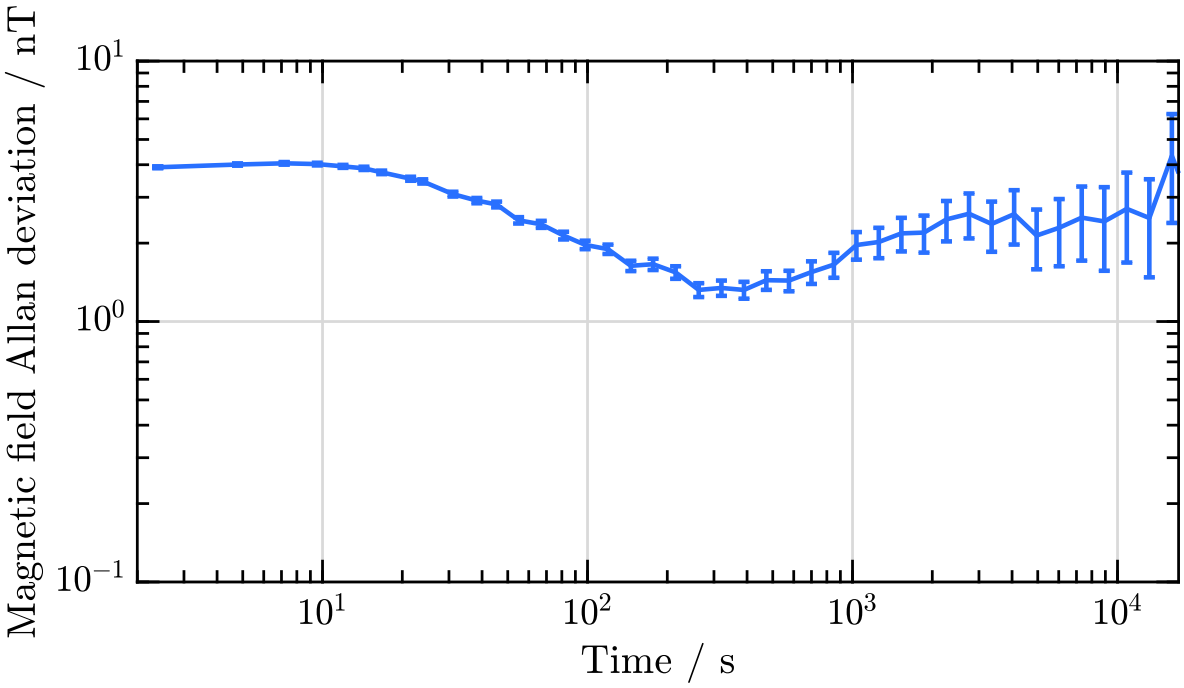

FIGURE 5.8: Stability over time of the ion's background magnetic field. This was assessed by monitoring the frequency difference of the $\Delta m_F = \pm 2$ components of the E2 transition as described in §2.4.1.

5.5 Electric quadrupole

The quadrupole electric field experienced by the ion was given in Equation 3.19 and contains both an AC and a DC element, U_1 and U_0[§§]. This quadrupole field, or any stray electric field gradient, can interact with the quadrupole moment of an atom. For $^{171}Yb^+$, the ground state ($^2S_{1/2}$ (F=0)) contributes no quadrupole moment due to its spherical symmetry. However, the upper states of both transitions ($^2D_{3/2}$ (F=2) and $^2F_{7/2}$ (F=3)) lack this symmetry and do interact with any residual DC quadruple field (U_0 in Equation 3.19), with the resultant frequency shift given by [166]

$$\Delta\nu = \frac{U_0}{2r_0^2 h}\, k(J, I, F, m_F)\, (3\cos^2\beta - 1)\, \Theta(L, J) \quad , \tag{5.25}$$

[§§]This equation assumes that the DC quadrupole contribution is completely on axis, i.e. comes completely from the electrodes. If this were the case the two radial modes would be entirely degenerate, and we know that they aren't (see §3.4.3). The residual contribution from e.g. patch potentials or the DC compensation electrodes makes its way into the non-linearity of the fit and is contained in the uncertainty.

where Θ is the quadrupole moment of the excited state, β is the angle between the quadrupole axis and the magnetic field and

$$k(J,I,F,m_F) = (-1)^{2F+I+J+1-m_F}(2F+1) \times \begin{pmatrix} F & 2 & F \\ -m_F & 0 & m_F \end{pmatrix} \times \begin{Bmatrix} J & 2 & J \\ F & I & F \end{Bmatrix} \begin{pmatrix} J & 2 & J \\ -J & 0 & J \end{pmatrix}^{-1} . \tag{5.26}$$

Here, (.) and {.} represent the Wigner 3-j and 6-j symbols. For the E2 transition $k = 4/5$ and for the E3 $k = 5/7$.

U_0 can be controlled by applying an equal offset to both end-cap electrodes, leaving the vertical electric field unchanged but altering its quadrupole component. This presents an opportunity: the residual quadrupole field is modified by altering the end-cap voltages and then the quadrupole shift is measured. In this manner, a point can be found where $U_0 \approx 0$. In order to measure the quadrupole shift, we use the fact that the $(3\cos^2\beta - 1)$ term in Equation 5.25 averages to zero when considered over three orthogonal fields. Monitoring the frequency offsets when the field is changed vs. a stable reference (the NPL Sr-lattice clock, see Ref. [195]) therefore reveals the magnitude of the quadrupole shift.

These measurements in combination with Equation 5.25 and the value of the $^2D_{3/2}$ quadrupole moment—found in [176] as $2.08(11)ea_0^2$, where e, a_0 are the elementary charge and the Bohr radius—allow the residual component of the trapping potential to be determined, as shown in Figure 5.9.

Operating the trap with the lower end-cap voltage set to $V_{ECB} = -0.70\,\mathrm{V}$ and the others set to minimise EMM therefore gives a maximum quadratic shift (for any

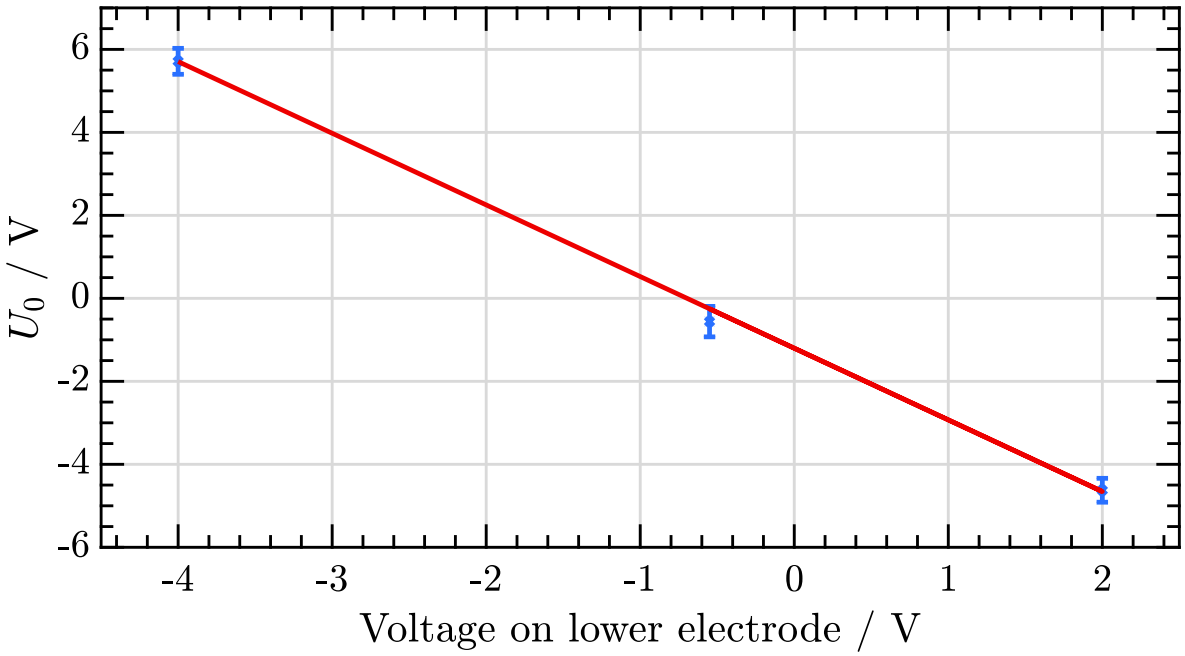

FIGURE 5.9: The DC component of the quadrupole potential in Equation 3.19. This was found by altering the voltage on one of the trap's end-caps, finding a new micromotion null, and observing the steps in the E2 transition's frequency as the ion's quantization axis is rotated through three orthogonal directions.

magnetic field) for the E2 transition of $\Delta\nu_{E2} = 0.00(5)\,\text{Hz}$ which, using $\Theta(F, 7/2) = -0.041(5)ea_0^2$ [196] gives

$$\left.\frac{\Delta\nu}{\nu}\right|_{\text{elec. quad.}} = (0 \pm 15) \times 10^{-19} \quad . \tag{5.27}$$

5.6 Phase noise on clock light

The clock light is produced by a laser operating in the IR (see Chapter 6) which is doubled using SHG to the blue light used to interrogate the clock transitions. Light is delivered from the laser to the doubler, from the doubler to the ion and from the laser to the measurement combs via fibres. These fibres have the potential to introduce frequency offsets. For example, drifting temperature could cause a change in the refractive index of the fibre core.

For this reason, the fibre links between laboratories are fully phase-noise compensated, using the method in [129]. The final stage of the light's path, the PCF which carries all the beams and delivers them to the ion, is not yet under active path-length stabilisation, and so a measurement of the noise it introduces was made.

This fibre is shielded by thermally insulating foam as well as being in a laboratory temperature stabilised at the 100 mK level to minimise its drift. §2.3.2 describes how the phase noise on this link, σ_P, was measured. We find $\sigma_p(\tau = 1000\,\mathrm{s}) = 0.056(20)\,\mathrm{mHz}$, giving

$$\left.\frac{\Delta\nu}{\nu}\right|_{\text{fibre noise}} = 0.88 \times 10^{-19} \quad . \tag{5.28}$$

Other sources of phase noise could be the chirp due to toggling of our AOM as the crystal heats under the RF drive power. Currently insufficient signal amplitude at our phase noise beat detection unit (BDU) prevents us from resolving this effect, however we note that other groups [197] have measured fractional shifts as large as 8×10^{-18}. Increasing the SNR of our beat detection to permit full, active path-length stabilization to the ion's location will therefore be a priority in the near future.

5.7 Shutter leakage

Silly as it may seem, uncertainty in the amount of light leaking through shutters has in the past been a significant contributor to our uncertainty budget. During the clock probe stage, all beams except the probe beam are extinguished. However, the AC Stark effect is largest for light close in frequency to strong transitions. This describes both our cooling beam at 369 nm and our repumping beam at 935 nm.

To quantify this effect, we ran a test in the dual servo configuration, intentionally leaking tiny amounts of 369 light during the clock probe to measure this sensitivity. This found a shift of $2.8(2)\,\mathrm{Hz\,nW^{-1}}$ for 369 nm light in our particular optical setup.

To measure the amount of light present with the shutters[198] closed, a PMT was coupled to the output of the fibre to the ion and the number of counts produced with the shutters closed was measured.

For both the 369 nm and 935 nm beams (and also the other, less critical beams), the reading was indistinguishable from zero.

For the PMT's worst-case rated sensitivity at 369 nm, we find the power present at the ion to be less than 5×10^{-17} W resulting in a fractional shift of $\Delta\nu/\nu < 3 \times 10^{-22}$. The PMT is not rated for use at 935 nm however it does have a rating at 800 nm. If we conservatively assume that the worst-case sensitivity at 935 nm is a factor of 100 less than that at 800 nm, we find that the shift due to the 935 nm leakage light (which, due to the lack of measurement sensitivity, dominates over all other closed-shutter Stark shifts) is

$$\left.\frac{\Delta\nu}{\nu}\right|_{\text{leakage}} = (0.0 \pm 1.5) \times 10^{-19} \quad . \tag{5.29}$$

5.8 Uncertainty budget

Adding together all the above uncertainties in quadrature gives the expected total inaccuracy of the clock when operated under the conditions described. These systematic effects are sometimes called *type B* uncertainties, in contrast to *type A* which typically dominate the clock's uncertainty for short runs. *Type A* uncertainty is known as *instability* in frequency metrology and is reduced by long operation, whereas the systematic effects listed here represent a hard limit to the clock's accuracy regardless of how long it averages for (see §1.1.2).

The values quoted in this chapter for the various systematic effects are true in the best-case scenario. Unfortunately, we do not currently operate in conditions that are simultaneously optimal for all the shifts presented, for technical reasons. Over the next

few years, we hope to overcome these technical challenges, so it is useful to consider the level of uncertainty that our current apparatus could reach in optimal conditions.

Table 5.1 shows the combined effect of all the systematic offsets listed in this chapter. By adding these uncertainty contributions in quadrature, we can produce a number for the $^{171}Yb^{+}$ clock's total systematic floor if all subsystems were operating at peak performance, predicting that our total systematic uncertainty could be as low as $\sigma/\nu_{E3} = 2.1 \times 10^{-18}$.

	E3 systematic shifts	
Source	$\delta\nu/\nu_0 \times 10^{-19}$	$\sigma/\nu_0 \times 10^{-19}$
Electric Quadrupole	0	15.4
BBR Stark		
coefficient		*8.9*
temperature		*1.2*
total	-650.0	9.0
Probe-induced Stark - level	$\delta\nu_{AC}/\nu_0$	5.4
RF Stark - intrinsic	-3	2
Second Order Zeeman	-291.5	1.7
Background collisions	0	1.5
Shutter leakage	0	1.5
Second Order Doppler - intrinsic	-7	1
Second Order Doppler - excess	0	2
RF Stark - excess	0	2
Fibre phase noise	0	0.88
Probe-induced Stark - overshoot	0	0
Total	$-951.5 + \delta\nu_{AC}/\nu_0$	21.2

Table 5.1: Total systematic uncertainty budget of the $^{171}Yb^{+}$ clock operating on the E3 transition, combining uncertainties calculated in previous sections. The value of the AC Stark shift $\delta\nu_{AC}$ depends on the mode of operation and is measured live, but its uncertainty is included here.
Note that this table only includes effects which we have characterized: there may be others not yet found that also contribute. Most notably, the size of the AOM chirp has not been measured yet: Ref. [197] suggests that this could result in a fractional shift of up to 8×10^{-18}. Also, the offset introduced by the servo algorithm has not yet been fully characterized.

5.9 Conclusions

In this chapter, a review of all the leading systematic effects that could result in an error in the determination of the unperturbed clock frequency have been listed and explored. The new design of ion trap (Chapter 3) has allowed us to reduce our fractional trap-

related uncertainty to 4.5×10^{-19}. Improved knowledge of the differential polarizability (Chapter 4, Table 4.3) has reduced the BBR shift uncertainty from 4.5×10^{-17}[19] to 9.0×10^{-19}. Despite operating with a conceptually simple extrapolation scheme, our AC Stark shift is now controlled at the 5×10^{-19} level.

The improvements presented in this chapter have together reduced the fractional accuracy of the E3 transition from 3.19×10^{-16} at the start of this project [19] to 2.1×10^{-18} now.

Our leading systematic uncertainty is now the electric quadrupole shift, currently nulled by careful choice of the DC compensation electrode voltages, the uncertainty of which is dominated by uncertainty in its measurement. In the new trap (see Section 3.6) the multi-layer mu-metal shielding will improve magnetic stability, allowing more confidence in the ion's quantization axis and a more accurate measurement to be made. Also, the pairs of compensation electrodes will allow for arbitrary DC electric field gradients to be applied, allowing us to null the effect of off-axis gradients. More temptingly, we may be able to set this effect exactly to zero: see §8.2.1.2.

Next comes the AC Stark shift from environmental Black-Body Radiation (BBR), whose uncertainty is dominated by uncertainty in the differential polarizability. Despite work by both us and PTB [7], this systematic effect again looms large in a budget that has shrunk considerable in recent years. The way forward is not yet clear: maybe a new, even more tightly controlled differential polarizability measurement is required; maybe an improvement in theoretical calculation will save us the trouble, or maybe the clocks of the future will incorporate cryogenics to take advantage of the T^4 scaling of BBR.

Following this is $^{171}Yb^+$'s perennial bug-bear: the probe-induced AC Stark shift. Originally thought an inevitable limitation of a clock transition with a spectral width in the nano-hertz, there are now several schemes that aim to cancel the AC Stark shift

(and other probe-related shifts) using novel interrogation schemes [199, 200]. We have now probably reached the limits of what extrapolation can give us, so the next version of our clock will use the auto-balanced Ramsey technique [201].

Of course, perhaps the main limitation of Table 5.1 is that it is an estimate based on measurements of the ion's environment. Although we have made all efforts to determine the effect of perturbations on the ion accurately, the true test of this budget is a comparison with another similar clock. This will be a key goal of the project in the upcoming future: to build an improved version of this setup and run the two simultaneously, experimentally demonstrating agreement at the levels estimated here both between the two local clocks and with our European partners (see Chapter 7).

Improving the local oscillator 6

> If you knew Time as well as I do, you wouldn't talk about wasting it.
>
> — *the Mad Hatter*

In Chapter 1 the three components of an atomic clock were introduced. The accurate reference, a trapped ion of $^{171}Yb^{+}$, was expanded upon in Chapter 3 and its perturbations were characterised in Chapters 4 and 5. Chapter 2 covered to some extent the readout mechanism, the femtosecond optical frequency comb, although a complete account of this topic deserves its own thesis. In this chapter, we examine the final ingredient: the stable resonator or *local oscillator*.

The local oscillator in an optical atomic clock is the laser used to interrogate the metastable clock transition. At long time-scales this local oscillator would drift if deprived of its frequency corrections to the atomic reference. However at short time-scales its performance impacts upon the clock's stability through several mechanisms.

Firstly, in order to probe the forbidden transitions used for atomic clocks in a reasonable length of time, Rabi frequencies of $\sim 10\,\mathrm{Hz}$ are required. In the case of the

E3 transition whose linewidth is on the order of 1 nHz, accumulating sufficient spectral density to drive the transition in a reasonable time requires a very narrow laser.* Since the transition's natural linewidth is so low, the minimum observable transition linewidth will be dominated by the laser's linewidth at the time-scale of interest, and affects the QPN limit (see §1.1.2).

Another contributor to the transition's observed linewidth is the Fourier broadening of the laser. This effect was discussed in §1.1.4 and is inversely related to the probe time. Since coherent driving of the transition requires probe times to be less than the coherence time of the light used to excite it, this sets a limit on the minimum observable linewidth, and hence maximum stability possible with a clock. For single-ion clocks such as ours, which typically operate at the QPN limit, this effect usually dominates their stability.

Finally, the stability of the local oscillator is very relevant during dead-time in the probe cycle when the oscillator runs freely, without reference to the atomic transition. This problem usually affects lattice-based clocks more severely than ion clocks due to the much larger dead-time fraction of their clock cycles. It is known as the Dick effect and is covered in detail by [54, 55, 202, 203].

This chapter will describe the design and construction of the local oscillator used by the $^{171}Yb^{+}$ clock. Section 6.1 will cover the multi-stage stabilisation scheme used and offer some background on the technicalities of locking a laser frequency to a cavity resonance. Section 6.2 will look at the potential sources of noise in light stabilised to a cavity and §6.2.1 will examine one of them, temperature, more closely. Section 6.4 will present a scheme used to distribute the consequent stability of our clock laser to

*The other option for increasing the Rabi frequency is to boost the power of the interrogating probe beam. For the E3 transition both approaches must be taken simultaneously, resulting in a large probe-induced a.c. Stark shift (see Section 5.2).

the family of atomic clocks around the NPL and Section 6.5 will show some of the performance obtained.

6.1 Locking scheme

In order to convert a stable frequency reference in the form of an optical cavity to a stable source of light, we need to lock the frequency of our clock laser to a cavity resonance. The clock light is produced by a Toptica TA Pro, a system consisting of an integrated DL Pro ECDL with typical free-running bandwidth from 10 to 300 kHz at 5 µs, injecting a tapered amplifier [204]. This laser architecture allows for fast frequency modulation by varying the diode current, and slow feedback by changing the angle of the external grating via a piezo element. Very slow feedback is also possible via the diode temperature, but we operate at a fixed temperature chosen for maximum mode-hop free tuning range.

In our laboratory, a multi-stage stabilisation scheme is used. First, the laser is locked to a local (Lab A) ULE cavity with good, but not extreme frequency stability. This servo is high bandwidth and serves to narrow the laser linewidth. Figure 6.2 shows the signal measured on Photodiode A when the system is in lock. The humps shown suggest a lock bandwidth of 1.7 MHz: the point at which the servo's phase response exceeds π.

The second stage involves a slow lock to another, more stable cavity. The noise processes in this cavity will dominate the laser's profile at all time-scales relevant for frequency metrology, so this cavity must be constructed and operated with utmost care. Section 6.2 will detail the considerations involved. The actuator for this lock is AOM A in Figure 6.1. When the frequency offset produced by this AOM is altered the local servo will act to change the laser frequency such that the shifted light after AOM A is

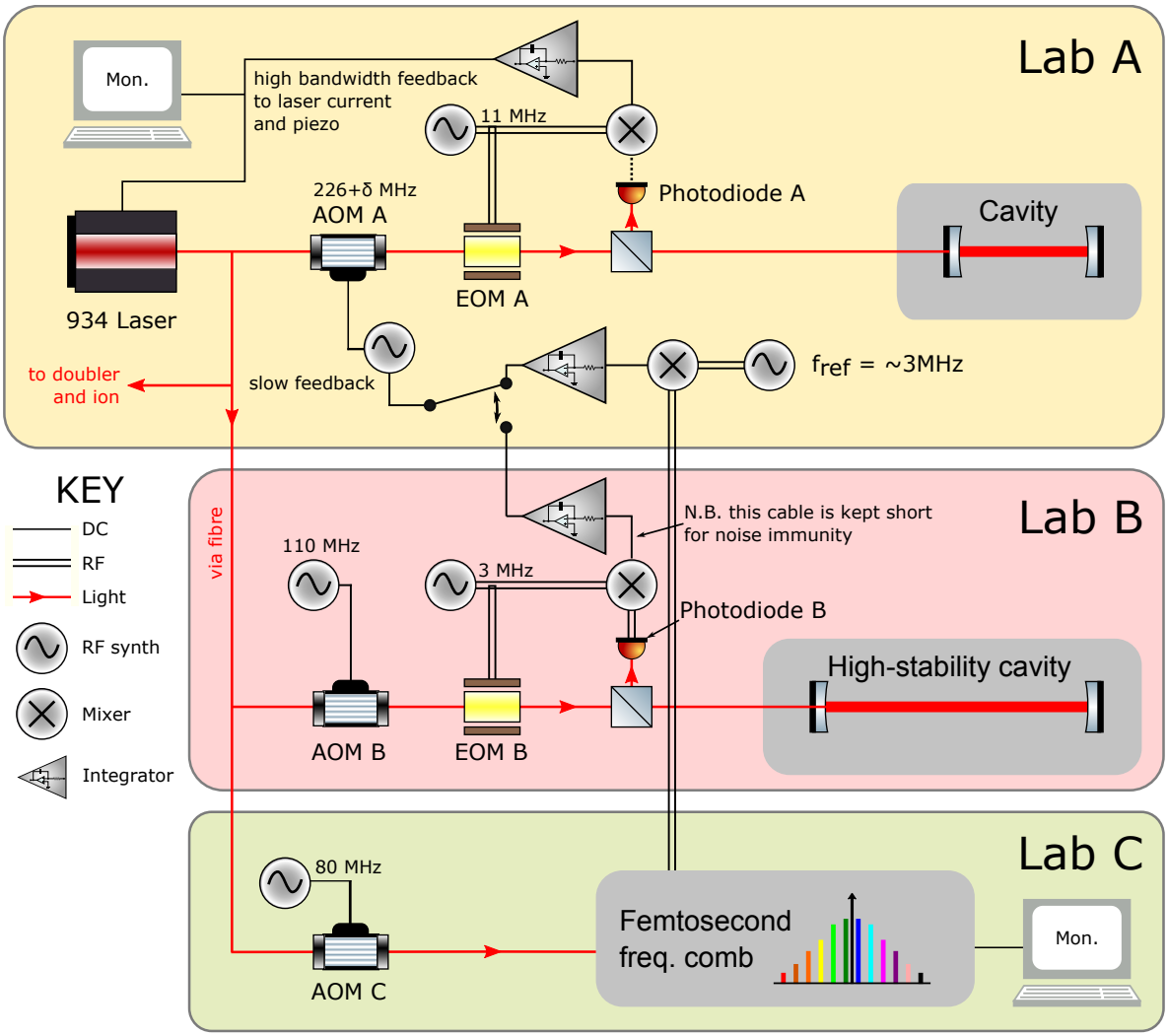

Figure 6.1: Experimental diagram of the 934 nm and 467 nm laser stabilisation setup. The light sent to the ion can be stabilised to either the remote, high-stability ultra-low expansivity (ULE) cavity (Figure 6.7) or any other clock-laser via the frequency comb (Section 6.4). The high-bandwidth local PDH lock provides line narrowing, whereas the slow (∼5 kHz) servo loop removes the local cavity's flicker noise. The actuator for the slow servo is AOM A: adjusting this frequency offset forces the local PDH servo to compensate by changing the laser frequency.
All fibre links also implement active fibre-noise cancellation (not shown) actuated by AOMs B and C. AOM frequencies are rounded to the nearest MHz. All DDS units and frequency synthesisers are referenced to a 10 MHz signal derived from NPL's local time-scale UTC(NPL).

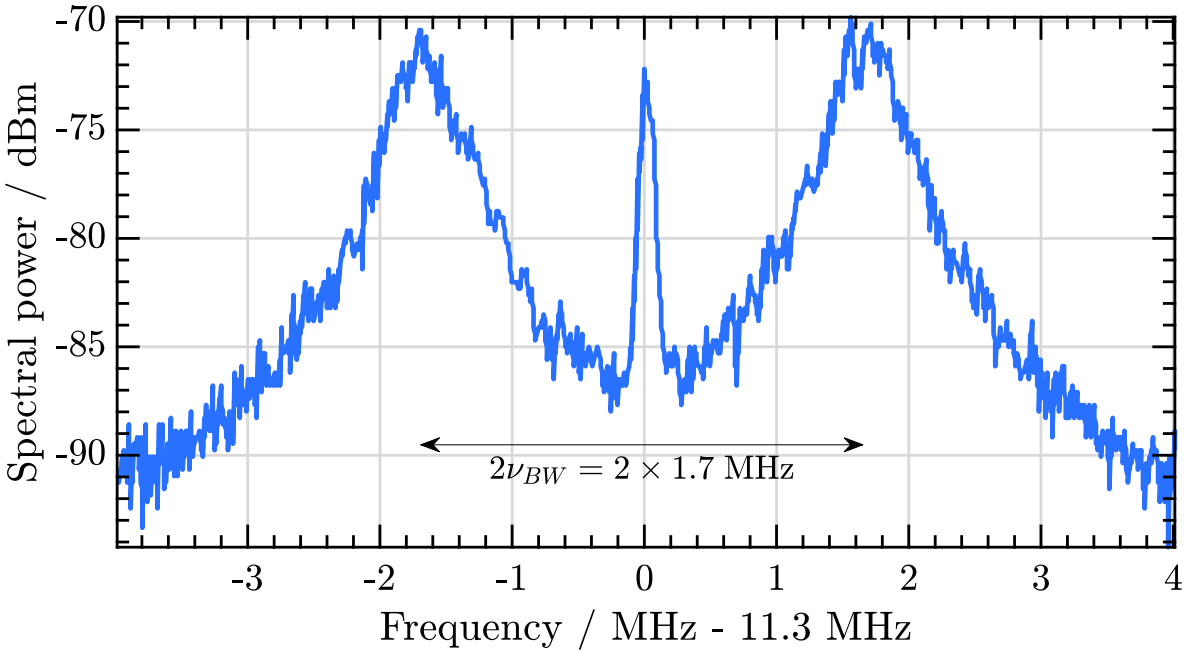

FIGURE 6.2: Power spectrum of Photodiode A's signal. The reduced noise in the area between the two humps is due to the servo bandwidth of $\nu_{BW} = 1.7\,\text{MHz}$. The middle peak is the PDH drive frequency, 11.3 MHz This spectrum was taken with resolution bandwidth (RBW) = 100 kHz.

still on resonance with the local cavity. In this way the frequency of the light sent to Lab B, Lab C and the trapped-ion will be changed.

The error signals for both the high-bandwidth local lock and the lower bandwidth remote lock are produced using the Pound-Drever-Hall (PDH) scheme. The PDH technique is a well-known method of locking a laser frequency (ω) to a resonance ($\omega_m = m\,\omega_{\text{FSR}}$, $m \in \mathbb{Z}$) and has been well covered in the literature [205–207]. Simply, it works by using a phase modulated laser (achieved in our case by using electro-optic modulators, EOM A and EOM B in Figure 6.1) to probe a cavity. Ignoring the modulation for a moment and considering only the carrier component of the beam, some fraction is reflected: $E_{ref} = F(\omega)E_I$ where E_I and E_{ref} are the complex amplitudes of the incident and reflected beams, and $F(\omega)$ is defined as the frequency-dependent reflection coefficient of the cavity. This reflection coefficient is complex, to represent the phase imparted

to the reflected beam. If ω is close enough to ω_m for a standing wave to exist within the cavity, E_{ref} actually consists of two components: the reflection from the first mirror (E_R) that never enters the cavity and the leakage of light from the standing wave within the cavity through the first mirror (E_L). The fields of these two reflected beams combine to form a sum given by [206]

$$E_{ref} = E_R + E_L \tag{6.1}$$

$$\stackrel{\text{def}}{=} F(\omega)\, E_I \tag{6.2}$$

$$= \frac{r(e^{2\pi i \frac{\omega}{\omega_{\text{FSR}}}} - 1)}{1 - r^2 e^{2\pi i \frac{\omega}{\omega_{\text{FSR}}}}}\, E_I \tag{6.3}$$

where r is the refection coefficient of each mirror. ω_{FSR} is the cavity's Free Spectral Range (FSR) and is defined in Equation 6.4.

This interference is completely destructive if $\omega = \omega_m$, but imparts a phase to the reflected beam if not. To measure this phase change from E_I to E_R, we need a reference frequency with a well-known phase relationship with E_I: this is the purpose of the sidebands introduced through phase modulation of the light. These sidebands are far from resonance with the cavity, giving full reflection ($F_{sidebands}(\omega) = 1$), and serve as phase-references for the carrier. The heterodyne optical beat between these sidebands and the reflected carrier beam E_{ref} contains a component at the modulation frequency if $E_{ref} \neq 0$. In Figure 6.1, this occurs at Photodiode B and is mixed down to a DC signal which is used to feedback to the laser's frequency.

6.2 Noise sources in an optical cavity

Optical cavities are simply Fabry-Pérot interferometers. These devices consist of two highly reflective parallel mirrors, between which light resonates constructively for integer multiples of the *free spectral range* (ν_{FSR}), determined by the optical path-length

L_0:

$$\nu_{\mathrm{FSR}} = \frac{c}{2L_0} \quad . \tag{6.4}$$

As such, most noise sources in an optical cavity are consequences of one of these parameters changing.

Noise sources in cavities are often split into two categories: technical and fundamental [208]. Technical noise sources are those that can potentially be eliminated by careful control of the cavity's environment, whereas fundamental noise sources are unavoidable for a given cavity design. The following sections will cover these and the work done to suppress them.

6.2.1 Temperature *(technical noise)*

Limiting and controlling the effect of temperature on the frequency of a cavity's modes is of critical, often limiting importance. Since this topic is a large one, it is covered separately in Section 6.3.

6.2.2 Vibration *(technical noise)*

Vibration from the cavity's environment can couple to the frequency of the cavity's modes, and hence the locked laser light. In order to reduce this effect, the cavity and associated optics are "floated" on a Minus-K platform. These devices employ negative stiffness to isolate systems from vibrations [209]. Figure 6.3 shows the typical vibration suppression profile of a Minus-K platform. Above the platform's resonant frequency of 0.5 Hz, extraneous vibrations are strongly suppressed.

Also, the cavity system is located in a "quiet-house" laboratory with infrequent access and fanless, heat-exchanger temperature control to minimise disturbances. The

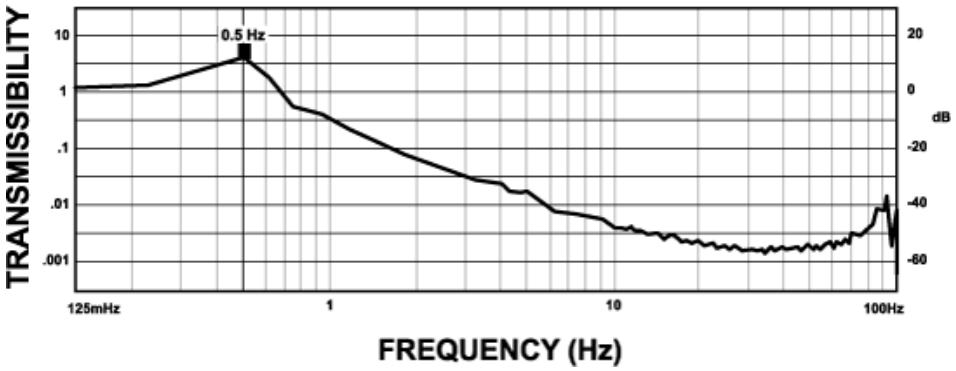

Figure 6.3: Typical frequency response of a Minus-K platform. Graph taken from [210].

cavity, optics and Minus-K platform are protected by an approximately 3 m^3 organic ligneous enclosure[†] lined with acoustic damping foam to prevent acoustic noise.

6.2.3 Pressure *(technical noise)*

Equation 6.4 shows the dependence of the mode frequency on n, the refractive index of the space between the cavity mirrors. This is dependent on the pressure of air between the mirrors [211], and pressure fluctuations would therefore limit the cavity's stability.

To combat this, we operate the cavity under ultra-high vacuum (UHV) conditions. The aluminium vacuum chamber shown in Figure 6.7 is sealed using indium. Before sealing, all components were thoroughly cleaned and the whole assembly was placed under vacuum using a turbo-pump and baked for $\sim$ 5 days at up to 110 °C, avoiding indium's melting point of 156.60 °C [212].

Pumping is provided by a SAES NexTorr non-evaporable getter (NEG) and ion-pump. The NEG pumps active gasses (H_2, H_2O, N_2, O_2, etc.) and the ion pump removes inert gasses. After full assembly, baking and pumping, the cavity's working pressure is measured as 1×10^{-8} mbar, as judged by the ion-pump's current draw.

[†]plywood box

Assuming a pressure dependance of the refractive index of $\frac{dn}{dP} = 2.3 \times 10^{-11}\,\text{mbar}^{-1}$ [213], this gives a total fractional frequency shift of 2×10^{-19}, eliminating pressure as a relevant source of technical noise.

6.2.4 Electrical *(technical noise)*

Unlike the noise sources in §6.2.1 to §6.2.3, electrical noise does not move the cavity's resonance. Instead, it manifests itself as an error in the lock-point of the PDH servo used to centre the locking laser's frequency to the cavity mode.

The PDH technique was described in Section 6.1. There are two main avenues for noise to affect this process. Firstly, although the PDH method achieves low-sensitivity to $1/f$ frequency noise by operating mostly at the modulation frequency (ν_M), after the mixer the signal is DC and therefore vulnerable. This is mitigated by keeping the cables delivering the error signal to the integrator very short. All long-range signals[‡] exchanged between laboratories are in-loop, so any $1/f$ noise caused by cable variation, diode junction rectification, ground loops or other effects [187, 191, 192] are removed by the servo.

Secondly, the RF modulation frequency ν_M may appear on Photodiode B's signal from sources other than the light. This would contribute a phase change to the PDH signal which becomes a constant offset from the lock point. If this offset changes over time, the cavity's stability is degraded.

This could occur due to electrical pickup of the amplified RF signal driving the EOM. To avoid this, the EOM is enclosed in a die-cast box, acting as a Faraday shield, and is connected to the amplifier via triaxial shielded cable.

Alternatively, ν_M could appear as amplitude modulation of the probe light which would then be detected by the photodiode. This effect is known as *residual amplitude*

[‡]Remember that this cavity is in a different laboratory to the actuator, AOM A (see Figure 6.1).

modulation or RAM and is commonly caused by light entering the EOM with polarisation misaligned to the crystal axis. The resultant polarisation modulation becomes amplitude modulation at any polarising optics in the beam path. This effect is reduced by monitoring the ν_M component of Photodiode B's signal while the light is far off-resonance from the cavity. Any modulation present under these conditions is extraneous and undesirable, and is removed using a waveplate preceding the EOM. Also, our EOM is temperature controlled, reducing variation in any RAM still present.

Techniques for active compensation of RAM do exist (see [214, 215]) and the next version of the cavity will incorporate such a scheme. However we find that under the careful conditions described, our RAM does not noticeably degrade the cavity stability.

As well as this, it is desirable for the PDH signal to be steep in the locking region, reducing the coupling of electrical noise to frequency noise on the laser. The gradient of the PDH error signal is related to the loss of the cavity, parametrised by the cavity's *finesse*,

$$\mathcal{F} = \frac{2\pi}{-\ln R_1 R_2} \tag{6.5}$$

with R_1, R_2 the reflectivity of the mirrors. This quantity can be understood as the average number of reflections undergone by a photon before it is lost from the cavity. For our cavity, ring-down measurements of the TEM_{00} mode indicate a finesse of $\mathcal{F} = 472\,000$, shown in Figure 6.12.

6.2.5 Phase noise

High finesse cavities such as these are often located in isolated laboratories where they are less likely to be disturbed. This separation means that light must be delivered to these cavities via fibre, however any temperature and vibrational fluctuations at the fibre cause a change to the optical path length through it. Although not technically

related to the cavity itself, phase noise in the fibre would therefore be a dominant noise-source if it were not compensated.

Fortunately, this effect can be almost completely removed. This technique works by using retro-reflected light to detect phase noise before using a frequency-modulated AOM to cancel it out. For much more detail on this technique, see Section 2.5.

6.2.6 Thermal *(fundamental noise)*

Finally, once other sources of cavity noise are suppressed, the remaining contribution comes from Brownian motion of the cavity mirror surfaces themselves. The Brownian thermal noise limit is dominated by the contribution from the mirrors, given in [216–218] by

$$\sigma_{\text{therm}} = \sqrt{\ln 2 \frac{8 k_B T}{\pi^{3/2}} \frac{1-\sigma_P^2}{E \mathrm{w}_0 L^2} \left(\phi_{\text{sub}} + \phi_{\text{coat}} \frac{2}{\sqrt{\pi}} \frac{1-2\sigma_P}{1-\sigma_P} \frac{t}{\mathrm{w}_0} \right)} \quad , \tag{6.6}$$

where σ_P, E and ϕ_{sub} are Poisson's ratio, Young's modulus and the mechanical loss for the mirror substrate (fused silica), w_0 is the laser beam's $1/e$ radius at the mirrors, T is the temperature of the mirrors, k_B is Boltzmann's constant and L is the cavity length. ϕ_{coat} and t denote the mechanical loss and thickness of the thin-film reflective coating.

Importantly, this quantity is proportional to $1/L$, and so σ_{therm} can be reduced by increasing the length of your cavity. It is for this reason that $L = 28\,\text{cm}$ in our design. Also, the area of the mirrors probed by the beam enters into Equation 6.6 through w_0; for this reason mirrors with a large radius of curvature $R_c = 500\,\text{mm}$ were used.

Using the values of these parameters reported in Ref. [218], we find a predicted fractional thermal floor of 8.8e-17.

6.3 Temperature stability and the ULE glass zero-crossing

The distance between the mirrors L is dependent on the temperature of the cavity spacer and its coefficient of thermal expansion (CTE) α_T, which couples directly to the locked mode's frequency:

$$\begin{aligned} \frac{\delta\nu_{\mathrm{FSR}}}{\nu_0} &= \frac{\lambda}{2n}\left(\frac{1}{L+\delta L} - \frac{1}{L}\right) \\ &\approx -\frac{\lambda}{2nL^2}\delta L = -\frac{\lambda\,\alpha_T}{2nL}\delta T \end{aligned} \tag{6.7}$$

where ν_0 is the locked mode's frequency, $\lambda = c/\nu_0$ and δT is a small temperature change. For this reason, ultra-low expansivity (ULE) glass is used to construct the cavity spacer. ULE has an extremely low CTE, specified for a maximum value of $\alpha_T = 10 \times 10^{-9}\,\mathrm{K}^{-1}$ [219]. Better, its CTE is temperature dependent, and undergoes a zero-crossing at close to room temperature.[§] By operating at this zero-crossing temperature, extremely low sensitivity to thermal changes can be achieved.

6.3.1 Finding the zero-crossing

In order to find this CTE zero-crossing, we make use of its change of sign. We lock our 934 nm light to the cavity resonance using the procedure outlined in Section 6.1. Then, we sweep the temperature of the cavity over a large range and monitor the frequency corrections that the servo applies to AOM B in Figure 6.1, allowing the frequency difference between Lab A's and Lab B's cavities' resonances to be deduced. This difference, shown in Figure 6.4, reveals Lab B's cavity's thermal response according to Equation 6.7, where α_T is now temperature dependent (Lab A's cavity's non-linear drift is on the order of $30\,\mathrm{mHz\,s^{-1}}$ and so can be neglected here). The frequency corrections therefore exhibit a stationary point at the CTE zero-crossing.

[§]The exact temperature of a ULE zero-crossing can usually only be predicted to within $\sim 10\,\mathrm{K}$.

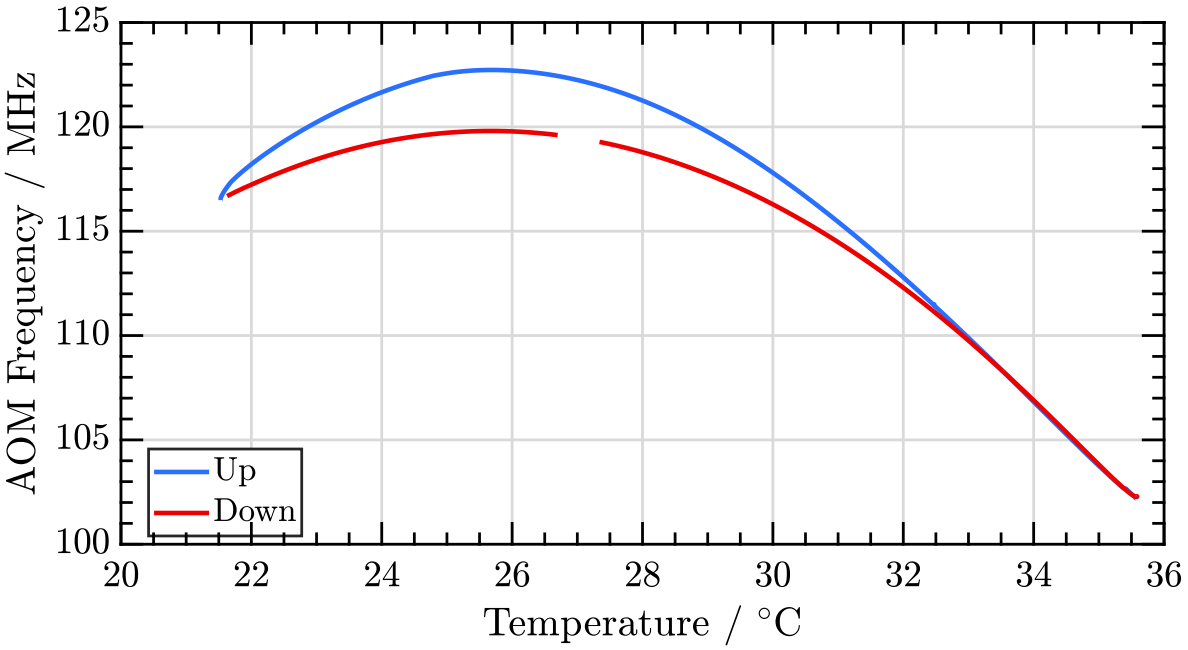

FIGURE 6.4: Temperature of Lab B's cavity spacer versus frequency difference between Lab B and Lab A cavities, recorded for both upwards and downwards sweeps. The stationary point at 25.5 °C occurs when the spacer is at its CTE zero-crossing. The upwards (downwards) temperature sweep was performed over 91 h (146 h). The difference in frequency between the two peaks is due to changed AOM offsets elsewhere in the system.

Since the cavity contains thermal shielding (see §6.3.3 and Figures 6.8 and 6.9), the temperature of the spacer lags significantly behind the monitored temperature of the outer-shield. In order to recover the stationary point it is therefore necessary to adjust the temperature of the cavity iteratively, monitoring the frequency correction on AOM B, until the extremum of the frequency difference observed previously is recovered.

6.3.2 Temperature control

Once the CTE zero-crossing has been located, the cavity must be held at this temperature. To do this, active feedback is applied via a Proportional Integral Differential (PID)-style digital servo. Since any drift in the locking point of the temperature servo would produce frequency instability, it was necessary to develop a high-precision

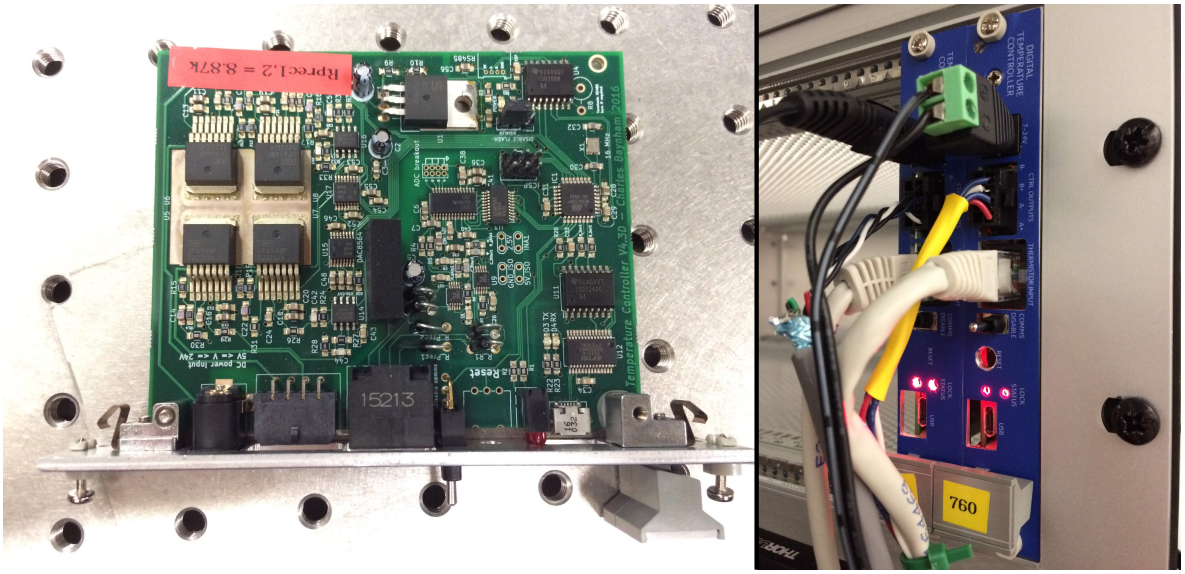

Figure 6.5: A high-precision temperature controller with heightened immunity to noise and external temperature variations, developed for temperature control of high-finesse optical cavities. For more information on this design, see Appendix C.

temperature controller with heightened immunity to noise and external temperature variations. This device implements a temperature transfer function given by

$$G(s) = -K\left(1 + \frac{1}{sT_I} + \frac{sT_D}{1 + \frac{sT_D}{N}}\right) \tag{6.8}$$

and is shown in Figure 6.5. The coefficients K, T_I, T_D and N are tuning parameters that are chosen to match the system under control. The modifications to the ideal "academic" PID transfer function implement a software low-pass filter, reducing sensitivity to measurement noise. For more details on the design and construction of this device, see Appendix C.

6.3.3 Passive shielding

In order to decrease the temperature variation experienced by the cavity further, a thermal shield was installed inside the vacuum chamber as shown in Figure 6.7. This shield, made of 2 cm thick aluminium, almost completely blocks line-of-sight between the vacuum chamber and the cavity spacer. Also, all interfaces between components

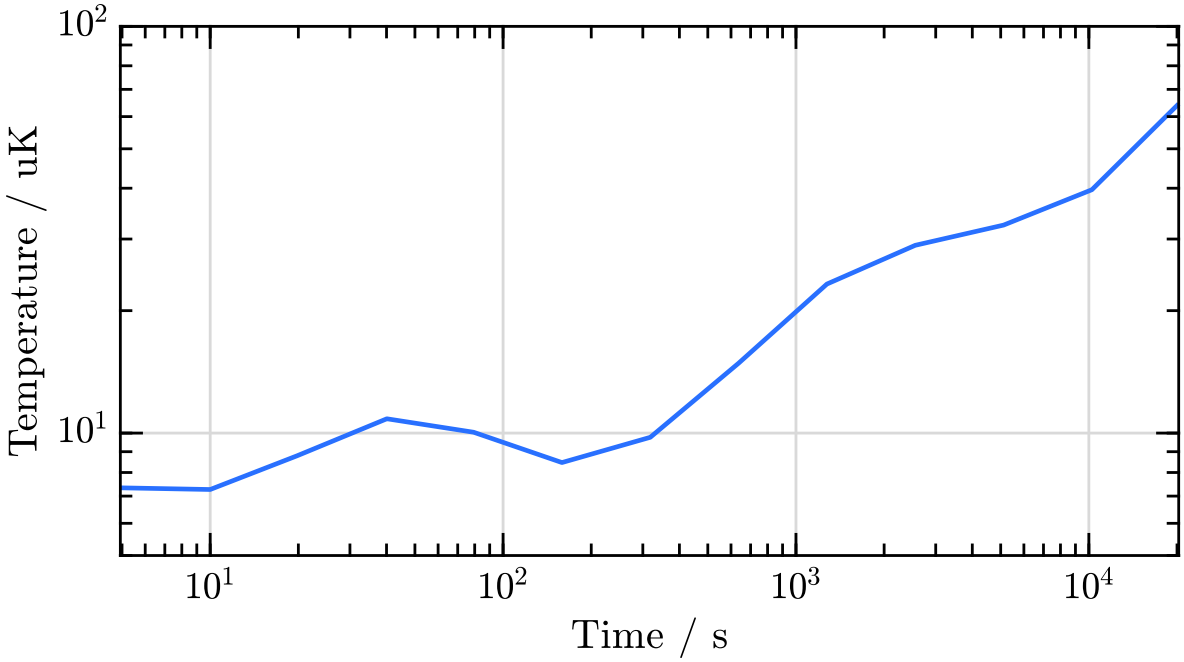

FIGURE 6.6: Allan deviation of the temperature stability of the cavity's vacuum chamber, as judged by an OOL thermistor monitored by a Keithley DVM.

(chamber–shield, shield–support and support–spacer) are mediated by spherical glass supports. These minimize thermal contact and therefore conductive heat transfer between the layers.

Since the chamber is evacuated to $< 1 \times 10^{-8}$ mbar and the glass supports prevent most direct thermal conduction, the dominant mechanism for heat transfer is radiative. The following simple model illustrates the effect of the shielding:

$$\begin{aligned} C_v \, d\dot{T}_v &= 2\pi\sigma_{SB} \, (r_v(T_{ext}^4 - T_v^4) - r_s(T_v^4 - T_s^4)) \, , \\ C_s \, d\dot{T}_s &= 2\pi\sigma_{SB} \, (r_s(T_v^4 - T_s^4) - r_c(T_c^4 - T_s^4)) \quad , \\ C_c \, d\dot{T}_c &= 2\pi\sigma_{SB} \, r_c(T_c^4 - T_s^4) \end{aligned} \tag{6.9}$$

where σ_{SB} is the Stefan-Boltzmann constant; C_i, r_i and T_i are the heat capacity per meter, external radius and temperature of the i^{th} cavity component and $i = v, s, c$ refers to the vacuum chamber, heat-shield and cavity respectively. T_{ext} is the external temperature, assumed to be an infinite heat-sink.

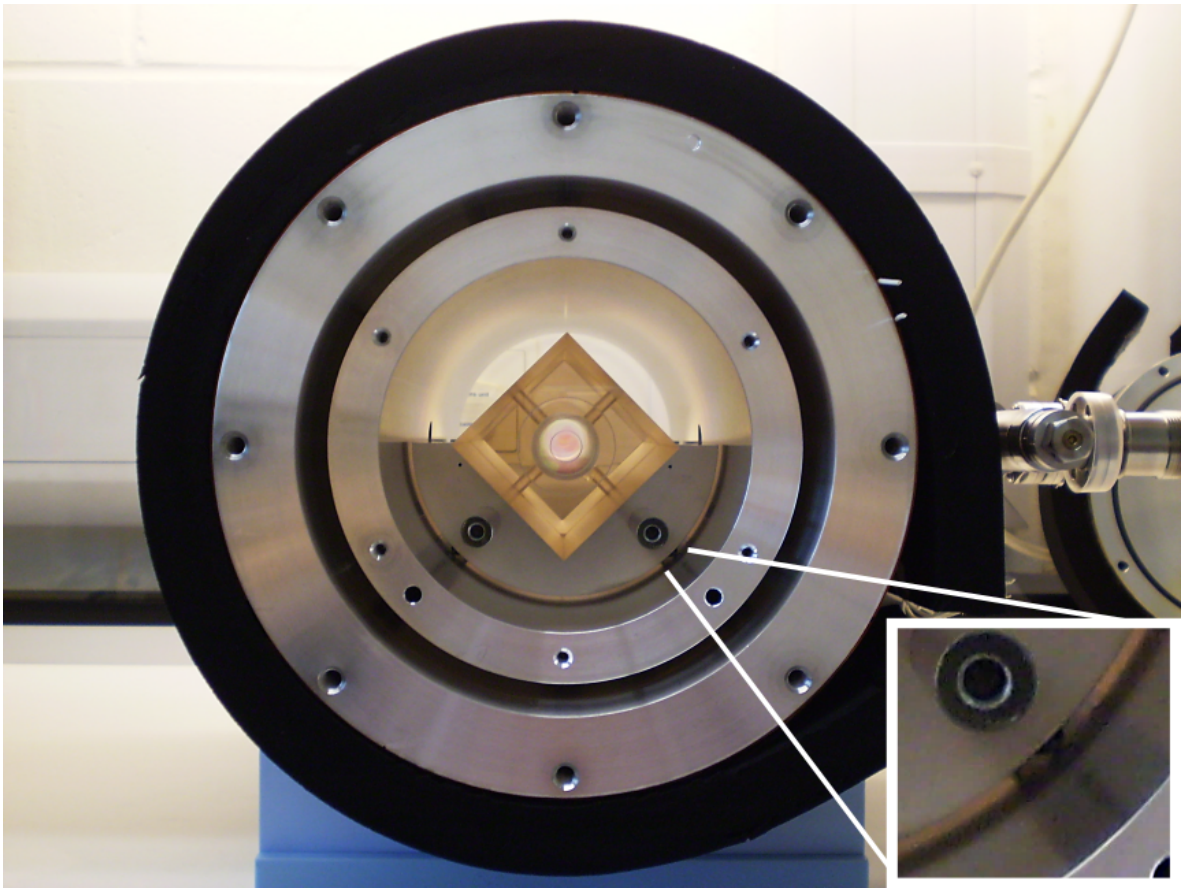

Figure 6.7: Photograph of the cavity and vacuum chamber in Lab B before baking and pumping. Note the spherical glass supports separating the vacuum chamber and the heat shield, the heat shield and the spacer support, and the support and the spacer itself.

This coupled set of ordinary differential equations (ODEs) was numerically solved, giving the step response shown in Figure 6.8 and the transfer function shown in Figure 6.9. The cavity's coefficient of 50 % response-time is 8.1 h and the impact of temperature oscillations at frequencies above 20 mHz is attenuated by more than 20 dB.

This model assumes that all surfaces are perfect black body emitters, a conservative assumption given that the reflectivity of even unpolished aluminium is typically high. However it neglects the effect of the holes cut into the heat shield and windows on the vacuum chamber for optical access.

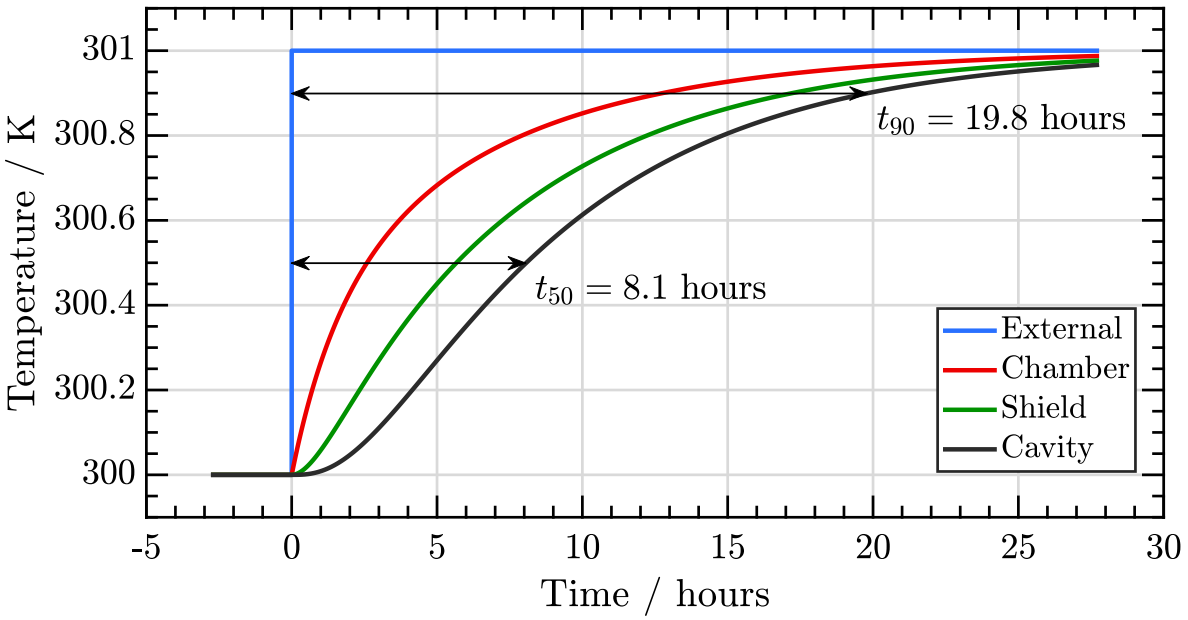

FIGURE 6.8: Modelled response of the cavity layers to a step change in external temperature, giving a 50 % response time of 8.1 h.

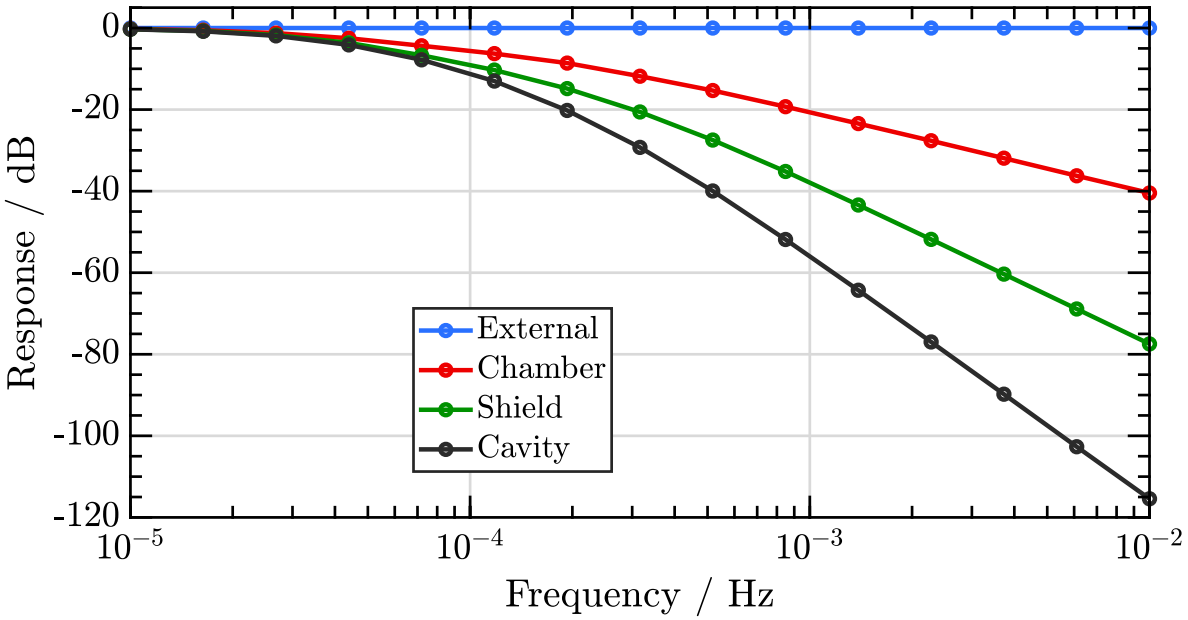

FIGURE 6.9: Modelled transfer function of the cavity layers for temperature noise in the external environment.

6.4 A "universal synthesizer"

Femtosecond optical frequency combs are a vital part of an atomic clock; the light from a clock may be stable and accurate but this is no use without a method to measure its frequency. Section 2.6 describes the principles and operation of the frequency comb used in this role. However, the existence of this high-precision machine at the hub of an NMI's optical clock operation presents another opportunity.

The rest of this chapter has dealt with the production of high stability light, for use with the $^{171}Yb^{+}$ clock. But it would be very convenient if that local oscillator could be used for multiple clocks to avoid duplication of work and allow for centralised roll-out of future upgrades. This was the motivation for the "universal synthesiser," so called for its ability to transfer stability from a single oscillator to frequencies in both the optical and microwave regimes.

Stability transfer is made possible due to the *transfer oscillator* scheme [220, 221] which allows a *virtual beat* between two diverse optical frequencies to be produced free from noise introduced by the comb. As described in Section 2.6, the beat note for laser i detected by the comb (f_i) is composed of the comb's CEO frequency f_0 and repetition rate f_R according to

$$\nu_i = f_0 + n_i f_R + f_i \tag{6.10}$$

where ν_i is the laser's optical frequency and n_i is the mode number of the comb's closest mode. Typically for precision metrology both f_0 and f_R are actively stabilised, however noise in these quantities is still present on the beat frequencies. By combining two optical beat frequencies together as shown in Figure 6.10, it is possible to arrange for the noise contribution of both quantities to be cancelled, resulting in a comb-noise-

free virtual beat between the two lasers, Δf_{12}:

$$\begin{aligned}\Delta f_{12} &= (f_1 + f_0) - \frac{n_1}{n_2}(f_2 + f_0) \\ &= (\nu_1 - n_1 f_R) - \frac{n_1}{n_2}(\nu_2 - n_2 f_R) \\ &= \nu_1 - \frac{n_1}{n_2}\nu_2 \quad . \end{aligned} \tag{6.11}$$

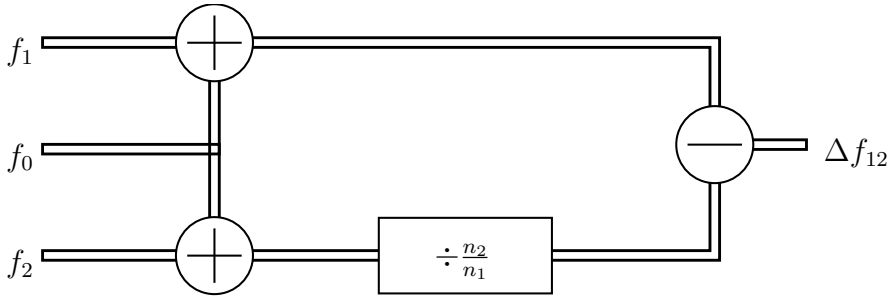

FIGURE 6.10: Simplified block diagram of the transfer oscillator scheme.[¶] f_0 is obtained by comparing a doubled tooth with its high-frequency pair in an octave-spanning comb [132].

By implementing a phase lock of this synthesised beat note Δf_{12} to an arbitrary reference frequency of our choice (f_{ref} in Figure 6.1), the frequency difference between the two lasers is fixed and the best stability is transferred to the slave laser.

Additionally, operation of a frequency comb at a diverse range of optical frequencies typically requires separate branches, each with their own distinct amplifiers (erbium-doped fibre amplifiers (EDFAs) in the NPL's case) and, if required, SHG doublers. The separation of these branches introduces non-common-mode noise processes which afflict inter-branch comparisons and are not removed by the transfer oscillator scheme. However, work done recently at the NPL [222] on a free space heterodyne beat detection unit has demonstrated that inter branch comparisons are possible with little added noise,

[¶]The division in this scheme is done by using a DDS clocked by the input signal with a tunable division ratio. To achieve this without hitting the Nyquist limit requires that $n_1 > 2n_2$. We therefore multiply n_1 by 8, and add another divider to the f_1 path, obtaining a transfer beat that is 8 times lower in frequency than the one shown in Figure 6.10.

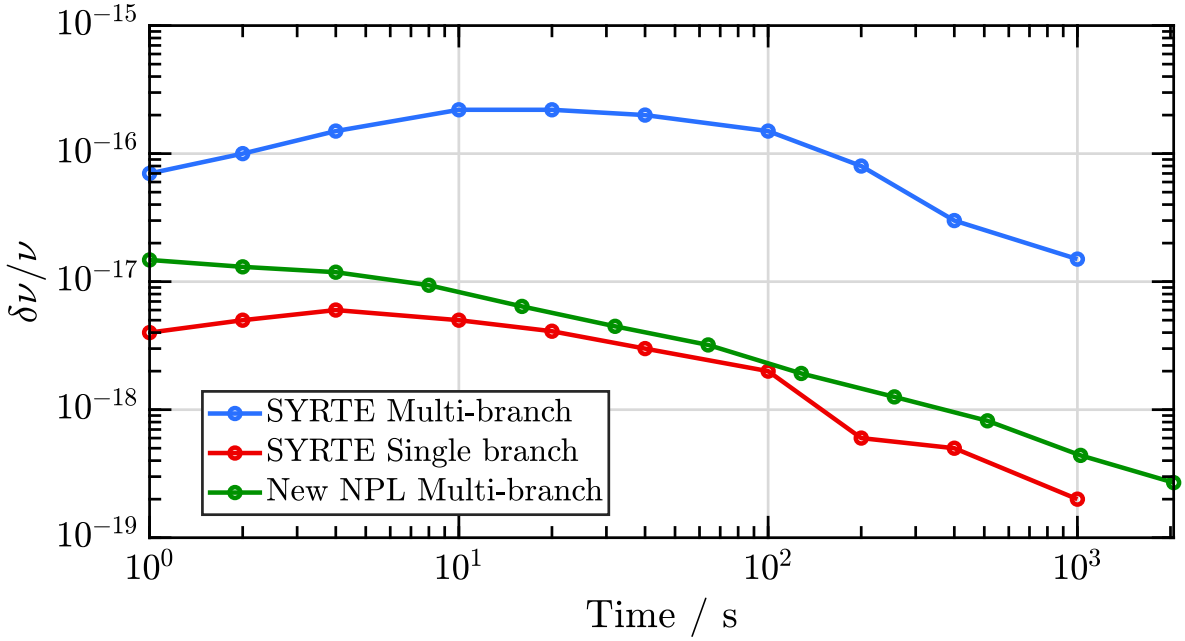

Figure 6.11: Comparison of typical multi-branch comb noise with new, lower noise resulting from recent changes to the NPL beat detection units (BDUs) [225]. Note that the fractional instability for the green line (representing the improved multi-branch performance) starts at 3×10^{-17} at $\tau = 1\,\mathrm{s}$ and averages down, making the transfer noise better then the best existing lasers at all time scales. SYRTE data taken from [224].

permitting comparisons at the $3 \times 10^{-17}\,(\tau/1\,\mathrm{s})^{-1/2}$ level between branches, as shown in Figure 6.11.

6.5 Measurements

Figures 6.12 and 6.13 show two different ways of measuring the cavity finesse, related to its Q-factor by $Q = \mathcal{F}\nu_0/\nu_{\mathrm{FSR}}$. A high finesse makes for a narrow line, which increases the gradient of the PDH error signal, reducing technical noise.

Typically when evaluating the performance of a high stability oscillator, two such devices are constructed and the stability of the beat between the two references is assessed [226–229]. In our project however only a single oscillator was built. We therefore use it to interrogate the E3 clock transition and extend the length of the clock

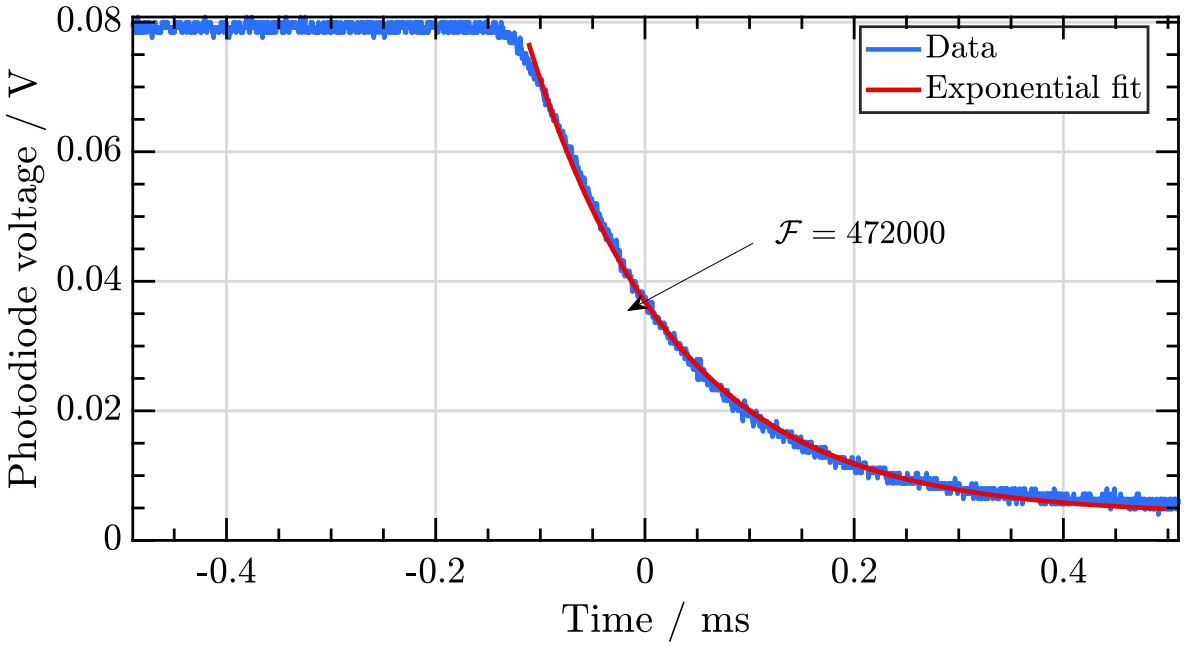

FIGURE 6.12: Ringdown measurement of cavity finesse. A photodiode measuring the transmission through the cavity for on-resonance light is monitored after the incident light is sharply extinguished using AOM B. The exponential drop in stored energy within the cavity is due to leakage through the cavity mirrors; its time-constant is proportional to the cavity finesse, giving $\mathcal{F} = 472\,000$.

pulse looking for decoherence.[‖]

Figure 6.14 shows the result of this, using probe times of $\tau = 500\,\text{ms}$. The E3 transition's linewidth is measured as 1.56 Hz. The Fourier broadening of a 500 ms pulse is 1.60 Hz, so no additional broadening due to laser noise is visible at this level. Hardware limitations prevented us from using probe times of greater than this, but a future hardware/software upgrade will resolve this problem.

[‖]Another method of evaluating the stability of a resonator is the "three cornered hat" technique [230]. This method uses simultaneous measurements of an oscillator compared with at least two others to determine the noise contribution from any individual device. We attempted such a measurement using our local ULE cavity and another, longer cavity but the far higher instability of our local ULE cavity (found to have $\sigma/\nu \sim 10^{-15}$) dominated the measurement.

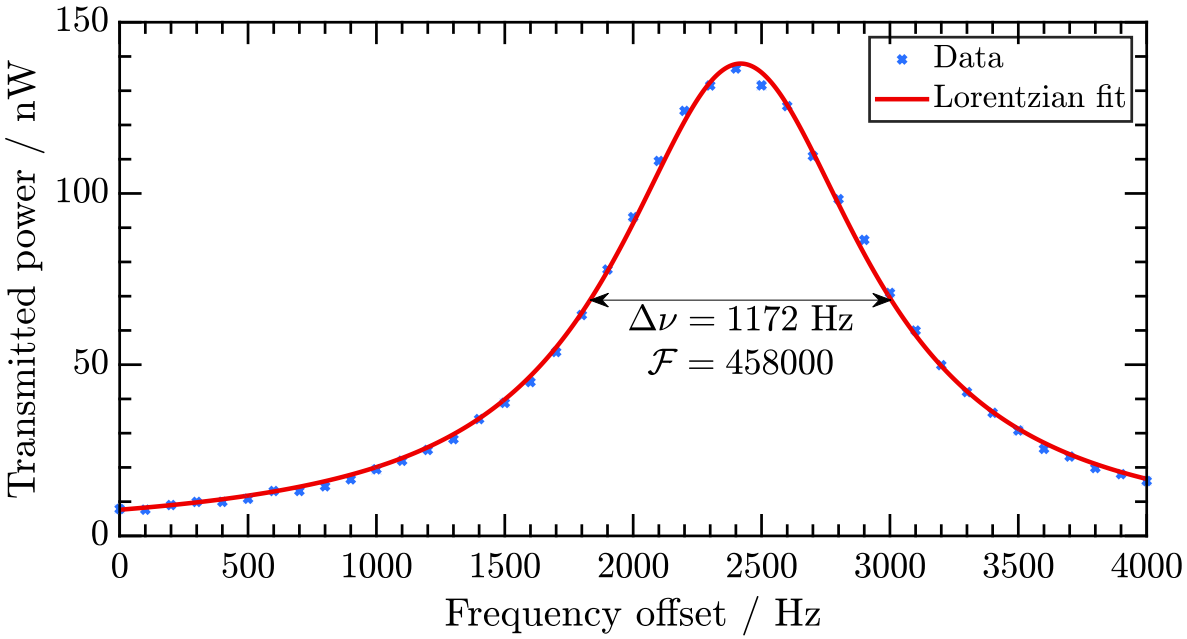

Figure 6.13: Lineshape of a cavity resonance, determined by measuring the transmitted light through the cavity with a photodiode. A Lorentzian profile fitted to this implies a finesse of $\mathcal{F} = 458\,000$, close to the value determined in Figure 6.12.

6.6 Conclusion

In conclusion, a 28 cm ULE-based optical cavity has been constructed and characterised. This cavity is used to provide stability not just to the $^{171}Yb^{+}$ clock but also to other clocks throughout the NPL with stability transferred via a frequency comb with no loss of fidelity. Use of this cavity has so far allowed us to reach stabilities of $1.9 \times 10^{-15}(\tau/1\,\mathrm{s})^{-1/2}$, shown in Figure 6.15.

The fundamental limit to cavity performance is thermal noise: it is for this reason that we chose to operate a long cavity. Other approaches to reducing this fundamental limit of optical cavities include operating at low temperatures [226–229] or using different mirror materials [231, 232]. Work is also under way to circumvent this limitation by using another system entirely: systems that exploit superradiance [233, 234]; approaches that burn spectral holes into substrates [235, 236]; that aim to cancel the inhomogeneities typical of thermal atomic beam spectroscopy [237]; or lattice clocks

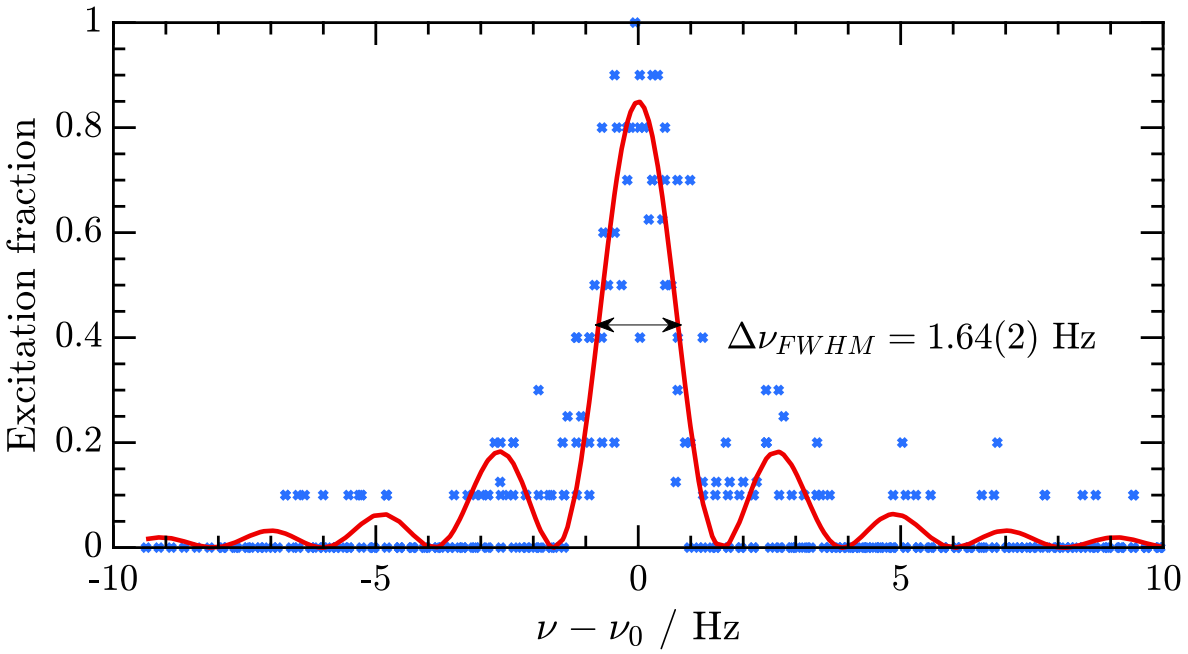

FIGURE 6.14: Scan over E3 transition, showing a linewidth of $\nu_{\mathrm{FWHM}} = 1.64(2)$ Hz for a Rabi probe of $\tau = 500$ ms. The Fourier limit for a 500 ms pulse is 1.60 Hz (§1.1.4) indicating that, at this time-scale, the laser is Fourier-limited. The fitted linewidth was produced by fitting a Rabi profile to a linear drift corrected, combined series of 5 scans taken over a 40 min period. The cavity drift over this period was $-1.57\,\mathrm{mHz\,s^{-1}}$.

that aim to achieve duty cycles of ∼100 %, removing the Dick effect entirely.

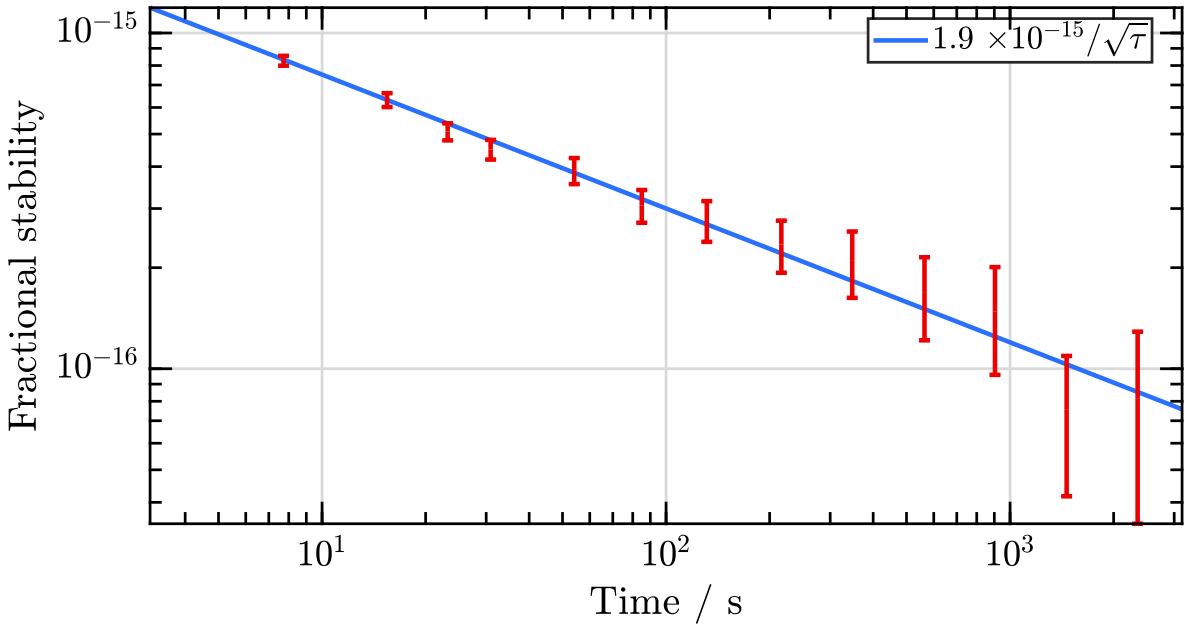

Figure 6.15: Allan deviation of the frequency difference between two independent "dual servo" locks. The locks were operated with probe-times of $\tau = 400\,\mathrm{ms}$. A fit to the profile gives the stability as $1.9 \times 10^{-15}\ (\tau/1\,\mathrm{s})^{-1/2}$, compared to the QPN limit of $1.5 \times 10^{-15}\ (\tau/1\,\mathrm{s})^{-1/2}$.

International clock comparisons 7

> A man with a watch knows what time it is. A man with two watches is never sure.
>
> — *Segal's Law*

Since the second is defined by the hyperfine transition in Cs, all "absolute" measurements of frequency must make reference to a Cs-based clock. This, however, poses a problem for next-generation atomic clocks: what to do if your clock has lower uncertainty than the caesium fountain? This scenario has already occurred as Figure 1.4 shows. In this case, the accuracy with which the absolute frequency of the (optical) clock transition can be determined is actually limited by the systematic uncertainty in the realisation of the SI second.

In fact, all "absolute" measurements are really ratio measurements, with one of the pair being a Primary Standard whose frequency is defined as a constant. The answer therefore is to replace the Cs fountain with another system with a comparable systematic floor to the optical clock, i.e. another optical clock. The number thus produced will be a ratio of the two clock-transitions' frequencies and its accuracy will be limited

by the uncertainty of the less accurate clock or by the method used to compare them. The improved potential accuracy of frequency ratios that do not involve ceasium is the argument for a future redefinition of the SI second based on an optical frequency standard.

A critical part of building an atomic clock is having a good understanding of the systematic limitations of your device: its uncertainty budget (see Chapter 5 for a detailed summary of these effects in the $^{171}Yb^{+}$ system). However, the only way to demonstrate the truth of your uncertainty budget, to protect yourself from "unknown unknowns," is to make a measurement at the level of your systematic floor. Before optical atomic clocks can take over the role of the definition of the SI second, it is vital not just that their evaulated performance exceeds that of the caesium fountain but that this has been thoroughly demonstrated.

However, work on good clock comparisons has uses beyond just validating the performance of optical clocks. As the primary standards of National Measurement Institutes (NMIs) are improved, so too must the methods of distributing this performance to remote locations improve [238, 239]. Beyond this, sensitive tests of the agreement of distributed frequency standards could reveal deviation from the time dilation predicted by special relativity [1, 92], be used for relativistic geodesy [240] or searches for topological dark matter [3].

This chapter will present a method of performing comparisons between clocks in different locations using a broadband microwave link routed via a satellite in Section 7.1. It will also present in Section 7.2 a new absolute measurement of the E3 transition in $^{171}Yb^{+}$ done by capitalising on the existing clock comparison network used for the production of TAI: a vital step if the second is to be redefined [8].

7.1 Satellite links

In June 2015, a broadband (1.7 MHz) segment of bandwidth on a geostationary satellite was rented for a period of 1+3 weeks, with the aim of performing clock comparisons between various European NMIs under the ITOC project. The comparison was carried out via the Two-Way Satellite Time and Frequency Transfer (TWSTFT) method, outlined below, between clocks based at the National Physical Laboratory (NPL), London; Istituto Nazionale di Ricerca Metrologica (INRIM), Italy; Observatoire de Paris (OP), France; and Physikalisch-Technische Bundesanstalt (PTB), Germany.

7.1.1 Overview of method

7.1.1.1 TWSTFT method

Two-Way Satellite Time and Frequency Transfer (TWSTFT) works by sending timing data in two directions at once, so that the uncertain timing delay caused by the exact path, satellite and electronics can be cancelled [239, 241]. Pulses are sent from NMI_i to NMI_j and vice versa every second, as timed by the sending NMI's frequency standard.

Each NMI records the delay between sending its pulse and receiving the partner NMI's pulse. With time-delays defined as in Figure 7.1(b), this time delay τ can be written:

$$\begin{aligned} \tau_i &= t_j^{\mathrm{UTC}} + t_{j\to i}^{\mathrm{SAT}} - t_i^{\mathrm{UTC}} \\ \tau_j &= t_i^{\mathrm{UTC}} + t_{i\to j}^{\mathrm{SAT}} - t_j^{\mathrm{UTC}} \end{aligned} \tag{7.1}$$

where t_i^{UTC} is the time at which the pulse at NMI_i was sent as it would be measured by a perfect reference clock and $t_{i\to j}^{\mathrm{SAT}}$ is the time required for a pulse to travel from NMI_i to NMI_j. The difference between the two time-scales can be recovered as:

$$\begin{aligned} x_{ij}^{\mathrm{M}} \overset{\mathrm{def}}{=} t_j^{\mathrm{UTC}} - t_i^{\mathrm{UTC}} &= \frac{1}{2}(\tau_i - \tau_j + t_{i\to j}^{\mathrm{SAT}} - t_{j\to i}^{\mathrm{SAT}}) \\ &\approx \frac{1}{2}(\tau_i - \tau_j) \end{aligned} \tag{7.2}$$

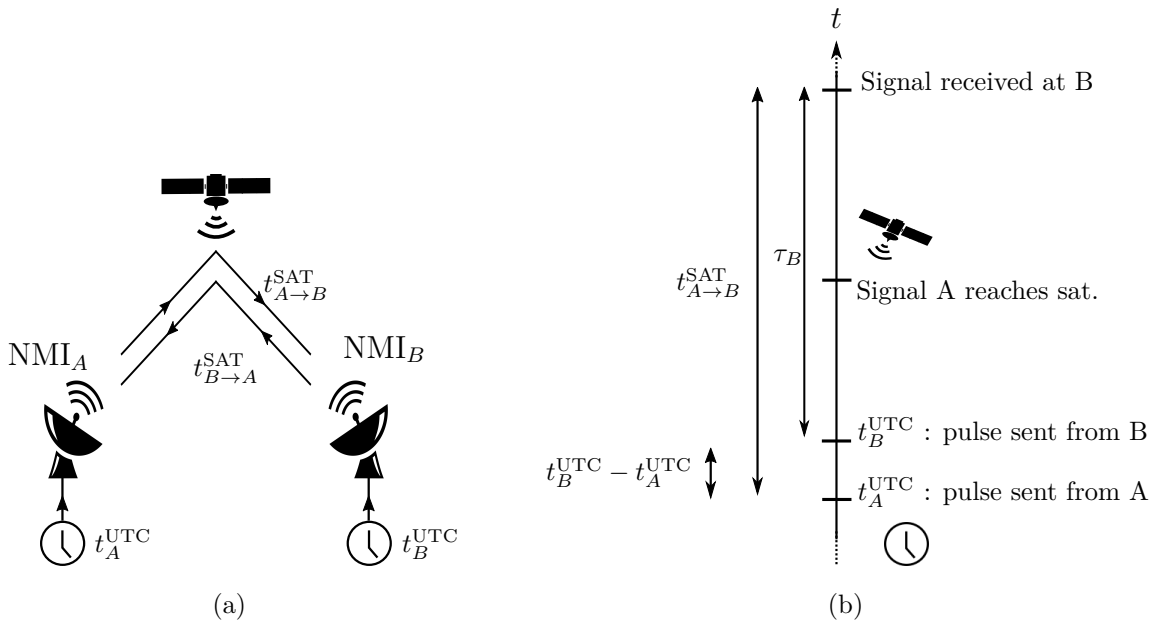

Figure 7.1: Time-scale comparison via TWSTFT method. *(left)* Path taken by pulses traveling between NMI$_i$ and NMI$_j$.
(right) Timeline of events relevant for the measurement recorded at NMI$_j$: τ_j.

Since the pulses reach the satellite almost simultaneously, the path that they follow is the same: this is the benefit of a "two-way" comparison.* This allows us to set $t^{\mathrm{SAT}}_{i\to j} - t^{\mathrm{SAT}}_{j\to i}$, canceling effects due to differences in path length or Doppler effects caused by residual motion of the satellite in the Earth's frame.† For a more detailed discussion of this process, see references [239, 241].

The true frequency of the maser generating the 1 pps timing signal at NMI$_i$ can be written

$$f_i^{\mathrm{M}}\left(t + \frac{\tau_0}{2}\right) = \frac{\tau_0}{t_i^{\mathrm{UTC}}(t+\tau_0) - t_i^{\mathrm{UTC}}(t)} f_0^{\mathrm{M}} \tag{7.3}$$

where $\tau_0 = 1\,\mathrm{s}$ is the nominal sample period and $f_0^{\mathrm{M}} = 10\,\mathrm{MHz}$ is the nominal maser

*Pulses arriving at slightly different times cause non-reciprocity of the signal path length particularly if the satellite is in motion. In principle this could be prevented by adding offsets to the base station emission times such that the pulses arrive simultaneously. However, in practice, this is rarely done since the effect is usually negligible [242, 241, §3.3].

†A slight adjustment to this approximation is made to account for the *Sagnac effect*, caused by the rotation of the Earth. See [239] for more details.

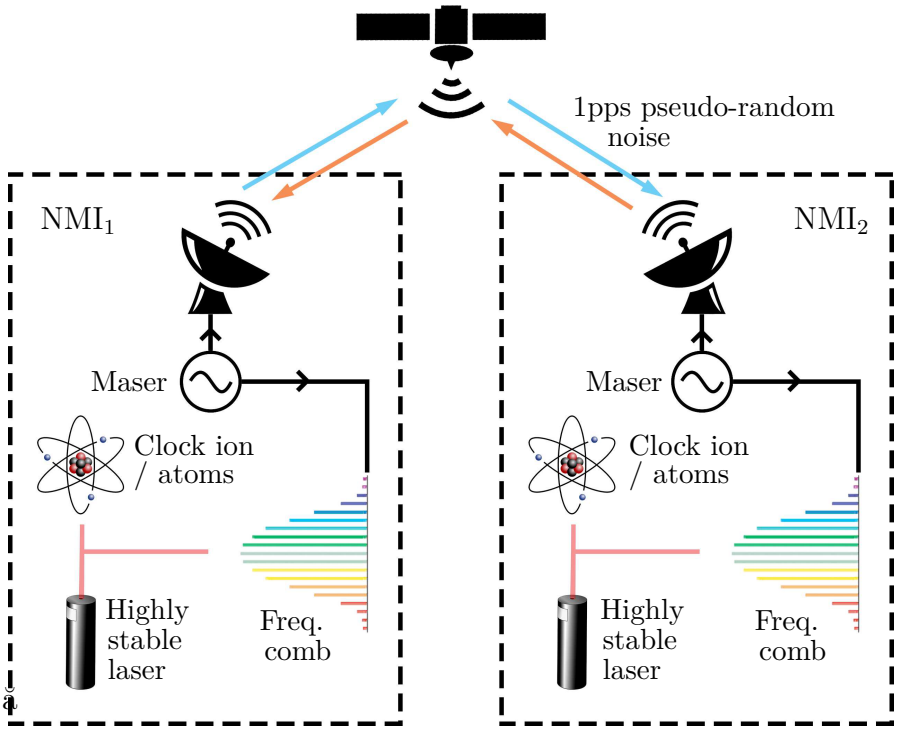

FIGURE 7.2: Overview of optical clock comparison via TWSTFT connection

frequency. This quantity cannot be actually be obtained from the data gathered, but the fractional difference between maser frequencies can:

$$\begin{aligned}\frac{f_i^{\mathrm{M}}(t+\frac{\tau_0}{2}) - f_j^{\mathrm{M}}(t+\frac{\tau_0}{2})}{f_0^{\mathrm{M}}} &\approx \frac{1}{\tau_0}\Big[- t_i^{\mathrm{UTC}}(t+\tau_0) + t_i^{\mathrm{UTC}}(t) \\ &\qquad + t_j^{\mathrm{UTC}}(t+\tau_0) - t_j^{\mathrm{UTC}}(t)\Big] \\ &= \frac{x_{ij}^{\mathrm{M}}(t+\tau_0) - x_{ij}^{\mathrm{M}}(t)}{\tau_0} \\ &\overset{\text{def}}{=} y_{ij}^{\mathrm{M}}(t+\frac{\tau_0}{2}) \quad . \end{aligned} \tag{7.4}$$

7.1.1.2 Linking the frequencies in the chain

The process described in §7.1.1.1 was used to compare hydrogen masers at the four NMIs. The extremely high reliability of hydrogen masers coupled with their fractional frequency stabilities of 2×10^{-15} at 1000 s [23] makes them excellent local oscillators.

Figure 7.2 shows the effective setup for the ITOC clock comparison campaign. All

NMIs exchange 1 pulse-per-second data produced by their local maser oscillators, allowing comparison between remote masers as previously described. Locally, each clock laser is measured using an optical comb (see Section 2.6) and compared to the 10 MHz signal derived from the NMI's H-maser, producing a ratio of their frequencies. By combining the two optical–maser ratios with the local maser–remote maser ratio, the contribution of the masers on each end of the link can be canceled out.

The goal of this exercise is to determine the ratio $R_{ij} \stackrel{\text{def}}{=} f_i/f_j$ for each clock-pair i, j. When considering the frequency ratio between clocks of different species, the expected frequency difference is many terahertz, whereas the target uncertainties are sub-hertz. To avoid the necessity for high numerical precision, we therefore record data for each clock in the format

$$y_i(t) \stackrel{\text{def}}{=} \frac{r_i(t)}{r_{0,i}} - 1 \tag{7.5}$$

where $r_{0,i}$ is the expected frequency ratio between clock i (f_i) and the local hydrogen maser f_i^{M}, chosen according to the International Bureau of Weights and Measures (BIPM) recommended values. Appendix E shows how R_{ij} can be recovered as

$$R_{ij} = \frac{r_{0,i}}{r_{0,j}} \times (1 + y_i - y_j + y_{ij}^{\text{M}}) \tag{7.6}$$

with y_{ij}^{M} defined as in Equation 7.4. The determination of this quantity and its uncertainty for each optical clock pairing is the goal of the comparison campaign and the subject of this section.

7.1.2 Data analysis

Over the one-month campaign period, each clock-clock pair produced three datasets (one for the link between NMIs and two for the local maser to optical clock ratio). Since some NMIs had more than one clock operating, the final tally was 12 TWSTFT datasets (two for each NMI pairing) and 6 clock datasets, all of ∼3 weeks in length. The optical

atomic clocks involved in the campaign demonstrated exceptional robustness, with uptimes for many clocks over 75 %. Nevertheless, the experimental nature of both the optical clocks and the broadband link meant that the data had a considerable number of gaps.

These gaps meant that the naïve approach of simply discarding all timestamps where one of the three linked datasets was unavailable would have resulted in discarding a large proportion of the total data. An alternative method of analysis that deals with these gaps was therefore developed by E. Benkler and F. Riedel [243–245] and will be described briefly in §7.1.2.1. The method is still being refined, and will differ substantially from that presented here. However both versions share an important feature: namely that evaluating their uncertainty is non-trivial. Since in the field of metrology the uncertainty of a measurement is of at least equal importance to its result, I spent some time developing a Monte Carlo method to evaluate the analysis scheme, presented in §7.1.2.2.

7.1.2.1 Method

The data analysis method developed aims to address four goals:

1. Elimination of H-maser fluctuation
2. Suppression of white phase noise and diurnal disturbances of the link
3. Handling of gaps in the data
4. Minimization of discarded data

To reduce sensitivity to high frequency noise, frequency measurements are commonly averaged over a set period τ_w.[‡] These weighting profiles are often referred to as

[‡]In the operation of a zero-crossing frequency counter, gating at some timescale is of course unavoidable. Data in the ITOC campaign was taken with 1 s hardware gate times, however this section refers to post-processed weightings over much larger timescales.

Π, Λ or Ω schemes, as shown in Figure 7.3.

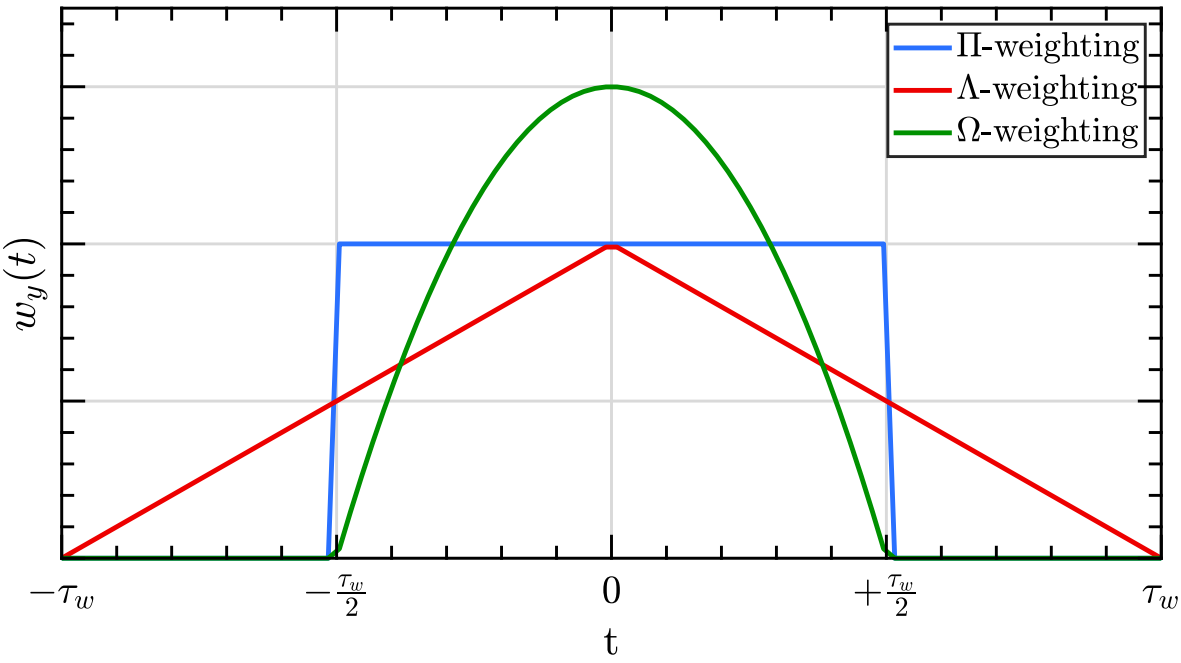

Figure 7.3: Comparison of weightings for Π, Λ and Ω schemes for a period τ_w, displayed in frequency space. The names of the weighting profiles refer to their shapes in frequency space, although for the phase data used in this chapter we will convert this frequency weightings to phase weightings and perform the averaging on phase data. In all cases, $\int_{-\infty}^{\infty} w(t)\ dt = 1$. The Ω profile is derived from the effective frequency weightings of a linear regression to phase over $t = -\frac{\tau_w}{2} \rightarrow \frac{\tau_w}{2}$. Note that Λ weighting actually uses data from a period $2\tau_w$ to produce a value for a single period τ_w, resulting in correlation between successive time periods.

In this campaign, deriving the frequency difference of the H masers at the two NMIs involved calculating the difference of the time differences x_{ij}^{M}, as shown in Equation 7.4 (the *double difference*). These x_{ij}^{M} are therefore phase data, since an instantaneous frequency difference at a point in time will affect all future values of x_{ij}^{M}. The optical clock data (y_i and y_j) however were recorded as frequency measurements, according to Equation 7.5.

Equation 7.6 requires us to convert our phase data to frequency data, but it is better not to do this on a point-to-point basis—since the satellite data contains gaps, converting to frequency would sacrifice the information that phase measurements contain about

what was happening in those gaps: one of the key benefits of phase measurements. It is therefore necessary to calculate the appropriate weighting functions to apply to the optical clock frequency data and the maser link phase data separately, before the link data is finally converted to frequency for each daily averaging period τ_{w} and the total frequency difference is calculated.

In the case of white phase noise, the expected noise profile of the satellite link, the optimum averaging method can be shown to be Ω-weighting, with Λ-weighting a close second and is significantly computationally easier [246]. For white frequency noise however, Π-weighting is preferable. We therefore choose Λ-weighting for the link data, but Π weighting for the clock-maser data. By choosing $\tau_{\mathrm{w}} = 1\,\mathrm{days}$ we minimize sensitivity to diurnal noise.

This frequency averaging could lead to systematic errors if gaps are not properly handled; to avoid this, the weighting functions are adjusted. If x refers to phase data, y to frequency data, w to the weighting function and τ_{w} to the weighing period, it can be shown that

$$w_x(t) = -\frac{d}{dt} w_y(t) \tag{7.7}$$

and from this, the phase weighting function associated with Λ-weighting becomes [246]

$$w_x(t) = \begin{cases} -\frac{1}{\tau_{\mathrm{w}}^2} & \text{for } t < 0 \\ \\ \frac{1}{\tau_{\mathrm{w}}^2} & \text{for } t > 0 \end{cases} \tag{7.8}$$

To make this function gap-tolerant, it is set to zero in the presence of gaps. This would lead to a bias, so both sides of the function are renormalized such that

$$-\int_{-\tau_{\mathrm{w}}}^{0} w_x(t)\, dt = \int_{0}^{\tau_{\mathrm{w}}} w_x(t)\, dt = 1; \tag{7.9}$$

The resultant weighting function is shown in Figure 7.4.

Applying this phase weighting function to the phase data x_{ij}^{M} however causes an offset: the zero-sensitivity parts of the weighting function result in the effective timestamp for the averaged dataset y_{ij}^{M} being changed from t to

$$t_{\mathrm{eff}}(t) = \int_{-\infty}^{\infty} \frac{|w_x(t'-t)|}{2}\, t'\, dt' \tag{7.10}$$

which is different to that of the clock data. To correct for this, a first order fit to the maser drift rate is calculated and used to extrapolate to the values at the centre of each day. These corrections are typically much smaller than the resultant uncertainty of this method.

The average maser frequency differences for each daily period can now be produced by calculating

$$y_{ij}^{\mathrm{M}}(t) = \frac{1}{\tau_{\mathrm{w}}} \int_{-\infty}^{\infty} w_x(t'-t)\, x_{ij}^{\mathrm{M}}(t')\, dt' + \mathrm{corr.} \quad . \tag{7.11}$$

A simple Π-weighting is applied to the optical clock frequency data to obtain y_i and y_j. Using Equation 7.6, the ratio R_{ij} between the two optical clocks comprising this pair can then be determined.

7.1.2.2 Analysis of uncertainty

The method presented above produces a series of average frequency differences between each clock spaced by 24 h periods. The standard deviation of these provides some information about the inherent uncertainty of the method, however this is liable to underestimate due to (a) the short length of the resultant datasets and (b) the potential for cross-correlation caused by the overlap of adjacent Λ-weighting profiles. In order to characterize the analysis method fully and confirm that it introduced no biases, a Monte-Carlo simulation of the three components of each link was performed and its output fed into the analysis routine.

In order to do this, it was necessary to estimate the PSD of the three datasets. The noise on the clock data, y_i and y_j is dominated by noise on the local NMIs' masers,

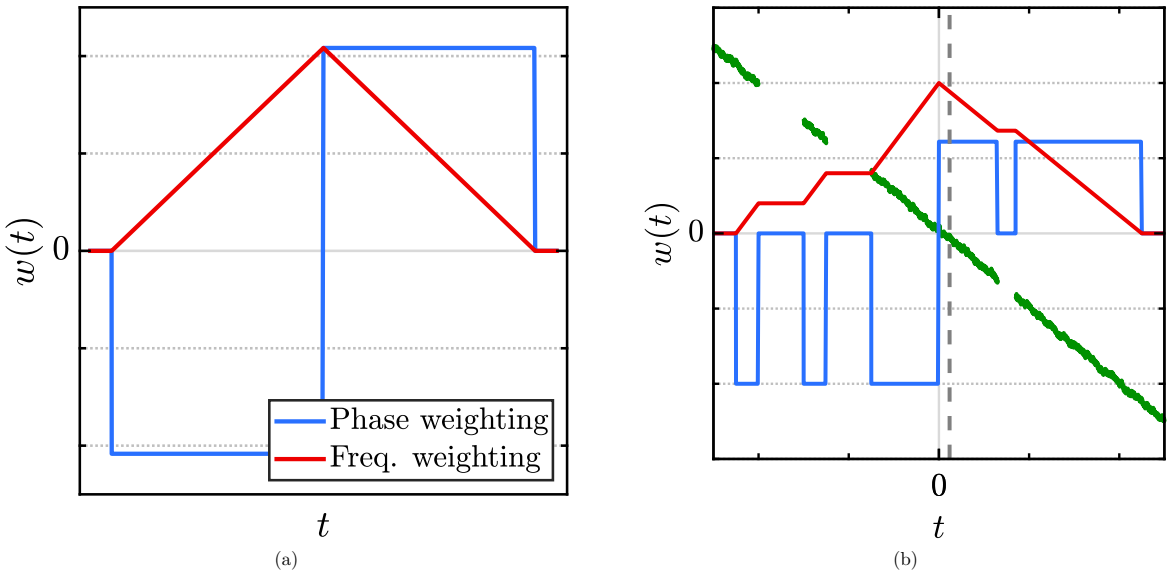

FIGURE 7.4: *(left)* Λ-weighting functions shown in frequency and phase space. The frequency-space weighting functions are derived from the phase-space functions using $w_y(t) = -\int_{-\infty}^{t} w_x(t')\,dt'$ and are shown for illustration only: they are not used in the analysis.
(right) Adaptation of the two weighting functions in the presence of gaps. The green phase data being weighted is x_{ij}^{M}. The effective timestamp for this time period τ_{w} when using the phase weighting function shown is marked by the dotted line (see Equation 7.10).

whereas the link data, x_{ij}^{M}, is dominated by noise introduced by the link itself. The usual definition of the PSD involves the Fourier transform of the auto-correlation function, however the auto-correlation function is difficult to estimate from irregularly sampled datasets such as those present here. For this reason, the Lomb-Scargle algorithm for a periodogram estimator is used. This algorithm can be considered to perform a least-squares fit at all frequencies: its output is proportional to the goodness-of-fit parameter χ for the fit at a given frequency [247]. Figure 7.5 shows typical PSDs estimated by this method for the NPL to OP Sr-lattice comparison.

With this done, simulated datasets for each part of the link were produced by generating noise with a white profile and then sculpting its Fourier transform according to the square root of a fit to the target PSD. Various methods of producing this

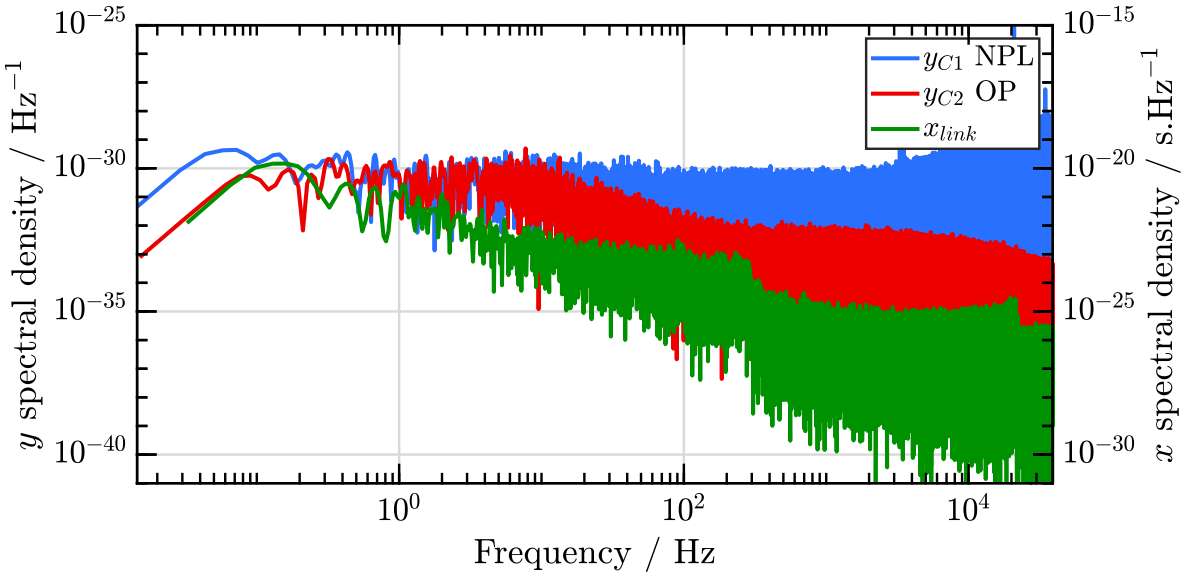

Figure 7.5: Lomb-Scargle periodogram estimates of the PSDs of the three links in the NPL to OP, Sr-lattice to Sr-lattice comparison. Note that the green link data x_{ij}^{M} is phase noise, plotted w.r.t. the RHS axes.

fit were tested, including Savitzky-Golay Finite Impulse Response (FIR) filters and Locally Weighted Scatterplot Smoothing (LOWESS), but the best fitting method was determined to be a simple moving average filter applied to the logarithm of the PSD. This fit defines the profile of the simulation data's power spectrum, which is then scaled to have a mean of 0.

The two noisy clock datasets then have a linear maser drift added onto them. The "perfect" link frequency data is produced from these profiles using Equation 7.6. Since as yet there are no gaps in the simulation data, this link frequency data can be used to produce valid link phase simulation data. The noise generated for the link data is then added to the perfect link data (the link noise is typically of order 50× greater than the maser noise) to produce a complete chain with noise added.

To this chain, gaps are then inserted into all three datasets. These are produced by considering the distribution of gaps in the true data and sampling this distribution at random, inserting gaps into the simulation data in random locations until the proportion

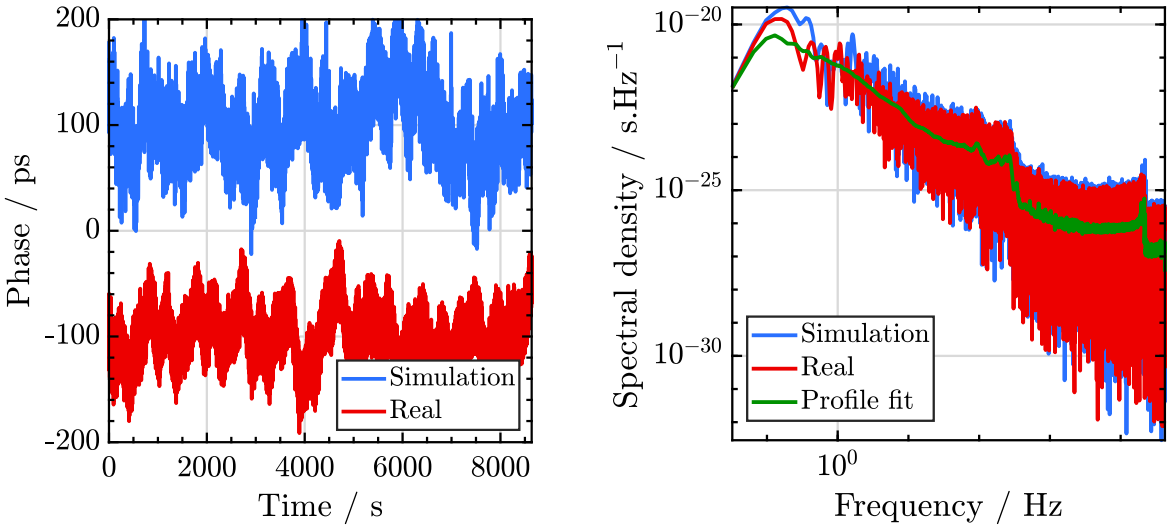

FIGURE 7.6: An example of a single set of real / simulated data for the NPL to OP maser link, x_{ij}^{M}. "Clock data" optical–maser ratio simulations y_i and y_B are produced similarly. (a) Phase data for a 8000 s chunk of the ∼700 000 s dataset. Arbitrary offsets of ±100 ps have been applied to the data for visibility which do not affect its frequency. (b) Periodogram of the same simulation run, also showing the fitted spectral density profile. Note that this is calculated from the entire dataset of ∼700 000 s (including gaps), not just the 8000 s segment used in (a).

of missing data in the simulation dataset is approximately equal to that of the real data. Note that gaps inserted in this way are uncorrelated, whereas the true distribution of gaps may show correlations with e.g. time of day (clocks are more likely to stay offline for longer at weekends or in the middle of the night). An extension of this work may therefore evaluate the impact of these correlations.

7.1.3 Results

The datasets thus produced (shown in Figure 7.6) are analysed using the same method software and code as the real data. This process is repeated many times ($N = 50$ in this case) and the resulting distribution of results is compared (a) with the known frequency offset of $\delta\nu/\nu = 0$ for the simulation data and (b) with the result for the real data. Figure 7.7 shows the daily averages produced by the simulation + analysis

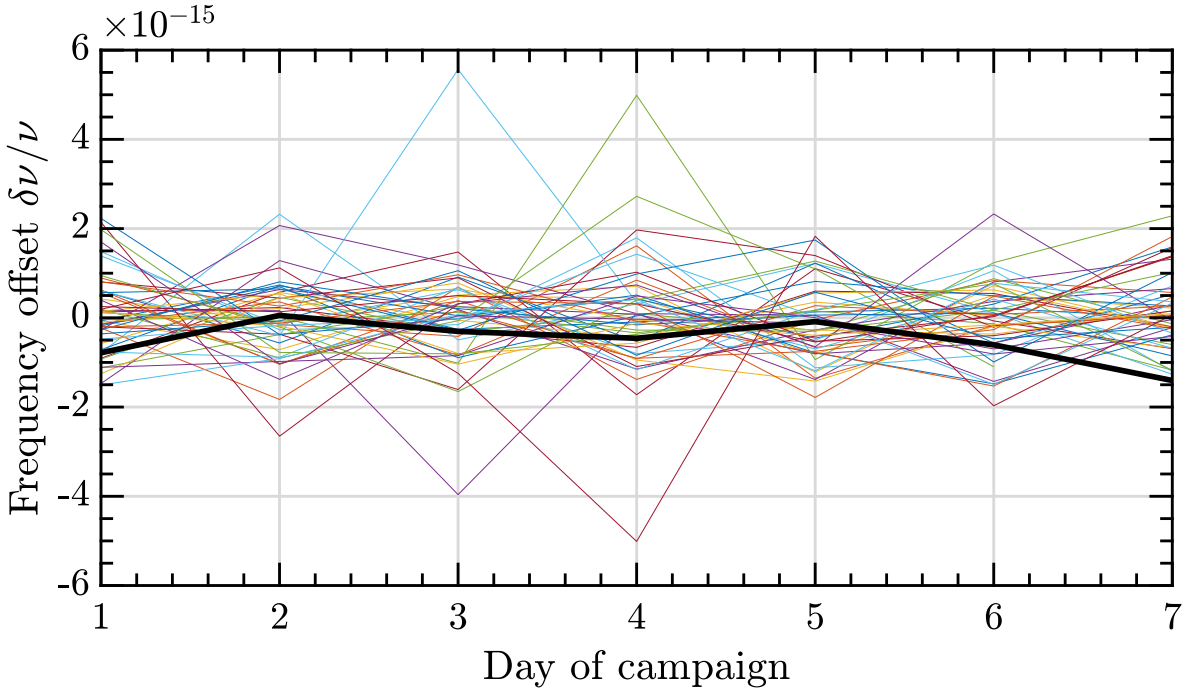

Figure 7.7: The results of 50 simulations of the NPL to OP Sr–Sr comparison. Thin lines show the daily frequency averages found for each simulation run and the thick line shows the results obtained for the real data.

method for 50 random trials, simulating the NPL – OP, Sr–Sr link, as well as the real value deduced from the campaign measurements. Figure 7.8 presents this same data in the form of a histogram, showing that the measurement obtained during the campaign for this pair of clocks falls within 1.8σ of agreement.

It must be emphasized that these values are illustrative only; the analysis method is still being developed by collaborators in PTB. The aim of the work presented here has been to develop a way of testing that method when it is completed. Nevertheless, Table 7.1 shows the results of the campaign as determined by the method outlined in §7.1.1 with uncertainties deduced by simulation. For each clock pair, $N = 50$ simulations were run just as shown in Figures 7.7 and 7.8. The standard deviation of the total means output by the simulation runs is recorded as the 1-sigma uncertainty, quoted in brackets. It is assumed throughout that any true disagreement between the clocks is

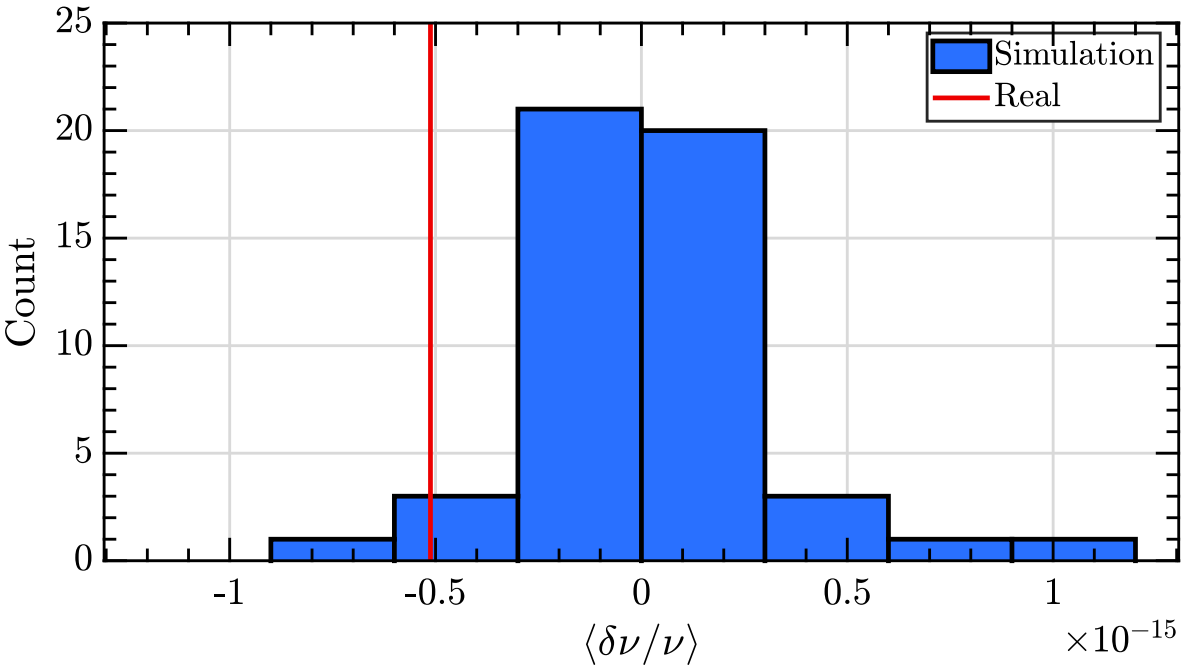

FIGURE 7.8: Histogram of the offsets of 50 simulations of the NPL to OP Sr–Sr comparison. The simulation was run with no intentional offset between the clocks: the offsets plotted here are the result of randomly introduced gaps and statistical noise. The red line shows the frequency offset calculated for the real data. The fractional standard deviation of the simulation results is 2.8×10^{-16}, mean $= 3.6 \times 10^{-17}$. The offset of the real data is $-5.1 \times 10^{-16} = -1.8\sigma$.

constant.

7.1.4 Conclusions

An international collaboration involving clocks at 4 European NMIs, connected via a broadband microwave link to a geo-stationary satellite, has been performed. The ITOC campaign ran over the course of a month, demonstrating wireless international clock comparisons with fractional statistical uncertainties at the low 10^{-16} level. The clocks involved exhibited exceptional uptime throughout the campaign, demonstrating the increasing technology readiness level (TRL) of optical clocks. The campaign also incubated a new analysis technique, robust against gaps in frequency data, whose techniques can be applied to future measurements.

Clock i \ Clock j	Sr-NPL	Yb-NPL	Sr-OP	Sr-PTB	Yb-PTB
Sr-NPL	0 (0)		-43 (28)	-19 (56)	-107 (55)
Yb-NPL		0 (0)	16 (29)	61 (56)	-48 (56)
Sr-OP	43 (28)	-16 (29)	0 (0)	52 (70)	-91 (40)
Sr-PTB	19 (56)	-61 (56)	-52 (70)	0 (0)	
Yb-PTB	107 (55)	48 (56)	91 (40)		0 (0)

Table 7.1: Fractional agreement between clock pairs with simulated uncertainties. Values reported are in the format $(R_{ij}/R_{ij}^{exp} - 1) \times 10^{17}$ where $R_{ij} \stackrel{\text{def}}{=} f_i/f_j$ and R_{ij}^{exp} is an expected ratio set to 1 for identical species and the ratio of BIPM recommended values for cross-species comparisons.
Note that these numbers, and in particular their uncertainties, will change with the new data analysis method.

The next generation of this experiment, a measurement campaign involving direct fibre links between European NMIs, has already occurred in the summer of 2017. Phase-noise compensated fibre links have been shown to enable frequency comparisons with greater stability than current optical clocks [128] so this new network will enable clock comparisons between NMIs at an unheard of level. The data from this campaign is currently under analysis and is expected to be published soon.

7.2 An absolute frequency measurement

During the ITOC campaign, we also took the opportunity to make an absolute frequency measurement of our $^{171}Yb^{+}$ E3 standard. The most direct approach to measuring the absolute frequency of an optical standard is to use a femtosecond optical frequency comb to determine the ratio between its frequency and that of a local caesium primary standard, which provides a realization of the SI second [18, 19, 197, 248–251]. However

an alternative means of accessing the SI second is via a frequency link to TAI [252–257].

TAI is a virtual time scale, computed monthly by the BIPM from clock data provided by approximately 80 institutes distributed around the world, with a latency of up to 45 days. It is computed at 5-day intervals and the offset of its scale interval from the SI second is published only as a monthly average in the BIPM bulletin Circular T. To access the SI second via this monthly value ideally requires optical frequency data to be acquired continuously over the whole month in order to avoid introducing additional uncertainty into the measurement. Long averaging times are also required to reduce the uncertainty contribution from the satellite-based time and frequency transfer techniques used to make the link to TAI. Since optical frequency standards do not yet commonly operate continuously over periods of many days, the dead time in their operation will therefore inflate the uncertainty of an absolute frequency measurement performed in this way. However an advantage of a TAI-based measurement is that several primary frequency standards contribute, reducing the potential systematic bias.

In Ref. [8], we reported a TAI-based absolute frequency measurement of the E3 transition in $^{171}Yb^{+}$ and in [9] we used newly available data from Circular-T to improve the calculation. The resulting fractional frequency uncertainty of 3.4×10^{-16} improves upon the best previously reported measurement of this transition frequency [18], which was made at the Physikalisch-Technische Bundesanstalt (PTB) in Germany, relative to local caesium primary frequency standards. To date, only two other TAI-based absolute frequency measurements have reached fractional uncertainties below 1×10^{-15}[256, 257]. In those cases, the low uncertainties were achieved by using an ensemble of local flywheel oscillators to reduce the uncertainty contributions arising from intermittent operation of the optical frequency standard and/or via special computations of the TAI scale interval with respect to the SI second over evaluation periods shorter than one month. In contrast, in our work we use a single local flywheel oscillator. The low uncertainty of

our absolute frequency measurement originates from the much higher up-time achieved for our $^{171}Yb^{+}$ optical frequency standard, which was operational for 76 % of a 25-day period in June 2015: coincident with the ITOC campaign described in Section 7.1. By performing a special calculation of the TAI scale interval we reduced our overall fractional uncertainty from 4.0×10^{-16} to 3.4×10^{-16}, however this improvement was due to non-overlapping measurement intervals. In a repeat measurement, the time period of operation of the optical clock and measurement of the TAI scale interval could be chosen to overlap, removing the need for this calculation.

7.2.1 Experimental overview

The experimental method required to perform this absolute measurement bears many similarities to that described in §7.1.1, and was executed in parallel. The $^{171}Yb^{+}$ clock's operation was identical, and is described in Chapter 2.

Traceability of our optical frequency measurement to the SI second is achieved in several stages. In the first step, a fibre-based femtosecond optical frequency comb is used to measure the optical frequency relative to the 10 MHz output signal from the hydrogen maser — a robust frequency standard, which runs continuously. The maser forms the local time scale UTC(NPL) by generating a series of pulse-per-second signals from its 10 MHz output. The measurement performed using the frequency comb thus determines the frequency ratio between the $^{171}Yb^{+}$ optical clock transition and the frequency of the local time scale, denoted here by $f(\mathrm{Yb}^{+})/f(\mathrm{UTC(NPL)})$.

In the second step, the local time scale UTC(NPL) is compared continuously to TAI via satellite-based time and frequency transfer links. The time offset between UTC(NPL) and Coordinated Universal Time (UTC) is computed by the BIPM at 5-day intervals and published in the monthly Circular T bulletin. The change in the time offset between the start and the end of each 5-day period reveals the mean frequency difference

between UTC(NPL) and UTC over that period. (Note that the frequency of TAI is the same as that of UTC since the two time scales differ only by an integer number of leap seconds). In this way we can determine the mean frequency ratio between UTC(NPL) and TAI, denoted here by $f(\mathrm{UTC(NPL)})/f(\mathrm{TAI})$, over any measurement period whose start and end times are aligned with the time grid on which the BIPM computations are performed.

In the final step, a correction must be made to account for the fact that the scale interval of TAI during the period of the measurement is not exactly equal to the SI second on the rotating geoid [258]. The fractional deviation, d, between the TAI scale interval and the SI second on the rotating geoid is estimated by the BIPM over each one-month interval of the TAI computation and is published in Circular T. Improved estimates are then provided later, derived from the BIPM's annual calculation of Terrestrial Time (TT).

In summary, if the optical frequency standard operates continuously throughout the one-month TAI reporting period, its absolute frequency can be evaluated as the product of three frequency ratios as depicted in Figure 7.9:

$$\frac{f(\mathrm{Yb^+})}{f(\mathrm{SI\ s})} = \frac{f(\mathrm{Yb^+})}{f(\mathrm{UTC(NPL)})} \times \frac{f(\mathrm{UTC(NPL)})}{f(\mathrm{TAI})} \times \frac{f(\mathrm{TAI})}{f(\mathrm{SI\ s})} \tag{7.12}$$

where $f(\mathrm{SI\ s}) = 1\,\mathrm{Hz}$ by definition.

In practice, however, there are dead times in the operation of the optical standard, and the start and end of the measurement periods do not coincide exactly with the start and end of the TAI computation period. Extrapolation of the frequency ratios is

therefore necessary, and the basic formalism of Equation 7.12 must be expanded to give

$$\begin{aligned}\frac{f(\mathrm{Yb}^+)}{f(\mathrm{SI\ s})} = &\frac{f(\mathrm{Yb}^+;\,\Delta t_1)}{f(\mathrm{UTC(NPL)};\,\Delta t_1)} \times \frac{f(\mathrm{UTC(NPL)};\,\Delta t_1)}{f(\mathrm{UTC(NPL)};\,\Delta t_2)} \\ &\times \frac{f(\mathrm{UTC(NPL)};\,\Delta t_2)}{f(\mathrm{TAI};\,\Delta t_2)} \times \frac{f(\mathrm{TAI};\,\Delta t_2)}{f(\mathrm{TAI};\,\Delta t_3)} \\ &\times \frac{f(\mathrm{TAI};\,\Delta t_3)}{f(\mathrm{SI\ s};\,\Delta t_3)}\end{aligned} \tag{7.13}$$

where the time interval for the determination of each measured frequency ratio (Figure 7.9(b)) is indicated by Δt_i. The second and fourth terms on the RHS of Equation 7.13 deal with the extrapolation periods, and the associated uncertainties introduced into the absolute frequency measurement are analyzed in §7.2.3.

7.2.2 Frequency correction of the optical standard

Comparisons between NPL's femtosecond optical frequency combs have shown that they themselves introduce negligible uncertainty in an optical-microwave frequency comparison [260]. The main source of uncertainty in such a measurement in fact comes from potential frequency offsets that may arise as the 10 MHz signal from the hydrogen maser used to generate UTC(NPL) is distributed between laboratories and used to synthesize a higher frequency (8 GHz) reference against which the repetition rate of the femtosecond comb is measured. This RF distribution and synthesis is estimated to contribute a systematic uncertainty of 1 part in 10^{16} to the frequency ratio measurement.

The $^{171}\mathrm{Yb}^+$ optical frequency standard itself runs at a value that is offset from the unperturbed atomic transition frequency due to the ion's interaction with its environment: the systematic shifts discussed in Chapters 4 and 5. The largest perturbation comes from the AC Stark shift of the relatively high intensity probe laser that is needed to drive the nanohertz linewidth E3 transition (Section 5.2). The major part of this AC Stark shift is removed in real time by using two interleaved servos, as described in §5.2.1. Any residual systematic error in the AC Stark shift extrapolation arising from

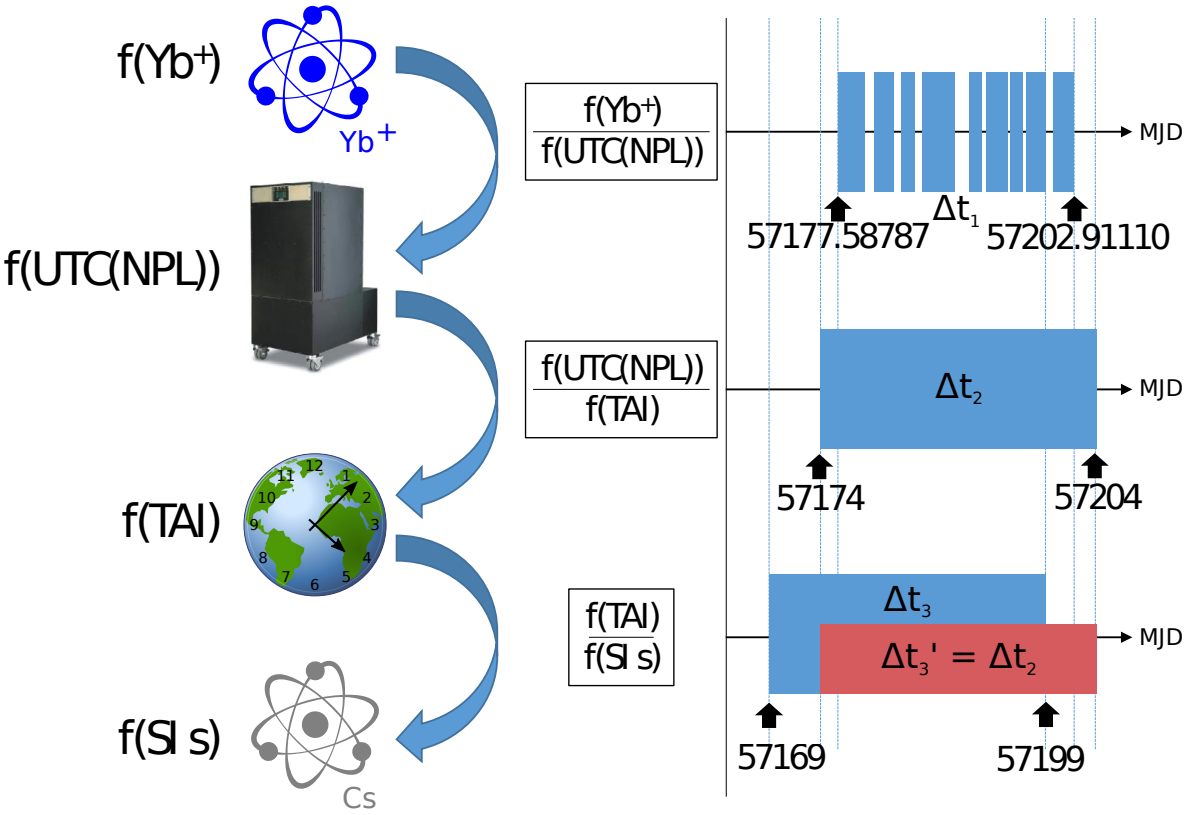

(a) (b)

FIGURE 7.9: *(left)* Schematic overview showing the chain of frequency ratio measurements used to compare the frequency of the optical transition in $^{171}Yb^{+}$ to the frequency of the microwave transition in Cs that is used to define the SI second.
(right) The time intervals (blue,red) over which frequency ratios are measured or computed, with the start and end points indicated as modified Julian date (MJD)[§]. The time interval Δt_1 consists of a number of discontinuous intervals, whereas Δt_2, Δt_3 and $\Delta t_3'$ are continuous. The time period Δt_3 is the interval over which the offsets between TAI and the SI second are usually calculated and published [259] whereas the alternative period $\Delta t_3' = \Delta t_2$ shows the period over which a special calculation of the TAI offset was performed for this work to avoid extrapolation-induced error.

an offset between the nominal and actual power ratios is measured by a calibrated, out-of-loop photodiode and removed in post-processing.

In this way uncertainties in the extrapolated frequency can reach the parts in 10^{18} level. Unfortunately, however, a hardware fault developed during this measurement campaign, such that the servo-controlled powers delivered to the ion were not indepen-

dently monitored at all times. As a result, the periods of data for which the power was not monitored had to be assigned a much more conservative uncertainty, with the result that the overall fractional uncertainty contribution from the AC Stark shift was 1.06×10^{-16}. This dominates the total $^{171}Yb^{+}$ systematic uncertainty of 1.08×10^{-16} arising from all the environmental perturbations combined.

Apart from the AC Stark shift, which was largely corrected in real-time, all other frequency offsets were corrected in post-processing in a similar manner to that described in Chapter 5 or [19].

In our previous absolute frequency measurement [19], a simple determination of the height difference between the optical standard and the local caesium fountain was sufficient to correct for the gravitational redshift arising from the gravity potential difference between the two. In this work, where we are using TAI to provide traceability to the SI second, the gravity potential difference relative to the geoid must be determined. For this we use a value derived through measurements and computations performed as part of the International Timescales with Optical Clocks (ITOC) project [261, 262]. The correction for the gravitational redshift is $-1.190(4) \times 10^{-15}$ and is included in the total fractional correction of $-9.11(1.08) \times 10^{-16}$ arising from all the frequency offsets on the ion combined.

7.2.3 Frequency correction in the link to TAI

The frequency ratio $f(\mathrm{Yb}^{+})/f(\mathrm{UTC(NPL)})$ was measured for 76% of the period MJD 57177.58787 - 57202.91110, with the sum of these non-continuous measurement periods denoted here as Δt_1. However due to the 5-day reporting interval in Circular T, the ratio $f(\mathrm{UTC(NPL)})/f(\mathrm{TAI})$ is available for a different interval, Δt_2 (MJD 57174 - 57204). UTC(NPL) must therefore be extrapolated over the dead times in the optical data. Since the centres of the two measurement periods Δt_1 and Δt_2 do not coincide,

a frequency correction must be applied to account for the long-term frequency drift of the maser used to generate UTC(NPL).

The maser's frequency drift is determined from the values of UTC−UTC(NPL) provided in Section 1 of Circular T. These values are differenced to give the mean fractional frequency offset of the maser from TAI over each 5-day period (Figure 7.10) and a least-squares fit to the data from MJD 57124 - 57209 reveals the maser's fractional frequency drift to be $-1.484(97) \times 10^{-16}$/day. Since the $f(\mathrm{Yb}^+)/f(\mathrm{UTC(NPL)})$ data is centred around MJD = 57191.10429, whereas the period Δt_2 is centred at MJD 57189, a fractional frequency correction of $-3.12(20) \times 10^{-16}$ must be applied to account for the maser drift.

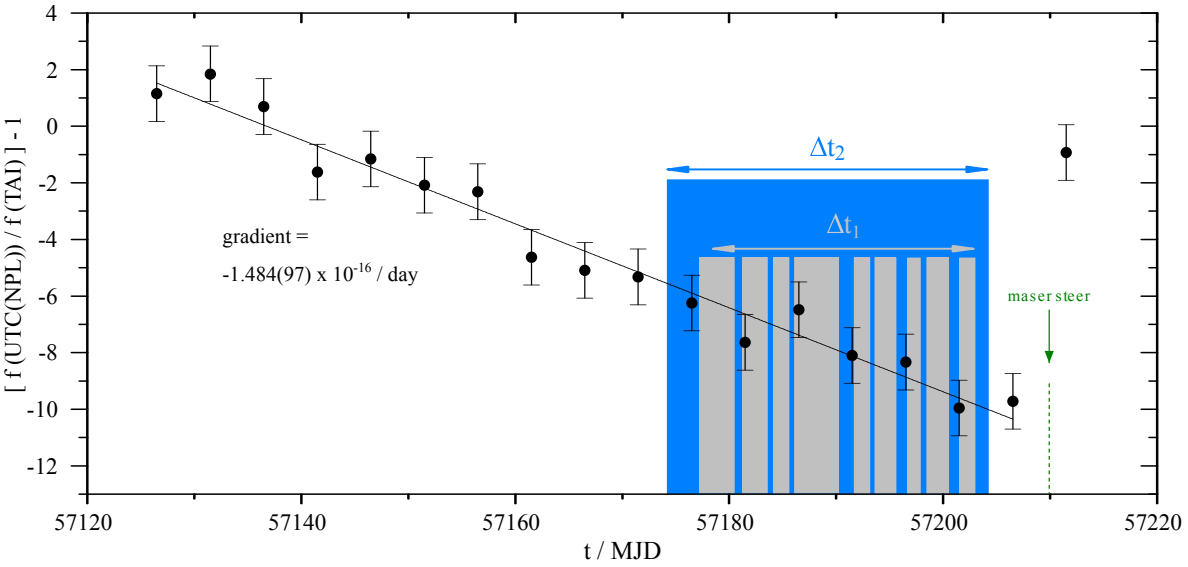

FIGURE 7.10: Mean fractional frequency deviations of $f(\mathrm{UTC(NPL)})$ from $f(\mathrm{TAI})$ over successive 5-day intervals, calculated from data published in Circular T. The frequency drift of the maser used to generate UTC(NPL) is known to be predominantly linear and so a linear fit is made to the data prior to MJD 57210, when a frequency steer was applied to the maser. The time intervals Δt_1 and Δt_2 correspond to those in Figure 7.9(b) as the time periods for which data was obtained for $f(\mathrm{Yb}^+)/f(\mathrm{UTC(NPL)})$ and $f(\mathrm{UTC(NPL)})/f(\mathrm{TAI})$ respectively.

The uncertainty associated with extrapolating $f(\mathrm{UTC(NPL)})$ over dead times in the operation of the $^{171}\mathrm{Yb}^+$ optical frequency standard is estimated by numerical simula-

tion, following the method outlined in [263] and also used in [264, 265]. The frequency noise characteristics of the NPL hydrogen maser, as determined from the frequency comparison against the $^{171}Yb^{+}$ optical standard, are modelled with the following contributions summed in quadrature, with τ in seconds: (i) white phase noise $4 \times 10^{-13}\,\tau^{-1}$, (ii) white frequency noise $6 \times 10^{-14}\,\tau^{-1/2}$ and (iii) flicker frequency noise 8×10^{-16}. Two hundred data sets of simulated frequency noise, representative of the hydrogen maser's noise processes, were generated using Stable32 [266]. The difference between the average frequency for the complete measurement period Δt_2 and for the actual measurement times Δt_1 was calculated for each data set. From the standard deviation of these frequency differences we estimate the fractional uncertainty associated with the extrapolation of f(UTC(NPL)) to be 1.20 $\times 10^{-16}$.

The mean frequency difference between UTC(NPL) and TAI during the period Δt_2 is readily obtained from the published numbers in Section 1 of Circular T, yielding a fractional offset of $[f(\text{UTC(NPL)})/f(\text{TAI}) - 1]$ equal to $-7.793(164) \times 10^{-15}$ [267].

7.2.4 Frequency correction in the link to the SI second

For the fractional frequency offset d between the scale interval of TAI and the SI second on the rotating geoid, in Ref. [8] we employed the BIPM computation TT(BIPM15) over the period Δt_3 (MJD 57169 – 57199). However, the error in the final measurement due to extrapolation required to account for the non-overlap of time periods Δt_2 and Δt_3 was the dominant term in the uncertainty budget. For this reason, a special calculation of the difference between TAI and the SI second on the rotating geoid was performed over a time period $\Delta t_3'$, chosen to match the period over which UTC(NPL) was measured (Δt_2).

The algorithm [268] that is used for the monthly computation of the offset d based on all available measurements of both primary and secondary frequency standards can

in fact be applied to any interval between two standard TAI dates, i.e. MJD ending in 4 or 9. Reported in Ref. [9], the fractional frequency offset between the scale interval of TAI and the SI second over the period $\Delta t_3'$ (MJD 57174 – 57204) is $f(\text{TAI/SIs}) = -0.76(23) \times 10^{-15}$. The uncertainty associated with this ratio is slightly higher for the interval $\Delta t_3'$ than it is for Δt_3: this is because the uncertainty of d from the algorithm in Ref. [268] is optimal if the reported intervals of operation of the standards and the interval of estimation of d are the same. As the individual measurements of primary standards usually match the monthly reporting period of Circular T, they are more in line with the interval Δt_3 than $\Delta t_3'$. However the overall uncertainty of the measurement is reduced since extrapolation between time periods Δt_3 and Δt_2 is no longer required.

By using a similar method to that given in §7.2.3 (full details are in Ref. [8]) the extrapolation error that would be present if this special measurement were not available can be calculated. Without this special calculation, the combined uncertainty for the TAI to SI second offset and the extrapolation from time period Δt_3 to Δt_2 would result in a fractional contribution to the uncertainty budget of 308×10^{-18}. By avoiding the error associated with extrapolation for $f(\text{TAI/SIs})$, this was reduced to 230×10^{-18} as shown in Table 7.2.

7.2.5 Results and conclusions

Applying all the fractional frequency corrections listed in Table 7.2 and summing the uncertainty contributions in quadrature leads to an absolute frequency of 642 121 496 772 645.17(22) Hz for the $^2S_{1/2} \rightarrow {}^2F_{7/2}$ transition in $^{171}Yb^+$. Our result is in excellent agreement with other recent measurements of this transition frequency (Figure 7.11), and its fractional uncertainty of 3.4×10^{-16} makes it the most accurate measurement of this optical transition to date. Notably, this was achieved without the need for a local caesium fountain primary standard, using a frequency link to TAI instead.

Ratio	Contribution	r_0	$[(r/r_0)-1]$ $/10^{-18}$	$u\,[(r/r_0)-1]$ $/10^{-18}$
$\frac{f(\mathrm{Yb}^+;\Delta t_1)}{f(\mathrm{UTC(NPL)};\Delta t_1)}$	Ratio at comb	r_0^{Yb}	9108	100
	Yb^+ statistics		0	16
	Yb^+ systematic correction		-911	108
$\frac{f(\mathrm{UTC(NPL)};\Delta t_1)}{f(\mathrm{UTC(NPL)};\Delta t_2)}$	H-maser drift	1	-312	20
	H-maser extrapolation		0	120
$\frac{f(\mathrm{UTC(NPL)};\Delta t_2)}{f(\mathrm{TAI};\Delta t_2)}$	H-maser offset from TAI	1	-7793	164
$\frac{f(\mathrm{TAI};\Delta t_2)}{f(\mathrm{TAI};\Delta t_3')}$	Free Atomic timescale (EAL) extrapolation	1	0	0
$\frac{f(\mathrm{TAI};\Delta t_3)}{f(\mathrm{SI\ s};\Delta t_3')}$	TAI offset from SI second	1	-760	230
$\frac{f(\mathrm{Yb}^+)}{f(\mathrm{SI\ s})}$	Total	r_0^{Yb}	-668	341

Table 7.2: Values (r) and uncertainties (u) of the five frequency ratios used to determine $f(\mathrm{Yb}^+)/f(\mathrm{SI\ s})$ according to Equation 7.13. For the ratio $f(\mathrm{Yb}^+)/f(\mathrm{UTC(NPL)})$ we (arbitrarily) choose a value of $r_0^{\mathrm{Yb}} = 642\,121\,496\,772\,645.6$ based on the 2013 CIPM recommended frequency value of the $^{171}\mathrm{Yb}^+$ optical clock transition.

Due to the very high up-time achieved for the $^{171}\mathrm{Yb}^+$ optical frequency standard (76% over 25 days), the uncertainty arising from the extrapolation of the local maser reference frequency over dead times in the optical frequency measurement data contributes only 1.2×10^{-16} to the overall uncertainty. The leading uncertainty in the measurement uncertainty budget was therefore in the linkage between TAI and the SI second. This could have been improved marginally by aligning the measurement period of the optical clock with the reporting period for Circular T, however this would only have resulted in a fractional improvement from 308×10^{-18} to 230×10^{-18}. The systematic floor of the primary standards therefore represents a significant contribution to the overall measurement: justification for a future redefinition of the SI second in terms of an optical standard. Absolute measurements such as this one are motivated by this redefinition, since accurate absolute measurements will be required to prevent a discontinuity in the SI second on redefinition.

Our new frequency measurement of the $^2\mathrm{S}_{1/2} \rightarrow {}^2\mathrm{F}_{7/2}$ transition in $^{171}\mathrm{Yb}^+$ is expected

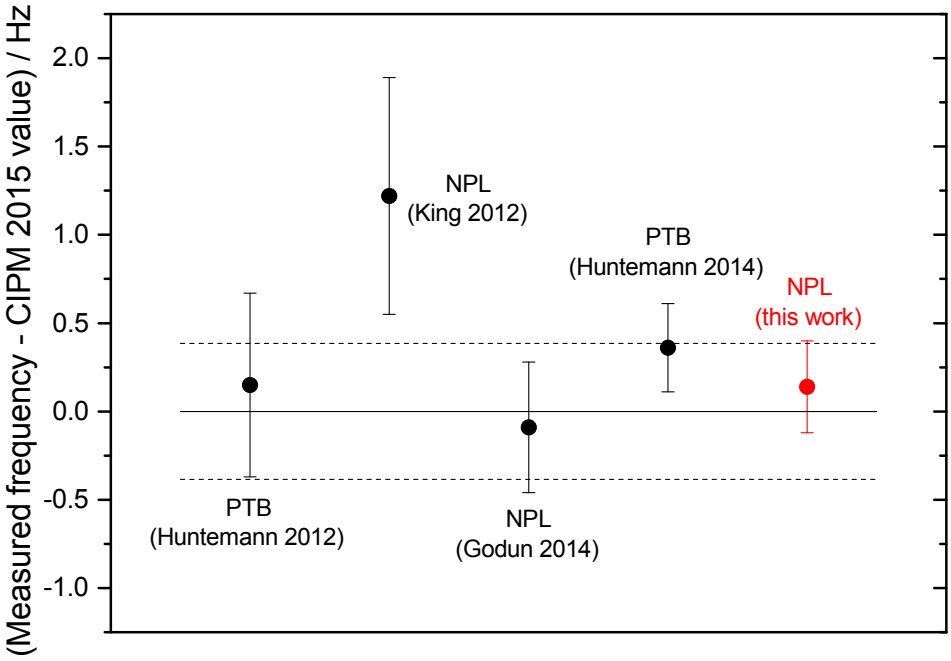

FIGURE 7.11: Recent absolute frequency measurements of the $^2S_{1/2} \rightarrow {}^2F_{7/2}$ transition in $^{171}Yb^+$. The solid and dashed lines represent the CIPM 2015 recommended value and uncertainty.

to contribute to the next update of the list of recommended frequency values [269] maintained by the Frequency Standards Working Group (WGFS) of the Consultative Committee for Length (CCL) and Consultative Committee for Time and Frequency (CCTF). The WGFS assigns frequency values and uncertainties by performing a least-squares analysis [270, 271] on a data set consisting of absolute frequency measurements and frequency ratio measurements performed by laboratories around the world. In this least-squares analysis procedure, care must be taken to account for any correlations between the input data properly, otherwise the calculated frequency values may be biassed and their uncertainties underestimated. In this context we point out that, because its traceability to the SI second is derived from TAI, the frequency measurement reported in this paper will be correlated at some level with measurements performed in other laboratories during the same period.

In fact an unusually large number of optical frequency measurements, as well as

several frequency ratio measurements, were performed during June 2015, as a result of the coordinated comparison ITOC campaign described in Section 7.1 [261]. As a result, our absolute frequency measurement is, for example, correlated with absolute frequency measurements of ^{87}Sr [197] and ^{199}Hg [272] optical standards performed at LNE-SYRTE and an absolute frequency measurement of the ^{87}Sr reference transition performed at PTB [250]. Calculation of the relevant correlation coefficients will require the laboratories concerned to exchange detailed information about exact up-times of the optical clocks and caesium fountains, as well as a knowledge of the weighting applied to each Cs fountain in the computation of TAI by the BIPM.

As the robustness and reliability of optical frequency standards continue to improve, up-times similar to those reported here will become more routinely achievable. This will make it possible to measure absolute frequencies at the low parts in 10^{16} level in an increasing number of laboratories, even those where local primary standards are not available, and to operate the optical standards as secondary representations of the second contributing to TAI.

Outlook and conclusions 8

> Experience is a good teacher; but she sends in terrific bills.
>
> *Minna Antrim*

This thesis has outlined the progress and achievements that I have contributed to on the $^{171}Yb^{+}$ optical clock project at the NPL over the last few years. In Section 8.1 I will recap some of the highlights. Looking to the future, there are many possibilities. Section 8.2 will examine a few of these and describe the experimental groundwork that is being laid toward their realisation.

8.1 Overview

A new ion trap has been developed and characterised. Ions have been confined with secular frequencies ranging from $\omega = 0.2$ to 1 MHz and cooled lifetimes on the order of weeks. Excess micromotion in the trap has been minimised to the resolution of our detection method and the ion's electromagnetic environment has been characterised thoroughly.

The anomalous phonon heating rate in the trap has been measured: in the secular mode with the worst observed heating rate we measured $\frac{\mathrm{d}}{\mathrm{d}t}\langle n\rangle = (-1.3 \pm 3.6)\,\mathrm{s}^{-1}$.

The differential polarizability of both the E2 and E3 clock transitions has been measured at a wavelength characteristic of room-temperature BBR: 7 µm. In combination with another measurement made by PTB, the AC Stark shift resulting from environmental BBR is now known at the 9.0×10^{-19} level. A large series of other changes to the clock system has also been made, resulting in improved control over the ion's environment. In combination with the new ion trap and improved knowledge of the ion's differential polarizability, the total systematic uncertainty for the E3 transition with all the clock's sub-systems operating at their best is now estimated at 2.1×10^{-18}.

The new cavity presented has improved the stability of our clock. A dual servo lock has demonstrated a frequency stability of $1.9 \times 10^{-15}\ (\tau/1\,\mathrm{s})^{-1/2}$ and an observed linewidth of 1.64(2) Hz. The local oscillator's performance has been distributed to other clocks in the NPL using links to a common local frequency comb.

An international collaborative campaign for the comparison of European optical clocks using TWSTFT has taken place. This has demonstrated international frequency comparisons at the low 10^{-16} level without a physical connection between clock partners. A key output of this campaign was the uptimes of the clocks involved: with several clocks showing uptimes of more than 75 %, optical clocks are in the process of becoming a service. The campaign also involved the development of a new technique to analyse data in the presence of gaps which can be applied to other, similar measurements.

A new absolute measurement of the E3 transition frequency has been made, finding $\nu_{E3} = 642\,121\,496\,772\,645.17(22)$ Hz, in good agreement with the literature. The uncertainty of this measurement is almost identical to the best published uncertainty [273] but was made with reference to the TAI timescale without the need for a local primary standard.

Finally, various improvements to the clock system have been made with the secondary aims of improved robustness, automation and compactness. To list some that have been mainly or exclusively my work, these include a compact RF–photon correlation system with a 15.6 kHz measurement rate; an automated software system to control and correct micromotion using the above; a high precision temperature controller for general use, built with the demands of cavities for ultra-stable lasers in mind; a high-bandwidth, high-accuracy amplification scheme for probe light power stabilisation; and automated software to control and monitor laser locks to remote cavities and virtual beats. Many of the every-day tasks involved in the running of a clock (ion loading, magnetic field compensation, micromotion nulling, clock laser relocking) are now automated with the goal of fully headless operation in the near future.

8.2 Future work

The $^{171}Yb^{+}$ project has many directions it could take, many simultaneously. Future work falls into two main categories: work to improve the clock and work to use these improvements for interesting experiments. Here I will briefly outline some of the options for both of these.

8.2.1 Operation as a clock

8.2.1.1 Clock comparison at the 10^{-18} level

The systematic budget presented in Chapter 5 is a huge leap forwards for the project. However, it is an estimate of our uncertainty based on measurements of all the environmental effects which we believe contribute to the transition frequency. To check the validity of this estimate and to search for "unknown unknowns" the gold standard for an uncertainty budget is an experimental demonstration. This involves the con-

struction of a second, independent system and a frequency comparison between the two. As I write this thesis, the new trap outlined in Section 3.6 is being built by my colleagues. Operating this with a parallel laser system and performing a comparison with the existing clock system will be a priority for the future.

8.2.1.2 Quadratic shift

The uncertainty budget presented in Section 5.8 has been greatly reduced from previous versions [5, 19]. The leading systematic uncertainty is now due to the interaction between the electron distribution in the non-spherically symmetric $^2\mathrm{F}_{7/2}$ state and any residual DC quadrupole fields in the trap. With some work, it should be possible to null the offset presented in Section 5.5 more thoroughly, but an alternative approach might set it identically equal to zero.

Equations 5.25 and 5.26 can be rewritten as

$$\begin{aligned}\langle \gamma JFm_F|\tilde{H}_Q|\gamma JFm_F\rangle =& \frac{-2(3m_F^2 - F(F+1))}{\sqrt{(2F+3)(2F+2)(2F+1)2F(2F-1)}} \\ & \times \frac{U_0}{2r_0^2}\langle \gamma JF|\tilde{\Theta}^{(2)}|\gamma JF\rangle\end{aligned} \tag{8.1}$$

where the quantum numbers refer to the upper state of the E3 transition: $^2\mathrm{F}_{7/2}$ (F=3) . For transitions of $\Delta m_F = \pm 2$ therefore, the quadrupole shift is identically equal to zero. This would eliminate our leading systematic, but would introduce another source of instability: since the transition is no longer magnetically insensitive to first order, it would be necessary to average the frequencies of the two Zeeman components to retrieve the unperturbed transition frequency. Any noise in the magnetic field between these two transitions would affect the deduced centre frequency, and inflate the instability of the clock. Additionally, if the magnetic noise is too great at short timescales, we may find that the transition is unacceptably broadened and hard to drive. To prevent the problems with this mode of operation, the new trap described in Section 3.6 has multiple layers of mu-metal shielding.

8.2.1.3 Advanced probe schemes

The method presented in Section 5.2 allowed us to cancel the AC Stark shift induced by the probe light at the 5.4×10^{-19} level. The simple Rabi scheme has no systematic offset introduced by non-ideal experimental conditions such as non-zero phonon heating rates of the ion during the probe, as have been a concern for various *hyper-Ramsey* style schemes [199, 200].

Nevertheless, there are new schemes which are immune to the AC Stark shift, and generally to other probe-related effects. One scheme, presented by Sanner et al. in [201], is known as *auto-balanced Ramsey*. This scheme provides immunity not just to the AC Stark shift, but also to "a wide variety of interrogation-induced line shifts often encountered in high precision spectroscopy, among them, in particular, light shifts, phase chirps, and transient Zeeman shifts" [201] although its sensitivity to phonon heating during the pulse is still a problem.

Additionally, the use of Ramsey spectroscopy reduces the linewidth of the central feature in a frequency scan by a factor of $\sim$2. This increase in $\mathcal{Q}$-factor directly impacts upon our stability via Equation 1.3, and so represents motivation to apply this technique even without the added systematic immunity.

8.2.1.4 Hybrid schemes

The NPL is lucky enough to possess not one but three optical atomic clocks; aside from the $^{171}Yb^{+}$ system there is an ion clock using Sr^{+} and a lattice clock operating with neutral Sr. The systematic shifts in an ion-based standard are typically easier to characterise than for the more complex system of an atomic lattice. However the large number of atoms present in the Sr system means that its QPN-limit is significantly lower than ours.

The clocks at NPL not only co-exist, but enjoy a level of integration. The local oscillator presented in Chapter 6 is being used by clocks in both labs since the frequency stability of our clock laser can be transferred via the frequency comb, as outlined in Section 6.4. Exploiting this connectivity to get the best of both worlds, we may be able to produce a "hybrid" clock where the Sr lattice experiment operates in a high-stability, low accuracy mode and is steered by contributions from the $^{171}Yb^{+}$ experiment.

8.2.1.5 Linear trap

Another approach to improve the stability of our trap (beside the local oscillator improvements already covered) would be to increase the number of ions in our trap, reducing the QPN instability by a factor of $\sqrt{N}$ for N ions. This would obviously not be possible in an end-cap trap such as ours without inducing huge trap-related shifts, so a new linear trap would be needed. Fortunately, other groups in the NPL have invested considerable effort into the construction of just such a trap [274].

Operation of a clock with multiple ions such as these would bring with it new challenges [275–277]. Not least amongst these would be inhomogeneity of the probe beam and therefore AC Stark shift over the ion chain, and the spatially varying electric quadrupole field induced by the confining electrodes and the ion–ion interactions. These two obstacles make the schemes presented in §8.2.1.2 & §8.2.1.3 particularly attractive as their successful implementation would result in the cancellation of both these effects.

8.2.1.6 Non-demolition measurements

The QPN limit in single-ion clocks is a problem. Here two schemes were proposed to lower it, either by using a highly stable local oscillator to extend coherence times (§8.2.1.4) or by boosting the frequency discriminating signal by increasing the number

of ions interacting with the beam (§8.2.1.5). Perhaps a better way though would be to side-step it.

In a Ramsey measurement, the frequency difference between your local oscillator and the transition's energy gap results in a phase accumulating between the ion's energy levels in the rotating wave approximation (RWA) [65, 66]. To read out this accumulated phase, a final $\pi/2$-pulse rotates the atom's state in the Bloch sphere representation, to convert the phase into a population difference between the $|g\rangle$ and $|e\rangle$ states. The atom's state is then read, projecting it into one of those two basis states.

This process destroys information: the atom is projected into a known state each time, so each measurement is independent of previous ones. If, instead, the phase could be measured non-destructively, our measurement would be subject to white phase noise instead of white frequency noise. For the time for which the non-demolition measurement (NDM)'s coherence can be preserved, the instability of the clock would therefore be proportional to τ^{-1} instead of $\tau^{-1/2}$.

There are various ways to achieve these NDMs [278–281]. For their application to a clock, schemes have been proposed that use Faraday rotation of light in the presence of confined atoms. [281] This would require a large number of atoms, another motivation for the investigation of quadrupole field insensitive operation (§8.2.1.2) and linear traps (§8.2.1.5). A feasibility study for the $^{171}Yb^{+}$ optical clock should be performed, but this method could potentially improve optical clock stability by an order of magnitude.

8.2.2 Fundamental physics

8.2.2.1 Variation of constants

§1.2.2 outlines a few of the interesting schemes possible with the $^{171}Yb^{+}$ optical clock. Some of these are possible today: the improvements made to the system and detailed

in this thesis have impacted the uncertainty budgets of both the E2 and E3 transitions, so a ratio between these (sensitive to variation of the fine structure constant) would yield more information than ever, particularly combined with the passage of time since the last measurement. Alternatively, the close integration between our system and the Sr-lattice clock at the NPL provides another method: the Sr $^1S_0 \rightarrow {}^3P_0$ transition has very low sensitivity to α, but is far more stable than our natural-linewidth limited quadrupole transition. It could therefore be more efficient to compare our E3 transition with Sr as a reference, mediated by the frequency comb.

8.2.2.2 Higgs coupling

Other schemes will require further modifications to be made. To test for the coupling between the Higgs boson to atomic electrons and u, d quarks requires consideration of the non-linearity of a King plot, as a transition is shifted between isotopes [22]. Ytterbium possesses many isotopes, but the practicalities of trapping and cooling these are complicated by their hyperfine structure. To this end, the laser system proposed in Section 2.7 will not only allow for superior robustness, compactness and efficiency, but will also provide the flexibility needed to support a range of isotopes. The use of waveguide EOMs means that repumping sidebands can be added to the light simply by changing the frequency of a DDS and the inclusion of a natural-abundance ytterbium oven in the new trap outlined in Section 3.6 will enable this experiment.

8.2.2.3 Lorentz invariance

The potential violation of LLI is another interesting effect that some theories predict [282, 283]. An experimental observation of this effect if it exists could be made by considering the magnetic sub-levels of an atom: by considering an orthogonal pair (e.g. $m_J = |1/2|, |7/2|$) with different responses to the Lorentz violating effect, the frequency

difference between these pairs should show a dependence on the laboratory frame's orientation in space [17, 284].

However, the magnetic field noise present at the ion would strongly obscure this signal if not compensated. We could attempt to shield the ion completely against magnetic noise, and this approach may yet bear fruit. A better method, however, would be to exploit a DFS, monitoring the phase evolution difference of e.g. the state $|\Psi\rangle = (|1/2, -1/2\rangle + |7/2, -7/2\rangle)/\sqrt{2}$ where $|m_1, m_2\rangle$ represents the state with $m_J = m_1, m_2$ for the first and second ion. This of course requires a second ion, and so would need a linear trap such as the one suggested in §8.2.1.5: again we see opportunities in fundamental physics arising from research initially targeted at improving the clock's performance.

8.3 Conclusion

And so we reach the end! But as I hope this chapter and this thesis in general have demonstrated, there is much more to be done. The atomic clock has long been the workhorse of the SI, but the historically low levels of inaccuracy being reached today mean that optical atomic clocks have applications far more exotic than mere timekeeping.

The $^{171}Yb^{+}$ system also has a lot more to give. Ion clocks have long been recognised for the high levels of environmental isolation they can provide, but new prospects for improving their stability indicate that we may be able to both have our cake and eat it.

Optical atomic clocks in general and ours in particular are fast making the transition from being experiments themselves to being sensitive instruments, capable of measuring the most minuscule of deviations between our understanding of physics from the real

world. Improvements in laser and optics technology have allowed experimenters to build systems more robust and autonomous than ever. This rise of the optical clock has not gone unnoticed: the BIPM is expected to adopt a redefinition of all the base units underpinning our science in 2018, placing the second at its heart [285]; and two atomic clocks will soon be orbiting the Earth aboard the ISS [90, 91].

The pace is accelerating, and the scientific output of optical clocks is just beginning. And so, if this thesis is to have one central message, let it be this: stay tuned!

AC Stark extrapolation A

§5.2.1 dealt with the cancellation of the AC Stark effect by operating at two different power levels. This takes advantage of the linearity of the effect w.r.t. the intensity of light at the ion, shown in Equation 5.10.

This process can be used to deduce the unperturbed frequency of the clock transition. However, is is important to understand how the extrapolation process impacts upon the stability of the clock. This involves two considerations:

1. The effect of greatly increased dead time for each frequency servo due time spent running the other one.

2. The relationship between uncertainty in a given servo's frequency and the resulting uncertainty in the extrapolated frequency.

We deal with these considerations in order.

A.1 Dead time

The stability of a single-ion frequency standard σ depends on the time taken to probe the atomic resonance and its linewidth. The linewidth is in turn related to the time spent probing according to the Fourier limit, so

$$\sigma_0 \propto \frac{\sqrt{\tau_1 + \tau_{D1}}}{\tau_1} \quad , \tag{A.1}$$

where σ_0 is the stability of a normal lock to servo 1, performed with π-pulses of length τ_1 with power P_1. The dead time in the cycle is τ_{1D}.

When extrapolating powers to cancel the AC Stark shift, we must run two servos simultaneously. The second servo counts as additional dead time for the first and vice versa, so the stabilities of servos 1 and 2 (σ_1 and σ_2) are degraded to

$$\sigma_i \propto \frac{\sqrt{\tau_1 + \tau_{D1} + \tau_2 + \tau_{D2}}}{\tau_i} \tag{A.2}$$

We now define the dead time in terms of the length of the first probe, setting

$$\tau_{D1} = \tau_{D2} \stackrel{\text{def}}{=} \gamma\tau_1 \quad . \tag{A.3}$$

to give

$$\sigma_i \propto \frac{\sqrt{\tau_1(1+2\gamma) + \tau_2}}{\tau_i} \quad . \tag{A.4}$$

If we assume that the higher power pulse at P_2 is also a π-pulse, the probe time τ_2 must be related to τ_1 by

$$\tau_2 = \sqrt{\frac{P_1}{P_2}}\tau_1 = \frac{1}{\sqrt{R}}\,\tau_1 \tag{A.5}$$

where $R = \frac{P_2}{P_1}$.

This now give expressions for the stabilities of the two servos as

$$\begin{aligned} \sigma_1 &\propto \sqrt{\frac{1 + 2\gamma + R^{-1/2}}{\tau_1}} \\ \sigma_2 &\propto \sqrt{\frac{R(1 + 2\gamma + R^{-1/2})}{\tau_1}} = \sqrt{R}\,\sigma_1 \end{aligned} \tag{A.6}$$

A.2 Effect on extrapolation

We must now ask "how do these uncertainties affect the extrapolated uncertainty?" The unperturbed frequency of the transition (f_0) can be deduced from the two servo frequencies f_1 and f_2 using Equation 5.11, reproduced here as:

$$f_0 = f_2 - \frac{f_2 - f_1}{P_2 - P_1} P_2 \tag{A.7}$$

$$\implies df_0 = \frac{P_2\, df_1 - P_1\, df_2}{P_2 - P_1} \tag{A.8}$$

which leads to

$$\sigma^2_{extrap.} = \frac{R^2}{(R-1)^2}\sigma_1^2 + \frac{1}{(R-1)^2}\sigma_2^2 \quad . \tag{A.9}$$

Substituting Equation A.6 gives an expression for the total degradation of stability due to both the additional dead time involved in running a second servo and the uncertainty involved in performing the extrapolation, under the assumption that both servos operate using π-pulses, as

$$\frac{\sigma_{extrap.}}{\sigma_0} = 1 + \epsilon = \sqrt{\frac{R(R+1)}{(R-1)^2} \times \frac{1 + 2\gamma + R^{-1/2}}{1+\gamma}} \quad . \tag{A.10}$$

Magnetic field orthogonality B

Effect of magnetic field orthogonality on the differential polarizability

In order to determine the ratio between scalar and tensor differential polarizabilities of the E2 and E3 transitions outlined in Section 4.3, knowledge of the orientation of the magnetic field experienced by the ion was necessary. Equation 4.1 shows that, for a given set of quantum numbers, a state's tensor shift is proportional to $(3\cos^2\theta - 1)$ where θ is the angle between the ion's quantization axis (set by the magnetic field direction) and the perturbing 7-µm laser's electric field. To obtain the scalar components of the differential polarizability, we taken advantage of the fact that this term sums to zero over three orthogonal magnetic field directions and so the mean of the shift to the clock transition's frequency in these three fields is entirely due to the scalar component of the differential polarizability.

In this appendix we will present the method used characterise the uncertainty introduced by this technique. This method takes two parts: firstly, the magnetic fields must be charactarised—this was covered in Section 2.4. Secondly, in Section B.1, we

evaluate the resultant impact of error in these field directions on the shifts caused by incident 7-µm radiation. We will find that this contribution is the dominant cause of uncertainty for the shifts to the E2 transition due to its large tensor differential polarizability, whereas the E3's smaller tensor component means that statistical uncertainty dominated for these shifts.

Although the analysis is described with one set of orthogonal fields, the polarizability ratios shown in Table 4.1 are an average of measurements taken in two independent sets of three field orientations as a consistency check. Labelling the magnetic fields in these two sets as B_{A1}, B_{A2}, B_{A3} and B_{B1}, B_{B2}, B_{B3}, the total set of fields used for this analysis is given by:

	B_{A1}	B_{A2}	B_{A3}	B_{B1}	B_{B2}	B_{B3}	B_x	B_{-y}	B_z
x component / µT	-8.37	-5.29	0.93	-9.36	-2.45	-2.55	10.00	0.00	0.00
y component / µT	-2.36	5.30	8.19	-3.27	3.68	8.72	0.00	-10.00	0.00
z component / µT	4.94	-6.63	5.67	1.31	-8.97	4.18	0.00	0.00	10.00

Table B.1: Magnetic fields used in this work. All fields have a magnitude of 10 µT and are given w.r.t. the axes shown in Figure 4.2.

B.1 Characterization of uncertainty

The effect of a small additional background field would be to modify the magnitudes and directions of all applied fields in the orthogonal set of 3 fields used in the experiment. This would lead to a non-orthogonal set of ion orientations, resulting in errors in the tensor shifts in Equation 4.1 and an incomplete cancellation of these shifts when averaging over them to determine the scalar shift.

Simulations were performed to evaluate the range of frequency offsets possible due to incomplete cancellation of the tensor component. This was done by computing a grid of all possible fields for the three sets of currents used during each experiment, selected

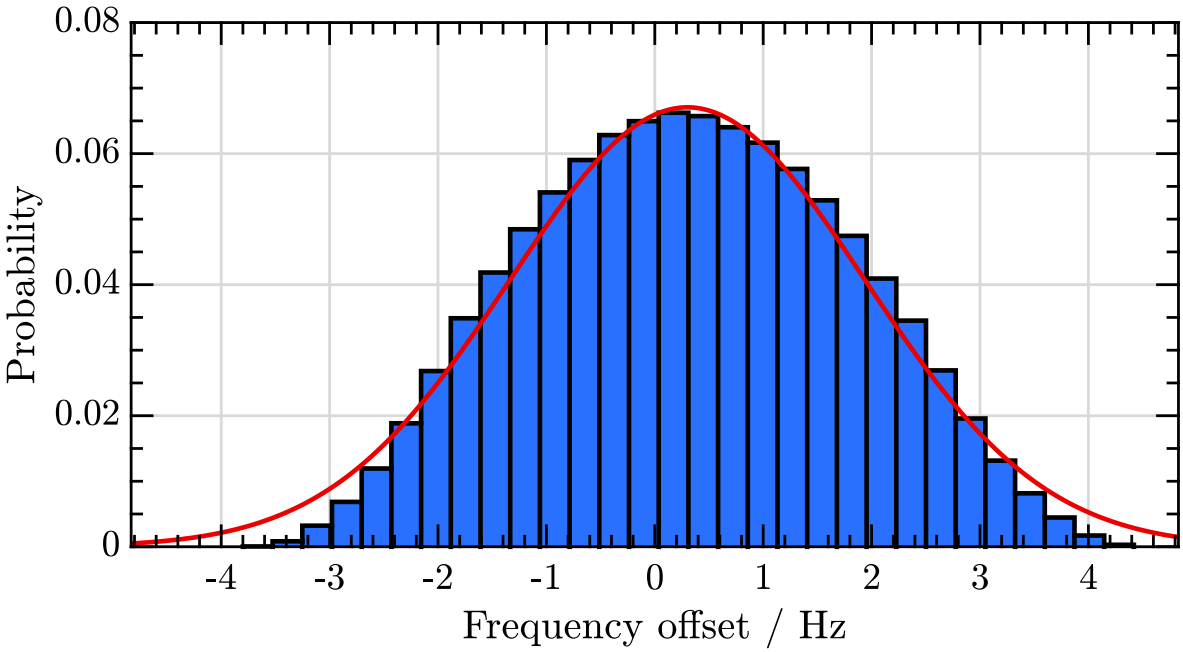

FIGURE B.1: Range of errors possible for the tensor component of the shift to the E2 transition when averaged over the three orthogonal fields used in Section 4.3. For this run of the E2 scalar:tensor ratio dataset the magnetic field uncertainty was found to be $\sigma_B = 0.250\,\mu\text{T}$ on a field of $10\,\mu\text{T}$. The normal distribution least-squares fit to this range has a mean of 0.30 Hz and a 1-sigma range of 1.64 Hz. The non-zero mean is due to granularity in our control of current in our trap's Helmholtz coils. For comparison, the scalar shift in this experimental configuration was 106 Hz.

to be compatible with the expected field to within the maximum offset observed in each dataset, σ_B. For each of these candidate sets of fields, the average frequency shift was computed.

For the ideal case of perfectly orthogonal fields this average should be zero, and our analysis in Table 4.1 uses this fact to extract the scalar component from the 3 measured 7-µm induced shifts. Figure B.1 shows the range of offsets possible when calculating the scalar component of the E2 transition's polarizability-related shift. The non-zero mean offset shown here is due to the limited resolution of our current sources powering the compensation coils: the currents used produced slightly non-orthogonal fields even without the addition of field noise. To be conservative in our estimate of the effect of magnetic field noise, we add the values of the mean offset and the 1-sigma width

of the distribution of offsets (1.9 Hz for this dataset) to produce the final magnetic field-related uncertainty for the scalar shift evaluated for this transition with this set of fields. For all ratio measurements, the scalar shift and uncertainty were evaluated in this way and repeated in an independent set of orthogonal fields. As a consistency check, the ratio measurements on three occasions and the mean values are reported in this paper. This simulation was also used to evaluate errors on the tensor components of the relevant shifts using the same method.

Temperature Controller C

This appendix briefly describes the design of the $^{171}Yb^{+}$ digital temperature controller. The controller is designed for taking high precision temperature measurements via a thermistor and applying low bandwidth PID feedback in response.

The device is controlled by an on-board microprocessor running at 16 MHz. It operates in headless mode and can be configured to automatically recover from power failures. Setup and monitoring is by USB connection, baud rate 57 600. This USB connection is electrically isolated from the rest of the board to prevent ground loops or digital noise.

Output is by OPA458 high power opamps. Output can be up to 1 A continuous, at supply voltages V_S up to 24 V depending on the power supply. The board contains space for four output channels allowing for voltages between 0 V and V_S. Alternatively the channels can be combined to form two bipolar output channels, permitting outputs up to $\pm V_S$. Note that these are not rail-to-rail opamps: the minimum possible output is around 300 mV, so applications that require lower voltages than these must use the bipolar configuration.

Error signal acquisition is done by taking a balanced measurement between a thermistor and a set resistor. The board produces an excitation voltage, usually 1.0 V, and measures the difference in current between the thermistor and resistor to produce a temperature measurement. For less demanding applications the set resistor can be on-board. For the highest stability, the precision resistor should be placed next to its paired thermistor.

This measurement is performed by an INA330 chip, of which there are two present on the board. The entire analogue section is electrically isolated from the rest of the board to prevent noise on the electrical ground affecting the measurement.

Control of the device is via virtual serial connection over USB. It accepts SCPI-formatted commands, and a Labview interface is also available which handles this communication.

Figure C.1 shows the schematic of this device and Figure 6.5 shows the assembled product. For the full schematic, PCB design files and microcontroller source code see https://github.com/charlesbaynham/DigitalTemperatureController.

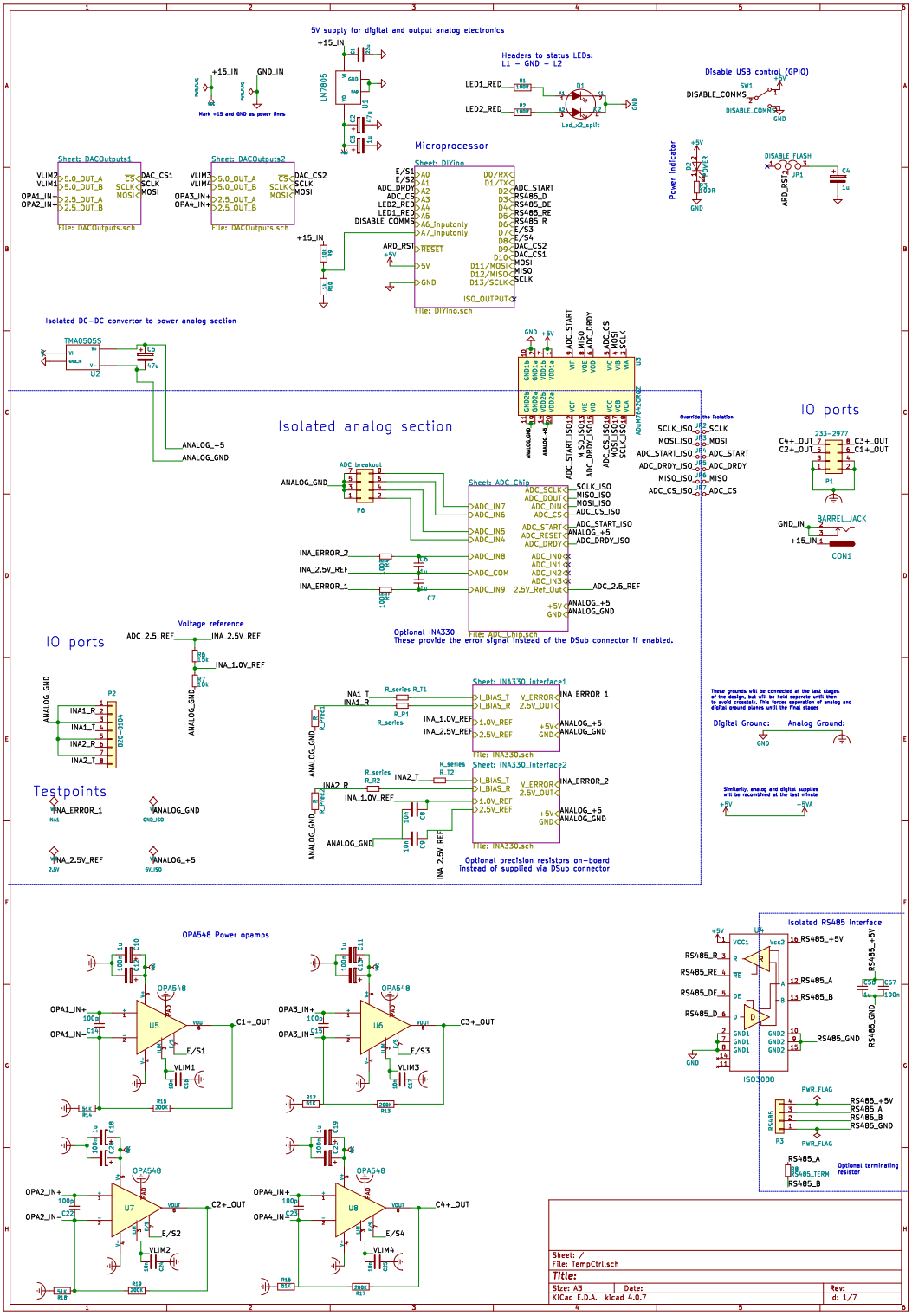

FIGURE C.1: Temperature controller schematic

RF–Photon correlator D

In order to evaluate the levels of micromotion in our trap, relevant for systematic evaluation and heating minimization, we use the RF–photon correlation technique described in §3.5.1. This technique relies upon accurate timing of small differences in arrival times between photons and the next falling edge of the RF trap drive, however commercial devices capable of measuring these events with the resolution required are often expensive and bulky.

For this reason, a device was designed for measuring time delays between up to 4 events whose arrival times range from 3.5 ns to 4 ms of the first, trigger event. The design features an on-board microcontroller, signal conditioning electronics, integrated TDC, buffering and distribution of the photon counter signal to other lab electronics and a high-speed photon counter. Interfacing to the experimental control system is possible either through a front-panel USB interface or RS-485 carried over an in-house backplane, both of which are galvanically isolated to prevent ground-loops and other unexpected system coupling.

Figure D.1 shows the schematic of this device and Figure 3.9 shows the assembled product. For the full schematic, PCB design files and microcontroller source code see `https://github.com/charlesbaynham/GP22_RF_Photon_Correllation`.

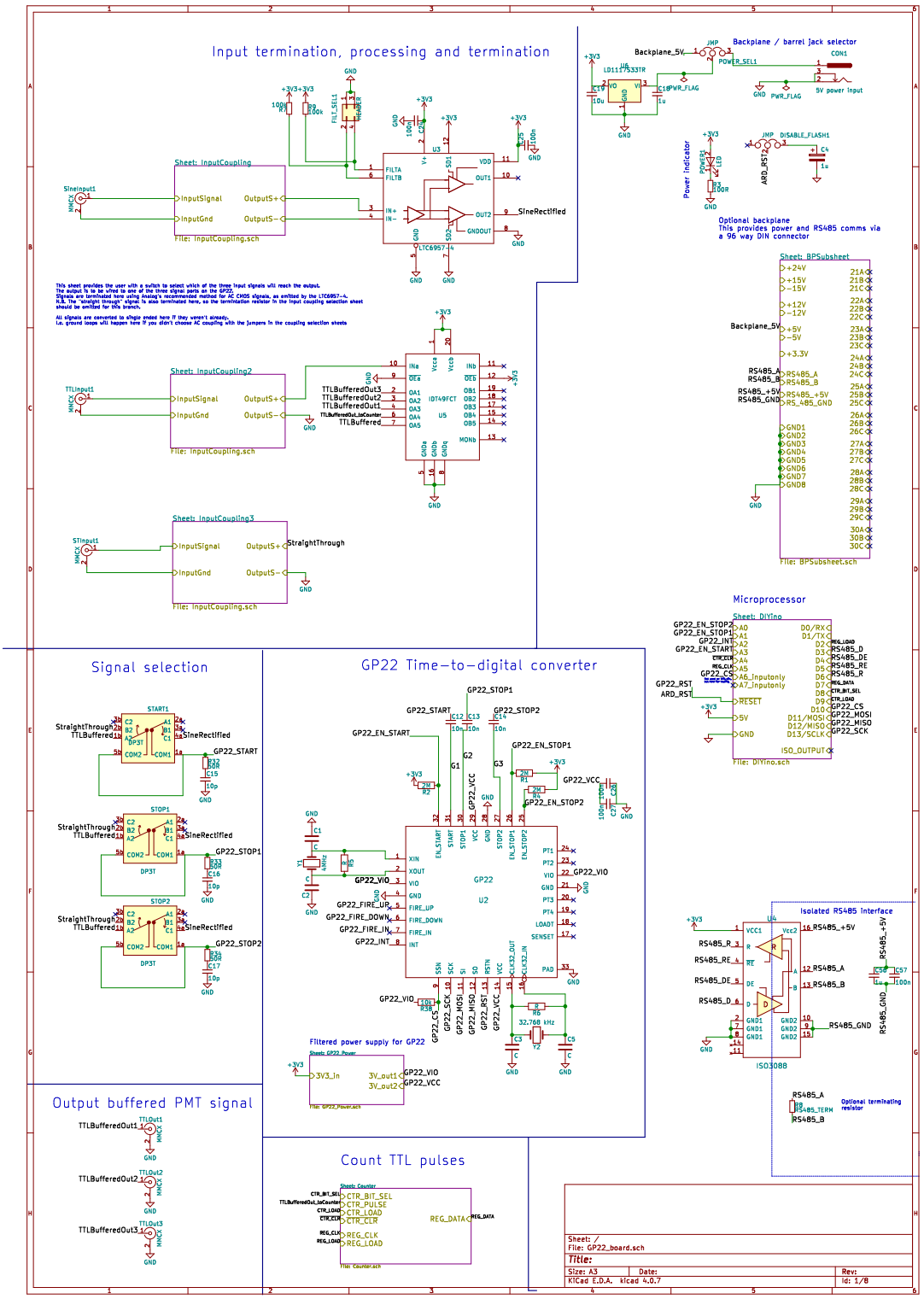

Figure D.1: RF–photon correlator schematic

ITOC data analysis E

This thesis deals heavily with the measurement of small numbers. This, however, presents a challenge when it comes to data analysis. Even with double data-types, floating-point arithmetic loses precision after 15-17 decimal digits [286]. For clocks that operate below this level of fractional uncertainty, care must therefore be taken to avoid this problem.

Part of the job of running an international clock comparison campaign such as the one reported on in Section 7.1 is to agree a data format that avoids this problem and, preferably, eases the job of data analysis. This appendix will briefly show how data was recorded for the ITOC campaign and the manner by which Equation 7.6 was derived.

Our objective in comparing remote clocks at two institutions is to find the ratio of their frequencies,

$$R_{ij}(t) \stackrel{\text{def}}{=} \frac{f_i(t)}{f_j(t)} \tag{E.1}$$

at all time-steps t. To do this, four sets of data are recorded. Locally, each optical clock is compared to the local hydrogen maser oscillator (with frequency of f_i^{M}), producing

a frequency ratio $r_i = f_i/f_i^{\mathrm{M}}$. For the reasons mentioned above, this is recorded as

$$y_i(t) \stackrel{\text{def}}{=} \frac{r_i(t)}{r_{0,i}} - 1 \tag{E.2}$$

where $r_{0,i}$ is the expected value for the measured ratio (chosen arbitrarily according to the BIPM recommended values).

Now, to recover $R_{ij}(t)$ we use

$$R_{ij}(t) = \frac{r_{0,i}}{r_{0,j}} \times \frac{1 + y_i(t)}{1 + y_j(t)} \times \frac{f_i^{\mathrm{M}}(t)}{f_j^{\mathrm{M}}(t)} \quad . \tag{E.3}$$

The optical clocks' contribution to this ratio is simply found. Since $y_i \ll 1$,

$$\frac{1 + y_i}{1 + y_j} = 1 + y_i - y_j + \mathcal{O}(y_i^2) \quad . \tag{E.4}$$

Terms of $\mathcal{O}(y_i^2)$ are utterly negligible, since $y_i \sim 10^{-13}$ at most.

To evaluate the maser frequency difference, we express f_i^{M} as $f_0^{\mathrm{M}} + \Delta f_i^{\mathrm{M}}(t)$ with the nominal maser frequency $f_0^{\mathrm{M}} = 10\,\mathrm{MHz}$. Now

$$\frac{f_i^{\mathrm{M}}(t)}{f_j^{\mathrm{M}}(t)} = \frac{f_0^{\mathrm{M}} + \Delta f_i^{\mathrm{M}}(t)}{f_0^{\mathrm{M}} + \Delta f_j^{\mathrm{M}}(t)} \tag{E.5}$$

$$= 1 + \frac{\Delta f_i^{\mathrm{M}}(t) - \Delta f_j^{\mathrm{M}}(t)}{f_0^{\mathrm{M}}} + \mathcal{O}\left(\left(\frac{\Delta f_i^{\mathrm{M}}(t)}{f_0^{\mathrm{M}}}\right)^2\right) \tag{E.6}$$

$$\stackrel{\text{def}}{=} 1 + y_{ij}^{\mathrm{M}} \tag{E.7}$$

The fractional maser frequency difference y_{ij}^{M} was found in Equation 7.4, proportional to the *double difference* of the time measurements (τ_i) taken by the modems. Putting this all together, expanding, and neglecting any terms of order y_i^2 recovers

$$R_{ij} = \frac{r_{0,i}}{r_{0,j}} \times (1 + y_i - y_j + y_{ij}^{\mathrm{M}}) \tag{E.8}$$

where

$$y_{ij}^{\mathrm{M}}(t + \frac{\tau_0}{2}) = \frac{1}{2\tau_0}\left[\tau_i(t + \tau_0) - \tau_j(t + \tau_0) - \tau_i(t) + \tau_j(t)\right] \tag{E.9}$$

with τ_0 equal to the sampling period as in Equation 7.4.

Bibliography

[1]P. Delva et al., “Test of special relativity using a fiber network of optical clocks”, Physical Review Letters **118**, 221102 (2017) 10.1103/PhysRevLett.118.221102.

[2]A. Derevianko and M. Pospelov, “Hunting for topological dark matter with atomic clocks”, Nature Physics **10**, 933–936 (2014) 10.1038/nphys3137.

[3]P. Wciso et al., “Experimental constraint on dark matter detection with optical atomic clocks”, Nature Astronomy **1**, 0009 (2016) 10.1038/s41550-016-0009.

[4]M. Roberts et al., “Observation of an electric octupole transition in a single ion”, Physical Review Letters **78**, 1876–1879 (1997) 10.1103/PhysRevLett.78.1876.

[5]S. A. King et al., “Absolute frequency measurement of the $^2S_{1/2} \rightarrow {}^2F_{7/2}$ electric octupole transition in a single ion of $^{171}Yb^+$ with 10^{-15} fractional uncertainty”, New Journal of Physics **14**, 013045 (2012) 10.1088/1367-2630/14/1/013045.

[6]P. B. R. Nisbet-Jones et al., “A single-ion trap with minimized ion–environment interactions”, Applied Physics B **122**, 1–8 (2016) 10.1007/s00340-016-6327-x.

[7]N. Huntemann et al., “Single-Ion Atomic Clock with 3×10^{-18} Systematic Uncertainty”, Physical Review Letters **116**, 063001 (2016) 10.1103/PhysRevLett.116.063001.

[8]C. F. A. Baynham et al., “Absolute frequency measurement of the optical clock transition in $^{171}Yb^+$ with an uncertainty of 4×10^{-16} using a frequency link to international atomic time”, Journal of Modern Optics **65**, 585–591 (2018) 10.1080/09500340.2017.1384514.

[9]R. M. Godun et al., “Absolute frequency measurement of the ytterbium ion E3 optical clock transition using international atomic time”, in 2018 European frequency and time forum (EFTF) (Apr. 2018), pp. 312–314, 10.1109/EFTF.2018.8409057.

[10]L. Vodolazhskaya, “Reconstruction of vertical and L-shaped ancient Egyptian sundials and methods for measuring time”, Archaeoastronomy and Ancient Technologies **2**, 1–18 (2014).

[11]M. Dehmoud, “The shadow of the Najafabad municipality on the oldest "water clock" of the city”, Amordad News (2014).

[12]R. T. Gould, “The Marine Chronometer: Its History and Development”, London: Holland Press, 287 (1923).

[13]A. N. T. Varzeliotis, *Time Under Sail: The Very Human Story of the Marine Chronometer* (1998).

[14]USA Department of Defense, "Global Positioning System Standard Positioning Service", Department Of Defense, 1–160 (2008).

[15]R. B. Langley, "Time, Clocks, and GPS", GPS World (1991).

[16]H. Li, L. Han, R. Duan, and G. M. Garner, "Analysis of the Synchronization Requirements of 5g and Corresponding Solutions", IEEE Communications Standards Magazine **1**, 52–58 (2017) 10.1109/MCOMSTD.2017.1600768ST.

[17]V. A. Dzuba et al., "Strongly enhanced effects of Lorentz symmetry violation in entangled Yb^+ ions", Nature Physics **12**, 4–9 (2016) 10.1038/nphys3610.

[18]N. Huntemann et al., "Improved limit on a temporal variation of m_p/m_e from comparisons of Yb^+ and Cs atomic clocks", Physical Review Letters **113**, 1–5 (2014) 10.1103/PhysRevLett.113.210802.

[19]R. M. Godun et al., "Frequency Ratio of Two Optical Clock Transitions in $^{171}Yb^+$ and Constraints on the Time Variation of Fundamental Constants", Physical Review Letters **113**, 210801 (2014) 10.1103/PhysRevLett.113.210801.

[20]Y. V. Stadnik and V. V. Flambaum, "Manifestations of dark matter and variations of fundamental constants in atoms and astrophysical phenomena", Arxiv, 1–32 (2015).

[21]P. Wciso et al., "Experimental constraint on dark matter detection with optical atomic clocks", Nature Astronomy **1**, 0009 (2016) 10.1038/s41550-016-0009.

[22]C. Delaunay, R. Ozeri, G. Perez, and Y. Soreq, "Probing atomic Higgs-like forces at the precision frontier", Physical Review D **96**, 1–7 (2017) 10.1103/PhysRevD.96.093001.

[23]Microsemi, "MHM 2010 Datasheet", 2–3 (2010).

[24]R. Li, K. Gibble, and K. Szymaniec, "Improved accuracy of the NPL-CsF2 primary frequency standard: Evaluation of distributed cavity phase and microwave lensing frequency shifts", Metrologia **48**, 283–289 (2011) 10.1088/0026-1394/48/5/007.

[25]D. W. Allan, "Statistics of Atomic Frequency Standards", Proceedings of the IEEE **54**, 221–230 (1966) 10.1109/PROC.1966.4634.

[26]J. Rutman and F. L. Walls, "Characterization of Frequency Stability in Precision Frequency Sources", Proceedings of the IEEE **79**, 952–960 (1991) 10.1109/5.84972.

[27]P. Lesage and T. Ayi, "Characterization of Frequency Stability: Analysis of the Modified Allan Variance and Properties of Its Estimate", IEEE Transactions on Instrumentation and Measurement **33**, 332–336 (1984) 10.1109/TIM.1984.4315235.

[28]L. Bernier, "Theoretical Analysis of the Modified Allan Variance", in 41st annual symposium on frequency control (1987), pp. 116–121, 10.1109/FREQ.1987.201012.

[29]D. Allan and J. Barnes, "A Modified "Allan Variance" with Increased Oscillator Characterization Ability", in Thirty fifth annual frequency control symposium (1981), pp. 470–475, 10.1109/FREQ.1981.200514.

[30]N. Poli, C. W. Oates, P. Gill, and G. M. Tino, "Optical atomic clocks", Rivista del Nuovo Cimento **36**, 555–624 (2013) 10.1393/ncr/i2013-10095-x.

[31]W. M. Itano et al., "Quantum projection noise: Population fluctuations in two-level systems", Physical Review A **47**, 3554–3570 (1993) 10.1103/PhysRevA.47.3554.

[32]CGPM, "CGPM 13th meeting, Resolution 1", in Resolutions of the 13th CGPM (1967).

[33]CGPM, "CGPM 25th meeting - Resolution 1", in Resolutions of the 25th CGPM (2014).

[34]M. Anticole, *What's the difference between accuracy and precision?*, (2015) https://www.youtube.com/watch?&v=hRAFPdDppzs.

[35]S. Hooker and C. Webb, *Laser Physics* (Oxford University Press, 2012).

[36]D. N. Klyshko, M. Chekhova, and S. Kulik, *Physical Foundations of Quantum Electronics* (2011).

[37]S. Bloom and H. Margenau, "Quantum theory of spectral line broadening", Physical Review **90**, 791–794 (1953) 10.1103/PhysRev.90.791.

[38]M. Eichhorn, "Quantum-Mechanical Fundamentals of Lasers", in *Laser physics* (2014), pp. 1–21, 10.1007/978-3-319-05128-4_1.

[39]M. Fox, *Quantum Optics* (Oxford University Press, 2006).

[40]V. Weisskopf and E. Wigner, "Berechnung der natrlichen Linienbreite auf Grund der Diracschen Lichttheorie", Zeitschrift fr Physik **63**, 54–73 (1930) 10.1007/BF01336768.

[41]J. Seke and W. N. Herfort, "Long-time deviations from exponential decay in the Weisskopf-Wigner model of spontaneous emission", Physics Letters A **126**, 422–426 (1988) 10.1016/0375-9601(88)90804-3.

[42]P. R. Berman and G. W. Ford, "Spectrum in spontaneous emission: Beyond the Weisskopf-Wigner approximation", Physical Review A - Atomic, Molecular, and Optical Physics **82**, 1–6 (2010) 10.1103/PhysRevA.82.023818.

[43]J. Sherman et al., "Progress on indium and barium single ion optical frequency standards", in Digest of the LEOS summer topical meetings, 2005. Vol. 2005, 2 (2005), pp. 99–100, 10.1109/LEOSST.2005.1528012.

[44]K. Matsubara et al., "Direct comparison of a Ca^+ single-ion clock against a Sr lattice clock to verify the absolute frequency measurement", Optics Express **20**, 22034 (2012) 10.1364/OE.20.022034.

[45]A. A. Madej et al., "$^{88}Sr^+$ 445 THz single-ion reference at the 10^{-17} level via control and cancellation of systematic uncertainties and its measurement against the SI second", Physical Review Letters **109**, 5–8 (2012) 10.1103/PhysRevLett.109.203002.

[46]N. Huntemann et al., "High-accuracy optical clock based on the octupole transition in $^{171}Yb^+$", Physical Review Letters **108**, 1–5 (2012) 10.1103/PhysRevLett.108.090801.

[47]T. Rosenband et al., "Frequency Ratio of Al^+ and Hg^+ Single-Ion Optical Clocks; Metrology at the 17th Decimal Place", Science **319**, 1808–1812 (2008) 10.1126/science.1154622.

[48]K. Yamanaka et al., "Frequency ratio of ^{199}Hg and ^{87}Sr optical lattice clocks beyond the SI limit", Physical Review Letters **114**, 1–5 (2015) 10.1103/PhysRevLett.114.230801.

[49]N. D. Lemke et al., "Spin-1/2 optical lattice clock", Physical Review Letters **103**, 10–13 (2009) 10.1103/PhysRevLett.103.063001.

[50]N. Poli et al., "Frequency evaluation of the doubly forbidden $^1S_0 \rightarrow {}^3P_0$ transition in bosonic ^{174}Yb", Physical Review A - Atomic, Molecular, and Optical Physics **77**, 7–10 (2008) 10.1103/PhysRevA.77.050501.

[51]T. Nicholson et al., "Systematic evaluation of an atomic clock at 2×10^{-18} total uncertainty", Nature Communications **6**, 6896 (2015) 10.1038/ncomms7896.

[52]S. Falke et al., "A strontium lattice clock with 3×10^{-17} inaccuracy and its frequency", New Journal of Physics **16** (2014) 10.1088/1367-2630/16/7/073023.

[53]G. Wilpers et al., "Absolute frequency measurement of the neutral ^{40}Ca optical frequency standard at 657 nm based on microkelvin atoms", Metrologia **44**, 146–151 (2007) 10.1088/0026-1394/44/2/005.

[54]A. Quessada et al., "The Dick effect for an optical frequency standard", Journal of Optics B: Quantum and Semiclassical Optics **5**, S150–S154 (2003) 10.1088/1464-4266/5/2/373.

[55]R. Hobson, "A Strontium Optical Lattice Clock", PhD thesis (University of Oxford, 2012), 10.1007/s12647-012-0008-y.

[56]V. Letchumanan, P. Gill, E. Riis, and A. Sinclair, "Optical Ramsey spectroscopy of a single trapped $^{88}Sr^+$ ion", Physical Review A **70**, 1–9 (2004) 10.1103/PhysRevA.70.033419.

[57]Keysight, "Keysight Technologies Full-featured CW Microwave Counters for Field , Factory or Lab",

[58]Nobel Media AB, *The Nobel Prize in Physics 1997*, (2014) https://www.nobelprize.org/nobel_prizes/physics/laureates/1997/.

[59]T. Udem, J. Reichert, R. Holzwarth, and T. Hänsch, "Absolute Optical Frequency Measurement of the Cesium D_1 Line with a Mode-Locked Laser", Physical Review Letters **82**, 3568–3571 (1999) 10.1103/PhysRevLett.82.3568.

[60]T. Udem et al., "Accurate measurement of large optical frequency differences with a mode-locked laser", **24**, 881 (1999) 10.1364/OL.24.000881.

[61]P. Del'Haye et al., "Optical frequency comb generation from a monolithic microresonator", Nature **450**, 1214–1217 (2007) 10.1038/nature06401.

[62]J. Binney and D. Skinner, *The Physics of Quantum Mechanics*, Vol. 55, 4 (Oxford University Press, Oct. 2013), pp. 340–341, 10.1080/00107514.2014.933262.

[63]Tokmakoff, "Light Interaction With Matter", 5.74 Introductory Quantum Mechanics II (2009).

[64]P. A. M. Dirac, "The Quantum Theory of the Emission and Absorption of Radiation", Proceedings of the Royal Society A: Mathematical, Physical and Engineering Sciences **114**, 243–265 (1927) 10.1098/rspa.1927.0039.

[65]C. J. Foot, *Atomic Physics*, English, 1 edition (Oxford University Press, Oxford ; New York, Feb. 2005), p. 346.

[66]G. K. Woodgate, *Elementary Atomic Structure* (1980), p. 20.

[67]C. W. Chou, D. B. Hume, T. Rosenband, and D. J. Wineland, "Optical clocks and relativity", Science **329**, 1630–1633 (2010) 10.1126/science.1192720.

[68]J. C. Hafele and R. E. Keating, "Around-the-World Atomic Clocks: Predicted Relativistic Time Gains", Science **177**, 166–168 (1972) 10.1126/science.177.4044.166.

[69]P. Delva and J. Lodewyck, "Atomic clocks: new prospects in metrology and geodesy", Acta Futura **7**, 67–78 (2013) 10.2420/AF07.2013.67.

[70]J. Flury, "Relativistic geodesy", Journal of Physics: Conference Series **723**, 6–11 (2016) 10.1088/1742-6596/723/1/012051.

[71]G. Sadlier, R. Flytkjaer, F. Sabri, and D. Herr, "The economic impact on the UK of a disruption to GNSS", London Economics (2017).

[72]G. Milburn, *Schrödinger's Machines* (1997).

[73]J. Pritchard and S. Till, "UK Quantum Technology Landscape 2014 UK", 1–94 (2014).

[74]J. D. Bekenstein, "Fine-structure constant: Is it really a constant?", Physical Review D **25**, 1527–1539 (1982) 10.1103/PhysRevD.25.1527.

[75]P. Brax et al., "Detecting dark energy in orbit: The cosmological chameleon", Physical Review D - Particles, Fields, Gravitation and Cosmology **70**, 18 (2004) 10.1103/PhysRevD.70.123518.

[76]P. Brax et al., "Chameleons with field-dependent couplings", Physical Review D - Particles, Fields, Gravitation and Cosmology **82**, 1–17 (2010) 10.1103/PhysRevD.82.083503.

[77]T. Damour and A. M. Polyakov, "The string dilation and a least coupling principle", Nuclear Physics, Section B **423**, 532–558 (1994) 10.1016/0550-3213(94)90143-0.

[78]T. Damour, F. Piazza, and G. Veneziano, "Runaway dilaton and equivalence principle violations", Physical Review Letters **89**, 081601/1–081601/4 (2002) 10.1103/PhysRevLett.89.081601.

[79]T. Damour and A. M. Polyakov, "String Theory and Gravity", General Relativity and Gravitation **26**, 1171–1176 (1994) 10.1007/BF02106709.

[80]J. P. Uzan, "The fundamental constants and their variation: Observational and theoretical status", Reviews of Modern Physics **75**, 403–455 (2003) 10.1103/RevModPhys.75.403.

[81]J.-P. Uzan, "Varying Constants, Gravitation and Cosmology", Living Reviews in Relativity **14**, 2 (2011) 10.12942/lrr-2011-2.

[82]V. A. Dzuba and V. V. Flambaum, "Relativistic corrections to transition frequencies of Ag I, Dy I, Ho I, Yb II, Yb III, Au I, and Hg II and search for variation of the fine-structure constant", Physical Review A - Atomic, Molecular, and Optical Physics **77**, 1–6 (2008) 10.1103/PhysRevA.77.012515.

[83]S. N. Lea, "Limits to time variation of fundamental constants from comparisons of atomic frequency standards", European Physical Journal: Special Topics **163**, 37–53 (2008) 10.1140/epjst/e2008-00808-6.

[84]M. A. Hohensee et al., "Limits on violations of Lorentz symmetry and the Einstein equivalence principle using radio-frequency spectroscopy of atomic dysprosium", Physical Review Letters **111**, 1–5 (2013) 10.1103/PhysRevLett.111.050401.

[85]T. Pruttivarasin et al., "Michelson-Morley analogue for electrons using trapped ions to test Lorentz symmetry", Nature **517**, 592–595 (2015) 10.1038/nature14091.

[86]A. L. Kagan et al., "Exclusive window onto Higgs Yukawa couplings", Physical Review Letters **114**, 1–5 (2015) 10.1103/PhysRevLett.114.101802.

[87]G. Aad et al., "Search for the standard model higgs boson decay to $\mu^+\mu^-$ with the ATLAS detector", Physics Letters, Section B: Nuclear, Elementary Particle and High-Energy Physics **738**, 68–86 (2014) 10.1016/j.physletb.2014.09.008.

[88]NASA, *Deep Space Atomic Clock (DSAC)*, (2013) http://www.nasa.gov/mission_pages/tdm/clock/clock_overview_prt.htm.

[89]R. Bondarescu et al., "Geophysical applicability of atomic clocks: direct continental geoid mapping", Geophysical Journal International **191**, 78–82 (2012) 10.1111/j.1365-246X.2012.05636.x.

[90]M. Augelli, "ACES Operations: an ISS External Scientific Payload Looking for Experimental Confirmations on the General Relativity Theory", in Spaceops 2016 conference, May (May 2016), 10.2514/6.2016-2407.

[91]ISS: ACES / PHARAO, *ISS Utilization: ACES (Atomic Clock Ensemble in Space) / PHARAO*, (2018) https://directory.eoportal.org/web/eoportal/satellite-missions/i/iss-aces-pharao.

[92]C. Lisdat et al., "A clock network for geodesy and fundamental science", Nature Communications **7**, 12443 (2016) 10.1038/ncomms12443.

[93]A. Arvanitaki, J. Huang, and K. Van Tilburg, "Searching for dilaton dark matter with atomic clocks", Physical Review D **91**, 015015 (2015) 10.1103/PhysRevD.91.015015.

[94]C. Lacroûte et al., "Compact Yb^+ optical atomic clock project: design principle and current status", Journal of Physics: Conference Series **723**, 012025 (2016) 10.1088/1742-6596/723/1/012025.

[95]S. Origlia et al., "Development of a strontium optical lattice clock for the SOC mission on the ISS", in , edited by J. Stuhler and A. J. Shields (Apr. 2016), p. 990003, 10.1117/12.2229473.

[96]Opticlock, *Opticlock*, (2018) https://www.opticlock.de/en/info/.

[97]S. Olmschenk et al., "Manipulation and detection of a trapped Yb^+ hyperfine qubit", Physical Review A - Atomic, Molecular, and Optical Physics **76**, 1–10 (2007) 10.1103/PhysRevA.76.052314.

[98]E. H. Pinnington, G. Rieger, and J. A. Kernahan, "Beam-laser measurements of the lifetimes of the 6p levels in Yb II", Physical Review A **56**, 2421–2423 (1997) 10.1103/PhysRevA.56.2421.

[99]A. S. Bell et al., "Laser cooling of trapped ytterbium ions using a four-level optical-excitation scheme", Physical Review A **44**, 3–6 (1991) 10.1103/PhysRevA.44.R20.

[100]R. W. Berends, E. H. Pinnington, B. Guo, and Q. Ji, "Beam-laser lifetime measurements for four resonance levels of Yb II", Journal of Physics B: Atomic, Molecular and Optical Physics **26**, L701–L704 (1993) 10.1088/0953-4075/26/20/003.

[101]C. Schrama, E. Peik, W. Smith, and H. Walther, "Novel miniature ion traps", Optics Communications **101**, 32–36 (1993) 10.1016/0030-4018(93)90318-Y.

[102]M. Kleinert, M. E. Gold Dahl, and S. Bergeson, "Measurement of the Yb I $^1S_0 \rightarrow {}^1P_1$ transition frequency at 399 nm using an optical frequency comb", Physical Review A **94**, 052511 (2016) 10.1103/PhysRevA.94.052511.

[103]A. Kramida, Y. Ralchenko, J. Reader, and NIST ASD Team, *NIST Atomic Spectra Database (ver. 5.5.2)*, 2018.

[104]D. J. Wineland, R. E. Drullinger, and F. L. Walls, "Radiation-pressure cooling of bound resonant absorbers", Physical Review Letters **40**, 1639–1642 (1978) 10.1103/PhysRevLett.40.1639.

[105]Thorlabs, *Thorlabs TLD001 T-Cube Laser Diode Driver*, https://www.thorlabs.com/newgrouppage9.cfm?objectgroup_ID=3355.

[106]S. Rauch and J. Sacher, "Compact Bragg grating stabilized ridge waveguide laser module with a power of 380 mW at 780 nm", IEEE Photonics Technol. Lett. **27**, 1737–1740 (2015) 10.1109/LPT.2015.2438545.

[107]NTT Electronics, *NTT Electronics*, https://www.ntt-electronics.com.

[108]Semrock, *Semrock Filters*, https://www.semrock.com/.

[109]Alexander Franzen, *ComponentLibrary*, (2018) http://www.gwoptics.org/ComponentLibrary/.

[110]K. Deilamian, J. D. Gillaspy, and D. E. Kelleher, "Isotope shifts and hyperfine splittings of the 398.8-nm Yb I line", J. Opt. Soc. Am. B **10**, 789–793 (1993) 10.1364/JOSAB.10.000789.

[111]R. J. Hendricks et al., "An all-optical ion-loading technique for scalable microtrap architectures", Applied Physics B **88**, 507–513 (2007) 10.1007/s00340-007-2698-3.

[112]Y. Hashimoto et al., "Trapping Laser Ablated Ca^+ Ions in Linear Paul Trap", Japanese Journal of Applied Physics **45**, 7108–7113 (2006) 10.1143/JJAP.45.7108.

[113]D. R. Leibrandt et al., "Laser ablation loading of a surface-electrode ion trap", Physical Review A **76**, 055403 (2007) 10.1103/PhysRevA.76.055403.

[114]K. Zimmermann, M. V. Okhapkin, O. A. Herrera-Sancho, and E. Peik, "Laser ablation loading of a radiofrequency ion trap", Applied Physics B: Lasers and Optics **107**, 883–889 (2012) 10.1007/s00340-012-4884-1.

[115]S. Olmschenk et al., "Measurement of the lifetime of the 6p $^2P_{1/2}$ level of Yb^+", Physical Review A - Atomic, Molecular, and Optical Physics **80**, 1–5 (2009) 10.1103/PhysRevA.80.022502.

[116]H. J. Metcalf and P. van der Straten, "Laser cooling and trapping of atoms", Journal of Optical Society of America **20**, 887–908 (2003) 10.1364/ON.12.12.000018.

[117]N. Yu and L. Maleki, "Lifetime measurements of the 4f 5d metastable states in single ytterbium ions", Physical Review A **61**, 022507 (2000) 10.1103/PhysRevA.61.022507.

[118]A. Kadri, *Vector Icons*, (2018) https://thenounproject.com/term/microcontroller/996888/.

[119]O. Bo, *Next Generation Beacons - DDS AD9912*, (2018) http://www.rudius.net/oz2m/ngnb/dds.htm (visited on 07/14/2018).

[120]J. P. Allouche, "Thue, combinatorics on words, and conjectures inspired by the Thue-Morse sequence", Journal de Theorie des Nombres de Bordeaux **27**, 375–388 (2015) 10.5802/jtnb.906.

[121]J. Schat, "Using the Thue-Morse Sequence to Cancel Low-Frequency Fluctuations", in Instrumentation and measurement technology conference proceedings (2007), pp. 1–6.

[122]S. Blundell, *Magnetism in condensed matter* (Oxford Master Series in Condensed Matter Physics, 2001).

[123]B. Odom, D. Hanneke, B. D'Urso, and G. Gabrielse, "New Measurement of the Electron Magnetic Moment Using a One-Electron Quantum Cyclotron", Physical Review Letters **97**, 030801 (2006) 10.1103/PhysRevLett.97.030801.

[124]MathWorks, *Trust-Region-Reflective Least Squares*, (2017) http://uk.mathworks.com/help/optim/ug/least-squares-model-fitting-algorithms.html#broz0i4.

[125]A. R. Conn, N. I. M. Gould, and P. L. Toint, *Trust Region Methods* (2000), 10.1137/1.9780898719857.

[126]THURLBY THANDAR INSTRUMENTS, "QL Series II Datasheet", THURLBY THANDAR INSTRUMENTS Datasheet.

[127]Bartington, "Mag-03 Three-Axis Magnetic Field Sensors", Datasheet (2019).

[128]N. R. Newbury, P. A. Williams, and W. C. Swann, "Coherent transfer of an optical carrier over 251 km", Optics Letters **32**, 3056 (2007) 10.1364/OL.32.003056.

[129]L.-S. Ma, P. Jungner, J. Ye, and J. L. Hall, "Delivering the same optical frequency at two places: accurate cancellation of phase noise introduced by an optical fiber or other time-varying path", Optics Letters **19**, 1777 (1994) 10.1364/OL.19.001777.

[130]Isomet, "AN0510 Acousto-Optic Modulation", Application Note **16**, 446 (2003) 10.1016/0141-9331(92)90030-W.

[131]J. L. Hall, "Nobel lecture: Defining and measuring optical frequencies", Reviews of Modern Physics **78**, 1279–1295 (2006) 10.1103/RevModPhys.78.1279.

[132]S. Droste et al., "Optical Frequency Comb Generation based on Erbium Fiber Lasers", Nanophotonics **5**, 196–213 (2016) 10.1515/nanoph-2016-0019.

[133]P. Gill, G. Huang, S. Lea, and H. Margolis, "An optical frequency chain for absolute frequency measurement of the 445 THz strontium trapped ion frequency standard", in Conference on precision electromagnetic measurements. conference digest. cpem 2000 (cat. no.00ch37031) (2000), pp. 206–207, 10.1109/CPEM.2000.850948.

[134]H. R. Telle, D. Meschede, and T. W. Hänsch, "Realization of a new concept for visible frequency division: phase locking of harmonic and sum frequencies.", Optics letters **15**, 532–534 (1990) 10.1364/OL.15.000532.

[135]G. Marra, H. S. Margolis, and D. J. Richardson, "Dissemination of an optical frequency comb over fiber with 3×10^{-18} fractional accuracy", Optics Express **20**, 1775 (2012) 10.1364/OE.20.001775.

[136]J. Kim, "Trapped Ions Make Impeccable Qubits", Physics **7**, 119 (2014) 10.1103/Physics.7.119.

[137]E. de Hoffmann and V. Stroobant, *Mass Spectrometry: Principles and Applications* (2007).

[138]M. Brownnutt, M. Kumph, P. Rabl, and R. Blatt, "Ion-trap measurements of electric-field noise near surfaces", Reviews of Modern Physics **87**, 1419–1482 (2015) 10.1103/RevModPhys.87.1419.

[139]L. Deslauriers et al., "Scaling and Suppression of Anomalous Heating in Ion Traps", Physical Review Letters **97**, 103007 (2006) 10.1103/PhysRevLett.97.103007.

[140]P. Dubé, A. A. Madej, Z. Zhou, and J. E. Bernard, "Evaluation of systematic shifts of the Sr^{88} single-ion optical frequency standard at the 10^{-17} level", Physical Review A **87**, 023806 (2013) 10.1103/PhysRevA.87.023806.

[141]E. Peik, T. Schneider, and C. Tamm, "Laser frequency stabilization to a single ion", Journal of Physics B: Atomic, Molecular and Optical Physics **39**, 145–158 (2006) 10.1088/0953-4075/39/1/012.

[142]H. Takahashi et al., "An integrated fiber trap for single-ion photonics", New Journal of Physics **15**, 053011 (2013) 10.1088/1367-2630/15/5/053011.

[143]Q. A. Turchette et al., "Heating of trapped ions from the quantum ground state", Physical Review A **61**, 063418 (2000) 10.1103/PhysRevA.61.063418.

[144]D. J. Berkeland and M. G. Boshier, "Destabilization of dark states and optical spectroscopy in Zeeman-degenerate atomic systems", Physical Review A **65**, 033413 (2002) 10.1103/PhysRevA.65.033413.

[145]LMA-PM-5 from NKT Photonics.

[146]M. Doleal et al., "Analysis of thermal radiation in ion traps for optical frequency standards", Metrologia **52**, 842–856 (2015) 10.1088/0026-1394/52/6/842.

[147]Shapal Hi-M Soft™ Machinable Aluminium Nitride.

[148]K. Sugiyama and J. Yoda, "Disappearance of Yb^+ in Excited States from RF Trap by Background Gases", Japanese Journal of Applied Physics **34**, L584–L586 (1995) 10.1143/JJAP.34.L584.

[149]M. Knoop, N. Madsen, R. C. Thompson, and U. Kingdom, *Physics with Trapped Charged Particles* (2013), pp. 1–25, 10.1142/9781783264063_0001.

[150]J. Keller, H. L. Partner, T. Burgermeister, and T. E. Mehlstäubler, "Precise determination of micromotion for trapped-ion optical clocks", Journal of Applied Physics **118**, 1–13 (2015) 10.1063/1.4930037.

[151]Minicircuits ZHL-5W-1.

[152]V. S. Letokhov, V. G. Minogin, and B. D. Pavlik, "Cooling and capture of atoms and molecules by a resonant light field", Zeitschrift Fur Physik **45**, 698 (1977).

[153]W. Paul, "Electromagnetic traps for charged and neutral particles", Reviews of Modern Physics **62**, 531–540 (1990) 10.1103/RevModPhys.62.531.

[154]É. Mathieu, "Mémoire sur le mouvement vibratoire d'une membrane de forme elliptique", Journal de Mathématiques Pures et Appliquées **13**, 137–203 (1868).

[155]F. G. Major, V. N. Gheorghe, and G. Werth, *Charged Particle Traps*, Vol. 37, Springer Series on Atomic, Optical, and Plasma Physics (Springer-Verlag, Berlin/Heidelberg, 2005), 10.1007/b137836.

[156]D. J. Berkeland et al., "Minimization of ion micromotion in a Paul trap", Journal of Applied Physics **83**, 5025–5033 (1998) 10.1063/1.367318.

[157]Part prices retrieved from octopart.com on 12-01-2018. PCB printing costs assume a batch of 10 boards printed by allpcb.com at a per-unit cost of 3.28 GBP.

[158]J. Jones, "An optical clock with a single ytterbium", PhD thesis (2017).

[159]P. E. Gill and W. Murray, "Algorithms for the Solution of the Nonlinear Least-Squares Problem", SIAM Journal on Numerical Analysis **15**, 977–992 (1978) 10.1137/0715063.

[160]National Instruments, *Using the Nonlinear Curve Fit VI*, (2011) http://zone.ni.com/reference/en-XX/help/371361H-01/gmath/levenberg_marquardt_theory/ (visited on 01/16/2018).

[161]C. Hewitt, "Actor Model of Computation", Inconsistency Robustness 2011, 1–25 (2011).

[162]M. Harlander, M. Brownnutt, W. Hänsel, and R. Blatt, "Trapped-ion probing of light-induced charging effects on dielectrics", New Journal of Physics **12**, 093035 (2010) 10.1088/1367-2630/12/9/093035.

[163]E. Biémont, J.-F. Dutrieux, I. Martin, and P. Quinet, "Lifetime calculations in Yb II", Journal of Physics B: Atomic, Molecular and Optical Physics **31**, 3321–3333 (1998) 10.1088/0953-4075/31/15/006.

[164]S. N. Lea, S. A. Webster, and G. P. Barwood, "Polarisabilities and blackbody shifts in Sr^+ and Yb^+", in EFTF proceedings, 6 (2006), pp. 302–307.

[165]S. G. Porsev, M. S. Safronova, and M. G. Kozlov, "Correlation effects in Yb^+ and implications for parity violation", Physical Review A - Atomic, Molecular, and Optical Physics **86**, 1–10 (2012) 10.1103/PhysRevA.86.022504.

[166]W. Itano, "External-field shifts of the $^{199}Hg^+$ optical frequency standard", Journal of Research of the National Institute of Standards and Technology **105**, 829 (2000) 10.6028/jres.105.065.

[167]N. L. Manakov, V. D. Ovsiannikov, and L. P. Rapoport, "Atoms in a laser field", Physics Reports **141**, 320–433 (1986) 10.1016/S0370-1573(86)80001-1.

[168]F. Le Kien, P. Schneeweiss, and A. Rauschenbeutel, "Dynamical polarizability of atoms in arbitrary light fields: General theory and application to cesium", European Physical Journal D **67** (2013) 10.1140/epjd/e2013-30729-x.

[169]Hamamatsu LE0088 with output power $\approx$ 20 mW. Diode current supplied by an ILX Lightwave LDX-3232 current controller. The LE0088 is a custom laser model, most similar to the range of diodes given at https://www.hamamatsu.com/jp/en/product/category/1001/1006/1021/index.html but with an integrated focussing optic as in the range at https://www.hamamatsu.com/jp/en/product/category/1001/1006/1027/index.html.

[170]NanoMover 11NCM001 actuators with Nanomotion II Model 11NCS101 driver unit by Melles-Griot.

[171]F. P. Mezzapesa et al., "Intrinsic stability of quantum cascade lasers against optical feedback", Optics Express **21**, 13748 (2013) 10.1364/OE.21.013748.

[172]E. Theocharous, S. P. Theocharous, and J. H. Lehman, "Assembly and evaluation of a pyroelectric detector bonded to vertically aligned multiwalled carbon nanotubes over thin silicon.", Applied optics **52**, 8054–9 (2013) 10.1364/ao.52.008054.

[173]I. I. Sobelman, *Atomic spectra and radiative transitions*, 12th ed. (Springer Science and Business Media, 2012).

[174]P. Taylor et al., "Investigation of the $^2S_{1/2} \rightarrow {}^2D_{5/2}$ clock transition in a single ytterbium ion", Physical Review A **56**, 2699–2704 (1997) 10.1103/PhysRevA.56.2699.

[175]S. G. Porsev and A. Derevianko, "Multipolar theory of blackbody radiation shift of atomic energy levels and its implications for optical lattice clocks", Physical Review A - Atomic, Molecular, and Optical Physics **74**, 4–7 (2006) 10.1103/PhysRevA.74.020502.

[176]T. Schneider, E. Peik, and C. Tamm, "Sub-Hertz Optical Frequency Comparisons between Two Trapped $^{171}Yb^{+}$ Ions", Physical Review Letters **94**, 230801 (2005) 10.1103/PhysRevLett.94.230801.

[177]A. Roy, S. De, B. Arora, and B. K. Sahoo, "Accurate determination of black-body radiation shift, magic and tune-out wavelengths for the $^{6}S_{1/2} \rightarrow {}^{5}D_{3/2}$ clock transition in Yb^{+}", Journal of Physics B: Atomic, Molecular and Optical Physics **50**, 205201 (2017) 10.1088/1361-6455/aa8bae.

[178]I. Lizuain, J. G. Muga, and J. Eschner, "Motional frequency shifts of trapped ions in the Lamb-Dicke regime", Physical Review A **76**, 033808 (2007) 10.1103/PhysRevA.76.033808.

[179]H. Dehmelt, "Radiofrequency Spectroscopy of Stored Ions I: Storage", in *In practice*, Vol. 617 (1968), pp. 53–72, 10.1016/S0065-2199(08)60170-0.

[180]D. J. Wineland, W. M. Itano, J. C. Bergquist, and R. G. Hulet, "Laser-cooling limits and single-ion spectroscopy", Physical Review A **36**, 2220–2232 (1987) 10.1103/PhysRevA.36.2220.

[181]B. R. Eichelberger, T. P. Snow, and V. M. Bierbaum, "Collision rate constants for polarizable ions", Journal of the American Society for Mass Spectrometry **14**, 501–505 (2003) 10.1016/S1044-0305(03)00134-X.

[182]P. Langevin, "Sur la théorie du mouvement brownien", C.∼R.∼Acad.∼Sci. **146**, 530–533 (1908).

[183]G. Moshe, J. Rayal, and H. Scott, "No Pain, High Gain: Building a Low-Noise Instrumentation Amplifier with Nanovolt Sensitivity", Analog Devices Application Notes, 1–3 (2015).

[184]J. W. Jaquay, "Designers Guide To: Instrumentation Amplifiers.", Analog Devices Application Notes **18**, 40–43 (1973) 10.1111/j.1747-1567.1973.tb01631.x.

[185]INA128 instrumentation amplifiers from Texas Instruments.

[186]Y. Lai, "Mt-061 Instrumentation Amplifier (In-Amp) Basics", Analog Devices Application Notes, 1069–1072 (2009).

[187]C. Kitchin, L. Counts, and M. Gerstenhaber, "AN-671 Reducing RFI Rectification Errors in In-Amp Circuits AN-671", Analog Devices Application Notes, 1–8.

[188]Y. Lai, "Mt-096 RFI Rectification Concepts", Analog Devices Application Notes, 1069–1072 (2009).

[189]Texas Instruments, "INA12x Precision , Low-Power Instrumentation Amplifiers", (2018).

[190]H. W. Ott, *Electromagnetic Compatibility Engineering* (2011), p. 872, 10.1088/0305-4624/18/2/I01.

[191]H. Johnson and M. Graham, *High-speed digital design: a handbook of black magic* (Prentice Hall Upper Saddle River, NJ, 1993).

[192]J. Williams, *Analog Circuit Design: Art, Science and Personalities* (Elsevier, 2013), p. 400.

[193]P. Rosenbusch et al., "AC Stark shift of the Cs microwave atomic clock transitions", Physical Review A - Atomic, Molecular, and Optical Physics **79**, 1–8 (2009) 10.1103/PhysRevA.79.013404.

[194]W. M. Itano, L. L. Lewis, and D. J. Wineland, "Shift of $^2S_{1/2}$ hyperfine splittings due to blackbody radiation", Physical Review A - General Physics **25**, 1233 (1982) 10.1103/PhysRevA.25.1233.

[195]I. R. Hill et al., "A low maintenance Sr optical lattice clock", Journal of Physics: Conference Series **723** (2016) 10.1088/1742-6596/723/1/012019.

[196]N. Huntemann et al., "Generalized Ramsey Excitation Scheme with Suppressed Light Shift", Physical Review Letters **109**, 213002 (2012) 10.1103/PhysRevLett.109.213002.

[197]J. Lodewyck et al., "Optical to microwave clock frequency ratios with a nearly continuous strontium optical lattice clock", Metrologia **53**, 1123–1130 (2016) 10.1088/0026-1394/53/4/1123.

[198]SR475 shutter heads, driven by a SR474 controller from Stanford Research Systems.

[199]R. Hobson et al., "Modified hyper-Ramsey methods for the elimination of probe shifts in optical clocks", Physical Review A **93**, 4–8 (2016) 10.1103/PhysRevA.93.010501.

[200]V. I. Yudin et al., "Hyper-Ramsey spectroscopy of optical clock transitions", Physical Review A **82**, 011804 (2010) 10.1103/PhysRevA.82.011804.

[201]C. Sanner et al., "Autobalanced Ramsey Spectroscopy", Physical Review Letters **120**, 053602 (2018) 10.1103/PhysRevLett.120.053602.

[202]G. Santarelli et al., "Frequency stability degradation of an oscillator slaved to a periodically interrogated atomic resonator", IEEE Transactions on Ultrasonics, Ferroelectrics, and Frequency Control **45**, 887–894 (1998) 10.1109/58.710548.

[203]H. Katori, "Optical lattice clocks and quantum metrology", Nature Photonics **5**, 203–210 (2011) 10.1038/nphoton.2011.45.

[204]Toptica, *Toptica TA Pro*, (2018) https://www.toptica.com/products/tunable-diode-lasers/amplified-lasers/ta-pro/.

[205]E. Black, "Notes on the Pound-Drever-Hall technique", Technology **4**, 16–98 (1998).

[206]E. D. Black, "An introduction to Pound-Drever-Hall laser frequency stabilization", American Journal of Physics **69**, 79–87 (2001) 10.1119/1.1286663.

[207]R. W. P. Drever et al., "Laser phase and frequency stabilization using an optical resonator", Applied Physics B Photophysics and Laser Chemistry **31**, 97–105 (1983) 10.1007/BF00702605.

[208]S. A. Webster et al., "Thermal-noise-limited optical cavity", CPEM Digest (Conference on Precision Electromagnetic Measurements), 58–59 (2008) 10.1109/CPEM.2008.4574651.

[209]MinusK, *MinusK Negative-Stiffness Vibration Isolators*, http://www.minusk.com/content/technology/how-it-works_passive_vibration_isolator.html.

[210]MinusK, *MinusK BM-1 isolation*, https://www.minusk.com/content/technology/transmissibility_curves_vibration_isolation_isolators_tables.html (visited on 11/30/2017).

[211]J. C. Owens, "Optical Refractive Index of Air: Dependence on Pressure, Temperature and Composition", Applied Optics **6**, 51 (1967) 10.1364/AO.6.000051.

[212]D. R. Lide, *CRC Handbook of Chemistry and Physics, 92nd Edition*, Vol. 53 (2011), pp. 4.146–4.152, 10.1136/oem.53.7.504.

[213]G. W. Kaye and T. H. Laby, "Tables of Physical and Chemical Constants", Zeitschrift fur Kristallographie - New Crystal Structures (1997) 10.1524/zkri.1997.212.5.400.

[214]N. C. Wong and J. L. Hall, "Servo control of amplitude modulation in frequency-modulation spectroscopy: demonstration of shot-noise-limited detection", Journal of the Optical Society of America B **2**, 1527 (1985) 10.1364/JOSAB.2.001527.

[215]W. Zhang et al., "Reduction of residual amplitude modulation to 1×10^{-6} for frequency modulation and laser stabilization", Optics Letters **39**, 1980 (2014) 10.1364/OL.39.001980.

[216]Y. Y. Jiang et al., "Making optical atomic clocks more stable with 10^{-16}-level laser stabilization", Nature Photonics **5**, 158–161 (2011) 10.1038/nphoton.2010.313.

[217]K. Numata, A. Kemery, and J. Camp, "Thermal-noise limit in the frequency stabilization of lasers with rigid cavities", Physical Review Letters **93**, 1–4 (2004) 10.1103/PhysRevLett.93.250602.

[218]T. Kessler, T. Legero, and U. Sterr, "Thermal noise in optical cavities revisited", **29**, 178–184 (2011) 10.1364/JOSAB.29.000178.

[219]Corning Incorporated, "ULE Corning Code 7972 Ultra Low Expansion Glass", Corning Incorporated (2008).

[220]E. Benkler, H. Telle, A. Zach, and F. Tauser, "Circumvention of noise contributions in fiber laser based frequency combs.", Optics express **13**, 5662–5668 (2005) 10.1364/OPEX.13.005662.

[221]H. R. Telle, B. Lipphardt, and J. Stenger, "Kerr-lens, mode-locked lasers as transfer oscillators for optical frequency measurements", Applied Physics B: Lasers and Optics **74**, 1–6 (2002) 10.1007/s003400100735.

[222]Work by Antoine Rolland and Benjamin Rauf, publication upcoming.

[223]Data provided by Helen Margolis, private communication 2017.

[224]D. Nicolodi et al., "Spectral purity transfer between optical wavelengths at the 10^{-18} level", Nature Photonics **8**, 219–223 (2014) 10.1038/nphoton.2013.361.

[225]Data provided by Helen Margolis, private communication 2017.

[226]W. Zhang et al., "An ultrastable silicon cavity in a continuously operating closed-cycle cryostat at 4 K", 1–5 (2017).

[227]D. G. Matei et al., "1.5 µm LASERS WITH SUB-10 mHz LINEWIDTH", Physical Review Letters **118**, 1–6 (2017) 10.1103/PhysRevLett.118.263202.

[228]C. Hagemann et al., "Ultrastable laser with average fractional frequency drift rate below 5×10^{-19}/s", Optics Letters **39**, 5102 (2014) 10.1364/OL.39.005102.

[229]T. Kessler et al., "A sub-40-mHz-linewidth laser based on a silicon single-crystal optical cavity", Nature Photonics **6**, 687–692 (2012) 10.1038/nphoton.2012.217.

[230]J. Gray and D. Allan, "A Method for Estimating the Frequency Stability of an Individual Oscillator", 28th Annual Symposium on Frequency Control, 243–246 (1974) 10.1109/FREQ.1974.200027.

[231]G. D. Cole et al., "High-performance near- and mid-infrared crystalline coatings", Optica **3**, 647 (2016) 10.1364/OPTICA.3.000647.

[232]G. D. Cole et al., "Tenfold reduction of Brownian noise in high-reflectivity optical coatings", Nature Photonics **7**, 644–650 (2013) 10.1038/nphoton.2013.174.

[233]B. T. R. Christensen et al., "Nonlinear spectroscopy of Sr atoms in an optical cavity for laser stabilization", Physical Review A **92**, 053820 (2015) 10.1103/PhysRevA.92.053820.

[234]M. A. Norcia and J. K. Thompson, "Cold-strontium laser in the superradiant crossover regime", Physical Review X **6**, 1–6 (2016) 10.1103/PhysRevX.6.011025.

[235]S. Cook, T. Rosenband, and D. R. Leibrandt, "Laser-frequency stabilization based on steady-state spectral-hole burning in Eu^{3+}: Y_2SiO_5", Physical Review Letters **114**, 1–5 (2015) 10.1103/PhysRevLett.114.253902.

[236]P. B. Sellin et al., "Laser stabilization at 1536 nm using regenerative spectral hole burning", Physical Review B **63**, 155111 (2001) 10.1103/PhysRevB.63.155111.

[237]R. W. Fox et al., "A high stability optical frequency reference based on thermal calcium atoms", 2012 IEEE International Frequency Control Symposium, IFCS 2012, Proceedings, 399–401 (2012) 10.1109/FCS.2012.6243750.

[238]R. Jozsa, D. S. Abrams, J. P. Dowling, and C. P. Williams, "Quantum Clock Synchronization Based on Shared Prior Entanglement", Physical Review Letters **85**, 2010–2013 (2000) 10.1103/PhysRevLett.85.2010.

[239]D. Piester et al., "Time transfer with nanosecond accuracy for the realization of International Atomic Time", Metrologia **45**, 185–198 (2008) 10.1088/0026-1394/45/2/008.

[240]C. Cecilia et al., "A fiber link for the remote comparison of optical clocks and geodesy experiments", in 2015 joint conference of the ieee international frequency control symposium and the european frequency and time forum (Apr. 2015), pp. 579–582, 10.1109/FCS.2015.7138911.

[241]ITU-R, "The operational use of two-way satellite time and frequency transfer employing pseudorandom noise codes", Recommendation ITU-R TF.1153-3 **3** (2010).

[242]P. Whibberley, *Private communication*, 2019.

[243]E. Benkler et al., "WP5 Outline 30 month", ITOC 30-month Review Meeting (2015).

[244]E. Benkler, *Private communication*, 2017.

[245]*Paper under preparation.*

[246]E. Benkler, C. Lisdat, and U. Sterr, "On the relation between uncertainties of weighted frequency averages and the various types of Allan deviations", Metrologia **52**, 565–574 (2015) 10.1088/0026-1394/52/4/565.

[247]J. T. VanderPlas, "Understanding the Lomb-Scargle Periodogram", 1–55 (2017).

[248]J. E. Stalnaker et al., "Optical-to-microwave frequency comparison with fractional uncertainty of 10^{-15}", Applied Physics B: Lasers and Optics **89**, 167–176 (2007) 10.1007/s00340-007-2762-z.

[249]G. P. Barwood et al., "Agreement between two $^{88}Sr^{+}$ optical clocks to 4 parts in 10^{17}", Physical Review A **89**, 050501 (2014) 10.1103/PhysRevA.89.050501.

[250]C. Grebing et al., "Realization of a timescale with an accurate optical lattice clock", Optica **3**, 563 (2016) 10.1364/OPTICA.3.000563.

[251]M. Pizzocaro et al., "Absolute frequency measurement of the $^{1}S_0 \rightarrow {}^{3}P_0$ transition of ^{171}Yb", Metrologia **54**, 102–112 (2017) 10.1088/1681-7575/aa4e62.

[252]C. Y. Park et al., "Absolute frequency measurement of $^{1}S_0(F = 1/2) \rightarrow {}^{1}P_0 F = 1/2)$ transition of ^{171}Yb atoms in a one-dimensional optical lattice at KRISS", Metrologia **50**, 119–128 (2013) 10.1088/0026-1394/50/2/119.

[253]D. Akamatsu et al., "Spectroscopy and frequency measurement of the ^{87}Sr clock transition by laser linewidth transfer using an optical frequency comb", Applied Physics Express **7**, 012401 (2014) 10.7567/APEX.7.012401.

[254]Y. Huang et al., "Frequency Comparison of Two $^{40}Ca^{+}$ Optical Clocks with an Uncertainty at the 10^{-17} Level", Physical Review Letters **116**, 1–6 (2016) 10.1103/PhysRevLett.116.013001.

[255]P. Dubé, J. E. Bernard, and M. Gertsvolf, "Absolute frequency measurement of the $^{88}Sr^{+}$ clock transition using a GPS link to the SI second", Metrologia **54**, 290–298 (2017) 10.1088/1681-7575/aa5e60.

[256]H. Hachisu, G. Petit, and T. Ido, "Absolute frequency measurement with uncertainty below 1×10^{-15} using International Atomic Time", Applied Physics B **123**, 34 (2017) 10.1007/s00340-016-6603-9.

[257]H. Hachisu et al., "SI-traceable measurement of an optical frequency at the low 10^{-16} level without a local primary standard", Optics Express **25**, 8511–8523 (2017) 10.1364/OE.25.008511.

[258]B. Guinot and E. F. Arias, "Atomic time-keeping from 1955 to the present", Metrologia **42**, S20–S30 (2005) 10.1088/0026-1394/42/3/S04.

[259]BIPM, *Mean fractional deviation of the TAI scale interval from that of TT*, ftp://62.161.69.5/pub/tai/scale/sitai15.ar.

[260]L. A. Johnson, P. Gill, and H. S. Margolis, "Evaluating the performance of the NPL femtosecond frequency combs: Agreement at the 10^{-21} level", Metrologia **52**, 62–71 (2015) 10.1088/0026-1394/52/1/62.

[261]H. S. Margolis et al., "International timescales with optical clocks (ITOC)", 2013 Joint European Frequency and Time Forum and International Frequency Control Symposium, EFTF/IFC 2013, 908–911 (2013) 10.1109/EFTF-IFC.2013.6702183.

[262]H. Denker et al., "Geodetic methods to determine the relativistic redshift at the level of 10^{-18} in the context of international timescales: a review and practical results", Journal of Geodesy, 1–30 (2017) 10.1007/s00190-017-1075-1.

[263]D. H. Yu, M. Weiss, and T. E. Parker, "Uncertainty of a frequency comparison with distributed dead time and measurement interval offset", Metrologia **44**, 91–96 (2007) 10.1088/0026-1394/44/1/014.

[264]H. Hachisu and T. Ido, "Intermittent optical frequency measurements to reduce the dead time uncertainty of frequency link", Japanese Journal of Applied Physics **54**, 112401 (2015) 10.7567/JJAP.54.112401.

[265]J. Leute et al., "Frequency Comparison of $^{171}Yb^{+}$ Ion Optical Clocks at PTB and NPL via GPS PPP", IEEE Transactions on Ultrasonics, Ferroelectrics, and Frequency Control **63**, 981–985 (2016) 10.1109/TUFFC.2016.2524988.

[266]Hamilton Technical Services, *Stable 32*, (2018) https://ieee-uffc.org/frequency-control/frequency-control-software/stable32/.

[267]BIPM, *Circular T*, https://www.bipm.org/en/bipm-services/timescales/time-ftp/Circular-T.html.

[268]J. Azoubib, M. Granveaud, and B. Guinot, "Estimation of the Scale Unit Duration of Time Scales", Metrologia **13**, 87–93 (1977) 10.1088/0026-1394/13/3/001.

[269]BIPM, "SI Brochure: Appendix 2", 2013.

[270]H. S. Margolis and P. Gill, "Least-squares analysis of clock frequency comparison data to deduce optimized frequency and frequency ratio values", Metrologia **52**, 628–634 (2015) 10.1088/0026-1394/52/5/628.

[271]H. S. Margolis and P. Gill, "Determination of optimized frequency and frequency ratio values from over-determined sets of clock comparison data", Journal of Physics: Conference Series **723**, 012060 (2016) 10.1088/1742-6596/723/1/012060.

[272]R. Tyumenev et al., "Comparing a mercury optical lattice clock with microwave and optical frequency standards", New Journal of Physics **18**, 113002 (2016) 10.1088/1367-2630/18/11/113002.

[273]N. Huntemann, "High-accuracy optical clock based on the octupole transition in Yb+171", PhD thesis (2014), 10.1103/PhysRevLett.108.090801.

[274]G. Wilpers, P. See, P. Gill, and A. G. Sinclair, "A monolithic array of three-dimensional ion traps fabricated with conventional semiconductor technology", Nature Nanotechnology **7**, 572–576 (2012) 10.1038/nnano.2012.126.

[275]T. E. Mehlstäubler et al., "Minimizing time-dilation in ion traps - Towards an optical clock with Coulomb crystals", 2012 IEEE International Frequency Control Symposium, IFCS 2012, Proceedings, 248–249 (2012) 10.1109/FCS.2012.6243653.

[276]N. Herschbach, K. Pyka, J. Kelle, and T. E. Mehlstäubler, "Linear Paul trap design for an optical clock with Coulomb crystals", Applied Physics B: Lasers and Optics **107**, 891–906 (2012) 10.1007/s00340-011-4790-y.

[277]K. Arnold et al., "Prospects for atomic clocks based on large ion crystals", Physical Review A **92**, 032108 (2015) 10.1103/PhysRevA.92.032108.

[278]J. M. Geremia, J. K. Stockton, and H. Mabuchi, "Tensor polarizability and dispersive quantum measurement of multilevel atoms", Physical Review A - Atomic, Molecular, and Optical Physics **73**, 1–14 (2006) 10.1103/PhysRevA.73.042112.

[279]M. Brune et al., "Quantum nondemolition measurement of small photon numbers by Rydberg-atom phase-sensitive detection", Physical Review Letters **65**, 976–979 (1990) 10.1103/PhysRevLett.65.976.

[280]G. Nogues et al., "Seeing a single photon without destroying it", Nature **400**, 239–242 (1999) 10.1038/22275.

[281]A. Jechow et al., "Controllable Optical Phase Shift Over One Radian from a Single Isolated Atom", Physical Review Letters **110**, 113605 (2013) 10.1103/PhysRevLett.110.113605.

[282]V. A. Kostelecký and R. Potting, "CPT , strings, and meson factories", Physical Review D **51**, 3923–3935 (1995) 10.1103/PhysRevD.51.3923.

[283]V. A. Kostelecký and N. Russell, "Data tables for Lorentz and CPT violation", Reviews of Modern Physics **83**, 11–31 (2011) 10.1103/RevModPhys.83.11.

[284]R. Shaniv et al., "New Methods for Testing Lorentz Invariance with Atomic Systems", Physical Review Letters **120**, 103202 (2018) 10.1103/PhysRevLett.120.103202.

[285]CIPM, *Proceedings of the 106th meeting*, tech. rep. (2017).

[286]IEEE Standards Board, "An American National Standard IEEE Standard for Binary Floating-Point Arithmetic", IEEE Standards (1991) 10.1109/IEEESTD.1987.81037.

List of Acronyms

AC	alternating current
ADC	Analogue to Digital Converter
AOM	Acousto-optic Modulator
AVAR	Allan variance
BBR	environmental Black-Body Radiation
BDU	beat detection unit
BIPM	International Bureau of Weights and Measures
BOM	bill of materials
CEO	carrier-envelope offset
CF	ConFlat vacuum flanges
CGPM	Conférence Générale des Poids et Mesures
CIPM	International Committee for Weights and Measures (Comité international des poids et mesures)
CMI	Czech Metrology Institute
CMRR	common-mode rejection ratio
COMSOL	COMSOL Multiphysics: a cross-platform FEM solver and multiphysics simulation software suite
CTE	coefficient of thermal expansion
CW	continuous-wave
DC	direct-current
DDS	direct digital synthesis unit
DFB	distributed feedback laser
DFS	decoherence free subspace
DPhil	Doctor of Philosophy
DVM	digital voltmeter

E1	electric dipole transition
E2	electric quadrupole transition
E3	electric octupole transition
EAL	Free Atomic timescale Échelle Atomique Libre
ECDL	external-cavity diode laser
EDFA	erbium-doped fibre amplifier
EEP	Einstein equivalence principle
EMM	excess micromotion
EOM	electro-optic modulator
EWMA	Exponentially Weighted Moving Average
FEM	finite-element method
FET	field-effect transistor
FIR	Finite Impulse Response
FOPDT	First-Order Plus Dead-time
FM	frequency modulation
FSR	Free Spectral Range
FWHM	full-width half-maximum
GBP	Gain-Bandwidth Product
GNSS	Global Navigation Satellite System
GPS	Global Positioning System
HV	high voltage
IC	integrated chip
IMM	intrinsic micromotion
INRIM	Istituto Nazionale di Ricerca Metrologica
IR	infra-red
ISS	International Space Station
ITOC	International Timescales with Optical Clocks
LHC	Large Hadron Collider
LHS	Left-hand side
LLI	local Lorentz invariance
LMA	Levenberg-Marquardt algorithm

LPI local position invariance

LSB least significant bit

LOWESS Locally Weighted Scatterplot Smoothing

MJD modified Julian date

MOT magneto-optical trap

MSB most significant bit

MVAR Modified Allan variance

NEG non-evaporable getter

NIST National Institute of Standards and Technology

NDM non-demolition measurement

NMI National Measurement Institute

NPL National Physical Laboratory

NA numerical aperture

ODE ordinary differential equation

OFHC oxygen-free, high thermal conductivity copper

OOL out of loop

OP Observatoire de Paris

PCB printed circuit board

PCF photonic-crystal fibre

PDF probability density function

PDH Pound-Drever-Hall (see [206])

PID Proportional Integral Differential control

PM polarisation maintaining

PMT photo multiplying tube

PSD Power Spectral Density

PTB Physikalisch-Technische Bundesanstalt

QCL Quantum Cascade Laser

QED quantum electro-dynamics

QHO quantum harmonic oscillator

QPN Quantum Projection Noise

RAM residual amplitude modulation

RBW resolution bandwidth
RF radio-frequency
RHS right-hand side
RMS root of the mean squared
RWA rotating wave approximation
SCPI Standard Commands for Programmable Instruments
SI International System of Units
SHG second harmonic generation
SHO simple harmonic oscillator
SMD surface-mount device
SNR signal-to-noise ratio
SRF series resonant frequency
SYRTE Systèmes de Référence Temps-Espace *(Reference Systems for Time and Space - a department of Observatoire de Paris)*
TA tapered amplifier
TAI International Atomic Time *(Temps Atomique International)*
TCR temperature coefficient of resistance
TDC time to digital converter
TDSE time-dependent Schrödinger equation
TRL technology readiness level
TT Terrestrial Time
TTL transistor–transistor logic
TWSTFT Two-Way Satellite Time and Frequency Transfer
UHV ultra-high vacuum
UI user interface
ULE ultra-low expansivity
USB universal serial bus
UTC Coordinated Universal Time
UV ultra-violet
UVFS UV-grade fused silica
VANTA Vertically Aligned Nanotube Array
XHV extremely high vacuum

Index